Forschungszentrum Karlsruhe
Technik und Umwelt

Nuclear Fusion Project
Annual Report of the
Association Forschungszentrum
Karlsruhe/EURATOM
October 1998 – September 1999

Projekt Kernfusion

Dezember 1999

Forschungszentrum Karlsruhe

Technik und Umwelt

Wissenschaftliche Berichte

FZKA 6400
EUR 19326 EN

Nuclear Fusion Project
Annual Report of the
Association Forschungszentrum Karlsruhe/
EURATOM
October 1998 - September 1999

compiled by G. Kast
Projekt Kernfusion

Forschungszentrum Karlsruhe GmbH, Karlsruhe
1999

Preface

Harnessing fusion energy is the primary motivation and the long-term objective of the coordinated fusion R+D effort in Europe. Worldwide, conversion of solar energy and the use of nuclear fusion power have a high potential to be the main sources of energy in the distant future when the supply of fossil fuels gets exhausted. This scenario may be accelerated by global warming effects due to emissions of carbon dioxide.

Fusion energy offers the promise of a safe, inexhaustible and environmentally clean energy source. In how far these features can become reality in a technically feasible and economically attractive system, remains to be demonstrated.

Development has progressed to a state where longer pulses and generation of multimegawatt power require new technologies integrated in a large experimental facility, the "Next Step". This Next Step, named International Tokamak Experimental Reactor (ITER) is nearing completion of its engineering design.

For the ITER project, Forschungszentrum Karlsruhe developed and started testing on a large scale of superconducting magnets to confine the plasma, of gyrotron type microwave generators to start the nuclear burn, and of exhaust gas pumping and fuel clean-up systems. ITER will demonstrate the physics of a reactor grade plasma implementing already these essential reactor technologies.

Tritium, one of the fuel components that catalyses the fusion reaction, will be produced in a nuclear fusion reactor by reactions of fusion neutrons within a lithium containing breeding blanket. Development of an energy convertor that delivers high grade heat and supplies enough tritium to maintain the operation is one of the most challenging engineering tasks undertaken by the Association in the frame of the European Blanket Project.

Cost and environmental characteristics of future fusion reactors will crucially depend on solutions to the structural materials issue. Radiation damage from fusion neutrons and high loads of heat and mechanical stresses are expected to limit the lifetime of plasma near components and to determine the amount and radioactivity of waste. The development of low activation radiation resistant steels requires a long term programme proceeding stepwise to final qualification in a large dedicated fusion neutron source. The Association devotes a major activity in this field of work.

The European fusion programme establishes the main frame of cooperation, intensified recently by the European Fusion Development Activity (EFDA). Within EFDA, the exploitation of the Joint European Torus is organised including contributions of Forschungszentrum Kalrsruhe to fuel cycle technologies.

The tokamak represents the main development line of the common programme. In parallel, the stellarator concept is under development to potentially improve the confinement for reactor operation. The Association, assisted by the University of Stuttgart, contributes the complete 10 megawatt microwave heating installation to the Wendelstein-7X stellarator, being built by the IPP-EURATOM Association in Greifswald, Germany.

About 150 professionals and technicians are involved in the Association fusion programme with additional support of the central technical departments.

Progress in 1999 is compiled in the present report that may inspire the reader to contact the experts or the project managers for more information.

J.E. Vetter

Contents   Page

Preface

EFDA Technology Programme related to the Next Step

EFDA Technology Programme related to the Next Step

The Association FZK-EURATOM contributes to various fields of the European Next Step Fusion Technology Programme. The work is strongly focused on the ITER Engineering Design Activity. Development of superconducting magnets and microwave heating systems are equally important for the stellarator project Wendelstein-7X.

In the field of superconducting magnet technology the Karlsruhe Research Center plays an important role in qualifying large superconducting magnets for the fusion application. Already under IEA collaboration of the Large Coil Task FZK had been involved in the development and pretesting of the Euratom Coil that had afterwards been integrated and successfully operated in a 6 coils assembly at ORNL, USA. The LCT coil, built from NbTi conductor is still serving as a background field coil to simulate forces and to increase the field of a neighbouring test coil. In 1999 the prototype coil for Wendelstein-7X underwent extensive testing with an overall satisfactory result.

The test facility TOSKA is prepared to receive, beginning of 2000, the toroidal field model coil for ITER, product of one of the 7 large projects of ITER r+d.

Additional EFDA work relates to structural integrity of the ITER coil system, studies on accident sequences and on qualification of materials at cryogenic temperatures. To decrease the heat flow to helium temperatures in the electrical fieldtroughs current leads are under development that profit from the reduced electrical resistivity of high temperature superconductors.

Microwave technology plays an increasing role not only for plasma heating, but also for non-inductive current drive and plasma shaping both for tokamaks and stellarators. The target are gyrotrons operating around 150 GHz with outputs of 1 MW or more in the cw-mode. In close collaboration with industry the development focuses on a novel high power gyrotron with a coaxial resonator and the potential for frequency tuning and energy recovery from the electron beam to improve the efficiency. For Wendelstein-7X FZK has the duty to provide the complete plasma heating system based on 10 gyrotrons with 1 MW output each at a fixed frequency of 140 GHz. An important component besides power generation is its transmission to the plasma chamber. Quasioptical transmission lines are developed at the University of Stuttgart, whereas the covers at both ends which have to be windows with minimal electrical losses and at the same time reliable barriers against vacuum and tritium leakage have evolved from a comprehensive research at FZK and collaboration with industry and JAERI. Synthetic diamond has proven to be the best solution because of its extremely favorable dielectric and thermal properties, and windows with an aperture of 80 mm have been realized that are suited for 1 MW cw transmission. Present investigations have to determine the maximum tolerable neutron load, an issue that is especially important for burning fusion devices.

Tritium recovery from various sources and systems in a Next Step device represents a major task. FZK has undertaken to develop a suitable method for tritium recovery from the plasma exhaust gas that at the same time complies with the requirements for reliability, ecology and safety. This method based on permeation, catalytic conversion and isotope exchange steps fulfils the specification of a decontamination factor in the 10^8 range and has been adopted for ITER. It is now being demonstrated on a technical scale in our Tritium Laboratory (the only one that will be available in Europe in the future for this purpose) with an inventory of presently 25 g tritium that can be increased up to 40 g if necessary. As a side effect a number of novel instrumentation, process control and accountancy issues are being realized and tested. The powerful infrastructure of the tritium lab is now also being used to address specific issues of JET operation wherever tritium comes into play.

In the context of exhaust gas handling torus pumping is also a subject of R&D work at FZK. It could be shown that cryopumping can comply with all boundary conditions of an ignited fusion device, e.g. tritium issues, helium and impurity removal, high magnetic fields, neutron load and radiation heating. Based on extensive experimental work a cryosorption pump was specified for ITER and a model pump at a 1:2 scale has been built by industry. Preparations for performance testing of this device at FZK are almost complete, and the test programme is expected to start in the first half of this year.

A small number of individual activities, based on available expertise and testing facilities, has been ongoing for ITER contributing to the field of Plasma Facing Components. They cover three different aspects of First Wall behaviour under the impact of the plasma: tritium uptake, plasma erosion and cyclic heat load.

Heating and Current Drive

DG 13
Ceramics for Heating and Current Drive and Diagnostic Systems (includes ITER Tasks DG 13 and ECH 2)

The material studies focused on the investigation of specific CVD diamond grades and geometries for assessing their spectrum of applicability in electron cyclotron resonance heating (ECRH) as well as in diagnostic systems. The development of output windows for Megawatt gyrotrons sustaining continuous wave operation required the characterization of the dielectric loss of large area discs (diameter $\geq$ 100 mm, thickness $\geq$ 1 mm) which were produced by De Beers (Charters, UK). The study of their tolerance to neutron irradiation was based on post-irradiation measurements performed with a set of discs with smaller diameter (30 mm or 40 mm) representing different development stages ('refinement', 'scale-up' and 'window' grade) at De Beers [1]. For diagnostic systems (such as ECE) alternative grades grown at FhG-IAF were selected to back-up the material spectrum for relaxed size requirements (30 mm dia.).

Large discs from De Beers were inspected which were produced with process conditions that are designed to give a trade-off between low millimeter wave losses and cost effectiveness. For a set of 4 discs (106 mm dia.) acquired by FZK within the gyrotron window development task, comparable loss profiles were found especially for the centre of the discs with certain individual increases towards the edges. The medium loss values ranged between $2.2 \cdot 10^{-5}$ and $3.4 \cdot 10^{-5}$ at 145 GHz [2]. Two of these discs, one with a thickness adjusted for 140 GHz gyrotrons (1.81 mm) and the other one adjusted for 170 GHz gyrotrons (1.86 mm) were measured in a newly established facility for high temperature measurements. Even though there remained some uncertainty because of different possible approaches in data evaluation, it was obvious that both discs exhibited very moderate increases in dielectric loss with increasing temperature at least up to 750 K (cf. Fig. 1) [3]. The large disc designed for 170 GHz gyrotrons was later irradiated at the HFR (Petten) facility to neutron fluence of $0.9 \cdot 10^{21}$ n/m^2. Preliminary post-irradiation experiments do not give marked indications for a critical degradation of dielectric properties.
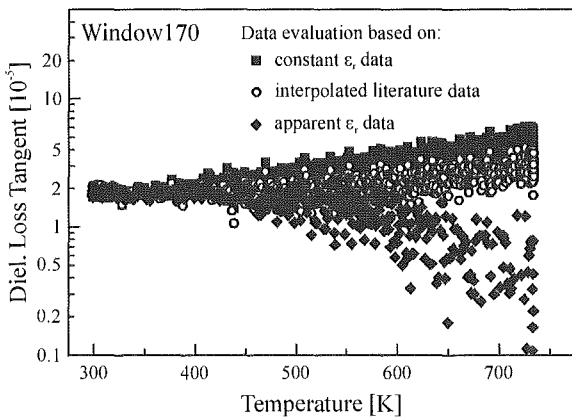
Fig. 1: The dielectric loss of a large area diamond window determined by high temperature open resonator measurements at 145 GHz

In parallel, a neutron irradiation to a fluence of 10^{22} n/m^2 (E > 0.1 MeV) at GKSS (Geesthacht) concluded the irradiation test sequence of the small CVD diamond discs. The post-irradiation measurements proved serious degradation of the thermal conductivity (cf. Fig. 2) [4], and the onset of significant changes in both the permittivitiy and the dielectric loss tangent [5].
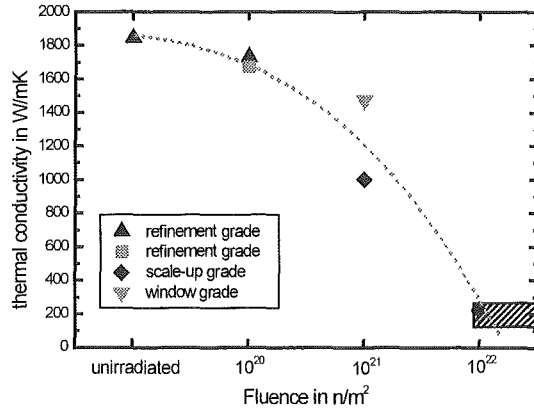
Fig. 2: The thermal conductivity measured in CVD diamond specimens after fast neutron irradiation.

Data sets for ECE diagnostic applications were obtained by measurement facilities covering the ranges of 90 – 100 GHz, 144 – 146 GHz and 188 – 190 GHz. The first investigations on the small neutron-irradiated discs showed no strong frequency variation. The pre-irradiation measurements for the discs produced by FhG-IAF proved that comparable loss levels can be realized with these grades (cf. Table 1). Further discs with 11 mm diameter were received for mechanical strength tests which were split into two sets. One set was irradiated at GKSS Geesthacht in September and will be tested together with the control set by the ball-on-ring method after delivery to FZK.

Table 1: Frequency variation observed for selected CVD diamond materials in the mm-wave range.

Specimen/grade	Tan δ [10^{-5}]		
	95 GHz	145 GHz	190 GHz
DB7/window (n-irr. 10^{21} n/m^2)	2.0 ($\pm$ 0.5)	2.0 ($\pm$ 0.5)	–
DB7/window (n-irr. 10^{22} n/m^2)	4.0 ($\pm$ 1.0)	5.0 ($\pm$ 1.0)	6.0 ($\pm$ 2.0)
ER55/diagnostic (unirradiated)	3.0 ($\pm$ 0.5)	1.5 ($\pm$ 1.0)	2.0 ($\pm$ 1.0)

Literature:

[1] R. Heidinger, A. Ibarra, J. Molla,
Pre- and post-irradiation studies on mm-wave losses in reference window materials for electron wave systems, J. Nucl. Mater. 258-263 (1998), 1822-1826

[2] R. Spörl, R. Heidinger, R. Schwab
Dielectric measurements on state-of-the-art CVD diamond materials
Proc. 11th Joint Russian-German Meeting on ECRH and gyrotrons, 23-29/06/99, Karlsruhe-Stuttgart-Garching

[3] R. Spörl, R. Heidinger, R. Schwab
Dielectric characterization of CVD diamond windows at elevated temperatures
Dig. 24th Int. Conf. on IR+MM Waves, Monterey (USA) 1999

[4] M. Rohde
Photoacoustic measurements of thermal conductivity in unirradiated and irradiated CVD diamond
Proc. 11th Joint Russian-German Meeting on ECRH and gyrotrons, 23-29/06/99, Karlsruhe-Stuttgart-Garching

[5] R. Heidinger
Post-irradiation studies of high power window materials
Proc. 11th Joint Russian-German Meeting on ECRH and
gyrotrons, 23-29/06/99, Karlsruhe-Stuttgart-Garching

Staff:

R. Heidinger
P. Severloh
R. Spörl

ITER ECH Window Development (ECH 2)

1. Introduction

Gyrotrons with high unit power (in excess of 1 MW) and high-efficiency significantly lower the cost of Electron Cyclotron Wave (ECW) systems by reducing the amount of the auxilliary support equipment (power supplies, cooling system, number of SC-magnets, ...). Continuous wave operation is required for some of the anticipated ITER applications: 3 s for start-up, 100 s for heating to ignition and 100-1000s for current drive. In order to perform these functions for ECW systems a window has to be developed to serve as both the tritium containment barrier on the torus and as the output window of the tube. The former application is technically more demanding as the torus window must also serve as a high pressure barrier during off-normal events (0.5 Mpa overpressure capability). It should not use FC-cooling liquids, must not degrade unacceptably under modest neutron and γ (including x-rays) irradiation, and, in the case of cryo-cooling, must be prevented by a cold trap from cryo-pumping.

A very promising material is chemical vapor deposited (CVD)-diamond which nowadays can be manufactured in window disks of up to 120 mm diameter and 2.5 mm thickness [1, 2]. A water cooled diamond window would provide two very important advantages, namely employing a cheap and simple as well as effective coolant.

2. 1 MW,170 GHz, CW CVD-Diamond Window

The design of a 1 MW, 170 GHz, CW, CVD-diamond window unit that fits to the Russian long-pulse ITER gyrotron was completed (see Fig. 1) [3-7]. The window unit employs a single, edge cooled (water, 20°C) CVD-diamond disk with an outer diameter of 119 mm, an aperture diameter of 100 mm and a thickness of 2.222 mm ($6\lambda/2$). The outer rim for water cooling is 5 mm wide. Thermal finite element computations for a power of 1 MW at 170 GHz, a loss tangent of around $2 \cdot 10^{-5}$, a thermal conductivity of 1800 W/mK (at room temperature) and a heat transfer coefficient of 12 kW/m^{2}K to the cooling water (water flow: 13.5 l/min, water flow velocity: 2 m/s) show that the central window temperature will not be higher than approx. 64° C and the edge temperature is about 28° C. The absorbed power is lower than 530W. The simulations also show that steady state conditions are achieved in approximately 5 seconds.

The 170 GHz CVD-diamond window unit (Fig.1) of the Forschungszentrum Karlsruhe was welded to the new GYCOM-M 170 GHz ITER gyrotron with a single-stage depressed collector (see Fig. 1). Up to now the experimental parameters are very promising: 0.7 MW, 0.5 s, 45% efficiency, without any problems with the window.

3. Irradiation studies

The post-irradiation studies on small disks of advanced CVD-diamond grades ('scale-up' and 'window' grade) were completed with the dielectric and thermophysical measurements performed on the specimen set irradiated to the final fast neutron fluence of 10^{22} n/m^2 (E > 0.1 MeV). After previous irradiations of 10^{20} n/m^2 and 10^{21} n/m^2 no apparent indications for the degradation of dielectric properties were observed. For the thermal conductivity however, at the latter neutron flux a slight reduction was already measured (650-1450 W/mK). Substantial radiation induced changes in the dielectric properties were identified at the fluence level of 10^{22} n/m^2. Independent of the diamond grade, the permittivity was shifted from 5.67 to 5.73 and dielectric loss levels were increased by a factor of 2-3 at

millimeter waves (90 GHz, 145 GHz). A very pronounced effect was found for the thermal conductivity, where after the final irradiation thermal conductivity levels of 200 W/mK were identified which have to be compared to the initially very high levels of 1700-1800 W/mK.
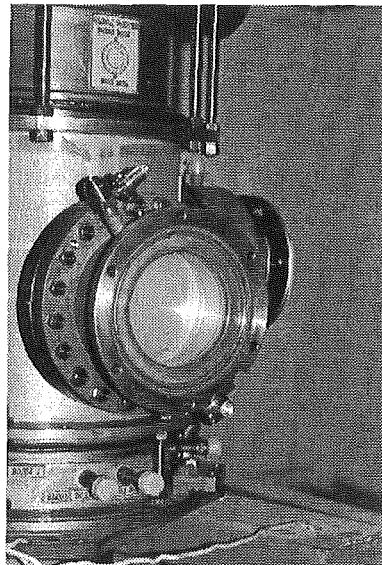
Fig. 1: 1 MW, 170 GHz, CW, CVD-diamond window.

For the test of a 170 GHz torus window unit for ITER which uses a CVD-diamond disk irradiated with fast neutrons to a fluence of 10^{21} n/m^2 (E > 0.1 MeV), the pre-irradiation characterisation of the window material was performed with respect to the dielectric parameters at millimeter wavelengths. Together with this disk (106 mm dia., 1.85 mm thick), another disk designed for a 140 GHz (106 mm dia., 1.80 mm thick) has been inspected for comparison. At 145 GHz, the temperature dependence of the dielectric loss was measured up to 750 K with a specially established dielectric measurement set-up. Also spatially re-solved loss measurements were performed at 145 GHz to de-termine the degree of homogeneity over the disks. Both disks, which were grown by DeBeers under conditions that give a trade-off between growth costs and low dielectric loss, showed very similar behaviour in the absolute levels of the temperature and frequency dependent losses. The important variations occurred within the disks where the loss profiles gave evidence of distinct zones with higher loss at the edge of disks. By ana-lysing the accumulated fraction of the disk with losses up to a given value, quantitative figures could be given to characterise the degree of the homogeneity. The 170 GHz window disk was found to have a 10% fraction with tanδ below 1.2×10^{-5} and a 90% fraction below 7.6×10^{-5} to be compared to values of 1.2×10^{-5} and 5.0×10^{-5} for the 140 GHz disk, respectively. Mean values were 3.4×10^{-5} and 2.9×10^{-5}, respectively. The 170 GHz disk was irradiated at the reactor HFR Petten with a fluence of 10^{21}n/m^2.

Literature:

[1] Thumm, M., Int. J. of Infrared and Millimeter Waves, 19, 3-14, 1998.

[2] Kasugai, A., Ballington, D.C., Beale, A., Brandou, I.R., Braz, O., Kariya, T., Sakamoto, K., Sussmann, R.S., Takahashi, K., Rev. Sci. Instr. 69, 1998, 2160-2165.

[3] Thumm, M.,Braz, O., Heidinger, R., Spörl, R., Severloh, P., Wissenschaftliche Berichte FZKA-6179 (Oct 1998).

[4] Thumm, M., Braz, O., Heidinger, R., Spörl, R., Arnold, A., Severloh, P., Wissenschaftliche Berichte FZKA-6257 (Feb 1999).

[5] Thumm, M., Braz, O., Iatrou, C.T., Heidinger, R., Henry, S., Makowski, M., Spörl, R., Szczesny, J., Wissenschaftliche Berichte FZKA-6255 (Feb 1999).

[6] Thumm, M., Arnold, A., Heidinger, R., Rohde, M., Spörl, R., Proc. 5th Biennial Int. Workshop on ECH Transmission Systems, Sept 1-3, 1999, Carmel, California.

[7] Thumm, M., Braz, O., Heidinger, R., Makowski, M., Spörl, R., Conf. Digest 24th Int. Conf. Infrared and Millimeter waves, 1999, Monterey, California, USA, PS-5.

Staff:

A. Arnold (Uni Karlsruhe)
R. Heidinger
M. Rohde
P. Severloh
R. Schwab
R. Spörl
M. Thumm

ITER ECH Gyrotron Development (ECH 3)

1. Introduction

Electron cyclotron resonance heating (ECRH) is one of the major candidates for additional heating and current drive (170 GHz, 50 MW) and for start-up (90-140 GHz, 3 MW) on the ITER tokamak and will be the main start-up and heating scheme on the stellarator W7-X (140 GHz, 10 MW) at IPP Greifswald, Germany.

The main physics advantage of ECRH is the possiblity of well localized power absorption, where the deposition region is defined by the crossing of the ECR layer with the rf-beam. The technology advantages of ECRH are as follows. Antennas can be located far from the plasma, thus avoiding impurity release and providing decoupling of heating from particle refuelling. Compact optical antennas allow very high injected power densities (in excess of 100 MW m^{-2}), implying the use of fewer ports. Millimeter-wave vacuum windows provide a tritium barrier in the waveguide separating the vessel from the source so that the sources can be placed in a "hands-on" location far away from the plasma.

Two gyrotrons operated in different modes are investigated at FZK. The FZK $TE_{22,6}$ tube has obtained a maximum output power of 2.1 MW at an efficiency of 53 % [1,2].

2. Advanced Coaxial Cavity Gyrotron

The limiting factors of conventional cavities can be considerably reduced with the use of coaxial cavities, which offer the possibility of operation in high order volume modes with reduced mode competition problems. Furthermore, the presence of the inner conductor practically eliminates the restrictions of voltage depression and limiting current. Therefore gyrotrons with coaxial cavities have the potential to generate, in CW operation, rf-output powers in excess of 1 MW at frequencies above 140 GHz.

The $TE_{31,17}$ coaxial cavity gyrotron [3,4] was operated with a single output window. The $TE_{31,17}$ mode was found to oscillate in a single-mode over a wide voltage range, in good agreement with calculations. A maximum rf-output power of 1.7 MW at a beam current of I_b = 69.7 A and a cathode voltage U_c = 93.2 kV was achieved with a pulse length around one ms. The maximum output efficiency of 27.3% was measured at an output power of 1.3 MW with I_b = 52.2 A at a magnetic field B_{cav} = 6.65 T. About 12% of the generated rf-power are estimated to be lost inside the tube (Ohmic and diffraction losses). There is good agreement between the experimental values and the results of numerical calculations. Because of the high Q-value of the cavity of about 3000 overbunching occured at the operating parameters which prevented higher efficiencies.

Measurements on step frequency tuning were performed by a slow variation of the magnetic field of the superconducting magnet with the gyrotron designed for operation in the TE-31,17 mode at 165 GHz. Since the maximum achievable magnetic field is limited to about 6.7 T, mainly modes below the design mode could be excited. In the frequency range between 134 and 169.5 GHz 19 different modes were excited in single mode operation with a spacing of about 2.2 GHz with significant rf-output power. The excited modes belong to four families, namely $TE_{-m,14}$, $TE_{-m,15}$, $TE_{-m,16}$ and $TE_{-m,17}$. The modes were identified by comparing the measured frequency with the calculated values. In all modes there was an agreement within ± 100 MHz. The magnetic field in the cavity varies approximately linearly with the frequency, $B_{cav} \propto f$. The cathode voltage and the

electron beam radius ($\propto$ magnetic compression b) were adjusted independently for the different modes. Due to the diode type gun the velocity ratio α varied between about 1.1 and 1.5 depending on the operating parameters. In the case of the $TE_{-33,17}$ mode the value of α was only about 0.9 because of the low maximum cathode voltage U_c = 75.6 kV which is a consequence of the limitation of the achievable magnetic field. Because of limited experimental time the operating parameters have not been optimized in all modes for maximum rf-output power. However, in the modes $TE_{-27,14}$, $TE_{-28,15}$, $TE_{-30,16}$, $TE_{30,17}$, $TE_{-31,17}$ and $TE_{-32,17}$ for which a careful parameter optimization was done an rf-output power between 1.1 and 1.3 MW with an efficiency between 26 and 27 % was achieved with a beam current $I_b \cong$ 50 A. This confirms the results of the step frequency tuning in the conventional gyrotron. The relatively low value of the rf-power in the $TE_{-33,17}$ mode at 169.5 GHz is due to the low operating cathode voltage.

Recently the coaxial gyrotron was equipped with a new 4.5 MW electron gun to be operated at 90 kV and 50 A. It is a diode-type gun which was designed by FZK [5,6]. Different from the LaB_6 IMIG currently used, the emission of the electrons is not directed towards the coaxial insert but towards the anode similar to conventional MIG gyrotron electron guns. The inner conductor is supported from the gun inner conductor side and can be aligned in a reproducible way in the fully assembled tube. The gun has been fabricated by TTE Vélizy. The advanced quasi-optical mode converter [7-9] for transforming the $TE_{31,17}$ cavity mode at 165 GHz into a single rf-output wave beam (only one output window) consists of a simple launcher and two mirrors. The first mirror is quasi-elliptical and the second mirror has a non-quadratic phase-correcting surface. The gyrotron tube was assembled with these new components and is ready for operation [10].

3. Fast Frequency Step Tuning

Fast frequency-tunable gyrotrons are of interest for controlling instabilities in magnetically confined plasmas. As a first step the possibilty of frequency tuning of the $TE_{22,6}$ gyrotron has been proven by a slow variation of the magnetic field. The main problem of this frequency step tuning is the large time constant of magnetic field variation in large superconducting magnets. To get a faster frequency tuning a small auxilliary normal conducting magnet located inside the superconducting-solenoids has been proposed [11].
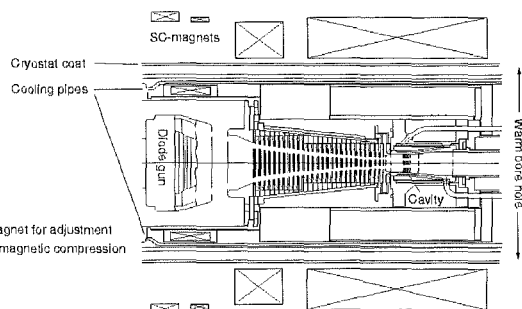
Fig. 1: Gyrotron with hybrid magnet system consisting of the cryostat magnets and two normal conducting solenoids inside the warm bore hole.

This magnetic system consisting of the superconducting magnets in the cryostat and two normal conducting magnets placed

in the warm bore hole around the gyrotron (Fig. 1) was designed and built [12].

Literature:

[1] Dammertz, G., Braz, O., Chopra, A.K., Koppenburg, K., Kuntze, M., Piosczyk, B., Thumm, M., IEEE Trans. on Plasma Science 27 (2), 1999, 330-339.

[2] Kuntze, M., Borie, E., Dammertz, G., Piosczyk, B., Thumm, M., Conf. Digest 24th Int. Conf. Infrared and Millimeter Waves, 1999, Monterey, California, USA, W-A6.

[3] Thumm, M., Piosczyk, B., Braz, O., Dammertz, G., Kuntze, M., Michel, G., Wissenschaftliche Berichte FZKA-6216 (Oct 1998).

[4] Dumbrajs, O., Anderer, I., Illy, S., Piosczyk, B., Thumm, M., Zewolsky, N.A., IEEE Trans. on Plasma Science 27 (2), 1999, 327-329.

[5] Piosczyk, B., Braz, O., Dammertz, G., Iatrou, C.T., Illy, S., Kuntze, M., Michel, G., Thumm, M., IEEE Trans. on Plasma Science 27 (2), 1999, 484-489.

[6] Piosczyk, B., Braz, O., Dammertz, G., Kuntze, M., Michel, G., Möbius, A., Thumm, M., Wissenschaftliche Berichte FZKA-6256 (Feb 1999).

[7] Michel, G., Wissenschaftliche Berichte FZKA-6216 (Dec 1998).

[8] Arnold, A., Wissenschaftliche Berichte FZKA-6108 (Nov 1998).

[9] Braz, O., Wissenschaftliche Berichte FZKA-6164 (Oct 1998).

[10] Piosczyk, B., Braz, O., Dammertz, G., Kuntze, M., Michel, G., Lamba, O.S., Thumm, M., Conf. Digest 24th Int. Conf. Infrared and Millimeter Waves, 1999, Monterey, California, USA, TU-A9.

[11] Koppenburg, K., Piosczyk, B., Thumm, M., Conf. Digest 24th Int. Conf. Infrared and Millimeter Waves, 1999, Monterey, California, USA, W-D5.

[12] Koppenburg, K., Piosczyk, B., Thumm, M., Conf. Digest 23rd Int. Conf. Infrared and Millimeter Waves, 1998, Colchester, 124-125.

Staff:

J. Anderer (Uni Karlsruhe)
A. Arnold (Uni Karlsruhe)
H. Baumgärtner
E. Borie
H. Budig
G. Dammertz
O. Drumm (Uni Karlsruhe from 01.04.99)
O. Dumbrajs (guest scientist from 01.02.99)
S. Illy
M. Kartikeyan (guest scientist from 26.11.98)
K. Koppenburg (Uni Karlsruhe)
H. Kunkel
M. Kuntze
G. Ling (guest scientist from 09.10.98)
G. Michel (Uni Karlsruhe to 30.06.99))
B. Piosczyk
J. Szczesny
M. Thumm
R. Vincon

Plasma Facing Components

DV 7a
Tritium Permeation, Retention, Wall Conditioning and Clean-up (Dust Removal, Baking)

Knowledge of trapping mechanisms of hydrogen isotopes in beryllium oxide is of interest to all beryllium applications for fusion technology. There are evidences that near-surface oxide layers govern the hydrogen permeability through beryllium [1]. Tritium retention in BeO might contribute significantly to the total tritium co-deposition, especially at elevated temperatures [2]. Chemical trapping by BeO inclusions plays essential role in tritium retention and release from neutron irradiated beryllium [3].

Thermal desorption spectra of D_2 and HD molecules from Be samples irradiated at 300 K are shown in Fig.1a. A single peak at 750 K is seen in spectrum of Be specimen irradiated to a low fluence of 2×10^{20} D/m^2. The release of practically all the implanted deuterium is registered in this peak. Thus, at low fluence ~100% retention is observed, in full agreement with results published earlier [4,5]. It is essential that no measurable desorption was detected from tBeO samples irradiated to the low fluence.

An additional peak at 470 K is developed in spectrum of Be irradiated to fluence of 2×10^{21} D/m^2 while both position and population of high temperatures peak, characteristic for low fluence irradiation, remain practically unchanged. For this high fluence, a significant desorption is registered also from tBeO samples. One feature of tBeO is that the spectrum is extended to 1100 K while heating only to 800 K is sufficient to degass fully the Be samples.

An important information about the nature of trapping sites is obtained from an evolution of TD spectra with increasing of irradiation temperature. The spectrum of Be irradiated to a fluence of 2×10^{21} D/m^2 at 600 K is shown in Fig.1b. A narrow peak is developed at 650 K while the peak at 470 K, found after R.T. implantation, is absent. We suggest that the sharpness of both peaks results from the fracture processes occurring in the ion stopping zone at temperatures where trapped deuterium starts to liberate from some deuterium complexes.

For 300 K irradiation, such complexes are deuterium atoms chemisorbed on the inner surfaces [6] and/or the inclusions of amorphous beryllium hydride BeD_2 formed under D ion irradiation [7]. Notice that the desorption of the first and decomposition of the second occur approximately at the same temperature of ~500 K. It is well established that the release of implanted deuterium around 700 - 800 K is controlled by dissociation of deuterium-vacancy complexes formed under D ion irradiation [8]. The nature of the peak at 650 K might therefore be in fracture processes caused by deuterium release from the vacancy complexes. Contrary to metallic beryllium, the tBeO samples exhibit the more deep deuterium trapping at elevated irradiation temperatures (Fig.1c). Increasing the irradiation temperature to 600 K and further to 900 K leads to development of a single well-defined peak at 900 - 1000 K that might be ascribed to the formation of additional deep traps for implanted deuterium.

Total amounts of retained deuterium determined by integration of D_2 and HD release spectra, as a function of irradiation temperature are shown in Fig.2. As seen, retained amounts for Be are slightly decreased whereas for tBeO remain unchanged with irradiation temperature.
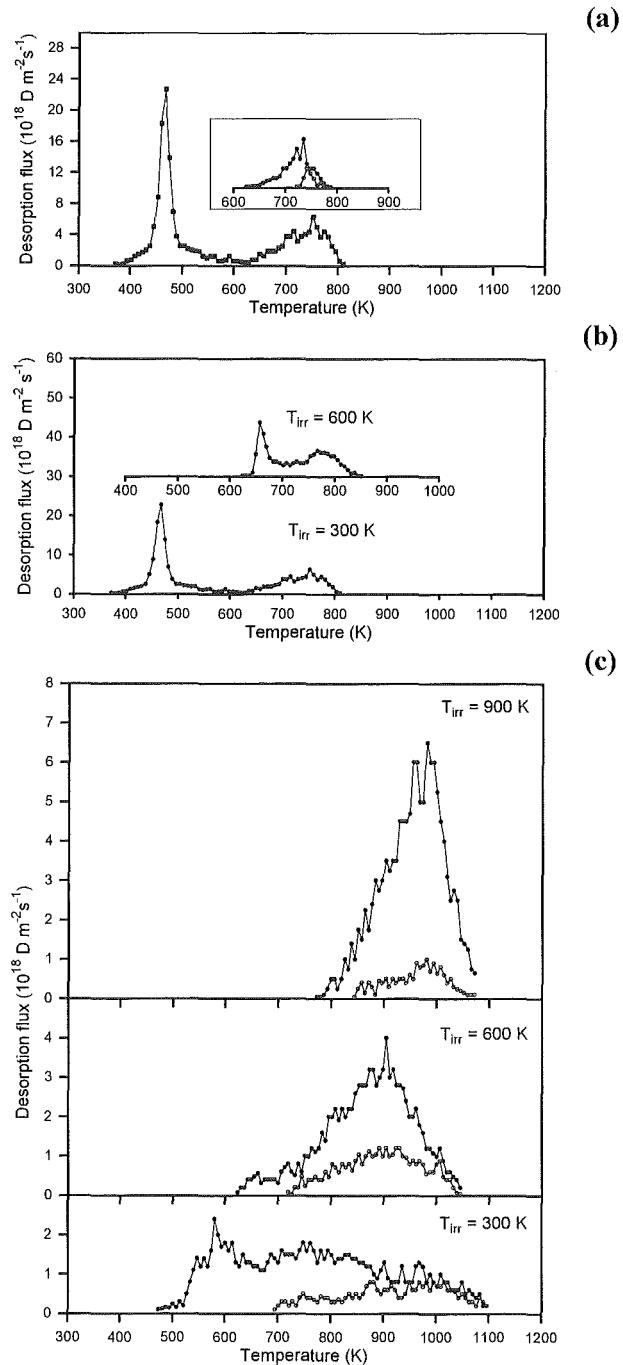
Fig. 1: Thermal desorption of D_2 (filled symbols) and HD molecules (open symbols) from Be irradiated with 400 eV D ions (a) to 2×10^{20} D/m^2 (shown in box) and to 2×10^{21} D/m^2 at 300 K, (b) to 2×10^{21} D/m^2 at 600 K and (c) from tBe irradiated to 2×10^{21} D/m^2 at different temperatures.
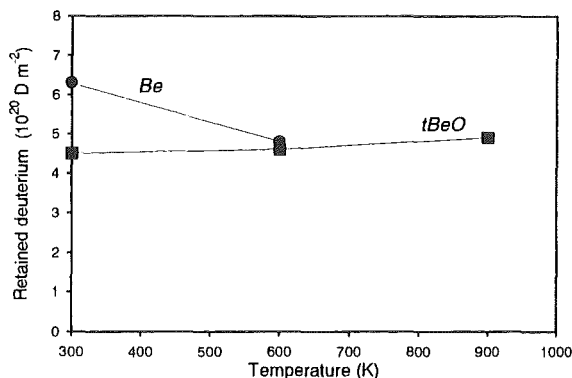
Fig. 2: Temperature dependence of deuterium retention in *Be* and *tBeO* irradiated with 400 eV D ions to 2×10²¹ D/m².

It is of interest to analize the results of present work from tritium codeposition standpoint. According to the remark in [9], hydrogen retention in codeposited layers might be readily related to hydrogen behavior in materials under ion implantation. In Fig.3 are collected the data on thermal stability of hydrogen saturated layers formed on the surface of D ion irradiated beryllium oxide, beryllium and graphite, obtained in present work, by Möller et al. [4] and Doyle et al. [10], respectively. Two dependences are shown for each material: (1) an amount of deuterium retained under RT ion irradiation as function of temperature of the isochronal post-implantation annealing or the linear temperature ramping and (2) the dependence of retained amounts on irradiation temperature. Both dependences are normalized to R.T. retention.
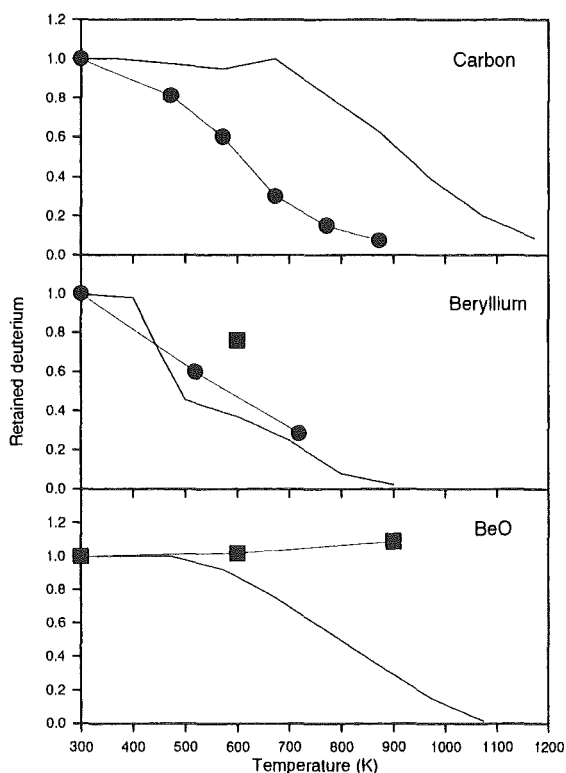
Fig. 3: Deuterium retention in carbon [10], beryllium (circles [4] and square [this work]) and beryllium oxide [this work] irradiated with D ions at different temperatures (symbols) as compared with thermal desorption curves measured after 300 K implantation. All data are normalized to retention at 300 K.

As seen from Fig.3, relative positions of (1) and (2) along the temperature axis are specific for each of the materials in question. Dependence (2) for carbon is shifted to left by about 300 K compared to (1) one. For beryllium metal, saturated amounts in the samples irradiated with 3 keV D ions at 520 and 720 K agree well with thermal desorption curve, whereas for beryllium oxide, present work evidences inverse position of the dependences as compared with carbon.

A possible reason for such a behavior might be the different microstructures formed in the materials under deuterium implantation. It is well established that re-emission flux from D ion irradiated carbon materials is formed via ion-induced detrapping and recombination processes occurring through the ion stopping zone [11]. In other words, there is a possibility for any deuterium traps to be dissociated followed by fast migration of formed D₂ molecules to the outer surface. Therefore, the binding energy of deuterium and carbon atoms is not the only factor governing retention at elevated temperatures.

For beryllium metal, the significant fraction of retained deuterium is located in the cavities [8]. In this case, close correlation between irradiation points and annealing curve found in [4] might be the characteristic property of the microstructure that is developed in beryllium under 3 keV D ion implantation. For irradiation with 400 eV D ions, it was observed that the 600 K point lies somewhat higher than thermal desorption curve.

Contrary to both carbon and beryllium, no temperature dependence of the irradiation points for beryllium oxide has emerged from present study. Again, this might be the characteristic feature of the ion fluence and the ion energy used. However a general trend seems to be obvious. This behavior is, in the context of TDS method, indicative of increasing in concentration of deep traps with rise of irradiation temperature.

There are evidences that a similar behavior seems to be the case for deuterium trapping in the co-deposited films. Fig.4 shows TDS spectra of deuterium from *sBeO* film deposited at 800 K. As seen the main part of retained deuterium is released in the peak centered at 1000 K. For R.T. co-deposition, one can refer to experiments of Mayer et al. [9] where heating to only 800 K was sufficient to complete deuterium release from D/BeO films produced at 300 K.
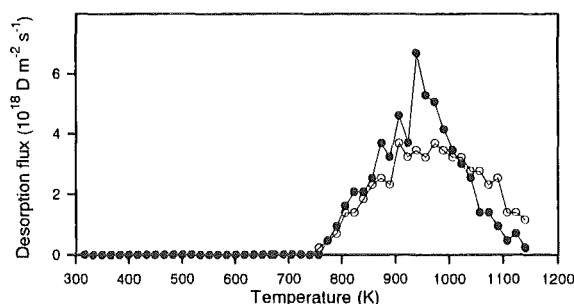
Fig. 4: Thermal desorption of D₂ (filled symbols) and HD molecules (open symbols) from *sBe* film.

Concerning the existence of phases in hydrogen-beryllium oxide system exhibiting high thermal stability, it is well known that apparent thermal stability of beryllium hydroxide depends strongly on preparation method or, another way, on the original microstructure [12]. While Be(OH)₂ starts to decompose at ~500 K, the heating up to ~1100 K is required for the reaction to be driven to completion. One possible explanation is that the residual water vapor is collected in closed pores formed in the course of hydroxide decomposition. If so, at the final stage the

decomposition is governed by slow permeation of water vapor from the pores, probably, in form of hydrogen. In principle, a qualitatively similar mechanism might be responsible for deep deuterium trapping in beryllium oxide observed in the present work for high temperature irradiation.

Literature:

[1]   R.A. Causey, W.L. Hsu, B.E. Mills, J. Ehrenberg, V. Philips, J. Nucl. Mater. 176&177 (1990) 654.

[2]   M. Mayer, J. Nucl. Mater. 240 (1997) 164.

[3]   F. Scaffidi-Argentina, H. Werle, Proc. of the Third IAE International Workshop on Beryllium Technology for Fusion, Mito City, 1997, p. 254-260.

[4]   W. Moller, B.M.V. Scherzer, J. Bohdansky, IPP-JET Report No.26, Garching,(1985).

[5]   W.R. Wampler, J. Nucl. Mater. 122-123 (1984) 1598.

[6]   V. Markin, V.N. Chernikov, S.Yu. Rybakov, A.P. Zakharov, J. Nucl. Mater. 233 - 237 (1996) 865.

[7]   B. Tsuchiya, K. Morita, J. Nucl. Mater. 233 - 237 (1996) 898.

[8]   V.N. Chernikov, V.Kh. Alimov, A.V. Markin and A.P.Zakharov, J. Nucl. Mater. 228 (1996) 47.

[9]   M. Mayer, R. Behrisch, H. Plank, J. Roth, G. Dollinger, C.M. Frey, J. Nucl. Mater. 230 (1996) 67.

[10] B.L. Doyle, W.R. Wampler, D.K. Brice, J. Nucl. Mater. 103 - 104 (1981) 513.

[11] W. Möller, J. Nucl. Mater. 162 - 164 (1989) 151.

[12] Dupuis T.C. r. Acad. sci., 250 (1950) 957.

Staff:

A. E. Gorodetsky
A.V. Markin
F. Scaffidi-Argentina
H. Werle
C.H. Wu
A.P. Zakharov

DV 7b
Plasma Disruption Simulation

1. Introduction

During the period to be reported here the main activities were on validation of the 2 dim radiation-magnetohydrodynamics (R-MHD) code FOREV-2 against results from russian disruption simulation experiments and on application of FOREV-2 for analysis of erosion of the ITER slot divertor during disruptions and ELMs. The damage analysis includes brittle destruction of graphite and melt layer erosion of metallic targets.

Shielding of divertor materials by their own vapor exists during plasma disruptions and ELMs [1]. After formation of a plasma shield the energy finally arriving at the target surface is by direct heating by the hot plasma particles not fully stopped in the plasma shield, by radiation and by thermal energy transfer. To predict erosion by vaporization for the ITER slot divertor a fully consistent 2 dim radiation magnetohydrodynamic (R-MHD) code is necessary not only because of the rather complicated divertor geometry, the reradiation from the plasma shield to the side walls and other nearby components, the finite width of the impacting hot SOL plasma and its characteristic power density profile across the SOL width, but also because of the diamagnetic effect of the plasma shield, and its influence on the plasma shield dynamics and on target erosion [2].

The 2 dim R-MHD code FOREV-2 with its 2 1/2 dim MHD model, its 2 dim angular dependent radiation transport and its consistent solution of the magnetic field equations in the bulk target and the plasma shield now is available for quantification of target erosion by vaporization. The system of equations used in FOREV-2 to solve the 2 dim R-MHD problem of hot plasma target interaction with an external magnetic field is discussed in [3]. Estimations on brittle destruction and melt layer erosion were obtained from 2 dim heat conduction calculations. The heat sources to the bulk target were obtained from Monte Carlo calculations [3].

2. 2 dim analysis of divertor erosion during Tokamak plasma disruptions

FOREV-2 was used for a systematic analysis of erosion by vaporization of the ITER slot divertor, for a study of side wall erosion by reradiation from the plasma shield and for a first analysis of long term plasma shield stability and shielding efficiency for times up to 10 ms. Classical diffusion was assumed for the diffusive part of the magnetic field equations. FOREV-2 was applied for horizontal and vertical graphite targets and tungsten side walls. The side wall distance was assumed to be 60 cm. Peak power densities along the separatrix were varied in the range from 3 to 100 MW/cm^2. The two impact energies 1 and 10 keV were assumed for the hot SOL plasma and the two different power density profiles Gaussian and realistic unsymmetrical were used [3-5].

Fig. 1 shows calculated plasma density distributions and the plasma flow pattern (arrows given as

$$N_c \bullet \vec{v}$$

with N_c the carbon density and $\vec{v}$ the plasma velocity) in a carbon plasma shield 500 μs after start of target heating for a realistic power density $\vec{v}$ profile across the SOL with a step gradient at one side and a less pronounced decrease at the other side of the separatrix for a horizontal target. As is seen from Fig. 1 the plasma all the time flows along the target to the side of the gradual decrease. The shielding layer at the position

of the peak power density continuously is depleted by this plasma flow.
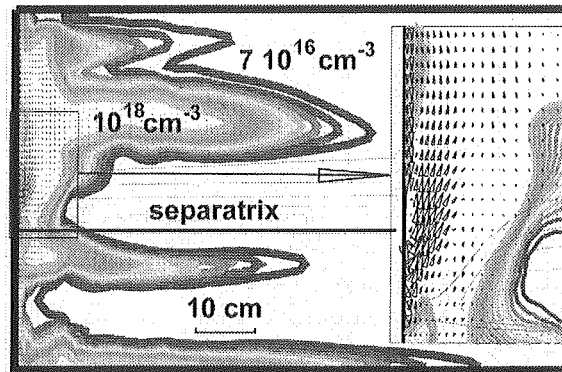
Fig. 1: Calculated 2 dim plasma density and plasma flow (arrows) at 500 μs. Incoming hot plasma 10 keV, realistic power density profile, halfwidth 5 cm, peak power density is 100 MW/cm^2.

Fig. 2 shows target erosion profiles at 0.5 ms for different peak power densities. The depletion of the plasma shield at the location of the peak power density (separatrix strike point) results in rather strong erosion. As long as the peak power density is above 10 MW/cm^2 erosion outside of this peak mainly is caused by radiation resulting in the rather broad erosion profile shown in Fig. 2. For peak power densities below 10 MW/cm^2 erosion during at least 0.5 ms is occurring practically only in the region of the separatrix strike point. Radiation is insufficient for broadening of the erosion profile.
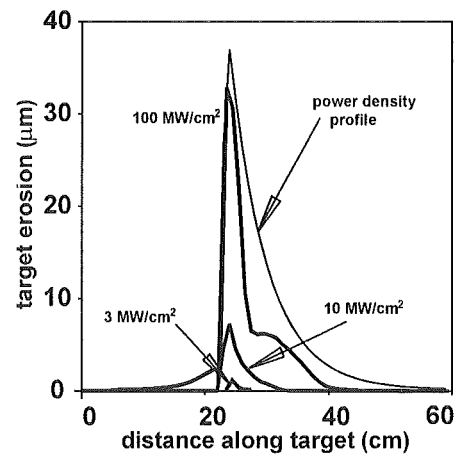
Fig. 2: Calculated target erosion for horizontal graphite target at 1 ms. Realistic power density profile with different peak power densities.

For vertical targets FOREV-2 calculations were performed for separatrix upstream and downstream. Plasma density profiles and the plasma flow pattern (arrows) in the plasma shield are shown in Fig. 3 for the separatrix strike point downstream at 740 μs for a peak power density of 10 MW/cm^2 along the separatrix. The density lines correspond to densities in the range of 7x10^{15} to 10^{17} cm^{-3}. Close to the target the plasma is flowing along the tilted target downwards, then changes its flow direction, forms a plasma bubble and moves outside of the hot plasma impact region towards the upper side wall and upwards (in x direction). The upward velocity typically is 105 cm/s. The plasma bubble with central plasma density of 3$\bullet$10^{17} cm^{-3} has plasma temperatures below 2 eV and is weakly heated by lateral

radiation fluxes of up to 5 kW/cm^2 from the target plasma shield. In case of upstream separatrix strike point, the downward flow results in a depletion of shielding at the position of the strike point, whereas in case of downstream separatrix strike point the downward flow results in an improved shielding at the strike point position and thus in a reduction of the target heat load by the hot SOL plasma. From Fig. 4 it is seen that the erosion profiles are markedly different for both cases and for the downstream separatrix erosion at the strike point is about a factor of 10 less than for the case with upstream strike point.
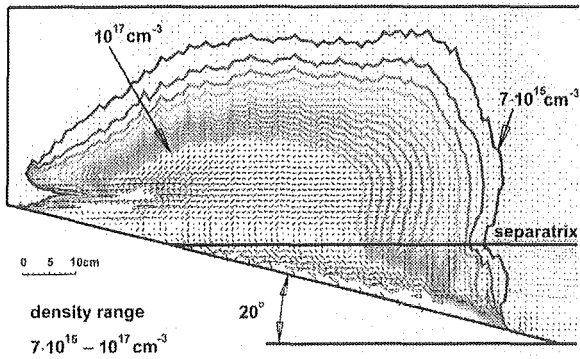
Fig. 3:   2 dim plasma density contours and plasma flow pattern (arrows) in the plasma shield at 740 µs for vertical target with downstream separatrix. Slot width 60 cm, peak power density along the separatrix 10 MW/cm^2.
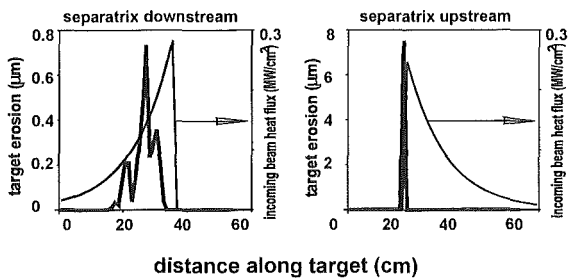
Fig. 4:   Erosion at 1 ms and hot plasma power density profiles for a vertical graphite target. Peak power density along the separatrix is 10 MW/cm^2.

Calculated erosion profiles and corresponding power density profiles again for the cases strike point up- and downstream are shown in Fig. 5 for a peak power density of 100 MW/cm^2. Despite of the tenfold increase of the peak power density the peak erosion for the upward strike point is about a factor of 2 smaller than for 10 MW/cm^2. In case of downstream separatrix erosion at 1 ms just reaches 1 µm and thus remains quite small. The increased width of the erosion profile upstream of the strike point where heating by the hot plasma is negligible indicates erosion by radiation. The vaporized material predominantly flows downward along the target surface as is seen from Fig. 3 and thus increases shielding at the separatrix strike point. This causes a drastic decrease of peak erosion.
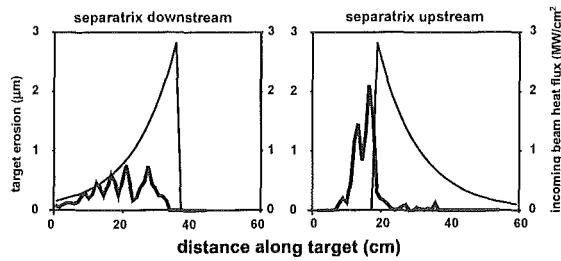
Fig. 5:   Erosion at 1 ms and hot plasma power density profiles for a vertical graphite target. Peak power density along the separatrix is 100 MW/cm^2.

In Fig. 6 calculated peak target erosion values are shown for the horizontal and the vertical graphite target with separatrix upstream for peak power densities of 10 MW/cm^2 and 100 MW/cm^2. Erosion of the horizontal and vertical target at 10 MW/cm^2 are comparable despite a factor of 3 lower heat load of the impacting hot plasma at the vertical target. Erosion of vertical targets and upstream separatrix is smaller at 100 MW/cm^2 than at 10 MW/cm^2. The reason is upstream target erosion by radiation in the 100 MW/cm^2 case and subsequent downward movement of the plasma shield providing increased shielding at the strike point of the separatrix. In the 10 MW/cm^2 case the plasma shield at the separatrix strike point permanently is depleted by downwards flow of the target plasma.
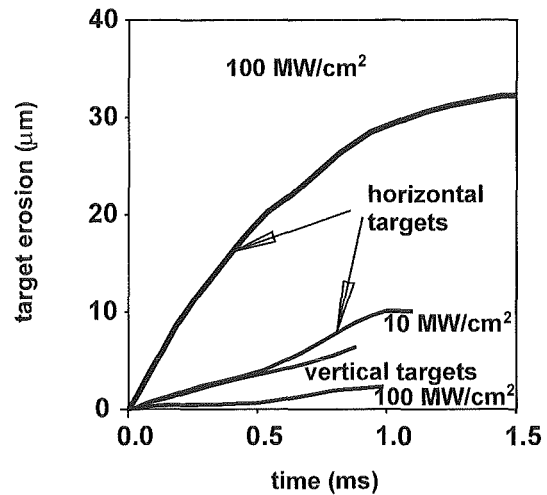
Fig. 6:   Comparison of target erosion for horizontal and vertical graphite target with upstream separatrix. Realistic power density profiles with peak power densities of 10 MW/cm^2 and 100 MW/cm^2 along the separatrix.

The results clearly demonstrate that the plasma shield dynamics sensitively influences the shielding efficiency. The plasma shield dynamics depends on the diamagnetic effect of the plasma shield [3], on the power density profile across the SOL width and on the target orientation. For hard disruptions vertical targets in comparison with horizontal ones favorable reduce the target erosion. For soft disruptions erosion of vertical and horizontal targets is comparable. The conditions for melting and vaporization of side walls by radiation from the evolving plasma shield were quantified. Melting of tungsten side walls occurs only in case of peak power densities above 10 MW/cm^2 along the separatrix.

3. Disruption simulation experiments in plasma gun facilities

The physical properties and the long term stability of plasma shields in the tokamak magnetic field have to be known for a reliable prediction of tokamak divertor erosion but can't be determined in existing tokamaks [3]. Therefore experiments in disruption simulation facilities which allow to produce Tokamak typical plasma shields are necessary together with a 2 dim numerical modeling of the plasma shield dynamics. Most recently obtained experimental results from disruption simulation experiments performed at the upgraded plasma gun facility MK-200 UG [6] at TRINITI Troitsk were compared with numerical results from FOREV-2. In the simulation experiments the targets are either perpendicular to the guiding magnetic field given initially as $\vec{B}_0 = \vec{B}(t = 0) = (B_{xo}, 0,0)$ or tilted with respect to B_{xo}.

3.1 Carbon plasma shield properties at the MK-200 UG facility

At the MK-200 UG facility local measurements of electron temperature and density were performed in a carbon plasma shield by Thomson laser scattering (TS) along the separatrix [6]. A ruby laser beam ($\lambda = 0.6943$ µm) was focused onto the plasma axis. Backward scattered light (at 160°) was detected by a set of photomultipliers. Optical interferometry (IF) was used for a measurement of line averaged electron density distributions along the target surface at different target distances [6]. The interferometer scheme consists of a Mach-Zehnder interferometer, a continuous gas laser ($\lambda = 0.51$ mm), a high speed camera as a recorder and associated optics. The scheme allows to study the evolution of the electron density in the plasma shield with 2 dim spatial resolution of 1 mm and temporal resolution of 0.5 µs.

FOREV-2 calculations were performed for the conditions of the MK-200 UG facility. The impacting hot plasma (ions of energy of 1 keV and Maxwellian distributed electrons of temperature of 0.3 keV) has a Gaussian power density profile of half width of 6 cm with peak power densities of up to 35 MW/cm² at the separatrix. The guiding magnetic field B_{x0} is 2 T. Figs. 7 shows the calculated plasma flow pattern and the electron density distribution in the carbon plasma shield at 24 µs and 38 µs. At early times and close to the target there is a flow of dense cold plasma towards the separatrix then along the separatrix up-stream and laterally outward thus forming lateral plasma jets outside of the separatrix. At 30 µs flow reversal occurs in the dense cold plasma close to the target and at 38 µs the plasma jets are rather well developed. At 24 µs the dense plasma layer at the separatrix has grown to a thickness of 2,1 cm whereas the lateral plasma jets extend over a length of about 6,5 cm. At 38 µs the dense plasma layer has grown to a thickness of 9 cm. Also indicated in Fig. 7 are lines of sight for the IF measurements and the Gaußian power density profile of the incoming hot plasma.

Fig. 8 shows calculated electron density distributions in the carbon plasma shield (in y-direction) along the IF lines of sight at 30 µs and 40 µs for different distances from the target. The lateral plasma jets are clearly to be seen as density peaks outside of the central axis evolving at target distances larger than 2 cm. Fig. 9 shows a comparison of calculated and measured line averaged electron density distributions along the separatrix at 3 different times. The calculated values were obtained by averaging over the density distributions shown in Fig. 8. There is agreement between measurement and calculation at 10 µs as seen from Fig. 9. At 30 µs and 40 µs the calculated values at distances larger than 2 cm from the target are also in good agreement with the measured values.
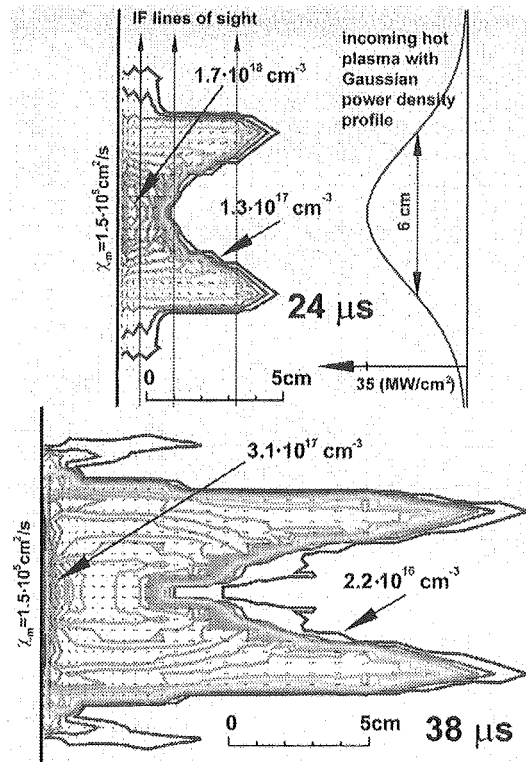
Fig. 7: Calculated plasma flow pattern and electron density distributions in a carbon plasma shield at 24 µs and 38 µs. Peak power density is 35 MW/cm².

distance along target (cm)
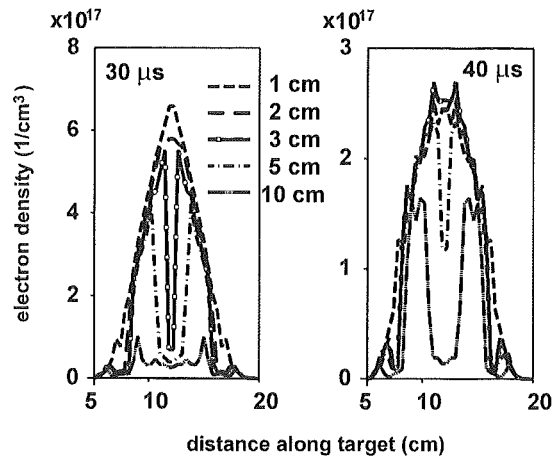
Fig. 8: Calculated profiles of electron density in a carbon plasma shield along the IF lines of sight at 30 µs and 40 µs at different distances from the target as indicated in the figure.

Fig. 10 shows a comparison of calculated and measured local electron temperature profiles along the separatrix. The temperature increase at 30 µs occurs at a target distance of 1.5 cm and at 50 µs at 8 cm thus indicating the extension of the dense cold plasma along the separatrix.
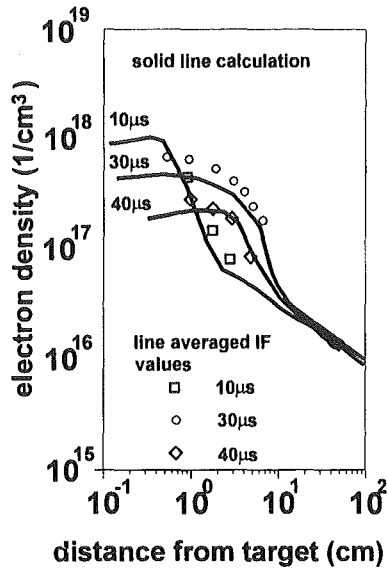
Fig. 9: Comparison of measured and calculated line averaged electron density distributions in a carbon plasma shield at different times.
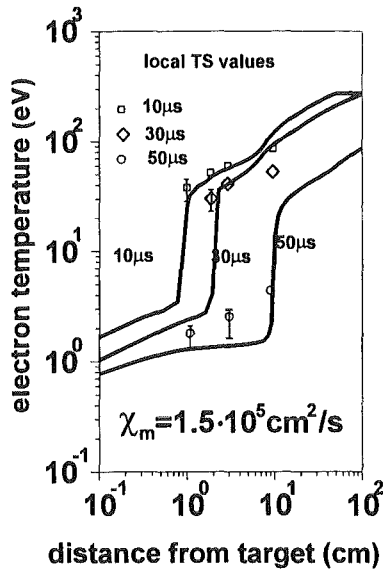
Fig. 10: Comparison of measured and calculated local electron temperature profiles along the separatrix.

Finally Table 1 gives a comparison of measured and calculated values of erosion by vaporization of graphite targets.

Table 1: Erosion of graphite

| facility | target | erosion (μm) | |
arrangement		measured	calculated
Perp	0,4	0,45	
MK-200 UG	tilted 20°	0,22	0,26
tilted 40°	0,34	0,4	

3.2 Melt layer erosion in hot plasma target experiments

The plasma gun facilities VIKA [7], QSPA [8] and PLADIS [9] use a hydrogen plasma stream of rather low impact energy and high density for performance of experiments on melt layer erosion. The target always has been perpendicular to the impacting plasma. The energy deposition in such facilities is onto the surface. The maximum temperature always will be

achieved at the target surface. If the incident energy flux is not compensated by the sum of the heat conductivity flux into the target and the heat flux for surface evaporation then the surface temperature can exceed boiling temperature. In this case overheating of the near surface material can occur. If the energy absorbed in the overheated region is sufficient for converting the material into vapour ($E_{abs} > m(cT + H_B)$ with H_B the specific heat for boiling, volumetric boiling with bubble formation, bubble collapse and splashing of melted material occurs for metallic targets and brittle destruction might occur for graphite.

VIKA and QSPA results on melt layer erosion of aluminium are shown in Fig. 11 for a pulse duration of 200 μs. Additionally shown are results of calculations of melt layer erosion by volumetric boiling for aluminium and beryllium. For energy densities of the incoming plasma up to 20 MJ/m^2 calculated and measured results for aluminium are in satisfactory agreement. At higher energy densities the calculation yields smaller erosion values. Fig. 11 shows also a comparison of calculated and measured erosion values for beryllium. The experimental results were obtained at the PLADIS facility. Pulse duration in this case was 100 μs. The agreement again is quite good demonstrating that in the heat load range above 5 MW/cm^2 volumetric boiling is indeed the dominating mechanism for melt layer erosion. Fig. 12 shows a comparison of calculated and measured results for aluminium for a pulse duration of 360 μs. Measurement and calculation show opposite trends. The measured erosion depth for the 360 μs case is considerably larger than for the 200 μs case whereas the calculation yields only slightly increased erosion values for the 360 μs case consistent with the fact that the reduced power density of the incoming plasma means a lower beam pressure thus lower overheating and thus a reduced splashing velocity. The considerably higher experimental values for the 360 μs case indicate that there could be active other effects for melt layer erosion.
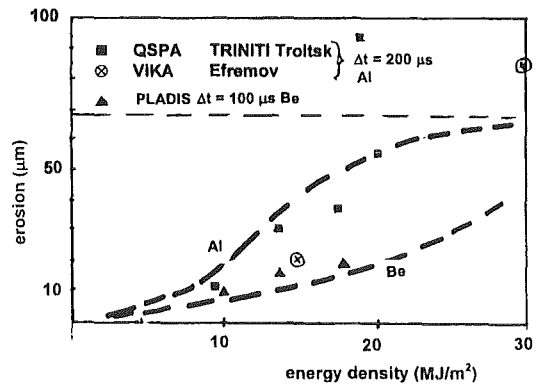
Fig. 11: Melt layer erosion of aluminum and beryllium under intense heat loads from plasma streams. Experimental results: no errors are given

Recently fluid dynamic instabilities were discussed as a possible mechanism for melt layer erosion [10]. An experimental proof of these models is still lacking. The only presented comparison of experimental results with calculations for aluminium and pulse duration of 200 μs repeat what is shown in Fig. 12 and for energy densities only up to 20 MJ/m^2. The results fully are explained by volumetric boiling, bubble collapse and subsequent splashing. Therefore existence of fluid dynamic instabilities and adequacy of theoretical modelling up to now are not demonstrated. A more detailed numerical analysis has to be performed and more systematic experiments are needed and especially inclined targets have to be investigated [11]. For these experiments a magnetised hot plasma stream is mandatory.
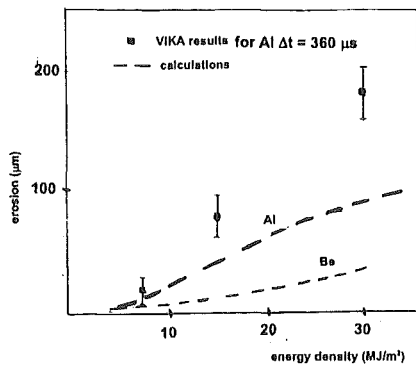
Fig. 12: Comparison of measured and calculated values of melt layer erosion of aluminum for a perpendicular impact of unmagnetised plasma. Duration of plasma stream is 360 µs. The error bars indicate the difference of erosion values as obtained from profilometry and mass loss measurements.

4. Disruption simulation experiments in electron beam facilities

4.1 Brittle destruction experiments at the GOL-3 facility

Brittle destruction of bulk material by hot plasma electrons was quantified in experiments performed at the GOL-3 facility. For graphite and tungsten and for energy densities of the impacting hot electrons above 10 MJ/m^2, there was observed rather large erosion which at energy densities of 30 MJ/m^2 reached 500 microns for graphite and 200 microns for tungsten [12]. For graphite a damage threshold energy of 10 kJ/g and for tungsten of 53 kJ/gmol was obtained. In order to understand the mechanism of brittle destruction a more detailed analysis of the interaction of hot electrons with graphite was performed. Due to volumetric heating the temperature increase inside the bulk target may lead to break up of bonds inside the lattice or between grains and crack formation can lead to brittle destruction [13].

An analysis of occurrence of brittle destruction under ITER disruption conditions was done for runaway electrons. Runaway electrons heat the target volumetrically. Because of the rather low threshold for target damage in case of volumetric heating it has to be checked whether hot electrons can cause brittle destruction of graphite under ITER disruption conditions. The energy density of the hot electrons at GOL-3 with 30 MJ/m^2 is close to the value expected for Tokamak runaway electrons. However the maximum electron energy at GOL-3 is only 1 MeV. Therefore extrapolation of the GOL-3 conditions to the conditions for runaway electrons was done using a Monte Carlo Code for calculation of the energy deposition. For an energy density of the impacting beam of 30 MJ/m^2 the destruction threshold of 10 kJ/g for brittle destruction of graphite is only reached for electrons of energy below 20 MeV. The erosion depth as function of impact time is shown in Fig. 13 for 2 MeV and 10 MeV runaway electrons. After 1 ms erosion for graphite due to brittle destruction can reach up to 650 µm.

4.2 Brittle destruction experiments at the JUDITH facility

In this facility [14] a 120 keV monoenergetic electron beam of time duration up to 5 ms impacting perpendicularly onto the target is used. Energy densities up to 7 MJ/cm^2 are achievable. Erosion results for Be as obtained at the JUDITH facility are shown in Fig. 14. The experimental values were obtained by profilometry and thus are describing the maximum erosion per pulse. Calculated erosion values are shown in Fig. 14 for comparison for different values of the damage threshold for a solid-melt phase transition. A damage threshold of 55 kJ/gmol

fits the experimental results quite satisfactory. Instantaneous brittle destruction was assumed to occur as soon as the energy threshold for damage is reached. At energy densities of the e$^-$-beam above 8 MJ/m^2 erosion becomes larger than the melt layer thickness.
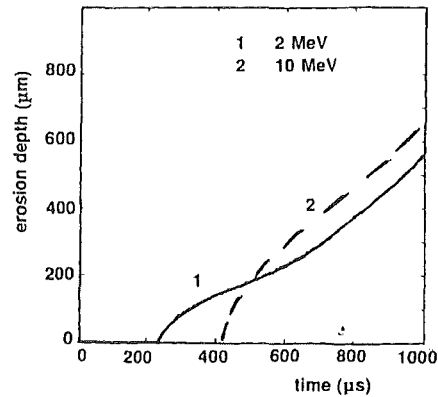
Fig. 13: Damage erosion by brittle destruction for runaway electrons of two different electron energies. The energy density of the beam is 30 MJ/m^2, the inclination angle of the hot electrons is 5°.
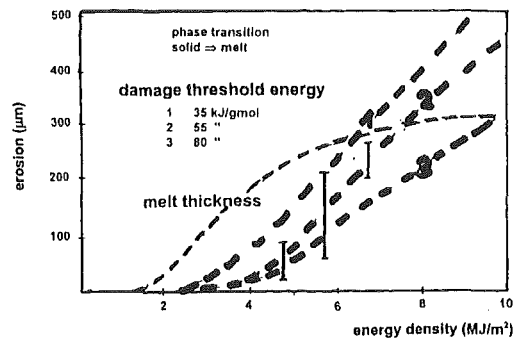
Fig. 14: Comparison of the calculated and measured erosion by brittle destruction of Be for the JUDITH facility.

5. Conclusions

The rather good agreement between the numerical and experimental results on plasma shield dynamics and erosion by vaporization in disruption simulation experiments with magnetized hot plasma streams allows to conclude that turbulent processes in the dense cold plasma layer which reduce the shielding efficiency are absent. Would they occur then there would exist a depletion of plasma in the center along the separatrix resulting in considerably higher plasma temperatures close to the target and larger peak erosion [2]. Plasma shield dynamics given for the whole time duration of the pulsed heat load which is up to 50 µs can be adequately described by the consistent 2 dim R-MHD model used in FOREV-2 with appropriate boundary conditions for the magnetic field at the target surface and with classical diffusion for the magnetic field diffusion coefficient in plasma shield.

The plasma shields in the simulation experiments are Tokamak typical. Therefore turbulent processes are also not occuring in the plasma shields produced in hot plasma divertor interactions during tokamak plasma disruptions. The long term plasma shield dynamics and its stability under tokamak conditions and divertor erosion thus can be adequately described by FOREV-2. The

understanding of the plasma shield dynamics in simulation experiments allows to conclude that such experiments adequately simulate ITER conditions for a disruptive hot SOL plasma and provide an answer to the important question of the diffusive regime in Tokamak typical plasma shields.

To complete the task of disruptive erosion by vaporization still are necessary an analysis of the long term stability of plasma shields [3], an analysis of the influence of ExB drift effects in the hot plasma cold plasma shield interaction region on erosion and plasma shield stability [15] an erosion analysis including existence and efficiency of plasma shields at power densities below 3 MW/cm^2, an analysis for a tungsten divertor and a more detailed analysis on occurrence of brittle destruction in hot plasma target interaction.

Concerning melt splashing the analysis performed has demonstrated that up to now no adequate validation of models is available. The experiments performed up to now at the plasma gun facilities VIKA, PLADIS and QSPA are not at all Tokamak typical and because of power densities above 2 MW/cm^2 mainly resulted in volumetric boiling and melt splashing by bubble collapse but not in triggering of fluiddynamic instabilities. Therefore models claimed to exist for describing those instabilities can't be verified and conclusions for the Tokamak situation can't be drawn up to now. Brittle destruction as observed in e-beam experiments with several 10 keV electron energies at the facilities GOL-3 and JUDITH is confirmed by numerical results based on volumetric heating and using empirical values for the destruction threshold inside the material which for graphite was determined to be 10 kJ/g and which for metals is around 50 kJ/g mol.

Literature

[1] H. Würz et al., Vapor shielding and erosion of walls during tokamak disruptions. Nucl. Instr. and Meth. in Phys. Res. A 415, 543, 1998.

[2] H. Würz et al., to be published in Fusion Eng. and Design

[3] H. Würz et al., Hot plasma interaction and quantification of erosion of the ITER slot divertor during disruptions and ELMs. Forschungszentrum Karlsruhe Report FZKA 6198, March 1999.

[4] H. Würz et al., A consistent 2D analysis of erosion of the ITER slot divertor, Fusion Technology 1998, Vol. 1 (1998) 271-274.

[5] H. Würz et al., A first consistent analysis of erosion of the ITER vertical targets for disruptions and ELMs. 25th Conf. Prag, June 29 – July 31, 1998.

[6] N.I. Arkhipov et al., Study of plasma target interactions with plasma streams of power density of 40 MW/cm^2, Fusion Technology 1996, Vol. 1 (1997) 507-510.

[7] J. Linke et al., J. Nucl. Mater. 212-215, 1994, 1195

[8] V.G. Belan et al., J. Nucl. Mater. 241-243, 1997, 402

[9] J.M. Gahl et al., J. Nucl. Mater, 196-198, 1992, 692

[10] A. Hassanein et al., J. Nucl. Mater. 241-243, 1997, p. 288

[11] H. Würz et al., Status and relevance of model validation. Workshop on Disruption Erosion, Nov. 24-26, 1997, St. Petersburg

[12] V. Astrelin et al., Nucl. Fusion Vol. 37, No. 11, 1997

[13] S.E. Pestchanyi et al., Fusion Technology 1998, Vol. 2 (1998), 275

[14] J. Linke et al., Fusion Technology 1996, Vol.1, 1997, p.271

[15] I. Landman, H. Würz, Electric fields and ExB drifts in hot plasma cold plasma interactions. Forschungszentrum Karlsruhe Report FZKA 6192, 1998.

Staff:

B. Bazylev
F. Kappler
I. Landman
S. Pestchanyi
V. Safronov
H. Wuerz

Vessel/Mechanical Structures

V 60/1
Blanket Mock-up Fabrication and Testing

Subtask 1: Binary Be Pebble Bed Thermal, Mechanical and Pebble Bed Filling Experiment

1. Mechanical Behaviour of Binary Beryllium Beds

The interaction of the beryllium pebble beds with the structural material is an important issue for the design of the ITER Breeding Blanket. For this purpose, test facilities for uniaxial compression tests and triaxial compression tests have been built-up in a glove box and experiments have been performed with binary Be pebble beds (large pebble diameters between 1.6 and 2 mm, small pebbles diameters between 0.1and 0.2 mm) and monosized pebble beds (only large pebbles). The pebbles are characterised by a relatively rough surface. The uniaxial tests were carried out in a temperature range between ambient temperature and 480 °C and pressures up to 8 MPa; the triaxial tests were performed at ambient temperature.

From the uniaxial tests (UCTs), correlations were established for the modulus of deformation for the first pressure increase and pressure decrease. Additionally, first measurements of thermal creep of Be pebble beds were performed. Stress-strain relations depend sensitively on the initial state of the bed and with this on the filling procedure. This is of special importance for binary beds where it must be ensured that a homogeneous distribution of small pebbles in the bed is obtained in the blanket for details, see [1,2].

With the triaxial tests (TCT), the inner friction of the pebble bed is determined.

Figure 1 shows a characteristic result. Because of the isotropic initial compression of the pebble bed to the value of the selected horizontal pressure p_2, the bed is more compressed at the beginning than that of a UCT. However, with increasing axial stress the axial strain becomes increasingly larger due to the ability of the pebble bed to deform in the radial direction. The maximum of the curve is reached when no further stress increase is required to generate further strain. This maximum is characteristic for "the state of perfect plasticity" and the internal friction angle at this position is of prime importance.
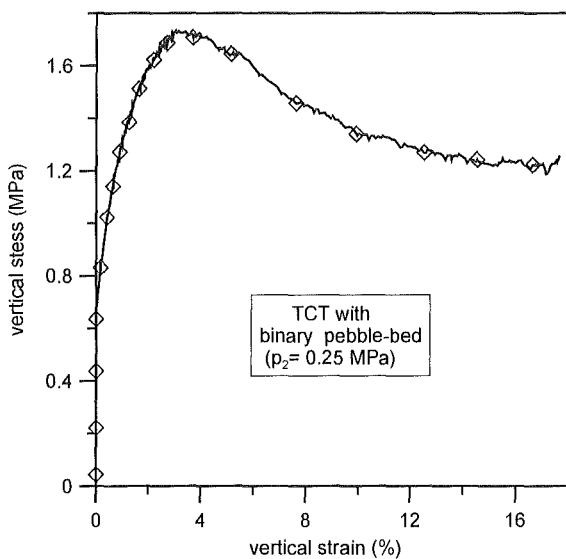
Fig. 1: Characteristic result of a TCT

Depending on the initial consolidation of pebble beds, the minimum required stress for further strain increase can be fairly constant or it can become smaller. The latter tendency is clearly Depending on the initial consolidation of pebble beds, the minimum required stress for further strain increase can be fairly constant or it can become smaller. The latter tendency is clearly Depending on the initial consolidation of pebble beds, the minimum required stress for further strain increase can be fairly constant or it can become smaller. The latter tendency is clearly observed for the beryllium pebble beds.

The analyses of the results show that the internal friction of monosized and binary beryllium beds is remarkably larger than that of beds with particles with smoother surfaces, characteristic for e.g. glass pebble beds and Li_4SiO_4 pebble beds. This means that the ability of beryllium pebbles to move macroscopically in the bed containment is more reduced compared to Li_4SiO_4 pebbles.

Literature:

[1] J. Reimann, E. Arbogast, M. Behnke, S. Müller, K. Thomauske, „Thermomechanical behaviour of ceramic breeder an beryllium pebble beds", ISFNT-5, Rome, Italy, Sept. 20.-24, 1999.

[2] J. Reimann, M. Behnke, "Experiments on the thermomechanical characterization of beryllium pebble beds", 4th IEA Int. Workshop on Beryllium Techn. for Fusion, Forschungszentrum Karlsruhe, Karlsruhe, Germany, Sept 15-17, 1999.

Staff:

J. Reimann
E. Arbogast
M. Behnke
K. Thomauske

2. Heat Transfer and Wall Contact Pressure of Binary Beryllium Pebble Beds

The heat transfer parameters of the binary pebble bed, namely the thermal conductivity and the heat transfer coefficient to the containing wall as well as the pressure exerted by the bed on the containing wall have been obtained by measurements performed at FZK in the SUPER-PEHTRA experimental device. The new experiments have been performed with the same principle as in the PEHTRA experimental device [3]. This new experimental device (SUPER-PEHTRA) operates with a heating power of up to 16 kW, in order to ensure an interference value comparable to that foreseen in the ITER breeding blanket also in presence of the volumetric swelling at the blanket-end-of-life ($\Delta\ell/\ell \approx 0.3\%$).

Contrary to the case of the PEHTRA experiments [3], with SUPER-PEHTRA only experiments with $\Delta\ell/\ell \geq 0$ were performed as the presence of the pressure sensors made the use of a thick and uniform thermal insulation on the outer tube impossible. Data for the $\Delta\ell/\ell = 0$ values were obtained with experiments in PEHTRA.

The filling of the bed was performed in successive steps increasing the amount of small pebbles at every step. The axial homogeneity of the bed was controlled by the axial temperature distribution on the surface of the inner heating rod. The stable and homogeneous structure was achieved with a packing factor

of the small pebbles of about 19.3% , thus giving a total packing factor of the binary bed of 82.5%.

The results of the stable binary bed in terms of pebble bed heat transfer parameters and wall contact pressure are described in this report.

The experiments were performed mainly with air cooling, as this allowed to obtain results with an average bed temperature higher than 200 °C. The results of these experiments and of the previous experiments performed in PEHTRA with a thermal insulation indicate that for binary beryllium beds with an average temperature higher than 200 °C the thermal conductivity for $\Delta \ell / \ell$ = 0 is practically independent of the temperature [3]. The thermal conductivity is determined only by thermocouples placed in the bed. The scattering of the measured temperatures is relatively small, considering the large temperature differences. The points can be well fitted by a straight line indicating that the thermal conductivity is practically constant across the bed. This was always the case for all tests performed during our experiments. The thermal conductivity as a function of the interference $\Delta \ell / \ell$ is shown in Fig. 2. The first experimental runs (1-7) represent the heating up of the bed. The curves to be used for design calculations are the 14-21 during the heating up phase and the 7-13 ones for the cooling down phase.
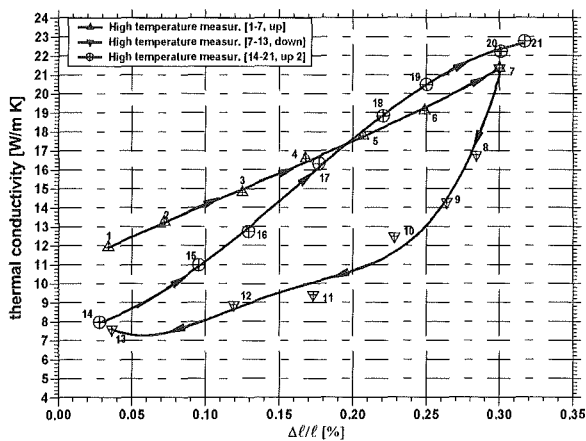
Fig. 2: SUPER-PEHTRA thermal conductivity of the stable binary bed as a function of $\Delta \ell / \ell$ (air cooling).

Fig. 3 shows the wall heat transfer coefficients at the inner rod surface. These account for the smaller packing factor at the inner rod wall, which acts as a disturbance to the pebble bed. They are obtained by the known heat flux at the wall and the difference between the measured temperature of rod surface and the bed temperature extrapolated to the rod surface. The heat transfer coefficients have a similar behaviour to that of the thermal conductivity. However the hysteresis of the curves 7-13 and 14-21 is much less pronounced and possibly within the accuracy of the experiments.

Fig. 4 shows the average pressure exerted by the bed on the four pressure sensors. The initial curve 1-7 shows quite clearly that the compression occurred essentially during the filling of the bed. As in the case of the wall heat transfer coefficient the hysteresis of the curves 7-13 and 14-21 is less pronounced than in the case of the thermal conductivity data.
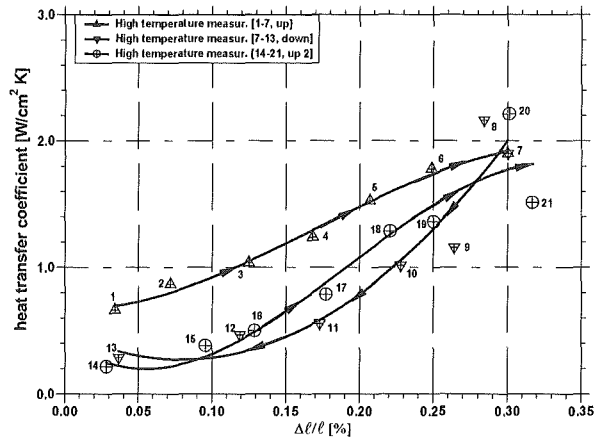
Fig. 3: SUPER-PEHTRA: Heat transfer coefficient at the inner tube wall as a function of $\Delta \ell / \ell$ (air cooling)
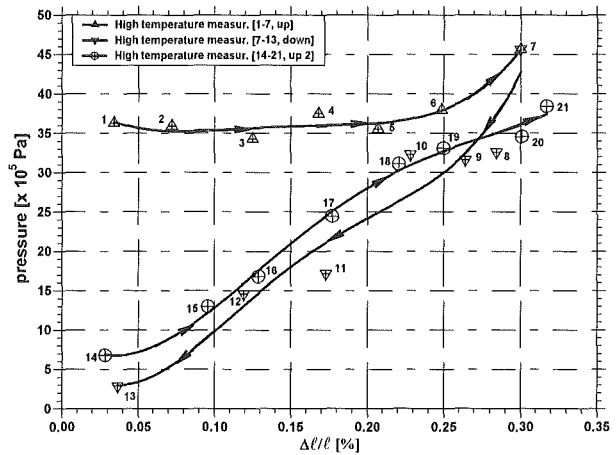
Fig. 4: SUPER-PEHTRA: Average pressure at the four sensors as a function of $\Delta \ell / \ell$ (air cooling)

Literature:

[3] M. Dalle Donne et al., "Measurement of the thermal conductivity and of the heat transfer coefficient of a binary bed of beryllium pebbles". Proceedings of the 3rd Int. Workshop on Beryllium Technology for Fusion, Mito, Oct. 22-24, 1997, JAERI-Conf. 98-001.

Staff:

A. Goraieb (Fa. Goraieb Versuchstechnik)
G. Piazza
F. Scaffidi-Argentina

T 362
Neutron Streaming Experiment for ITER

In the framework of ITER task T362, the neutronic performance of the ITER shielding system had been investigated on the basis of an integral experiment for a shield mock-up with open streaming channel. The mock-up simulates the first wall, the shielding blanket, the vacuum vessel, the toroidal field coil and a radial channel through the shielding blanket used for the mechanical attachment of the blanket module, see Fig. 1.
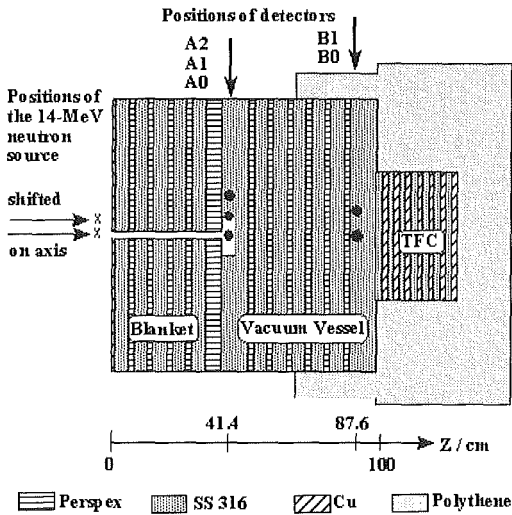
Fig. 1: Horizontal cut of the mock-up assembly with neutron source and detector positions indicated.

Measurements of the neutron and photon flux spectra as well as computational analyses on the basis of Monte Carlo calculations with the MCNP code [1] and FENDL-1 nuclear cross-section data [2] have been reported previously [3]. In addition to these, analyses of the flux spectra with the newly released FENDL-2 data library [4] and of design relevant nuclear responses such as the Helium production, the displacement damage and the photon nuclear heating rates have been performed over the reporting period [5].

Comparisons of measured and calculated neutron and photon flux spectra are shown in Figs. 2 and 3 for the deep position B0 with the neutron source on axis. The measured fast (E> 0.1 MeV) neutron flux in general is underestimated, in the order of 10% at the bottom of the streaming channel (position A) and in the order of 30 % at the back of the vacuum vessel mock-up (87.6 cm penetration depth). The measured photon flux spectra can be well represented by the calculations, in particular at the deep location B. The same is true for the photon fluxes at A1, A2 and A0 with shifted source whereas for A0 with the neutron source on axis, it is underestimated by 15 – 20%. In that case, a large amount of the photons is produced by 14-MeV neutrons streaming through the channel; this component, however, is underestimated by the calculations. With regard to FENDL-1 vs. -2 data, there is no large difference in the spectra calculated for the two locations in the ITER streaming experiment, although there is a clear trend for a better reproduction of the photon spectra with FENDL-2 at deep locations.

For checking design relevant nuclear responses with the experiment, the measured flux spectra were used to derive the Helium production, the displacement damage rate as well as the energy deposition by photons. By using the same approach with the calculated flux spectra, C/E (calculation/experiment) data relevant for the design validation have been obtained. These data are presented in Table 1. The Helium production is given for SS-316 taking into account the α-production on
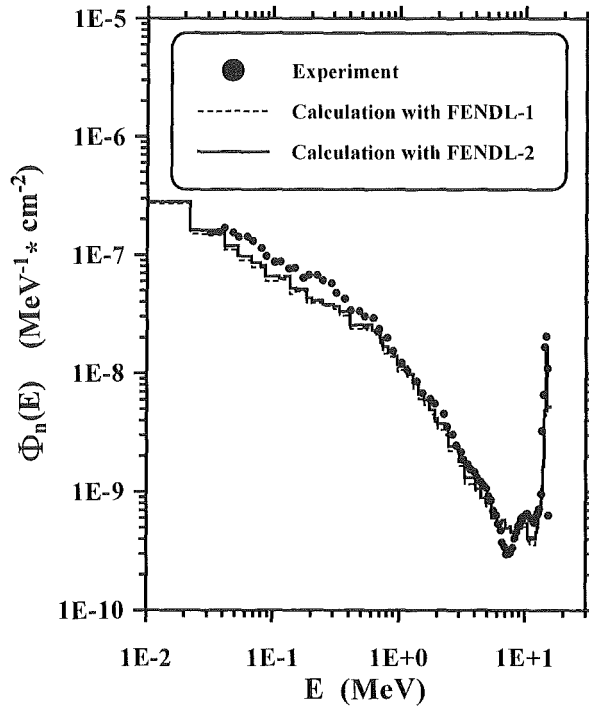
Fig. 2: Measured and calculated neutron fluence spectra at detector position B0 with neutron source on axis.
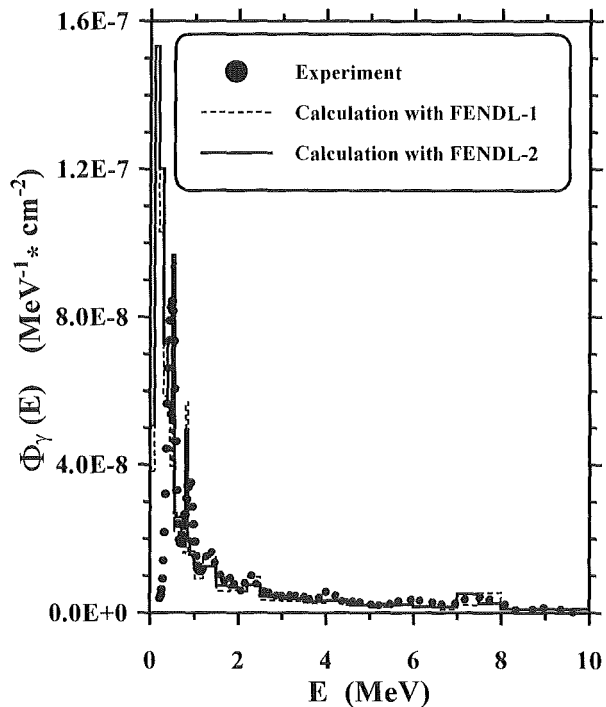
Fig. 3: Measured and calculated photon fluence spectra at detector position B0 with neutron source on axis

^{54,56,57,58}Fe, ^{50,52,53,54}Cr and ^{58,60,61,62,64}Ni. For ^{56}Fe , a recently evaluated α-production cross section was used [6]. For the other nuclides, the FENDL cross sections were used. The underestimation of about 20% and 10% at A0 with source on axis and with shifted source, respectively, and of about 30% at B0 is mainly related to the underestimation of the 14 MeV neutron flux at these positions.

The displacement damage values of Table 1 represent the number of displacements for 10^{24} atoms of Fe in SS-316. The IRDF-90 damage cross sections [7] for Fe were used to calculate the damage rates in steel by folding with the measured and the calculated neutron flux spectra. The underestimation of the damage at A0 with source on axis is due to the underestimated neutron flux for E > 10 MeV. At position B0, the underestimation of the damage rate is caused by the underestimation of the fast neutron flux (E > 0.1 MeV).

The heating values in Table 1 were derived from the spectral photon fluxes with kerma data from the FENDL transport libraries. As these heating numbers strongly increase with the photon energy, the C/E obtained are sensitive to the flux components with the highest energy. Note that only at A0 with source on axis, C/E deviates more than 10% from 1.0.

Table 1: Helium production, displacement damage and γ-heating as calculated from measured and calculated spectra using FENDL-1 and –2 response data (normalised to one source neutron)

	α-particles from 10^{24} atoms of SS-316	Displace-ments of 10^{24} Fe-atoms in SS316	γ-heating (MeV/g)
A0 source on axis			
Experiment	$1.95 \cdot 10^{-6}$	$9.26 \cdot 10^{-2}$	$1.29 \cdot 10^{-6}$
FENDL-1 C/E	0.81	0.84	0.83
FENDL-2 C/E	0.82	0.84	0.83
A0 source shifted			
Experiment	$8.48 \cdot 10^{-8}$	$6.67 \cdot 10^{-3}$	$6.52 \cdot 10^{-7}$
FENDL-1 C/E	0.89	0.95	1.05
FENDL-2 C/E	0.93	0.96	1.03
B0 source on axis			
Experiment	$1.08 \cdot 10^{-9}$	$7.51 \cdot 10^{-5}$	$3.32 \cdot 10^{-9}$
FENDL-1 C/E	0.66	0.71	0.88
FENDL-2 C/E	0.70	0.76	0.95
B0 source shifted			
Experiment	$6.83 \cdot 10^{-11}$	$8.73 \cdot 10^{-6}$	$1.00 \cdot 10^{-9}$
FENDL-1 C/E	0.71	0.77	0.99
FENDL-2 C/E	0.82	0.82	1.10

Literature:

[1] J. F. Briesmeister (Ed.), "MCNP - A general Monte Carlo n-particle transport code, version 4A", Report LA-12625, Los Alamos, September 1993.

[2] S. Ganesan and P. K. McLaughlin, "FENDL/E – Evaluated nuclear data library, version 1.0", Report IAEA-NDS-128, International Atomic Energy Agency, Vienna, May 1994.

[3] Nuclear Fusion Project, Annual Report of the Association Forschungszentrum Karlsruhe/EURATOM October 1997 – September 1998, FZKA-6200, EUR-18621EN (November 1998), pp. 20-21.

[4] M. Herman, Validation and improvements of the FENDL-2.0 transport sub-libraries, International Atomic Energy Agency, Report INDC(NDS)-395, March 1999.

[5] K. Seidel et al., Investigation of Neutron and Photon Flux Spectra in a Streaming Mock-up for ITER, 5th International Symposium on Fusion Nuclear Technology, Rome, 19-24 September 1999.

[6] A. B. Pashchenko, Improvement of measurements, theoretical computations and evaluations of neutron induced helium production cross sections, International Atomic Energy Agency, Report INDC(NDS)-359, December 1996.

[7] N. P. Kocherov and P. K. McLaughlin, The International Reactor Dosimetry File (IRDF-90), International Atomic Energy Agency, Report IAEA-NDS-141, October 1993.

Staff:

U. Fischer
H. Freiesleben
W. Hansen
D. Richter
K. Seidel
S. Unholzer

T 216
Shield Blanket Fabrication and Testing

Experimental Evaluation of Mock-ups

Testing of three shield blanket first wall mock-ups was continued and finished during the report period. A short description of the test is repeated below.

As part of the ITER work package WP4.1 three small scale first wall mock-ups (MU) shown in Fig. 1 have been received in November 1997 for thermal fatigue testing in the FIWATKA facility. According to the first wall (FW) design at that time the MUs were manufactured by NNC and Framatome from DS- or PH-copper (Cu) and 316L stainless steel (SS) using the solid HIP joining technique. HIP joints are located

- between the SS shield blanket block and the Cu layer,

- between the two half shells of the Cu layer, and

- between the Cu layer and the embedded SS FW cooling tubes

- The MUs did not have a Be protection layer.

In order to fatigue-test the HIP joints the MUs were designed such that under testing conditions and at the HIP joints they develop maximum stresses and stress ranges which are close to those in a real module [1].

Thermal fatigue testing of the three MUs in parallel was started in January 1998. Each testing cycle consisted of 200 seconds of thermal load (burn time) and of 100 seconds of no thermal load (dwell time). The heat flux to the MU surface was close to 78 W/cm². Temperatures in the MUs were measured in three positions (Fig. 1) and they compared well with the FEM calculated predictions.

After 13 000 cycles without obvious defects, the MUs were checked by ultrasonic examination (NDE), which did not reveal any changes compared to the pre-test condition. Fatigue testing was continued, until 20 000 cycles were reached in early August 1998. Again no obvious defect had developed.

After continuation up to a total of 30 000 cycles the test was terminated in November 1998. No obvious defects were found and a final ultrasonic NDE at VTT again did not show any changes compared to the pre-test condition.

The final report on the task was published in April 1999 [2]. It may be concluded that the HIP joints survived 30 000 typical load cycles without damage.

Literature:

[1] G. Hofmann, M. Kamlah; Selection of Test Conditions for Thermo-mechanical Tests of Small Scale ITER Primary Wall Mock-Ups; Forschungszentrum Karlsruhe, Interner IATF-Bericht (December 1996)

[2] G. Hofmann, E.Eggert; ITER First Wall Small Scale Mock-up Thermal Fatigue Testing in FIWATKA; Final Report on EU Task T216; Forschungszentrum Karlsruhe, Interner IKE-Bericht (April 1999)

Staff:

E. Eggert
G. Hofmann
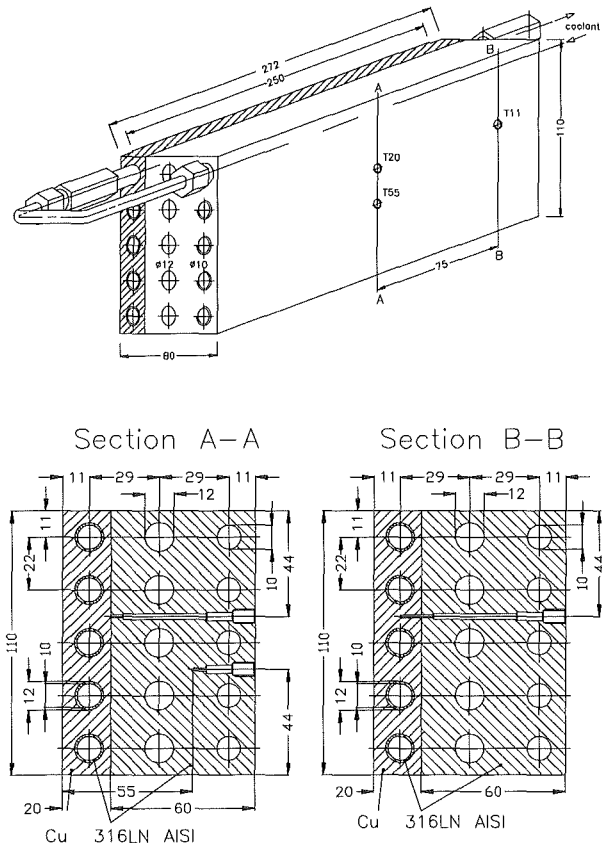
Fig. 1: ITER first wall small scale mock-up

This task aims to compare the numerical analyses for lifetime prediction performed by the participating laboratories:

- Commissariat à l'Energie Atomique, Grenoble, France

- ITER Joint Central Team, Garching, Germany

- Joint Research Centre of the European Community, Ispra, Italy

- Forschungszentrum Karlsruhe, Germany.

The main objectives of these analyses are:

(1) the assessment of the integrity of a first wall structure after the determined number of cycles (13000) by using 'lower bound' data as recommended by the code

(2) the scientific evaluation of experiments by using 'best fit' data in order to give a best estimate of the expected lifetime of the structure. A two step approach was foreseen. In the first step, thermal and elastic calculations were carried out. Based on these first results, the second step to perform inelastic calculations appeared to be indispensable.

The mock-up analyzed is made of a 10 mm thick beryllium layer joined to a 20 mm thick heat sink made of DS Copper Al 0.25. This heat sink is joined to a 60 mm thick plate made of stainless steel 316L-IG. Both, the copper and the steel plate are actively water cooled. The steel plate includes also a row of 12 mm

inner diameter tubes, which contain electrical heaters to simulate nuclear heating. The component is loaded by a cyclically changing surface heat-flux.

In a common report the analyses of the different participants have been compared.

The results reported are temperatures at several predefined locations for the thermal analysis and stresses components, equivalent stresses for the mechanical analyses (elastic and plastic) as well as equivalent plastic strains in case of inelastic analysis.

The cyclic response of any of these quantities as well as their overall maximum and minimum are given. Also prior to the analysis, criteria have been defined to qualify the agreement of the calculations.

According to these criteria, the results of the thermal as well as of the elastic analyses are in excellent agreement between all participants. The results of the inelastic analyses are in good agreement. For the inelastic analyses some of the data necessary for a fully qualified comparison are missing. These quantities, which are not an intrinsic output of a finite element analysis, were not evaluated by some of the participants.

Staff:

E. Diegele
G. Rizzi

T 204
Plasma Arc Cutting of ITER Containment Vessel

Introduction

The objective of this technology programme is the development of cutting techniques for the field disassembly of segments for the ITER containment vessel, required for remote replacement in the event of failure of TF coils. Following successful earlier work in the definition of plasma cutting parameters and basic trials with a reciprocating backside protection concept, work will be carried out to develop these techniques further.

Evaluation of high temperature resistant materials for melt flow absorption

In ITER stages F2-F4 4 mm silicon carbide plates fixed on a 3 mm copper plate were tested. Although the thermal resistance of this material proved to be sufficient, the backside plate had to be replaced after each cutting.

To take further suitable materials into account, a literature study was carried out to compare their thermal characteristics.

The paractical tests of various different heat protective materials were carried out under following refernce conditions (Fig. 1).
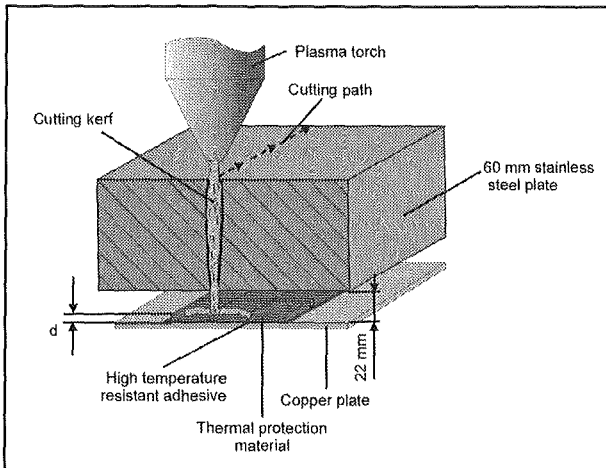
Fig. 1 : Experimental set-up for tests of ceramic materials

The most efficient thermal protection of all tested materials was achieved by the application of composite fibre carbon plates (CFC SIGRABOND type 1501G) of a thickness of 7.5 mm. Although during the cutting trial the CFC sample got red hot, it showed only insignificant damage. That is why one expect that the material is suitable even for repeated use in the reciprocating backside protection system.

Design of backside protection system

The backside protection system (Fig. 2) consists of a frame of 44 x 22 mm aluminium profiles which fitted in the assumed gap of 35 mm between the two 60 mm Cr-Ni plates. The total dimensions of the frame system were 840 x 520 x 35 mm, assuming a maximum segment size of 200 x 200 mm to be cut in one sequence. The actual thermal protection shield consisted of a 350 x 300 x 2 mm copper plate which carried the thermal protection tiles. Therefore, 50x50x8 mm tiles of CFC were fixed on the copper plate by using a high temperature adhesive (WH-2-component-refractory-adhesive 1500 R by W. Haldenwanger GmbH & Co. KG, Berlin). The use of small sized tiles instead of a bigger plate allowed the limited exchange of smaller areas which might be thermaly damaged.
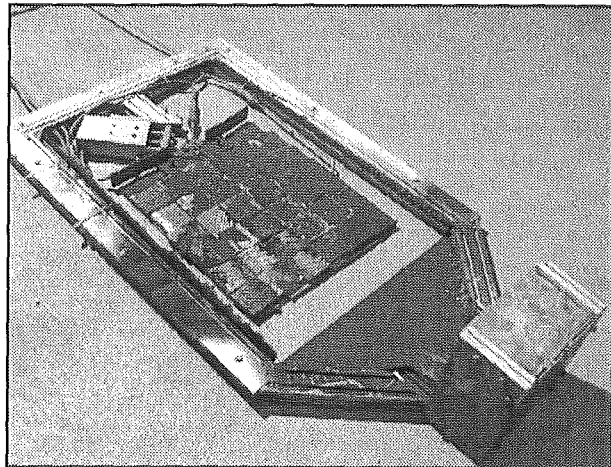
Fig. 2 : Backside protection system

To reduce the conglomeration of dross, which had shown to be critical using ceramic tiles in earlier trials, and to achieve a broader heat-affected zone, the thermal protection shield was moved by a bi-directional pneumatic actuator. The actuator was mounted onto the frame at an angle of 45° so that there was always a relative motion to the cutting direction (vertical or horizontal). To cool the hot melt flow and to reduce oxidation of the CFC tiles a gas nozzle system was integrated.

The outer aluminium frame was sealed against the 60 mm stainless steel plates by wire brushes. On the bottom of the protection system a dross reservoir was adapted which collected the bigger particles.

Cutting trials

The cutting trials were carried out in a test basin which includes an adaptable workpiece mounting. For removal of fumes and gases the basin is connected to a suction system. The plasmatorch is guided by a 6-axis industrial robot (KUKA KR 15).

The test cuts on the mock-up were carried out with a plasma torch Kjellberg PB-S 150 powered by two current sources PA-S 75 CNC. For the first cut the plasma torch was positioned 20 mm below the plate edge to carry out a 200 mm vertical upward cut. The cut continued in horizontal direction to the right at a length of 100 mm. To improve the edge sharpness, the cutting speed of 0.4 m/min was reduced to a speed of 0.3 m/min for a distance of 10 mm before and after the edge. The second reference cut was started 200 mm right from the starting point in vertical upward direction. This cut continued in left direction at a length of 100 mm so that the complete segment was cut out. The segment could be easily removed after the cut.

Fig. 3 shows the CFC tiles after the second cut. In the cutting path area the CFC tiles were thermally damaged only partially, i.e. the total thickness of 8 mm was reduced to a minimum of 4 mm in some areas, although there was no gas cooling and no oscillation caused by technical defect during this cutting sample. Another advantage is that nearly no dross sticks on the tiles.

Optimisation of edge start/stop parameters

The plasma arc cutting process at plate thicknesses of more than 40 mm can only be started at the plate edge. To ensure the cutting process is reproducible and to ensure that the plate is cut through totally the cutting speed has to be reduced when cutting the first 10-20 mm of the plate. Caused by different temperature gradient at the plate edge and the bigger power density which is

put into the workpiece because of the lower cutting speed in this area, the cutting kerf is widened here. At a plate thickness of 60 mm this means e.g. a kerf width up to 20 mm intstead of 5-10 mm. Besides, the angular deflection of the kerf is higher than the normal 2°. However, for the rewelding process kerf surfaces with a constant shape are absolutely necessary.
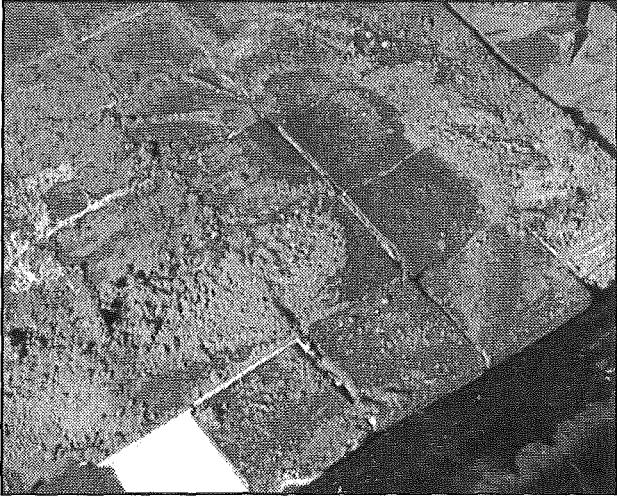
Fig. 3: CFC tiles after the cut

Fig. 4: Kerf compensation at cut start and stop

Therefore, cutting tests with edge starts and stops with the 600-A-plasma cutting torch on 60 mm plate thickness were carried out. To achieve one straight, plain kerf side, the first idea was to compensate the curved kerf contour of a straight cut (Fig. 4 #1) by cutting a path which is opposite to the kerf contour of a straight cut (Fig. 4 #2). The other kerf side will be even more curved, but this side is not relevant for the rewelding process. Fig 4 #4 shows the graph of the cutting speed in dependence on the cut distance.

After these trails, the kerf compensation was successivly optimised and leaded to strategy which is illustrated in Fig. 4 #3.

Cutting test in overhead position

Plasma cuts in overhead position (horizontal workpiece with vertical plasma torch) may expect difficulties because the upward melt flow is directed opposite to its gravity force. This could result into the effect that the liquid melt streams back onto the nozzle which cause thermal damage of the brazen torch nozzle and cap.

Therefore, a special protection cap for the plasma torch was designed. The protection can be set easily onto the existing brazen torch cap. To avoid the high costs and times of manufacturing of producing special parts of ceramic materials in small batch sizes, a special machinable, highly heat and temperature shock resistant material (COTRONICS RESCOR 960 by POLYTEC GmbH, Waldbronn) was choosen.

The protection cap was tested sucessesfully with the 600 A plasma cutting torch on a 60 mm workpiece in overhead position. A damage of the nozzle or other parts of the torch could not be detected.

Further proceeding

The objective of the running program for cutting test with circular geometry is the development of a backside protection system for inserting into a 25 mm gap between two circular shaped 60 mm CrNi-steel plates. The prototyp of the backplate protection system for application in a 35 mm gap will be modified to include circular geometry. To obtain a more complete extraction of fumes and particles caused by the plasma process, the sealing concept has to be improved significantly and modified for the flexible protection system.

Although the concept of an oscillating protection plate itself showed to be suitable it will be difficult to adapt the backside protection system including a wire brush sealing, dross reservoir and pneumatically driven oscillating system into a curved geometry. In view of the very good thermal resistance of CFC plates without an oscillating motion, the modified protection system will be realized with a fixed backside protection system.

Staff:

H. Haferkamp
G. Schreck
Unterwassertechnikum Hannover
des Instituts für Werkstoffkunde
Universität Hannover
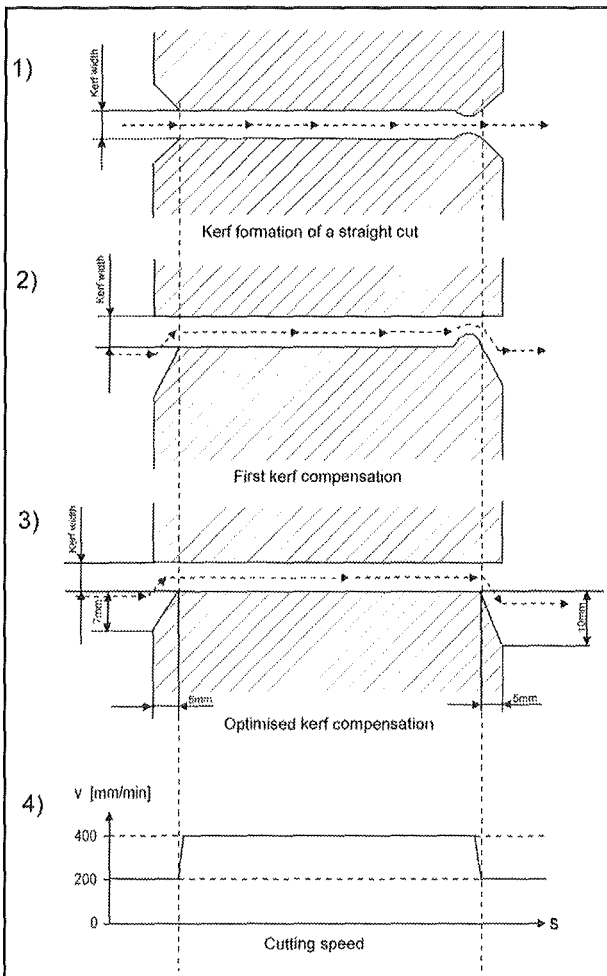
Coil System

M 44
TFMC Installation and Test

The TOSKA facility at Forschungszentrum Karlsruhe is being upgraded for testing the ITER TF model coil. The facility has been taken into operation in the following steps:

- Test of the LCT coil at 1.8 K (1996/1997)

- Test of the stellarator prototype coil W-7X (1999)

- Start of the test of the TFMC (End 2000).

The first step qualified the LCT coil for the use as background coil for the TFMC test configuration. The basic facility with its electrical and cryogenic supply system as well as data acquisition and control was taken into operation. The specific facility configuration needed for the TFMC test is in its final stage of completion. The installation of the 80 kA dump circuit and the 20 kA power supply were completed. The commissioning is running. The fabrication of components for two 80 kA current leads was completed. The assembling is being running. Two extensions of the TOSKA vacuum vessel for the vertical installation of the current leads were specified and ordered in industry.

The W-7X prototype coil was installed and tested in the TOSKA facility. The test was successfully completed in August 1999. The work for removal and shipping from TOSKA was completed in October 1999.

The fabrication of the TFMC in the European industry is in progress. The five pancakes were stacked, vacuum impregnated and the outer conductor joints between the pancakes were electron beam welded. The final machining of the coil case is running. The intercoil structure (ICS) was ordered by a subcontractor. The fabrication is running. The fabrication and the preparation of the test programme of the TFMC are accompanied by the special skills of the European superconducting laboratories. The work areas of Euratom Association Forschungszentrum Karlsruhe are:

- Instrumentation (included in M44)

- Conductor measurements (NET Contract No.: NET/97-458)

- Mechanical material and component testing (EU Task No: M45)

- High voltage component delivery and testing (NET Contract No.:NET/96-438)

- Finite element analysis (EU Task No.M12)

- Electromagnetic and thermohydraulic analysis (included in M44 and IRS 3 D quench analysis with code system MAGS)

- Transient voltage behaviour of the TFMC (included in M44)

The installation of the TFMC is scheduled for 2nd quarter 2000 and the test at the end 2000.

1. The TOSKA facility

The remaining components are:

- The 80 kA current leads are being in the assembling stage

- The 80 kA dump circuit and the 20 kA power supply are being in the commissioning phase.

- The manufacturing of 120 t lifting beam and the supporting structure of the configuration (gravitational support) were completed.

- Data acquisition, cryogenic supply and control system was configured for testing the W7-X Prototype coil and has now to be modified for testing the TFMC.

The 80 kA current leads: The fabrication of all components and the machining of parts in the workshops were completed. The assembling work of the heat exchangers and the accompanying quality assurance procedures are running.

For the vertical installation of the current leads two pieces of superconducting bus bars are needed for each current polarity (Fig. 1).
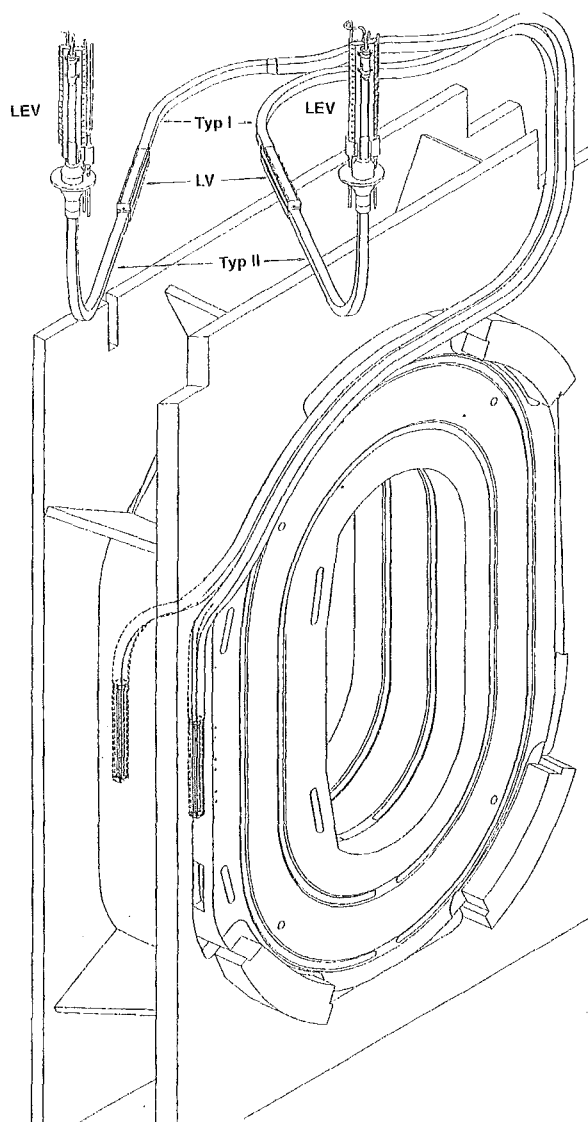
Fig. 1: The ITER TF model coil in the intercoil structure (ICS) and the superconducting busbar system type I and type II (LEV: conductor terminal to current lead; LV: Joint between busbar I and busbar II)

The so called busbars type I are directly connected to the winding ends and will be delivered with the TFMC. After installation of the TFMC the busbars type I will be joint with the busbars type II which have at their other ends the terminals for the joints with the current leads. For the busbars type II, an extensions of the TOSKA vacuum vessel are necessary in which they have to be installed. The extension for the TOSKA vacuum vessel were design, specified and ordered. An assembling procedure for the vacuum vessel extension, busbar type II and current lead was elaborated (Fig. 2).
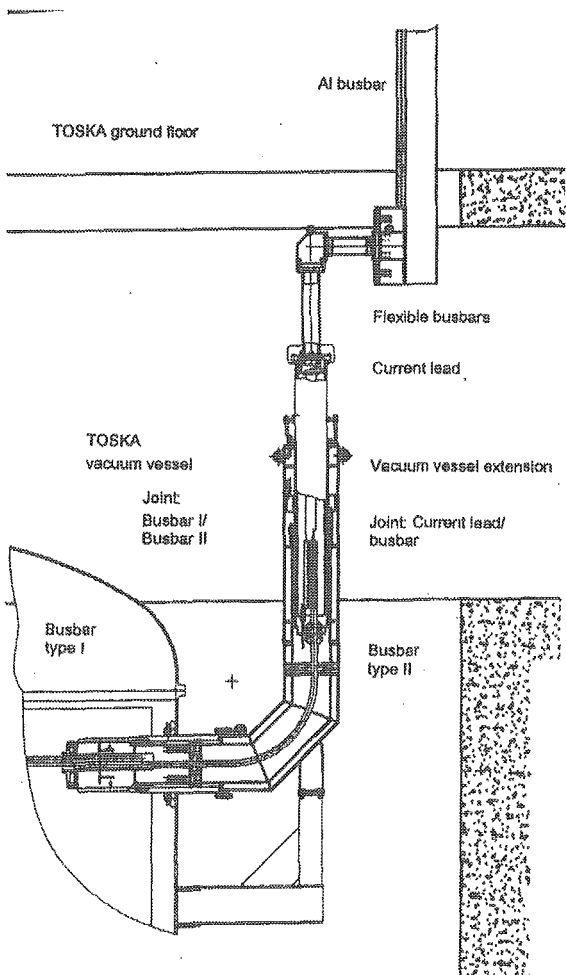
Fig. 2: The extension of the TOSKA vacuum vessel for the vertical installation of the current leads.

The as built dimensions of the busbars type II were measured at the factory of the manufacturer. They will be implemented in the detailed design of the cryostat extension.

According to results of the analysis for achieved contact resistances for dismountable clamped joints between super-conducting components a redesign of the joint between the bus bar type II terminal and the cold end of the current lead was indispensable for avoiding to high heat loads to the refrigerator. For achieving a joint resistance in the range of 1 nΩ, a surface pressure of 20 MPa is necessary [1]. Therefore a reinforced clamping system was designed and checked by FEM calculations.

The 80 kA dump circuit: The installation of the complete switching circuit was completed in April 1999. The

commissioning had to be interrupted during the test of the W 7-X prototype coil. It will be resumed beginning October 1999.

For investigating transient voltage behaviour of the TFMC winding type, conductors embedded in radial plates, discharges will be performed by the POLO switching circuit at 25 kA with a counteracting current switch.

The 20 kA power supply: The TFMC is supplied by a current of 80 kA by two existing power supplies (50 kA and 30 kA) in parallel operation. Therefore a third power supply is needed for the operation of the LCT coil. The installation of the 20 kA power supply was completed. The commissioning is running. The 20 kA power supply was installed at a stage above the LCT coil dump circuit (Fig. 3).
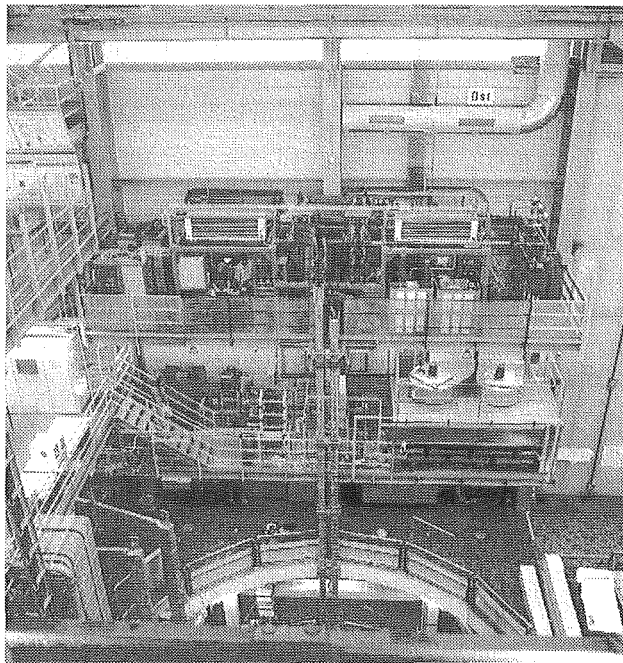
Fig 3: A view at the 20 kA upper supply (upper stage) and the 20 kA dump circuit of the LCT coil (lower stage).

Tooling for assembling: The fabrication of the lifting beam for the TFMC test configuration (about 120 t) in the TOSKA vacuum vessel was completed. The support frame on which the TFMC, intercoil structure and the LCT coil rest is available. As consequence of a change in the test programme (Testing of the TFMC in the first run without LCT coil) an auxiliary structure replacing the LCT coil was manufactured. It is available and ready for delivery.

Cryogenic system: The cryogenic system has to be adapted for the requirements of the TMFC especially for the much higher mass flow rate of 220 g/s compared to 4.8 g/s for the W7-X coil. Also the relief system has to be adapted to the much higher expelled mass flow rate after a quench. In addition the cooling circuit has to be modified to allow an operation of winding, case and ICS in parallel during cool down and an operation in series during steady state conditions. The hardware and the software of the control system will be adapted and upgraded to the changes mentioned above.

Data acquisition and control system: Signal routing of the high voltage signals have to be modified due to the other compensation method compared to the W 7-X. The transient and the cyclic data acquisition has to be extended in order to satisfy all requirements of the different testing modes. The configuration of the DAS and control system is in progress.

2. Preparations for the test programme of the TFMC

In collaboration with the European superconducting laboratories the preparing work for the test programme and related analysis for the TFMC was continued .

The following progress was achieved in the different areas:

Electromagnetics : From the I_c–measurement of strand material used for TFMC cable the constants were derived for calculating the critical data for the load line for the different test conditions.

Thermohydraulics: The main effort was concentrated for elaborating a joint data set of the thermohydraulic data with which all involved laboratories can perform their thermohydraulic analysis. This will easy the comparison of results.

Mechanics: The FEM model of AGAN was transferred to the IRS of Forschungszentrum Karlsruhe. The model was taken into operation. The load case of testing TFMC alone was analyzed. A further item was the investigation of the effect of friction and none friction between winding and coil case on the stresses in winding and case (see also Task M12).

Dielectrics: A network model was elaborated in collaboration with the Institut für Energieübertragung und Hochspannungs-technik (IEH) of the University of Karlsruhe. The resonance frequency of the TFMC network was about 200 kHz. It is much higher than that for TF full size coil at 4 kHz. That means that the common switching transients with rise times of about 30 µs will not excite internal oscillations combined with over voltages. First transients with rise times < 1 µs are able to excite oscillations. The comparison of measurements and calculations will serve as the validation of the network model which can later be used for predicting the transient behaviour of the full size coils [2], [3].

Instrumentation: The instrumentation of TFMC and the ICS was fixed. The implementation in the fabrication drawings is concluded.

Test procedure: The coarse frame is fixed and will be elaborated in detail in next time.

Literature:

[1] R. Heller, Estimation of joint resistances and quench analysis of the ITER TFMC NbTi busbar system, Forschungszentrum Karlsruhe, Institut für Technische Physik, Interner ITP-Bericht, März 1999

[2] A. M. Miri et al., Finite element model for the investigation of the transient oscillations in the ITER toroidal field (TF) model coil, Proc. 11th Int. Symp. High Voltage Eng. London, UK 23 – 27 August 1999

[3] A. M. Miri et al. Influence of the radial plates on the transient oscillations in the ITER TF model coil using a finite element approach, Proc. MT-16, Ponte Vedra Beach, Fl, USA, Sept. 26 – Oct. 2, 1999

Staff:

A. Augenstein
H. Barthel (till April 30, 1999)
H. Bai (since Dec. 1, 1999)
S. Darweschsad
G. Dittrich
P. Duelli
S. Fink
G. Friesinger
A. Götz
P. Gruber (till March 31, 1999)
A. Grünhagen
R. Heller
W. Herz
P. Hutapea (since July 1, 1999)
R. Kaufmann
A. Kienzler
L. Lang
O. Langhans
W. Lehmann
V. Marchese
W. Maurer
I. Meyer
G. Nöther
U. Padligur
K. Rietzschel (till July 31, 1999)
P. Rohr
G. Schleinkofer
K. Schweikert
E. Specht
H.-J. Spiegel
M. Süßer
A. Ulbricht (for 2)
D. Weigert
F. Wüchner
G. Zahn (for 1)
H.P. Zinecker
V. Zwecker

M 31
Development of 60 kA Current Leads Using High Temperature Superconductors

Introduction

The aim of the task is to develop a 60 kA current lead for the ITER Toroidal Field Coil system using high temperature superconductors (HTS) in the temperature range between 4 K and 77 K to reduce the steady state heat load at the 4 K level. The task is being done in collaboration with the Fusion Technology Division of the Centre Recherches en Physique des Plasmas of the Ecole Polytechnique de Federale de Lausanne (CRPP-EPFL).

The development program is consists of three stages:

A-1   Test of different materials and concepts in 1 kA modules

A-2   Test of a 10 kA HTS binary current lead using the material selected in stage A-1

B   Design and test of a 20 kA HTS binary current lead to prove modularity and scale-ability of the design

C   After completion of stage B, a 60 kA current lead could be designed to replace an existing 80 kA current lead in the TOSKA facility. This stage is an option, the decision will be made after completion of stage B

Design of the 10 kA module and description of test cryostat

At the end of stage 1, it was decided to proceed with task stage 2, i.e., the construction and test of a 10 kA HTS current lead. As material, it was decided to use stabilized tapes because of their larger safety margin. Because for the design of the 20 kA HTS lead (stage 3), two 10 kA modules are needed, it was chosen to order one 10 kA module in industry and construct and built a second one at the Forschungszentrum Karlsruhe.

The first 10 kA module was ordered from American Superconductor ASC. The design of the module is similar to those leads manufactured for the LHC project at CERN or for Fermilab, i.e., an appropriate number of Bi-2223 tapes sintered together, forming so-called stacks, and soldered on top of a sophisticated stainless steel support tube. At both ends, copper end caps are placed for current transfer to adapt the HTS module into the apparatus of the customer. The support structure also serves as an additional heat sink in case of a quench. In our case, the safety requirement is such that the module has to withstand the full current of 10 kA for 10 s in case of loss of active cooling of the copper heat exchanger part of the lead without reaching room temperature. The number of tapes are such to get a critical current of more than 12 kA at 70 K. The total length of the lead is 600 mm. To have the possibility to measure current imbalances during transients, e.g., during quench, four of the stacks are equipped with voltage taps. The voltages of both end caps are monitored too. In addition, four temperature sensors are positioned at 100%, 90%, 70%, and 50% of the HTS length, measured from the cold end, to evaluate the temperature profile. Figure 1 shows a picture of the HTS module.

The test facility at CRPP consists of a cryostat with He shield, one conventional forced cooled 10 kA current lead of the bundle type, a copper heat exchanger (70 K - 300 K) of the same design as for the conventional current lead, and a NbTi connection which is immersed in a helium bath. The 60 K He will be done by mixing helium of the shield cooling of the transfer line and 4.5 K helium. The cold end of the HTS module is immersed in liquid helium whose volume is separated from the

bath required for the NbTi connection and for the conventional lead. The heat load of the HTS module will be measured by means of the mass flow rate of the evaporated helium. A heater is installed to calibrate the flow meter. In addition, voltage drops and temperature profile of both the conventional and the HTS leads will be measured.

The test at CRPP covers both the steady state and transient behaviour of the current lead. The critical current of the HTS module will be measured, too. Because the maximum current available in the test facility is limited to 12 kA (only short time operation) and if If I_c is larger than 10 kA, the critical current would then have to be evaluated by increasing the upper temperature of the HTS module. From the steady state tests, mainly the temperature profile along the whole lead, the thermal heat load at 4.5 K, and the 60 K He mass flow rate needed to fix the upper temperature of the HTS module to roughly 70 K will be obtained. The transient test will be done to study the quench behaviour of the HTS module and to compare the results to the expectations.

A special feature of the test equipment is the installation of small sized Hall probes to measure the azimuthal com-ponent of the magnetic field near to the outer surface of the HTS module. These data are used to deduce the current flowing in the individual stacks.

Test results

The operation up to steady-state currents of 10 kA was rather successfull. No problems occured during various runs using the same operation current with the same parameters getting the same results. Short time runs up to 12 kA could also be done without any problems concerning the current lead; these runs were limited by the power supply. Figure 1 shows the measured and calculated temperature distributions as a function of length.

The contact resistances were measured to be 25.4 nOhm at 70 K and 0.87 nOhm at 4.5 K. These numbers include both the transition between the HTS stacks and the copper end cap and between the copper end cap and the other parts of the current lead.

The evaluation of the thermal heat load at 4.5 K was difficult because the calibration of the flow meter FI3 which measures the mass flow rate of the evaporated helium shows a strongly nonlinear behaviour which is not caused by the flow meter itself. So, the measured heat load has a rather large inaccuracy. At a temperature of the upper end of the HTS stacks of 70 K, the conduction losses are measured to be (1.46±0.25) W whereas for 10 kA the corresponding losses are (1.99±0.35) W. The difference is due to the ohmic losses at the 4.5 K level resulting in a total resistance of 5.3 nOhm. Using the contact resistance of 0.87 nOhm and the resistance of the Cu/NbTi pin which was measured electrically to be 3.35 nOhm, one gets about 4.2 nOhm which is in the same order of magnitude.

The quench current of the HTS module at 70 K is much larger than 12 kA. So the limit of the module could only be achieved by increasing the temperature above 82 K. For all runs, the current was switched off when the voltage along the stacks reached levels being much lower than 1 mV. Figure 2 shows the critical current of the HTS module expected from critical current data of short samples given by the manufacturer and the quench current of the HTS module using the voltage taps of three stacks. Here, the quench current is defined as that current where the voltage drop along the specific stack is 1 μV. Obviously, it is not possible to measure the critical current with a well defined criterion since there is a sharp temperature gradient along the HTS module. The dashed is an extrapolation of the critical current data by a factor of 1.4 which seems to be the

outer boundary of the quench current data evaluated from the experiment. Using the solid line as the lower boundary curve, the critical current density at 77 K in self field can be derived to be j_c = 39 kA/cm^2 or j_e = 11.7 kA/cm^2 where j_c and j_r denote the critical and the overall or engineering current density. This gives a quench current of about 18 kA at 70 K, and no degradation of the critical curent has been found.

To study the current distribution in the HTS module, seven small Hall probes were positioned at the outer surface of the module about 30 mm below the upper contact area, the active area being perpendicular to the broad surface of the individual stacks to measure the azimuthal component of the magnetic field. To determine the current flowing in the stacks from the local magnetic field measured by the Hall probes, the magnetic field distribution was calculated using the code MAXWELL. From this, the contributions of each stack to the local magnetic field B_{tot} measured by the Hall probes were obtained.The measurement results show that there is a rather inhomogenious but constant current distribution between the stacks which is driven by the contact resistances. Figure 3 shows the stack currents as a function of time for an operation current of 10 kA.

Running the HTS module in the current sharing regime, i.e., at resistive voltages along the stacks of several μV, a current redistribution takes place between the stacks resulting in a much smaller distribution. The Hall sensors positioned around the HTS module which have been used to determine the current distribution between the seven stacks were also used to measure the behaviour during quench. In Figure 4, the stack currents are plotted as a function of the temperature at the upper end of the HTS stacks. For comparison, also the voltage signals are shown. It can be clearly seen, that there is a redistribution of the stack currents if the current reaches the critical current. The stacks where the lowest currents are flowing get more and more current while the ones with the highest start decreasing. In total, the current distribution gets more narrow, which means that in the resistive region, the relatively flat U-I trace forces the stack currents to flow more homogeneous in the stacks.

The safety margin of the HTS module was measured by looking on the behaviour of the current lead during a switch off of the 70 K helium mass flow rate of the copper heat exchanger while the transport current was kept constant. These runs were performed at 7.5 kA and 10 kA. It turned out that the conventional part of the current lead was less stable against the thermal runaway than the HTS module. The transition of the upper end of the HTS module to the normal conducting state could only be observed at 10 kA and a start temperature of the warm end of about 90 K. Even in this case, the time difference between switch off of the helium mass flow and the switch off of the transport current, which was done at a resistive voltage of about 0.4 mV, was measured to be more than 70 s. Comparing this to the requirements of the discharge scenario of the ITER TF-coil system, i.e., a time delay of 2 s until a discharge will be inititated and a time constant of the exponential discharge of 12 – 15 s, there is a high margin.

Most of the runs were done using a quench detection level of less than 1 mV. To look on the behaviour of the HTS stacks at higher voltages, one run was performed with a quench detection level of the HTS module of 5 mV. Also at this level, there was no measureable temperature increase. Due to the good thermal contact between the different stacks via the stainless steel tube in which the stacks are soldered, the temperature measured on top of stack #1 is also representative for the other stacks.

One question could not be answered in the test: what is the behaviour of the HTS module at even larger voltages, i.e. 50 – 100 mV?

To look on the behaviour of the currrent lead at higher current ramp rates, a few runs were performed using a ramp rate of 500 A/s (most of the runs were done at 25 A/s). Here, the effect of the unequal contact resistances result in a current distribution which is smaller immediately after the ramp up and spreads up afterwards.

To conclude, the design of the 10 kA HTS current lead is robust and could be used in coil experiments without any problems.

The phase A-2 was concluded with the test of a 2nd 10 kA module fabricated by ASC. Two 10 kA modules are now available for phase B.
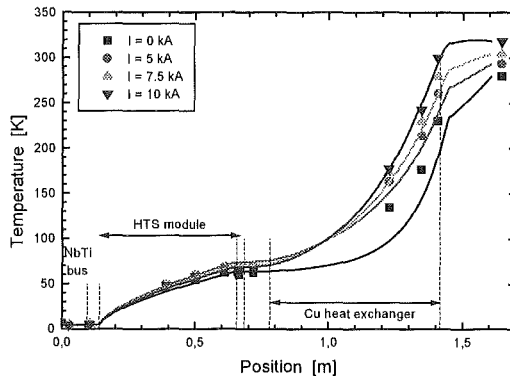
Fig. 1: Measured and calculated temperature profiles of the 10 kA HTS current lead for 0, 5, 7.5 and 10 kA
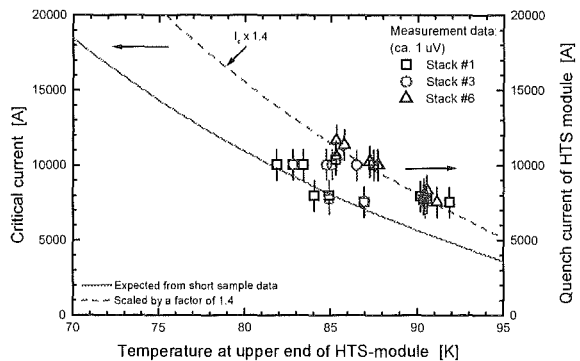
Fig. 2: Critical current of the HTS module vs temperature as expected from short sample data and quench current with different stacks as indicators. The dashed line indicates the upper boundary curve of the quench current data.
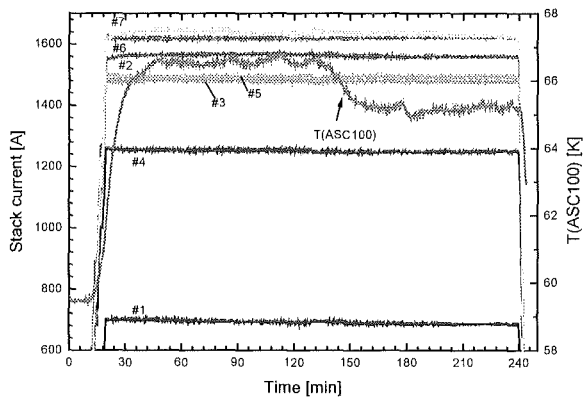
Fig. 3: Stack current #1 - #7 as a function of time for a transport current of 10 kA
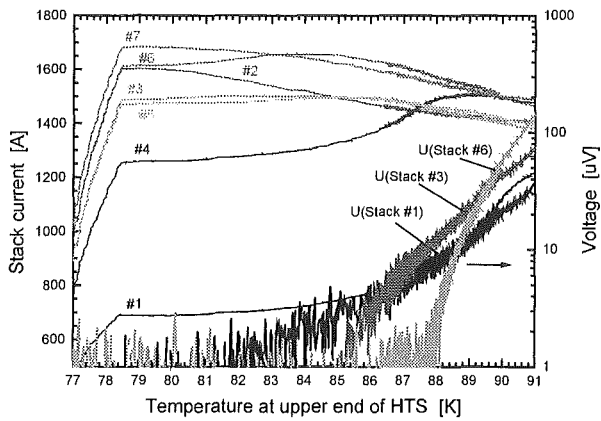
Fig. 4: Stack currents and voltage signals vs temperature at upper end of the HTS stacks

Design of the 20 kA HTS current lead

Parallel to the test of the 10 kA HTS module, the design of the 20 kA HTS current lead has been completed. The curren t lead consists of the conventional heat exchanger of the FZK current lead type, whereas the 20 kA HTS module is constructed such to connect two of the 10 kA modules in parallel. The status of the 20 kA current lead is as follows: the heat exchanger is completed, the adapter pieces between the heat exchanger and the HTS modules resp. the HTS modules and the clamp contact at the cold end are being fabricated and will be completed as soon as the HTS modules will be arrived from CRPP.

Literature:

R. Heller et al., "Test Results of a 10 kA Current Lead using Ag/Au stabilized Bi-2223 Tapes", *presented at 16th International Conference on Magnet Technology,* Jacksonville, FL, 26. Sept. –2. Oct. 1999

Staff:

G. Friesinger
W. Goldacker
R. Heller
H. Orschulko
R. Nast (ab 1.7.98)
M. Tasca
S. Zimmer

M 12.1
Stress Analysis for the TFMC Tests in TOSKA

After some contributions to the design of the TFMC-LCT-coil-test assembly [1,2], now under the new contract finite element electro-magnetic and mechanical stress analyses will be performed to prepare, support and evaluate the TFMC tests in TOSKA.

During the engineering design the test assembly, consisting of the TFMC, the intercoil structure ICS and the LCT-coil, has been modelled by the manufacturer. This model was transferred to Forschungszentrum Karlsruhe being the starting point for an extended global model for the stress analysis of the test assembly.

In a first step complementary to the mechanical FE-model an electromagnetic model, consisting of the winding packs of both coils, was developed allowing for calculation of the electromechanic fields and the Lorentz-forces [2]. Both models use the same grid, allowing a rather easy transfer of the load input into the mechanical model for the different current scenarios applied to the coil test. As an example, the figure shows the calculated magnetic field for both coils current loaded.
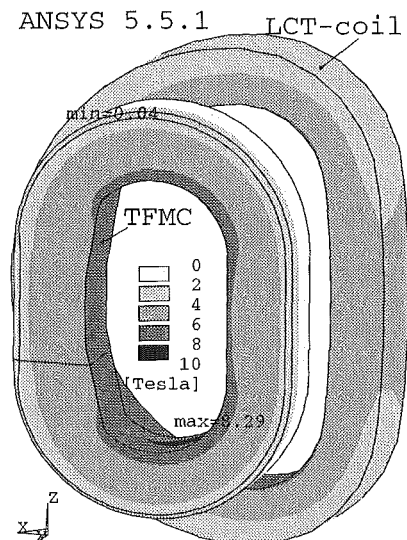
Fig. 1: Electromagnetic field B (Tesla) of the winding packs for TFMC and LCT-coil loaded by 70 and 16 kA current, respectively.

Using the Lorentz force results now mechanical analyses are performed for the TFMC tested alone and in the background field of the LCT-coil as well. Special features of these calculations are the nonlinear friction effects at different contact surfaces between the winding pack and the coil casings and between the coils and the intercoil structure.

Literature:

[1] "Nuclear Fusion Annual Report of the Association Forschungszentrum Karlsruhe/EUTRATOM"
Oct. 1994-Sept. 1995, FZKA 5688, EUR16749EN
Oct. 1995-Sept. 1996, FZKA 5858, EUR17512EN
Oct. 1996-Sept. 1997, FZKA 6050, EUR18156EN
Oct. 1997-Sept. 1998, FZKA 6200, EUR18621EN

[2] R. Meyer "Mechanical analysis of busbars and busbar joints, Forschungszentrum Karlsruhe, Interner IRS-Bericht (May 1999)

[3] "Stress Analysis for the TFMC Tasks in TOSKA - Electromagnetic Global Model", Forschungszentrum Karlsruhe, Interner IRS-Bericht (June 1999)

Staff:

G. Hailfinger
R. Krieg
R. Meyer (till December 1998)
S. Raff
F. Yang (from April 15 till June 30, 1999)

M 45
ITER Coil Casing and Intercoil Structures

Within the course of this Technology task the tensile and fracture toughness properties of heavy section castings and forgings (100-250 mm thick, 1-66 ton) Type 316LN steel commercial products have been determined at 7 and 4.2 K with respect to the application of these structural materials for the most critical parts of the full size ITER TF coil casing. The homogeneity of the material properties, together with the influence of material defects, was investigated by testing tensile (4 and 22 mm gauge diameter) and fracture toughness (standard CT and 6 mm diameter EDM notched bar) specimens machined in all three spatial orientations. In addition, data are presented on the fatigue crack growth rates (FCGR) of the candidate jacket materials for the ITER central solenoid model coil that were measured at 7 K and R - values of 0.1 and 0.4. Besides the jacket material's weld metal FCGR properties also FCGR measurements were performed with respect to the heavy cast steel material at 7 K.

Materials, Specimens, and Experimentals

The supplied materials for the cryogenic mechanical investigations are given in the following:

- Heavy samples were procured from various manufacturing stages of the 65 ton ingot till the final 40 ton square tube forging representing the full scale Model 1. The relevant samples were machined out from various spatial positions. The ingot was melted by Thyssen, Germany and the forging was processed by R. KIND, Germany using a 6000 ton capacity press (see. Fig. 1).

- Representative blocks were machined from different spatial positions of the one ton trial casting representing in thicknesses and in the solidification rate the 25 ton full scale Model 2 presently manufacturing at Creusot Loire Industries, France (see. Figures 1 and 2).
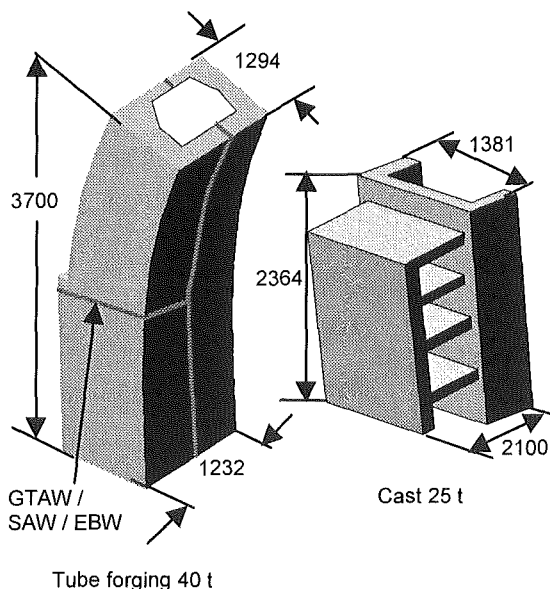
Fig. 1: Full size mock-ups for the ITER full size coil casing.
Model 1 (forging) and Model 2 (casting).

Besides the material testing activities for a reduced scale toroidal field coil for electrical tests an industrial manufacturing task was placed for the two full scale models of the inner upper case leg (model 1) and of the OIS (Outer Intercoil structure>)

region (model 2) . To manufacture these parts successfully a material testing program has been initiated to characterize the procured materials at 4 K and establish a data base to demonstrate the technological feasibility with the realization of full scale sections of the case and the OIS. The selected material was Type AISI 316LN with N = 0.16 - 0.20 % and reduced level of impurities (Cu, Co, S, and Si). The chemical compositions of the investigated base metals are given in Table 1.

Table 1: Chemical composition of the investigated Type 316LN forged and cast stainless steels in weight %.

Mat. / Codes	C	Si	Mn	P / S	Cr	Mo	Ni	N
Forged tube Model 1	.030	.37	2.0	.028/ .002	17.23	2.52	13.46	.182
Casting Model 2	.016	.78	6.0	.022/ .005	17.6	3.01	13.9	.184

The type of specimens used for tensile, fracture, and FCGR investigations were as follows:

Round smooth tensile: gauge diameters of 4 mm machined from the plates, of 4 and 12 mm from the 66 tons forging, and 4, 12, 18, and 22 mm from one ton cast steel.

Compact tension (CT): ASTM proportional 63 x 60, with thicknesses of 15 and 25 mm. FCGR CT specimens of 40 x 43 x 4 mm. Additionally, for fracture toughness verification of cast steel two CT specimens of 109 x 100 x 40 mm.

EDM (Electro Discharge Machined) notched round bar: 50 mm long with a shaft diameter of 6 mm and a net diameter after notching around the girth of about one third of the shaft diameter.
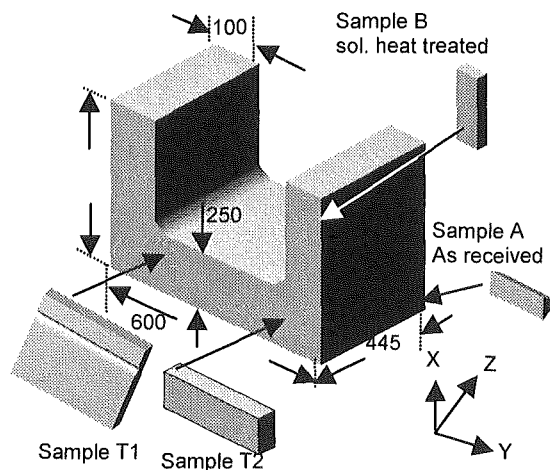
Fig. 2: Casting samples cut from the one ton trial casting was supplied from the EFDA for the planned investigations. The position of removed samples is illustrated according to the designated spatial orientation.

All investigations were carried out either at 7 K or in LHe according to the size of the specimens. Several tensile measurements with specimens having different gauge sections machined from provided samples (cast steel; A, B, T1, and T2 of Figure 2) were performed at 7 K and in LHe to ensure a size and test environment independence especially for the cast steel results. The tensile tests with 12 mm gauge diameter specimens were performed in LHe using the 200 kN screw driven tensile

test machine, whereas the 4 mm gauge diameter specimens were tested at 7 K using the servo hydraulic 25 kN capacity machine [1]. The tensile specimens with 18 mm and 22 mm gauge section diameters machined from a sample cut from the cast steel section (T3, at the vicinity of T1 position) were tested at Breda Istituto Scientifico, Milan, Italy using a 1200 kN capacity servo hydraulic machine (Dartec) equipped with a LHe dewar. The data acquisition for all these tests were performed using the procedure with two extensometers attached onto the specimen.

In addition, ambient temperature measurements were carried out with the cast steel to estimate the macroscopic Young's modulus using a non destructive testing method for the cross check reason of the determined tensile Young's modulus data. The test method consisted of the sound vibration technique by using the impulse excitation of a vibrated rectangular block sample. The sample sizes were ~120 mm x ~20 mm x ~10 mm. The used commercial equipment was the Grindo Sonic, an ASTM Standards C323, C848, C747, and C215 compatible device. Owing to the fact of an expected high anisotropy of the material properties the heavy trial cast steel was investigated thoroughly in all spatial directions.

Results

Table 2 gives the determined tensile and fracture toughness results of the tested materials for both mockups. The tensile

tests with the series T601 (transverse), L600 (length) , and R602 (radial) of Model 1 tube forging show a high yield strength and a scatter of the elongation results compared to the series of T604, L603, and R605. The latter received batch was from samples in fully annealed condition (1080°C/3 h, water quench) , whilst the first series were from a preliminary batch with presumable improper annealing (1050°C/4 h and most probable no water quenching). The first series showed also precipitates reflecting to the low elongation and low fracture toughness results of the two measurements. Comparing the tensile results of the three tests with the radial orientation (R602) it is obvious that between 4 mm gauge diameter specimens, tests conducted at 7 K and a specimen with 12 mm gauge diameter tested at LHe there are no size or environmental effects within the given test conditions. The same is also true in case of specimens from cast samples as given in Table 2. All received cast samples beside the sample A were in fully annealed condition. The obtained yield strengths vary according to different test orientations due to the strong anisotropical behavior of the one ton casting. The designated Y - orientation is inferior to X - and Z -orientations. The specimens having gauge diameters between 4 and 22 mm at 7 K and in LHe show again no significant differences with respect to tensile values. During the tensile tests a strong scatter of the Young's modulus results were observed. This phenomenon can be partly attributed to the local anisotropic properties of the produced cast steel. Further investigations of the Young's modulus properties at 295 K using the sound

Table 2: Tensile and fracture toughness test results of the samples provided from the tube forging and cast steel of Type 316LN materials at 4.2 K and at 7 K.

Material designation test codes and sample orientation in ( )	Young's Modulus GPa	Yield Strength MPa	Ultimate tensile strength MPa	Uniform Elongation %	K_{IC} E-813 MPa√m	K_{IC} JETT [3, 4] MPa√m
Forg. T601 (trans.)	209/209	1185/1165	1625/1635	46.5/40.5		238/163
Forg. L600 (long)	204/207	1113/1062	1620/1624	47/61		206/192
Forg. R602 (radial)	207/207	1140/1168	1457/1418	13/7		218/210
Forg. R602 (radial) [b]	199	1155	1467	15		-
Forg. T604 (trans.) [a]	210	1010	1523	44		-
Forg. L603 (long) [a]	201	1083	1525	45		-
Forg. R605 (radial) [a]	209	934	1473	48		-
Cast sample A (Y)	180/186	954/925	1206/1233	10/10	-	179/132
Cast sample B (Y)	150/155	668/688	1090/1133	31/23	>200 [c]	181/148
Cast sample T2 (X)	196/186	859/877	1167/1108	37/12		
Cast sample T1 (X)	135	811	1069	28		
Cast sample T1 (X) [f]	121	918	1111	35	>230 [g]	
Cast sample T3 (X) [d]	132	936	1283	27		
Cast sample T2 (Z)	158/150	744/738	1142/1196	26/34		
Cast sample T2 (Y)	105/146	693/663	1096/1112	34/37		
Cast sample T1 (Y) [b]	158	652	900	23		
Cast sample T1 (Y)	107/100	769/827	1061/1184	24/27		
Cast sample T1 (Y) [b]	184	770	1073	27		
Cast sample T3 (Y) [e]	132	668	1094	24	>230 [h]	
Casting EBW zone	133/133	974/862	1179/1177	37/35		193/235
Forging EBW zone	161/198	993/1070	1460/1545	30/50		190/212
Forging LBW zone	192	987	1377	18		>220

[a] sample removed from the core of the forging and is in fully annealed condition.
[b] specimen tested at LHe. Gauge diameter = 12 mm.
[c] CT specimens of 15 mm thickness tested at LHe
[d] specimen tested at LHe. Gauge diameter = 18 mm. The sample T3 was provided to Breda.
[e] specimen tested at LHe. Gauge diameter = 22 mm. The sample T3 was provided to Breda.
[f] specimen tested at 4.2 K gas helium. Gauge diameter = 12 mm.
[g] CT specimen of 25 mm thickness tested in LHe.
[h] CT specimen of 40 mm thickness tested in LHe.

vibration technique revealed that in certain local regions the value can be as low as 100 GPa. The elastic analysis of a rectangular block machined from sample T1 resulted a macroscopic Young's modulus of 146 GPa by the vibration test method at 295 K. Machined 4 mm gauge diameter specimens (four specimens) from this particular sample yielded afterwards Young's modulus values of 166, 215, 179, and 107 GPa at 295 K. Therefore, it can be concluded that the macroscopic Young's modulus of the cast steel must have a minimum value of ~ 160 GPa at 4 K.

The fracture toughness results determined with small round bars (JETT, J - Evaluation on Tensile Test) show also a scatter owing to the local anisotropic conditions. For these reason CT specimens were tested up to 40 mm thickness. All the results were so far not valid according to the E 813 crack front profile. Alone the fatigue precrack appearance reveal after the CT specimen fracture a quite different behavior than usual plate materials of similar type. However, a minimum macroscopic fracture toughness of > 200 MPa√m can hold certainly for this newly developed cast steel. Further tests is planned to investigate the toughness properties of this new class alloy.

The last three rows of the Table 2 refer to the EBW (electron beam weld) and LBW (laser beam weld) zones of the forging and cast steel. To determine the EBW metal behavior of these alloys the weld transverse orientation were measured using a 3 mm gauge length small extensometer system. The LBW metal of the forging was measured in weld longitudinal direction with a flat tensile specimen, whose reduced zone (cross section; 2 mm x 1.5 mm) consisted of completely the weld metal.

FATIGUE CRACK GROWTH RATE TESTS

To characterize the cyclic properties of the superconducting conduit weldments for the ITER central solenoid model coil, small size aged (650°C / 200 h) compact tension specimens were machined from the produced Incoloy 908 tubes. The crack plane of the tested four specimens from two production bars were prepared carefully by etching and proper positioning of the notch in long transverse (L-T) orientation along the orbital weld seam. In addition, similar size CT specimens from manufactured and aged Type 316LN steel and Incoloy 908 superalloy from a former batch, detailed recently [5] were tested at R = 0.1 and 0.4 load ratios. All these FCGR measurements were carried out at 7 K as previously given [1, 5]. To characterize the new cast steel of the one ton trial casting three CT specimens were machined from all three spatial directions in as received fully annealed condition. Figure 3 represents all the results of these measurements performed at 7 K. The weld FCGR of the Incoloy 908 is approximately 30% higher than the base metal of the superalloy tested in compacted, bent, and straightened condition. The 0.4 load ratio FCGR tests of both alloys, aged 316LN and Incoloy 908 base metal show a higher growth rate compared to the 0.1 load ratio measurements. The cast stainless steel showed no anisotropic behavior of the FCGR data and therefore all three orientation results are merged to one data set. The measurements carried out at 7 K show for the casting material a superior FCGR behavior compared to both alloys. The fatigue precrack surface appearance of the tested cast steels differ also considerable from the 316LN type structural steels. The high resistance against the cyclic loading with respect to crack growth can be attributed to the completely different microstructure owing to the big grain sizes, a common feature of cast steels.

Literature:

[1] A. Nishimura, J. Yamamoto, and A. Nyilas, Fatigue crack growth of SUS 316 and weld joint with natural crack at 7 K, in: "Advances in Cryogenic Engineering (Materials)," vol. 44, Plenum, New York (1998) p. 81

[2] A. Nyilas and B. Obst, A new test method for characterizing low temperature structural materials, in: "Advances in Cryogenic Engineering (Materials)," vol. 42, Plenum, New York (1996) p. 353

[3] A. Nyilas, B. Obst, and A. Nishimura , Fracture mechanics investigations at 7 K of structural materials with EDM notched round and double edged - bars, in: "Advances in Cryogenic Engineering (Materials)," vol. 44, Plenum, New York (1998) p. 153

[4] A. Nishimura, J. Yamamoto, and A. Nyilas, Fracture toughness evaluation of a round bar with circumferential notch at cryogenic, in: "Advances in Cryogenic Engineering (Materials)," vol. 44, Plenum, New York (1998) p. 145

[5] A. Nyilas, B. Obst, and D. R. Harries, Mechanical investigations on aged stainless steel and Incoloy 908 materials at 4.2 K and 7 K, in: "Advances in Cryogenic Engineering (Materials)," vol. 44, Plenum, New York (1998) p. 17

Staff:

A. Nyilas
H. Baumann (till 31. 8. 99)
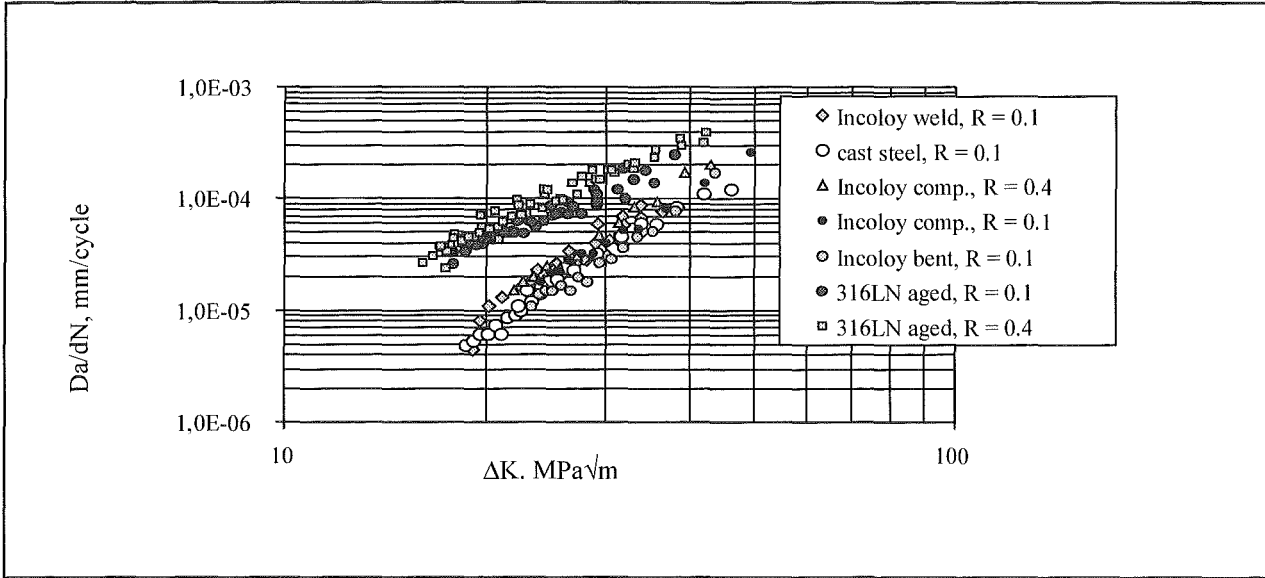
Fig. 3: Fatigue crack growth rate of aged Type 316LN and Incoloy 908 jacket Materials at 7 K. The cast steel FCGR represent the measurements at 7 K in all three spatial orientation.

Materials Development

T 228.1
Influence of Higher Hydrocarbons on Vacuum Pumping

1 Radiochemistry

Because the radioactive decay of tritium takes place without activation energy, the progressive formation and accumulation in cryopump adsorption panels of tritiated reaction products with high specific tritium cannot be excluded. As pointed out below (Task VP1), the presence of high molecular weight substances in contact with the charcoal of the cryosorption panels would necessitate highly demanding regeneration techniques. It should therefore be kept at a minimum level. Thus an investigation of the products from the radiation-induced reaction between an equimolar deuterium-tritium mixture or pure tritium with carbon oxides was undertaken and a kinetic study of the reactions in the gas phase was performed. This work aims at defining the conditions needed to avoid the formation of undesired substances.

For the rate measurements conditions simulating those expected in the Tritium Plant of ITER-RC/RTO, i.e. low concentrations of CO (1.5 - 6 %) in hydrogen isotopes with He (3 %) were chosen. The experiments were carried out with the PETRA facility of the Tritium Laboratory Karlsruhe. Tritium, supplied by CFFTP, Canada, was of high purity, i.e. 99.8 % T, 0.1 % D and 0.1 % H. Reaction products were identified by infrared analysis, omegatron mass spectrometry, and radio gas chromatography.

The product distribution of the radiation-induced reaction between tritium and CO is dependent upon the initial composition of the reaction mixture. At low CO partial pressures this reactant is almost completely consumed after reaction with DT or T_2. Mainly polytritiated methane as well as other polytritiated higher hydrocarbons, e.g. polytritiated ethane and propane, were identified as products (see fig. 1). Other products were CO_2, traces of tritiated water and possibly polytritiated formaldehyde and ethylene. In addition, there were indications that high molecular weight condensable products, perhaps even polymers, were also formed.

Replacing DT by T_2 nearly doubled the initial rate of carbon monoxide conversion. The initial rates of total pressure

decrease and of carbon monoxide partial pressure decrease were found to be proportional to the initial partial pressure of tritium from a total of 24 experiments with DT and T_2, the ion pair yield was calculated to be 1.6 ± 0.8.

The rate of consumption of CO was studied at initial constant composition of 94 % DT, 3 % CO and 3 % He at several total pressures. The change in concentration of CO in these runs was determined by infrared spectroscopy. As apparent from the fig. 2 the rate is strongly dependent on the CO partial pressure.
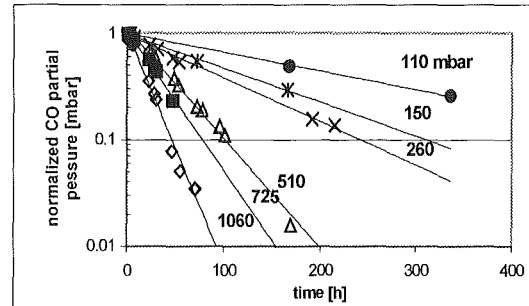
Fig. 2: Effect of pressure on the initial CO - tritium reaction rate

The change in CO depletion rate is determined by the relative fractions of β-particle energy absorbed by the gas and by the walls of the cell.

Staff:

U. Berndt
C. Caldwell-Nichols
Chr. Day
S. Grünhagen
W. Hellriegel
E. Kirste
R. Lässer
R.-D. Penzhorn
J. Wendel
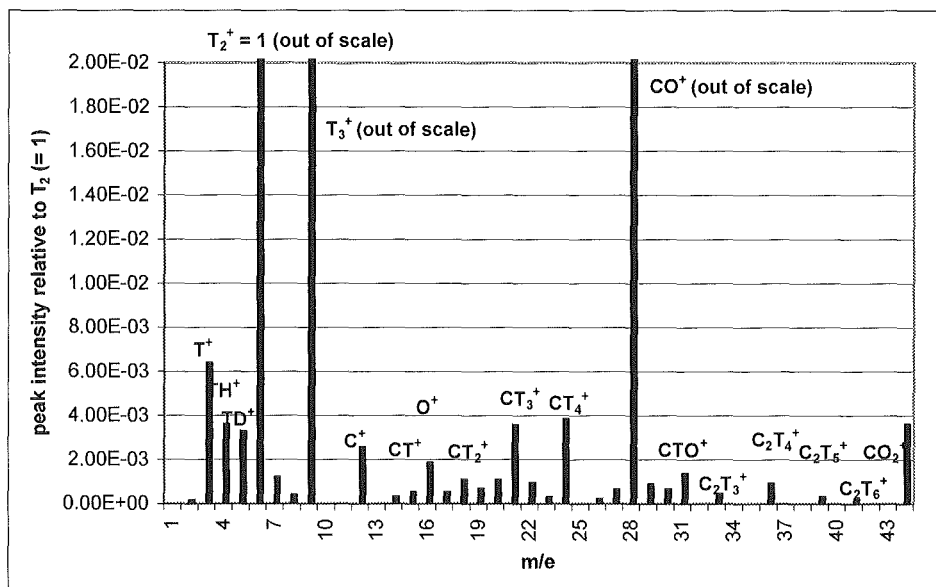
Fig. 1: Omegatron mass spectrum of a T_2-CO mixture (qualitative only)

2 Cryosorption aspects

In parallel to the above described experiments, a new facility was set up to study the radiochemistry of tritium with CO and the formation of hydrocarbons directly at the cryosorbent (activated charcoal) contact under cryogenic temperature conditions. It is based on a two-stage Gifford McMahon closed cycle helium refrigerator, which is able to provide about 10 K at a representative charcoal sample (some g). The sample holder allows to investigate charcoal in the form of loose granule material or bonded to a metal substrate to simulate cryopanel conditions most neatly. The temperature of the sample can be monitored by cryogenic silicon diodes. The second stage of the refrigerator is equipped with a resistance heater to make the whole temperature range between 10 K and 80 K available. Fig. 3 shows a systematic flow diagram of the facility.
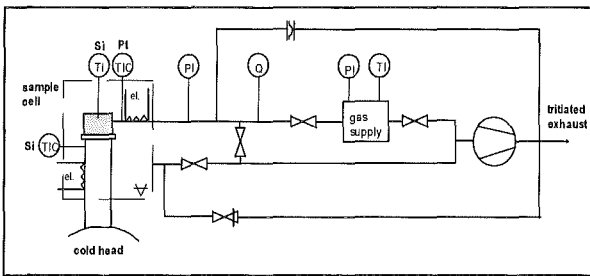
Fig. 3: Systematic flowsheet of the experimental set-up

The facility was set into operation under non-active conditions (i.e. outside a glove-box) using the pure gases D_2, H_2 and CO and a mixture of D_2 containing 6 mol% CO in preparation of experiments to be performed using the facility PETRA. The charcoal used was a granule material (type SC-II by CHEMVIRON, 1.68 mm mesh size, 1500 m²/g BET surface) and is identical with the sorbent material foreseen for the coating of the cryosorption panels in the ITER ultra high vacuum system. In the frame of the initial tests of the facility, sorption equilibria were measured under isochoric conditions. These tests were repeated under variation of the initial gas load and the cell volume. Some typical results for sorption isotherms, as derived from the direct measurement results are depicted in Fig. 4. For temperatures below 60 K, the adjusted initial gas load of 200 (mbar·l)$_N$/g charcoal (referenced to 1 atm and 0 °C) was less than saturation according to the experimentally accessible pressure range. It is revealed that the sorption capacity for deuterium is about 20 % larger than that for hydrogen.
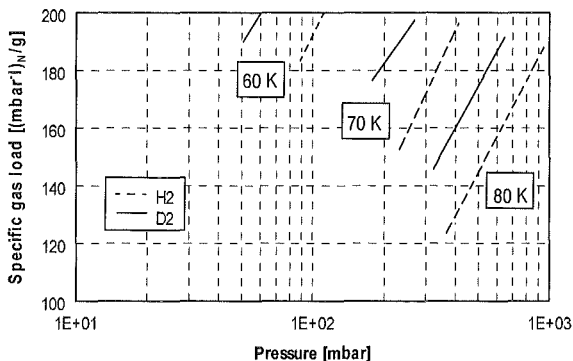
Fig. 4: Sorption isotherms for two hydrogen isotopes

Fig. 5 presents measured thermal desorption data. It gives a comparison between the sorption characteristics of the loose granules and the same material embedded in a binder on a cryopanel segment. The bondage was realized by means of an inorganic cement with high temperature conductivity, which has been qualified for use in ITER [1]. The curves in Fig. 5 were measured under identical pre-loading conditions of 200 (mbar·l)$_N$/g charcoal.
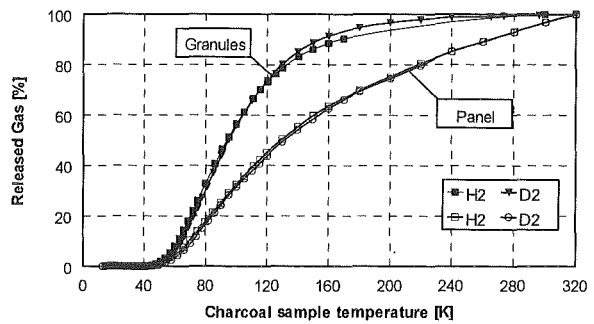
Fig. 5: Desorption characteristics for two hydrogen isotopes from the same charcoal material, in loose or in bonded state

The difference between the two hydrogen isotopes is quite small, although the corresponding pressures do differ (see Fig. 4). It is revealed that bonding leads to considerably retarded gas release behaviour. This retardation effect explains very well the discrepancies found in former experiments. There, desorption tests of cryopanels always yielded a slower gas release than what was expected from literature desorption data, which were exclusively measured with loose material [2]. However, it should be pointed out that the release characteristics shown in Fig. 5 cover a pressure range up to 1 bar and are therefore not quantitatively representative for the ITER cryopanel regeneration, which will be performed in the low pressure range and thus at considerably lower desorption temperatures. In further runs, the low pressure regime will also be assessed experimentally.

The tests made demonstrated the correct functioning of all parts of the facility. At present, the facility is under refurbishment and will then be integrated into a glove-box to be able to start reaction tests with tritiated gas mixtures.

Literature:

[1] H. Haas, Report on Long-term Temperature Cycling Test of Panels, Forschungszentrum Karlsruhe, Interner HIT-Bericht.

[2] Chr. Day and A. Schwenk-Ferrero, Pumping Speed and Selectivity Phenomena for Cryopumping of ITER relevant Exhaust Gas Mixtures, Proc. 17th Symp. on Fusion Engineering, San Diego, CA, USA, Oktober 1997, pp. 1109-1112.

Staff:

U. Berndt
Chr. Day
E. Kirste
A. Mack
R.-D. Penzhorn

Fuel Cycle

VP 1
Cryopump Development and Testing

1. Introduction

The acceptance tests at the contractor's premises for the model pump have been finished.

After that the model pump was shipped to FZK and installed in the TIMO facility. Pump housing, test vessel and cryotransfer lines were baked out and pumped down. Data acquisition and process control system were checked. TÜV approval was achieved. A detailed test programme has been prepared.

The acceptance tests at the contractor's premises of the 3000 l control cryostat for upgrading the TIMO and the manufacturing of the cryotransfer lines are under work.

In the TITAN facility tests were performed to study the influence of H_2O and higher hydrocarbons on the pumping behaviour of ITER-relevant exhaust gas mixtures.

Tests are prepared in the upgraded OMNISORP facility to determine sorption data of different materials at 5 K and find out the optimized one for the pumping of ITER exhaust gas.

2. Model pump

2.1 Scope of acceptance tests at contractor's premises

The acceptance tests at the contractor's premises have been performed for the model pump which is grouped into five subassemblies [1]:

- Cryopump housing,
- Internal structures,
- Main valve with bellow assembly and pneumatic actuator,
- Cold valve box,
- Cryotransfer line.

All pressure vessel were designed and tested according to the German TÜV-rules. Functional tests of all valves and valve actuators are required. All surfaces in contact with vacuum were treated according to the rules for ultra high vacuum.

The components to be operated with supercritical helium (SCHe) or liquid nitrogen (LN) have been leak tested at room temperature and in cold state after exposing the parts to thermal shocks.

2.1.1 Pump housing

The pressure barrier of the pump housing is consisting of: Outer cylindrical shell, main valve disk, bellow arrangement, pump plug. All these parts are designed for a maximum allowable overpressure of 0.9 MPa. The reason for this design pressure is the risk of an oxyhydrogen explosion in case of an air inbreak.

2.1.2 Internal structures

The internal structure comprises the 4.5 K panels, 80 K-Louvre baffle and 80 K-shielding.

All parts of the internal structure are designed and manufactured as pressure vessel components for a maximum allowable operation pressure of 1.7 MPa abs. according to German TÜV rules. The leak rate is fixed to less than 10^{-9} Pa·m^3/s.

The pressure drop in the cooling channels of the 4.5 K panels from inlet flange to outlet flange of the cold valve box must not exceed 0.015 MPa at a SCHe-mass flow of 250 g/s. For the 80 K-GHe circuit of the shielding and the Louvre baffle a pressure drop of 0.1 MPa with a flow rate of 200 g/s was required.

The pressure drops were simulated at room temperature with N_2-gas using the same Re-number as in cold state for He.

2.1.3 Metal bellow assembly and actuator for main valve

The main valve closes the pump entrance during regeneration. In case of high pressure upstream of the pump inlet, the valve must throttle the process gas flow to achieve molecular flow conditions inside the pump. The valve disk is driven by pneumatic actuator at the rear side of the pump connected by a shaft.

A metal bellow arrangement is used as moving sealing element between pump housing and atmosphere along the actuator shaft. The bellow arrangement is divided into four sections which are connected to each other by flange rings. The maximum allowed travelling distance of each segment is limited by guided rods which are fixed on the flange rings.

The initial bellow arrangement was manufactured in Inconel 625. Several acceptance tests showed that the specified leak rate of less than 10^{-4} Pam^3/s couldn't be achieved. Because of uncertainties concerning the reason, it was decided to perform cycling tests by the manufacturer with comparable bellow samples made in Inconel 625 and stainless steel (316 L). Both samples withstood 3×10^5 cycles without failures.

The final bellow arrangement was manufactured in stainless steel (316 L). Improvements were made on the geometry and sealing concept. Additionally an antirotation system was installed in front of the main valve disk to avoid induction of torsional moment. An auxiliary tool was used, which fixes the actuator shaft and the bellow arrangement during installation.

The accurate positioning of the pneumatic actuator was checked. The required data were achieved.

2.1.4 Cold valve box

The cold valve box is a vacuum vessel including all valves and pipes needed for controlling the flow rates of SCHe, 80 K-GHe and 300 K-GHe during the different operating modes of the cryopump. For the outer shell a leak rate of 1.9×10^{-9} Pa·m^3/s was achieved. The inner circuits were designed for a maximum allowable operation pressure of 2 MPa and tested with 2.2 MPa.

Leak rates of the inner circuits were checked after thermal shock of the total system by filling with LN and afterwards heating up to room temperature. Integral leakrates of less than 10^{-9} Pa·m^3/s were achieved.

The valves were submitted to open/close tests with response of the limit switches.

2.1.5 Cryotransfer line model pump/cold box

The cryotransfer line connects the model pump with the cold box. The outer tube serves as shell for the vacuum insulation for the go and return lines of SCHe-, 80 K-GHe- and 300 K-GHe-supply of the model pump. The supply lines are connected to the model pump and the cold box by KENOL-couplings.

Leak rates of less than 10^{-7} Pa·m^3/s were achieved at the KENOL couplings. The outer tube had to be adapted to the position of the model pump and the cold box. Therefore, an optical 3D-measurement was performed after positioning of the model pump and the cold box.

The outer tube was manufactured according to the coordinates of the 3D-measurement. Final adaptation could be done by an adjustable link in between the line. After installation the total leak rate of the vacuum insulation volume was less than 10^{-7} Pa·m^3/s.

3. TIMO facility

The test facility for ITER model pump (TIMO), see Fig. 1, is installed in the building 406 on site of Forschungszentrum Karlsruhe. This test device, manufactured and installed, in parallel to the manufacturing of the model pump, is designed for testing the model pump under ITER-relevant operating conditions.

3.1 Installation of model pump

The model pump was shipped to Forschungszentrum Karlsruhe in May 1999 and installed in the test vessel (see Fig. 2). All cryogenic and vacuum lines were connected. All circuits were leak tested, purged, baked and pumped out. Preliminary cooling down tests to 80 K have been started.

3.2 Process control and data acquisition

The analogue and digital values are stored in the CAMAC-Crate, which is storing the pre-programmes process control. The CAMAC-Crate is connected with the data acquisition system (MES) where the analogue signals 0...10V are converted into physical values by the computer, which is storing the data at the file-server. In the data evaluation system (MAS) the physical values are converted into diagrams when the selected data are extracted from the file-server. The MES, MAS and the file-server are interconnected via a FDDI star coupler.
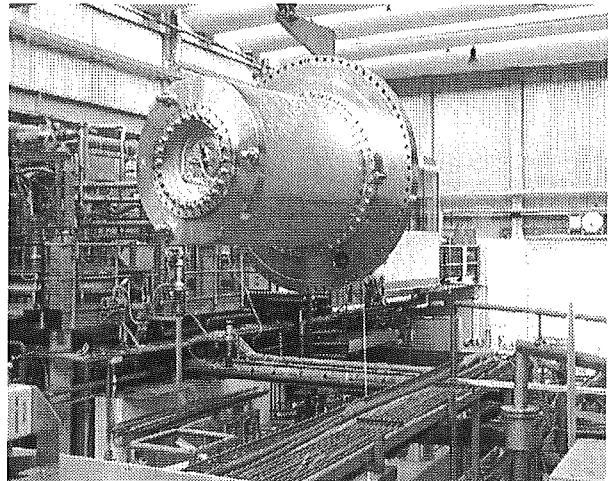
Fig. 2: ITER Model Pump – Installation to the TIMO test facility.

The process control is carried out by use of a SPS SIMATIC-S5-135U controller. Analogue signals, which are required for the process control, are directly registered, all other physical values are registered by the MES via a serial port connection. The mimicking of the flowcharts are carried out by COROS, which is operating regulators, valves, pumps and registering alarms and messages, which are indicated on an alarm page.

The system has been connected to the model pump and tested.

3.3 New control cryostat

The control cryostat to be used for the final acceptance tests has a buffer volume of 700 l and a cold blower with a maximum flow rate of 50 g/s. It was taken over from an existing former test device. For the test programme with the ITER model pump, higher buffer volume and higher flow rates are needed to achieve the required pump cycles, the cooling down time and the temperature homogeneity across the panel. Manufacturing

Exhaust line
Process gas

Valve Box

Transfer line

Safety devices

Safety devices

TIMO
Test chamber

Regeneration
lines

Valve actuator

Vacuum pump
stations

Pump plug
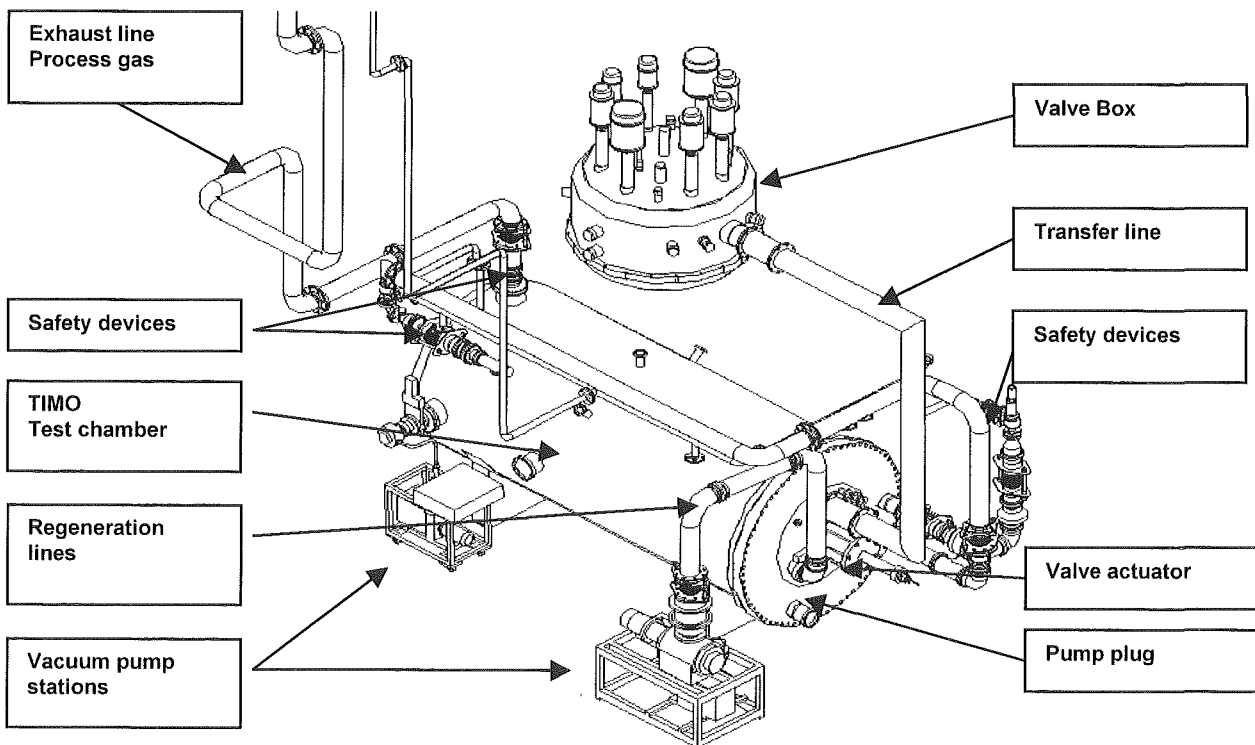
Fig. 1: 3D view of TIMO test facility

of the new control cryostat is finished. Tests at the contractor's premises are under work.
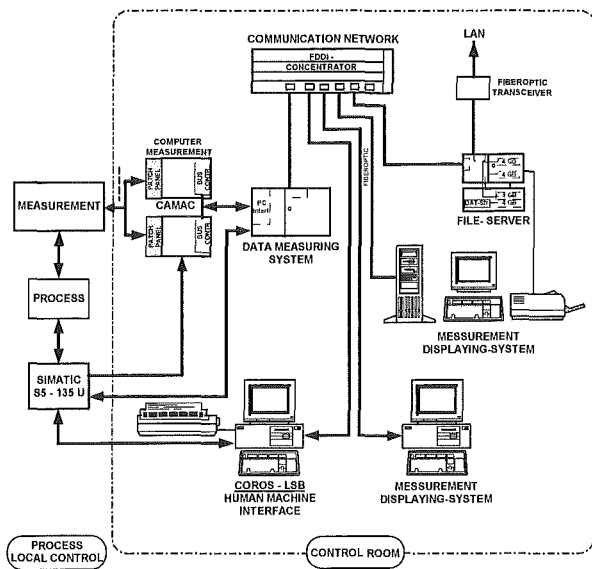
Fig. 3: Process control and data acquisition

3.4 Cryotransfer lines cold box/control cryostat

The cryotransfer lines between new control cryostat and cold box are manufactured. Acceptance tests have been started.

4 Tests to determine the effect of water on sorption panel performance in the TITAN facility

The TITAN facility has been used to perform a test campaign to define the reactivation conditions of the charcoal material used for the cryopanels. The developed regeneration concept comprises three different regeneration levels to cope with different groups of pumped gases.

In former experiments, it was revealed that the accumulation of typical impurity components present in the fusion exhaust gas (carbon oxides, noble gases) during several subsequent pumping cycles can be tolerated up to a certain level, when the sorbent is regenerated after each cycle at about only 85 K [2]. At this temperature, the hydrogens and helium, which form the major part of the fusion exhaust gas, are released completely, whereas the heavier impurity species are allowed to accumulate. The second stage of regeneration to be performed at about 250 K to 300 K after approximately 10 partial regeneration cycles is designed for release of air-like impurities (N_2, O_2, CH_4 etc.). On top of that, a third regeneration step is necessary at even less frequent intervals, mainly to limit the accumulated tritium inventory in form of tritiated impurities, such as water or higher hydrocarbons. These substances will at first be condensed at the inlet baffle system (at 80 K) and, from that respect, will not immediately influence the sorption performance of the panels downstream. However, within the 2nd regeneration level, the condensed species will evaporate. The released molecules, then in gaseous phase, will instantaneously be sorbed by the charcoal, as the sorption capacity is still relatively high at this temperature level. Until now, no theory has been developed, which could correctly account for all the different observed behaviours for ad-/desorption of water-like substances on bonded charcoal. An experimental approach has therefore been chosen to investigate the conditions needed for release of these species and to assess quantitatively their poisoning influence on pumping of ITER exhaust gas mixtures.

4.1 New dosage system

The experimental idea was to preload the panel with water according to a defined value and to perform pumping speed and regeneration tests with this panel. Consequently, the TITAN facility had to be upgraded in order to be able to handle water-like substances, which are in the liquid state at ambient conditions and can therefore not be processed by the available thermal mass flow controllers via the PNEUROP dome. To cope with that, a bubble column was developed, which allowed to moisturize a gas stream. This wet gas stream could then be injected into the facility so that the moisture would be adhered by the sorbent. A photographic view of the bubble column in operation is shown in Fig. 4:
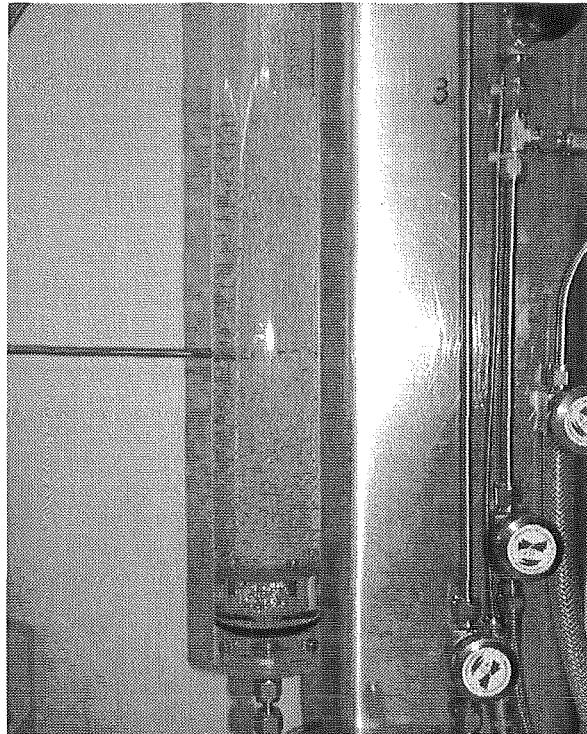
Fig. 4: Installed bubble column, operated with 1000 sccm He in water (level of liquid hold-up is 250 mm).

The wetting device was calibrated with water and two liquid hydrocarbons (n-hexane and i-octane) as representatives of the water-like species and with air, nitrogen and helium as carrier gas species. The relative humidities achieved at different states of operation were validated with a self-developed psychometric sensor.

The injection of the wet gas into the facility has to assure that the water-likes will be completely sorbed out of the gaseous phase by the sorption panel. Thus, a separate pipe was installed, which ends up directly above the panel. The efficiency of that constructive solution was demonstrated: only about 0.4 % of the dosed water molecules leave the shielded volume of the cryosorption panel area unsorbed.

4.2 Test programme

The water gas load under interest in this investigation is given by the order of magnitude typical for ITER. The plasma exhaust gas has a specified maximum water content of 0.5%. Related to the installed panel surface, this leads to accumulated water gas loads in the order of less than 0.01 ($Pa \cdot m^3$)/cm^2 (equivalent with 0.05 mol/kg). This is far below the sorption capacity of SCII-charcoal for water at ambient conditions, which is more than two orders of magnitude larger [3]. However, higher water loads may

arise e.g. in water-leakage scenarios. Therefore, measurements were made at maximum gas throughput (2.6 $(Pa \cdot m^3)/(s \cdot m^2)$, related to the cryopanel surface) and various high water pre-loadings (0, 0.01, 0.05 and 0.1 $(Pa \cdot m^3)/cm^2$) and for two different ITER exhaust model gas mixtures, so as to simulate DT-shot conditions and H_2-shot conditions.

4.3 Pumping behaviour

Fig. 5 highlights the influence of water preloading for these mixtures. It is revealed that, already for small water gas loads, the pumping speed is reduced by approximately 10%, uniformly throughout the whole pumping period. However, in the case of high gas loads, the amount of preadsorbed water does not bear a strong influence in the investigated range.

The moderate poisoning effect compares very well to the poisoning behaviour reported earlier for other impurities [2]. In this sense, water does not play an extra role. The required pumping speed for ITER of about 1 $l/(s \cdot cm^2)$ can still very well be complied with. Nevertheless, even if enough pumping speed is available, the water has to be released from time to time, e.g. due to limitations of the accumulated tritium [4]. This aspect is considered in the next section.

4.4 Desorption behaviour

From fundamental physics there are two different driving forces to stimulate desorption, one is pressure reduction, the other temperature increase. For the application in ITER, a 300 K GHe supply circuit is readily available for warming up the cryopanels. However, if higher temperatures would be considered to be necessary for the release of water-like impurities, this would have major repercussions on the design of the GHe system and the cryogen consumption within the subsequent re-cooling process. Therefore both drivers were investigated to check their potential for use in ITER.
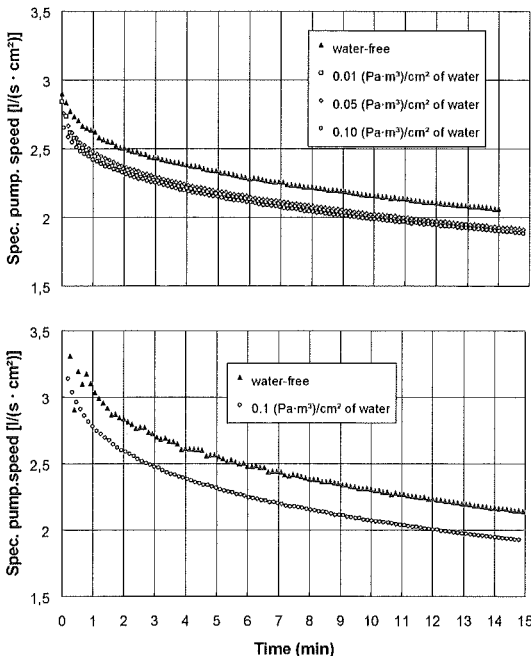
Fig. 5: Pumping speed results as a function of pumping time at maximum throughput conditions and various water pre-loadings. Top: measurements for a D_2-based system (85.96% D_2, 10.99% He, remainder impurities), bottom: measurements for a H_2-based system (90.75% H_2, 5.67% He, remainder impurities).

The temperature influence is depicted in Fig. 6, which gives the amount of released water (measured by quadrupole mass spectrometry at peak 18.0) due to temperature increase. It is clearly shown that the water is almost completely released at a temperature of about 100 °C. The 20 % difference in mass balance between water dosed in and released water, which was repeatedly found during our experiments, is attributed to a coverage of the wall surface between panel and mass analyser, which has to be operated via a pressure reduction system.
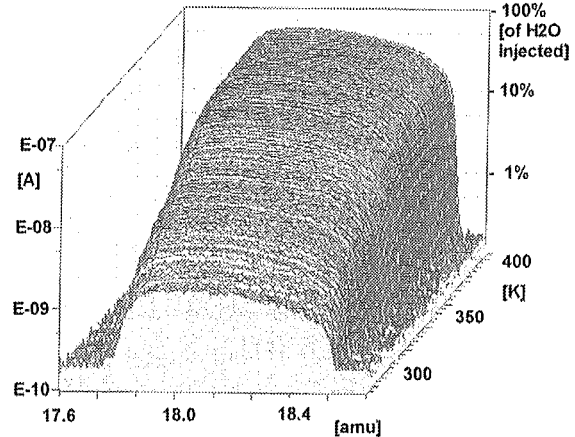
Fig. 6: Release of sorbed water by temperature induced desorption (at a total pressure of 1.2 kPa and an initial pre-loading with 0.009 $(Pa \cdot m^3)/cm^2$) of water.

In principle, the same residual gas load can also be achieved by pressure decrease. However, in ITER, the achievable vacuum for desorption of the cryopanels is in any case limited by the end pressure of the forepump trains used, i.e. about 1 Pa (the available pressure will be even worse than that due to conductance losses between cryopump and mechanical pump).

Three tests to elaborate the pressure influence are shown in Fig. 7, which compares (left ordinate) the pump out curves of the TITAN facility volume (filled with helium up to $5 \cdot 10^4$ Pa) in case of an unloaded, freshly baked-out panel, and in case of the panel loaded with water. The pump down curves have been measured using a turbomolecular pump set with 500 l/s nominal pumping speed and are in terms of time demands not to be scaled up to ITER conditions. The curves show two different regimes: the high pressure regime, characterised by the pump out of the helium gas and therefore identical for all three curves, and the low pressure regime, characterised by a deviation from the reference curve for pure helium. The inflection point is caused by water desorption, which starts earlier at higher loads.

The measured water peak intensities are also given in Fig. 7 (right ordinate). They as well reveal the sudden release of water at the inflection point. Comparing the increase in signal level with the situation depicted in Fig. 6 shows that the release efficiency of the two different desorption mechanisms is of comparable magnitude, but somewhat smaller for pressure induced desorption.

The shape of the pump out curves reveals another general drawback of pressure induced desorption, that is the very much increased time needs to achieve a certain pressure level. However, as soon as the inflection region is reached, the water release starts quite rapidly. Thus, if regeneration time is limited, which must not necessarily always be the case, the available forepump pumping speed should be increased to such an extent that the required pressure comes to lie in the steep decreasing part of the pump down curve. The applicability of pressure induced desorption is limited by the ultimate pressure of the

forepump train, which corresponds directly to a certain remaining water gas load, which cannot be further diminished.
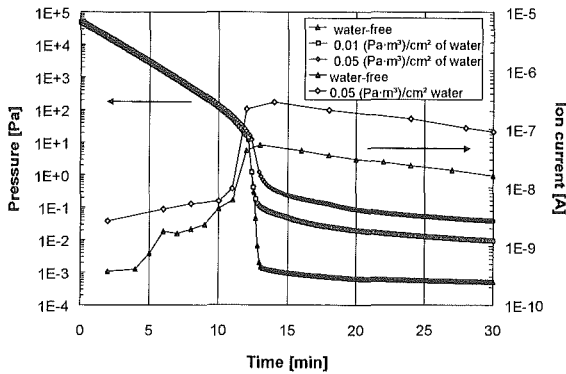
Fig. 7: Release of sorbed water by pressure induced desorption (at ambient temperature)

4.5 The next step

Our experimental programme could demonstrate that the poisoning effect due to water sorbed at the cryopanels stays within moderate boundaries for the regions typically encountered in ITER and will not be a limiting factor in the cryopump operation. A level of about 100 °C turned out to be necessary to regenerate solely by temperature increase. To achieve sufficient desorption velocity at reduced energy expenditure, a combination of both desorption mechanisms looks the most promising.

The investigation will be pursued to include other substances with strong sorption capacity, such as higher hydrocarbons, which have different thermophysical properties in terms of polarity and intensity of dispersion forces between adsorptive and carbon. These substances have been detected in other tokamak machines and may play a predominant role even if present only in small amounts, as they exhibit a very strong interaction with charcoal still at high temperatures. This item is also of special interest as these kind of substances are presently under discussion for use as spiking additives in the detection of leaks of the cooling water circuits [5]. Besides the technological points dealt with in this task VP1, the question of how these substances can originate in the torus vessel from other sources, mainly chemical reactions under tritium is tackled in task 228.1, see below.

5. Characterisation and optimisation of cryosorbent materials

The desorption and poisoning tests in the component test facility TITAN showed that helium is most sensitive to poisoning effects of the sorbent material. During pumping, helium is enriched over the pumping cycles, thus leading to a considerable decrease of overall pumping speed [6]. This behaviour is attributed to the low sticking coefficient of helium and the partly blocked charcoal pores of the sorbent material by the other gases present in the exhaust gas to be pumped.

Therefore, the sorbent material should be especially optimized for the pumping of exhaust gases. Apart from the improvement of the storage capacity for relevant gases, the problem of competitive gas sorption has to be solved. A further aim of the investigations is to gain a general understanding of the elementary mechanism of sorption at low temperatures and to provide a theoretical framework to predict cryosorption processes quantitatively.

As sample material, charcoal of different manufacturers will be used, either as loose material or in the form of a fixed layer, bonded to a copper sheet with inorganic cement. The latter configuration is to simulate the cryopanel set up most neatly.

The experimental part of the task involves the development and design of a special facility dedicated to determine sorption data in the ITER relevant very low temperature range down to 4 K. There are no solutions available on the commercial market. A concept was developed, based on an existing apparatus for sorbent characterisation at 80 K (liquid nitrogen cooled). This device, an OMNISORP 100 analyser (by company Omicron Technology Corporation) was used in former times to characterise molecular sieve materials [7]. It is based on the continuous sorption method, which uses a continuous flow rate of adsorbate gas to the sample. The flow rate, the pressure and the experimental time can be measured automatically to determine the adsorbate rate and derive sorption isotherms. To obtain a more versatile facility, especially dedicated to low temperature application, the apparatus will be equipped with a two-stage Gifford McMahon refrigerator (by comp. SUMITOMO), which provides 4 K at its cold head. Aside from the cold head, the low temperature part of the facility comprises a sample chamber, a heat shield and a vacuum chamber. The analyser and the sample chamber will be connected with a gas transfer line, and form together the new facility COOLSORP. It has the advantage of providing the complete operation temperature range between 4 and 80 K and is working continuously as no cryogenic liquids are needed anymore. Fig. 8 shows the elementary set-up of the COOLSORP facility.
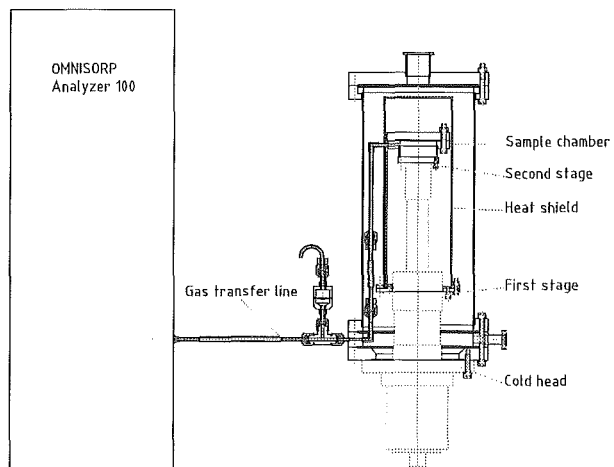
Fig. 8: Sketch of the COOLSORP facility.

Literature:

[1] A. Mack et at., ITER Primary Vacuum Pump, Proc. 20th SOFT, Marseille, France, September 1998, pp 1037 - 1040.

[2] Chr. Day et al., The Experimental Basis for the ITER Cryopump Regeneration Concept, Proc. 20th SOFT, Marseille, France, September 1998, pp. 921-924.

[3] R.H. Bradley and B. Rand, A Comparison of the Adsorption Behaviour of Nitrogen, Alcohols, and Water Towards Active Carbon, Carbon 29 (1991) 8, 1165-1172.

[4] D.K. Murdoch et al., Tritium Inventory Issues for Future Reactors; Choices, Parameters, Limits, 20th SOFT, Marseille, France, September 1998, accepted for publication in Fusion Engineering and Design.

[5] K.S. Forcey and R.A.H. Edwards, Detection and Localisation of Leaks from Cooling Circuits, Deliv. 1 of Task VP3, Ispra, Italy, February 1999.

[6] Chr. Day et al., Pumping performance of Cryopanels Coated with Activated Carbon, Adv. Cryogenic Engng. 43 (1998) 1327-1334.

[7] D. Burghardt et al., Investigation of Nitrogen and Helium Cryosorption on Molecular Sieves, Vacuum 45 (1994) 547-550.

Staff:

Chr. Day
A. Edinger
J. Grimm
H. Haas
V. Hauer
T. Höhn
W. Höhn
H. Jensen
B. Kammerer
J. Laier
A. Mack
H. Reinhard
K. Sachs
R. Simon
J. Weinhold
St. Zabeschek
D. Zimmerlin

TR 1
Tokamak Exhaust Processing

Demonstration of CAPER with Tritium

The facility CAPER at the Tritium Laboratory Karlsruhe (TLK) merges the former two stage CAPRICE (Catalytic Purification Experiment) process and the PERMCAT (Permeator Catalyst) concept to set up an integral and fully continuous three stage clean-up process for fusion reactor exhaust gases. In the first step molecular deuterium and tritium is removed with the help of a so-called front-end palladium/silver permeator. The second step comprises an impurity processing loop with a nickel catalyst bed and a copper chromite catalyst bed for hydrocarbon cracking and the water gas shift reaction, respectively, combined with another palladium/silver permeator for removal of liberated deuterium and tritium. Any remaining deuterium and tritium is recovered by counter current isotopic swamping in the PERMCAT as a third, final clean-up step.

The main objectives of the experimental campaigns with CAPER are to demonstrate high overall decontamination factors of about

10^8 for typical off-gases of RTO/RC-ITER at a relevant scale and to prove the process with tritium in long term experiments. At the same time a new catalyst bed and a new pump will be tested. The new catalyst bed combines the hydrocarbon cracking bed and the water gas shift bed into a single outer containment. The new pump is a five-stage positive displacement compressor with ceramic coated pistons and cylinders.

The CAPER facility is well instrumented and equipped with quite a number of control loops for the variation of experimental parameters and for a proper characterization of components rather than of component combinations. Therefore the data measured with CAPER can be used to design a clean-up facility for RTO/RC-ITER and properly scale the equipment with respect to the final requirements of ITER.

Table 1 gives an overview of the CAPER control loops. The controlled parameters are listed together with the objective of the control loop and its range.

Table 1: Experimental Caper Control loops

Loop Nr.	Controlled parameter	Location	Purpose	Range
1	Vacuum	Pure hydrogen isotope side of Front-end Permeator	Front-end Permeator performance tests independent of pumping speed of Permeate Pumps	400 Pa to 50 kPa
2	Pressure	Bleed side of Front-end Permeator	Test of Front-end Permeator performance independent of Impurity Buffer Vessel pressure	20 kPa to 160 kPa
3	Pressure	Discharge side of Permeate Pumps	Test of Front-end Permeate Pump System performance	20 kPa to 100 kPa
4	Flow rate	Front-end Permeator inlet	Test of three isotope permeation flow rate as function of impurity concentration	0.1 mol/h to 18 mol/h
5	Flow rates	Torus Mock-up section	Control composition of Front-end Permeator feed gas (3 independent impurity inlet flows)	0.0 mol/h to 1.8 mol/h
6	Flow rate	Inlet to Vaporizer	Test of liquid water processing by water gas shift reactions at different throughputs	0.1 mol/h to 15 mol/h
7	Pressure	Vaporizer outlet	Test of liquid water processing by water gas shift reactions at different water partial pressures	20 kPa to 100 kPa
8	Pressure	Impurity Loop	Pressure dependence tests of Impurity Loop performance	20 kPa to 160 kPa
9	Pressure	Impurity Loop Permeator	Examination of decontamination factors as a function of Impurity Loop Permeator inlet pressure	20 kPa to 160 kPa
10	Flow rate	Impurity Loop	Examination of decontamination factors as a function of Impurity Loop flow rates	0.1 mol/h to 2.5 mol/h
11	Pressure	Pure hydrogen isotope side of PERMCAT	Test of PERMCAT performance as a function of PERMCAT pure hydrogen isotope side pressures	0.5 kPa to 10 kPa
12	Flow rate	Hydrogen to PERMCAT	Examination of decontamination factors as a function of swamping ratios	0.02 mol/h to 0.2 mol/h
13	Flow rate	Hydrogen to impurity feed of PERMCAT	Examination of decontamination factors as a function of swamping ratios	0.0 mol/h to 0.05 mol/h
14	Flow rate	PERMCAT impurity feed	Examination of decontamination factors as a function of PERMCAT throughput	0.1 mol/h to 0.5 mol/h
15	Pressure	PERMCAT inlet pressure	Examination of decontamination factors as a function of PERMCAT inlet pressure	0.5 kPa to 10 kPa

Not only because of the numerous control loops, but also due to possible options for sending the process gas through alternative routes and due to a variation of the actual operation temperatures of catalyst beds or permeators a large quantity of experimental parameters can be covered.

All initial tests of the CAPER facility have been successfully finished. The licensing process is completed as well and tritium tests will start with front-end permeator and front-end permeator / hydrocarbon cracker tests. These experiments will investigate the effect of high hydrocarbon concentrations in the feed gas of CAPER or the effect of high inert gas loads such as argon, helium, neon or nitrogen, which may be added to enhance cooling of the divertor of ITER.

The off-gas from these experiments will be processed continuously in the impurity processing loop and in the technical PERMCAT of CAPER. Thereby experimental parameters will be varied to reveal the optimum process conditions for long term tests.

The methanation reaction as an unwanted side reaction was found to be supported by the nickel catalyst in the PERMCAT – methane was observed each time the process gas contained carbon oxides. Since this side reaction leads to a reduced throughput of the PERMCAT, a new catalyst was developed. In first screening tests nickel catalysts were partially poisoned by copper until the material lost its activity to convert carbon oxides and hydrogen to methane. However, at the same time the catalyst lost its activity to exchange hydrogen isotopes on hydrocarbons as well, and these reactions are certainly essential for the PERMCAT. Therefore a variety of palladium and palladium/gold catalysts on alumina or kieselguhr as support were tested with respect to their activity for methanation and hydrogen isotope exchange on hydrocarbons, respectively. The properties of the catalysts were found to not only depend upon their composition, but also strongly upon calcination temperatures. Finally a material with 20% of palladium on kieselguhr was chosen for the technical PERMCAT of CAPER. This catalyst was demonstrated to be highly active for isotope exchange, but does not support the methanation reaction at 400°C.

Staff:

M. Glugla
K. Günther
R. Lässer
T.L. Le
Fa. D. Niyongabo
R.-D. Penzhorn
K.H. Simon

TR 2
Development of Tritium Instrumentation

Analysis of Tritiated Species by Laser Raman Spectroscopy

Laser Raman spectroscopy is well suited to provide real-time quantitative analyses in tritiated gas mixtures of all tritiated chemical species simultaneously, including excellent differentiation among hydrogen isotopes, as well as analyses of impurities and other species. However, it has heretofore suffered from limited sensitivity of just under a millibar and bulky equipment that has rendered on-line implementation difficult.

In this ongoing work begun in 1996 at the Tritium Laboratory Karlsruhe (TLK), development of a new Laser-Raman spectroscopy system LARA for tritiated species analysis has invoked novel concepts to achieve substantial enhancements in sensitivity and on-line implementation. These concepts comprise the enhancement of Raman signals using an Actively Stabilized External Resonator (ASER) in conjunction with a single-frequency laser and the enclosure of all the optical components including the laser head and Raman detector within the tritium-containing glovebox. In the initial work, the LARA system was designed, some key hardware was acquired, and initial observations of Raman enhancement were made.

Recently the critical aspects of these concepts have been proven. Notably a virtually indefinite operation of the ASER has been achieved revealing that the Raman-scattered light can be significantly enhanced using the prescribed concept by 200 fold, as inferred from measurements of circulating power within the ASER.

The optical components of the LARA system can be seen in the photograph (Fig. 1) that was taken while the laser-beam intensity was enhanced within the ASER. The laser (Verdi, Fa. Coherent), mounted on the optical table at far right in the photograph, delivers up to 7 Watts of single-frequency green light at 532 nm through a recently installed optical isolator seen in front of the laser. After a 90° horizontal turn the beam goes through a phase modulator and laser-focus lens onto a mirror that directs the beam upwards into the ASER. It consists of a partially transmitting injection mirror, mounted on the vertical plate above the vertical-turning mirror, the Raman cell with two hand-valves, and the retro-mirror mounted on a piezoelectric translator at the top of the photograph. Raman collection lenses, largely hidden from camera view by the Raman cell, image the Raman-scattered light into the ISA Triax-320 spectrometer/CCD detector seen in background. The strong enhancement by the actively stabilized external resonator is seen by the camera or by the eye from the much higher laser-beam intensity between the Raman cell and each mirror, in contrast to the laser intensity below the injection mirror.

The initially procured LARA hardware did not include the optical isolator. However, initial tests were conducted with concern regarding the potential need for such an optical isolator between the laser and the external resonator, in order to avoid optical-frequency destabilization of the Verdi laser through feedback and hence loss of reliability in the active stabilization. Neither the manufacturer of the laser (Coherent) nor the company who provided the components for the ASER (LAS) had previous experience regarding this situation.

The optical isolator designed and built to LARA specifications consists of an input polarizer, a 45° polarization rotator based upon the Faraday effect from a TGG crystal within a permanent magnetic field, an output polarizer, and a 45° polarization rotator based upon a crystal-quartz half-wave plate. Therefore vertically polarized incident light at 532 nm leaves the isolator also

vertically polarized, in order to maintain best sensitivity and quantitativeness using Polarized Raman Scattering in LARA, while providing > 30 dB isolation against reflected 532 nm light.

The ASER requires careful design, specially developed optical alignment procedures, and appropriate electronic control parameters in order to achieve reliable active stabilization of a linear external resonator for enhancement of Raman scattering.

Significant progress has been made on each of these aspects. For example, a New-Focus 9016 5-axis fiber-optic launcher fastened by a custom-designed mount to the optical table was installed to hold the tip of the fiber-optic as part of the ASER control servo's Error Signal. Experimental characterization of the LARA optical components has shown that the others are close to their optimal values, such as the injection mirror transmissivity of about 1.5% that is close to equal to the sum of round-trip optical losses in the ASER of about 1.0%.

A variety of alignment tools, for instance various laser-drilled pinholes that can be mounted in position corresponding to the exact center of the Raman cell, a mirror mount to direct the laser beam from the position of the Raman cell center into the spectrometer, and a vertical-beam alignment tool that carries a photodiode and/or an iris aperture at various positions on the vertical plate, have been designed and procured. These tools go together with the development of specialized optical alignment techniques for LARA, such as translating the resonator mirrors to the exact separations from the Raman cell center for optimal transverse mode matching of the ASER to the incident laser beam both without and with the Raman cell present in the ASER.

Enhancement of the scattered light has been seen on the CCD through the spectrometer using the 532-nm Rayleigh scattering, and quantitative determination of this enhancement is currently underway through calibration of the linearity range of the Raman detector. We expect that this calibration will lead to confirmation of the enhancement factors inferred above and thereby lead to demonstration of detectabilities for tritiated molecules in the microbar range unprecedented by Raman spectroscopy.

Staff:

M. Glugla
C. Caldwell Nichols
Fa. D. Taylor
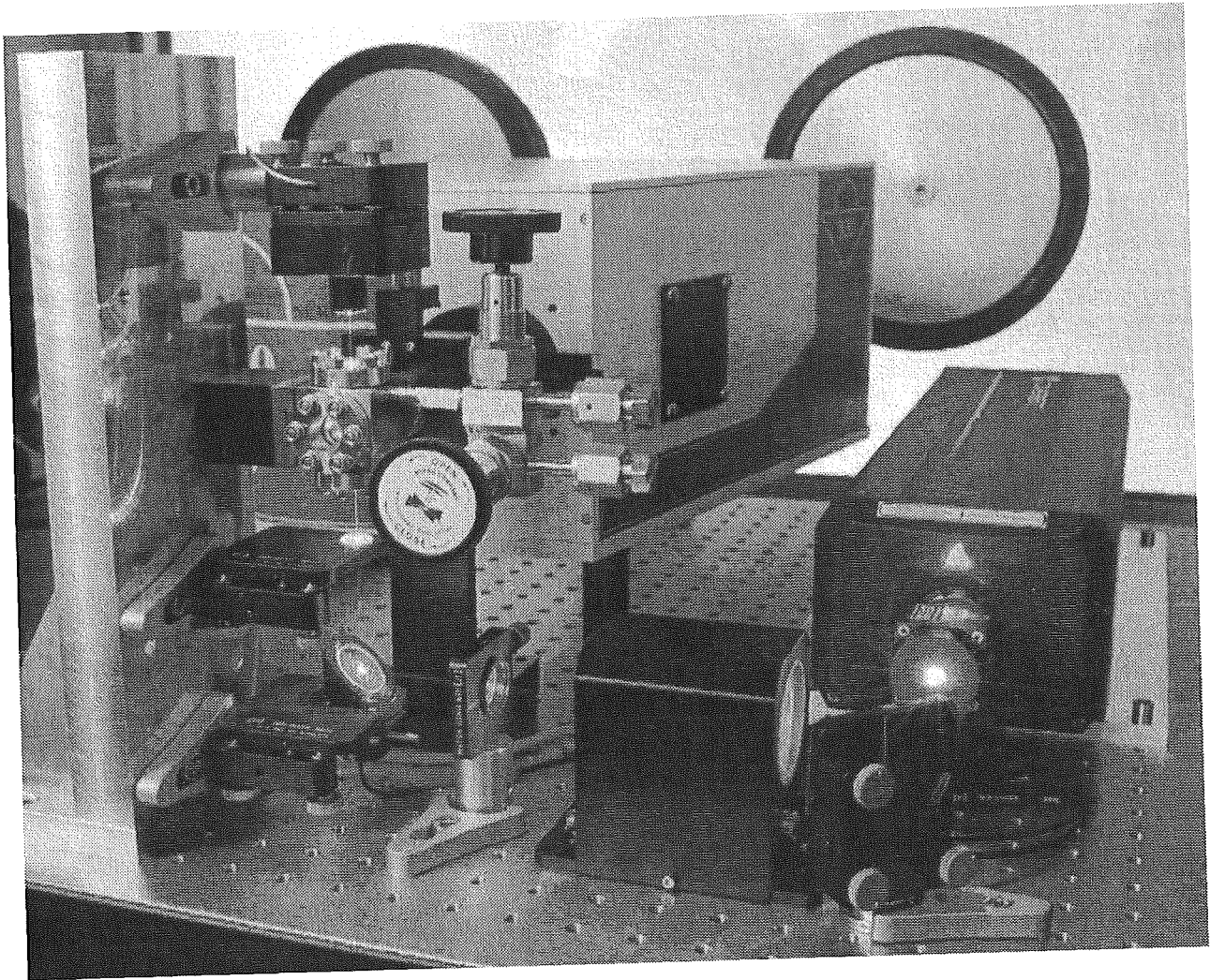
Fig: 1: Optical components of LARA inside the glovebox to allow tritium work

TR 3
Extended Life-time Tests of Key Tritium Plant Components

Within the frame of a collaboration with JET a modification of the Active Gas Handling System of JET is in progress. In particular, it is intended to replace the formerly used getter beds by an improved PERMCAT version. The new PERMCAT incorporates the experience gained in experiments with tritium and results from modelling. The improvements essentially consists

- in an increase of the number of permeation tubes from 6 to 21 and

- of the length of each tube from 530 to 900 mm.

While essentially linear scaling is achieved by increasing the tube number, the effect of length increase has exponential impact on the decontamination factor.

The PERMCAT component to be installed at JET has been manufactured at the workshops of FZK. First tests will be performed as soon as a new catalyst becomes available.

Recent efforts have concentrated on the development of a suitable catalyst that promotes the catalytic exchange between molecular protium and tritium bonded to hydrocarbons without causing formation of methane by reduction of carbon oxides. Numerous screening tests have been performed in a flow apparatus provided with a Fourier transform infra red spectrometer for the analysis of gases. A catalyst fulfilling the required properties based on palladium supported on Kieselguhr, has been identified and will be used for the PERMCAT devices installed in CAPER and to be installed in the Active Gas Handling System (AGHS) of JET.

Staff:

M. Glugla
R. Lässer
D. Niyongabo
R.-D. Penzhorn
K.H. Simon

TEP 3A
Tritium Storage

Under prolonged thermal cycling in the presence of hydrogen the hydrided getter $ZrCoH_x$ ($x \leq 3$), tends to disproportionate yielding the more stable hydride ZrH_2, which is associated with a performance degradation, i.e. loss of the ability to reversibly absorb hydrogen isotopes. To improve the understanding of the disproportionation mechanism comparative measurements were performed with protium and deuterium to uncover possible isotope effects. Based on the structural modifications that samples undergo during hydrogenation an attempt to explain at least qualitatively the mechanism of disproportionation was made.

The disproportionation and reproportionation of ZrCo has been demonstrated employing protium and deuterium with small storage beds as well as with pure tritium using large storage beds such as used in the Tritium Storage System of the TLK. By X-ray diffractometry it was shown that fully disproportionated zirconium cobalt can be quantitatively reproportionated, i.e. reconverted into the starting intermetallic alloy, at comparatively mild conditions, i.e. < 500 °C under vacuum for several hours. The loading/deloading process with hydrogen induces considerable changes in the crystallographic structure of the getter material. Whereas, originally ZrCo has a cubic structure with a lattice parameter of a = 3.196 Å after hydriding and formation of $ZrCoH_3$, its structure is orthorhombic with four unit formulas per unit cell. This transformation represents a volume expansion of about 20 %. During the transformation four asymmetric octahedral sites and eight symmetric tetrahedral sites are generated in which hydrogen or deuterium can be stabilised. During a heating phase hydrogen from the tetrahedral sites is expected to be liberated first, the remaining intermediate compound can then be assumed to be in the metastable orthorhombic ZrCoH form. In the latter almost only octahedral sites are occupied with hydrogen. Such intermediate compound will disproportionate to give the more stable compounds ZrH_2 and $ZrCo_2$, provided the temperature is sufficiently high and hydrogen is present at more than a certain pressure.

As ZrH_2 is very stable, the reproportionation reaction will require heating under vacuum at high temperature (> 400 °C) to release hydrogen. After reproportionation ZrCo will recover its cubic structure and its hydrogen isotope absorption capability. Fig. 2 illustrates the suggested mechanism.
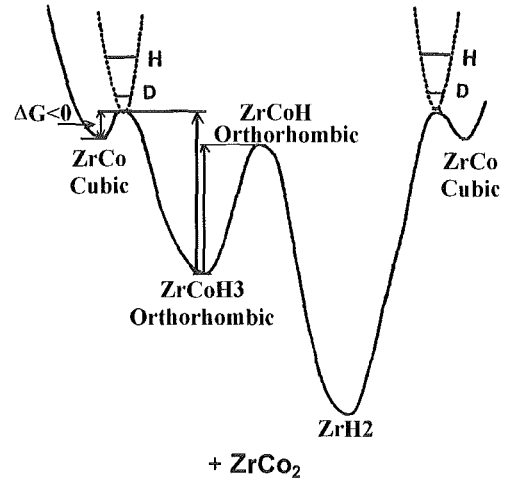
Fig. 2: Schematic potential energy diagram for the disproportionation of ZrCo

It can be concluded that the driving force of the disproportionation is given by the continuous change in crystal structure when the sample undergoes successive hydriding/dehydriding cycles, and especially during the formation of the intermediate orthorhombic ZrCoH which is metastable. The presence of hydrogen causes the phase separation between ZrH_2 and $ZrCo_2$.

Staff:

U. Besserer
N. Bekris
R.-D. Penzhorn
M. Sirch
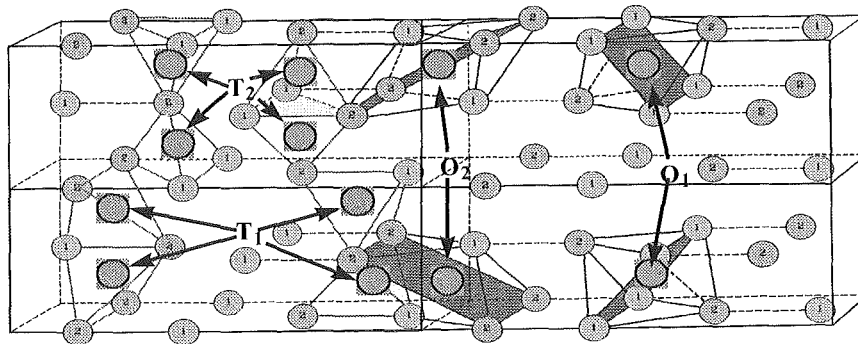
Fig. 1: Tetrahedral and octahedral sites of the $ZrCoH_3$

TR 4
Tritium Extraction from Plasma-exposed Graphite and CFC tiles

Extensive measurements with small graphite and CFC disks obtained from cylindrical specimens cut from tiles previously exposed to the plasma of a fusion machine have been carried out to determine the total tritium surface and depth content of the tiles and to investigate the thermal release behaviour of co-deposited and implanted hydrogen isotopes. Surface and depth profile measurement were performed by fully burning under a moist air or noble gas stream numerous sample disks. The samples were heated either with an external oven or directly by high frequency induction heating. The released tritium was fully converted into water by air and a Cu/CuO bed, collected in bubblers and then quantified by liquid scintillation counting.

A new facility carrying the acronym TIDE (Tritium Decontamination) has been nearly completed. The facility is designed to perform detritiation tests with actual graphite or CFC tiles with the aim of validating previous small-scale experiments. Tiles are rapidly heated up to temperatures above 1000 °C with a 330 kHz high frequency coil. The tiles are housed in an appropriate containment to avoid tritium release into the glove box. A closed loop chiller system has been incorporated into the high frequency coil to avoid possible contamination of the laboratory cooling water. Tile temperatures are measured with a pyrometer. Power is supplied by a 20 kW generator, now fully installed and tested. The tiles can be moved alongside the HF coil with a servo motor to achieve full exposure of the whole tile surface. A closed loop comprising the tile housing has been built to accomplish full oxidation and collection of the released tritiated gases. For safety reasons a nitrogen glove box atmosphere has been selected.

The plasma-exposed graphite specimens were also characterised by Accelerator Mass Spectrometry at the Forschungszentrum Rossendorf. For depth profiling a caesium sputter ion source is used. For the detection of tritium an appropriate facility was installed at the 30 ° beam line of the 3 MV Tandetron. After acceleration the tritium ions are first separated from HD^+ ions and then counted with a surface barrier detector.

Fig. 1 below depicts the depth profile of carbon, beryllium and tritium on the plasma-exposed side of a tile that had been previously installed at JET. As seen, in the layer immediately below the surface, carbon, beryllium and tritium do co-exist. As expected, with progressing depth, i.e. beyond 10 μm, carbon becomes the dominant species.

Deuterium, tritium, protium, carbon and beryllium profiles were determined before and after the thermal treatment (range 200 – 500 °C) with moist gases (air and noble gases) of plasma-exposed graphite disks drilled from a JET tile. The Figure below shows typical tritium depth profiles after treatment of plasma-exposed disks with moist helium at 500 °C for progressively increasing times. It is seen that fairly high temperatures are required for a full detritiation of the surface layer.

Among the methods recently examined for the detritiation of tiles an argon plasma burner, as normally used for welding, was tested. The experiments were carried out in a hood as well as in an glove box having an argon atmosphere. In both cases, that is also under a full argon environment, very high yields of detritiation were achieved in only a few seconds. Properly applied it is possible to essentially heat only the plasma exposed surface of a tile keeping its rear side at considerably lower temperature. The method has potential of application both outside as well as inside of a tokamak. Important advantages of the new procedure are

• Very high degree of tritium release in a short period of time, and

• Practically no surface oxidation of the tile during the liberation of tritium, particularly when the detritiation is carried out under an argon atmosphere, and

• Well known standard procedure.

Another method tested successfully consists in a short exposure of the tile surface to an open flame. Under these conditions a rapid heating of predominantly the exposed tile surface takes place and a very high decontamination factor (DF) be achieved. The main drawbacks of this technique are a considerable surface oxidation of the tile (unwanted within the tokamak) and the safety concerns associated with the use of burnable and explosive gases inside of a closed containment.
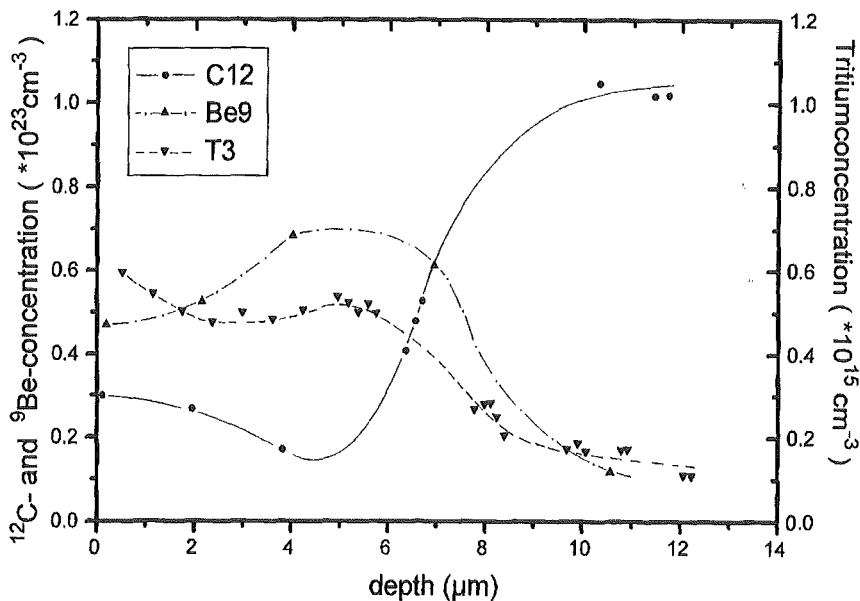
Fig. 1: Depth profile of Be, C and T on a JET tile as determined by AMS
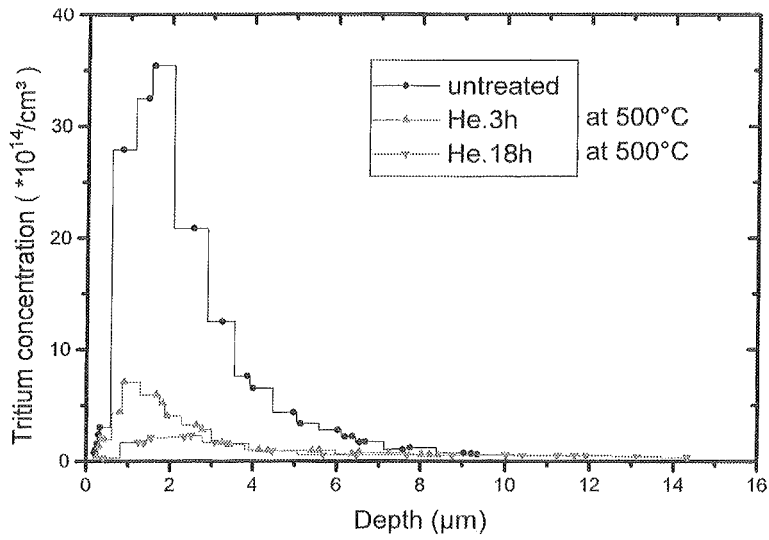
Fig. 2: Accelerator mass spectrometry depth profiles of specimens treated with moist helium

Staff:

N. Bekris
M. Friedrich (FZ Rossendorf)
W. Pilz (FZ Rossendorf)
W. Jung
R.-D. Penzhorn

TR 5
Tritium Recovery from Liquid and Solid Wastes

Within the frame of a contract with JET work on the detritiation of oils from various vacuum pumps has started at the TLK. These oils may represent an operational and disposal hazard. The principal aim of the work is to identify techniques suitable for the achievement of large decontamination factors with production of little or no secondary waste. The screening tests under way include full combustion, gas/liquid as well as liquid/liquid isotopic exchange with and without a catalyst, high pressure isotope exchange, thermal de-sorption, etc. Because each of the oils under examination has its own chemical composition, i.e. higher aliphatic and aromatic hydrocarbons, and own degree of contamination, it is necessary to identify detritiation methods suitable for each of them. The selected methods should be demonstrated under realistic conditions.

During recent maintenance and upgrading campaigns at the TLK involving the facilities CAPER and PETRA much experience has accumulated on the typical degree of contamination of equipment, valves, tubing, gaskets, etc., used in primary systems exposed to high concentrations of tritium and gaseous impurities such as carbon oxides, water, aliphatic and olefinic hydrocarbons, and other condensable products. In total 10 m of highly contaminated piping were removed from the facility CAPER and 32 m new piping were installed together with 26 valves and instrumentation. The contamination of 1 cm of tubing was found to be below 0.6 GBq. To a large extent it is possible to trace back the previous temperature history of the examined components. The data obtained constitute the basis for the development of appropriate detritiation procedures.

The Tritium Laboratory Karlsruhe is equipped with numerous Tritium Retention Systems, installed locally next to every glove box, and with a Central Tritium Retention System, which serves the whole laboratory. All Tritium Retention Systems comprise an oxidation followed by a molecular sieve adsorption step. The Central Retention System removes the tritium from the ring-manifold, to which all glove boxes are connected. The highly contaminated gaseous streams arising from the exhausts of the experimental and infra-structure systems are pre-processed in a separate section of the Central Retention System.

A total of 195 beds containing 3 tons of molecular sieve adsorber mixture (3A and mordenite) have been regenerated up to now employing the facility AMOR. In this facility the beds are processed sequentially in closed loop operation with nitrogen as carrier gas. The liberated tritiated water is removed from the carrier gas initially with a condenser and towards the end with another molecular sieve bed integrated into the loop. The performed regenerations have been accomplished without contamination of personnel or of the environment. The recovered tritiated water has been disposed-off together with the contaminated water produced from wet chemistry ongoing in the Laboratory by the Central Decontamination Department of Forschungszentrum Karlsruhe. In total approx. 350 l containing 1.2×10^{13} Bq of tritium have been collected over the past years. The maximum tritium concentration found in a single bed has been 5×10^{11} Bq.

Staff:

H.-D. Adami
N. Bekris
U. Besserer
M. Glugla
R. Lässer
R.-D. Penzhorn

TR 6
Tritium Extraction and Helium Purification

1. Introduction

In the last year, the design of the test facility PILATUS (*Pilot-Anlage zur Tritium Separation*) has been described which will be operated in the Tritium Laboratory Karlsruhe (TLK) to test and to optimize the tritium extraction process steps for two helium loops of a solid breeder blanket, i.e. the Tritium Extraction System (TES) and the Coolant Purification System (CPS).

The main components of the test facility are

- a continuously working gas supply system,

- a cryogenic cold trap,

- a cryogenic adsorber (molecular sieve bed),

- a catalytic oxidizer, and

- a sophisticated system of analytical tools.

The progress achieved in the past twelve months can be summarized as follows:

1. The gas supply system has been procured and installed,

2. A small pretest facility has been set up for inactive tests with a cryogenic cold trap taken over from KFA Juelich,

3. A set of three different analytical instruments for the measurement of the test gas humidity level at the inlet and outlet of the cold trap has been supplied,

4. The layout of a new versatile cold trap has been started and will be completed as soon as sufficient test results with the Juelich cold trap are available.

2. Pretest Facility for Cold Trap Tests

To reduce the humidity level in the blanket purge gas from an initial concentration of max. 10 ppm to about 0.1 ppm one has to carefully control the cool down velocity of the gas at temperatures below - 70°C. If the cool down is too fast one will get a critical supersaturation and a spontaneous generation of ice aerosol particles which may be carried through the trap. In this case, it would be impossible to obtain a good removal efficiency. (Application of an aerosol filter is not recommendable due to possible clogging effects which would lead to a strongly increased flow resistance.)

The cryogenic cold trap was originally designed at KFA for the removal of xenon from the dissolver off-gas of a reprocessing plant. It consists of two pre-cooling zones and a main freezing zone in which temperatures can be varied between -190°C and about -150°C by electrical heating. Some additional design parameters of the trap are given in the following

Throughput:	≤ 10 Nm^3/h
Gas pressure:	1 - 8 bar
Freezing area:	1.3 m^2
Volume of the freezing zone:	26 l
Heater power	300 W
Diameter (incl. isolation):	350 mm
Height (incl. pre-cooling zones):	1433 mm

It is the aim of the pretests to study the H$_2$O removal efficiency and the process of ice formation as a function of

- temperature profile in the cold trap,

- initial humidity of the test gas,

- gas flow rate.
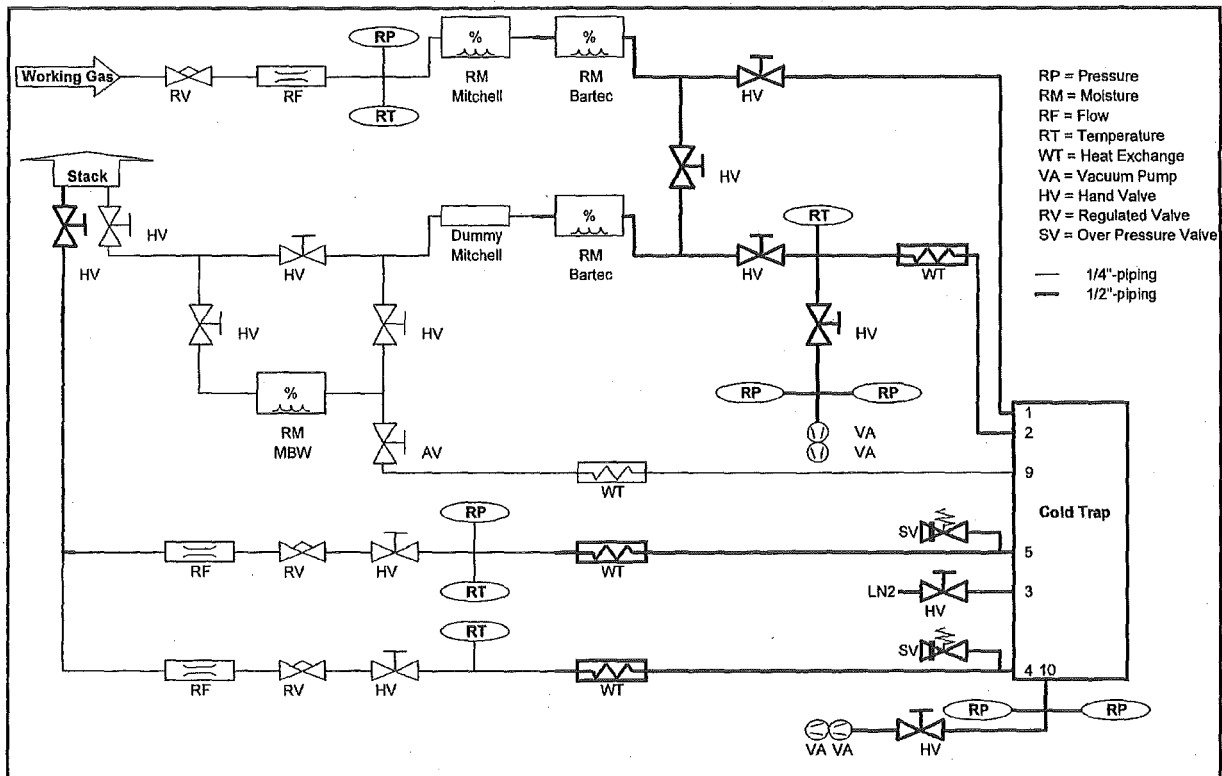
Fig. 1: Flowsheet of the PILATUS Pretest Facility

The temperature profile can also be varied by the amount of liquid nitrogen which is filled into the trap. When this amount is small, the temperature in the freezing zone will be mainly determined by the temperature of the evaporated nitrogen which can be increased by the electrical heater.

The initial humidity will be varied between 10 and 50 ppm. A premixed test gas containing helium 5.0 as carrier gas will be used. During the starting phase of a test, however, pure helium is used until the temperature profile in the cold trap has become constant. The test gas flow rate will be varied between 0.3 and 3 Nm³/h.

Staff:

H. Albrecht
E. Hutter

Safety Analysis and Environmental Impact

SEA 3
Reference Accident Sequences – Magnet Systems (2)

Subtask 2: Magnet System Safety

Within the subtask 3.2 FZK investigates the thermal behavior of magnet systems during accidents. In terms of code development the following items have been considered:

At CEA experiments will be performed in which water vapor is frozen on liquid N_2 cooled surfaces (EVITA). This process corresponds to the accident scenario 'leak in a cryostat wall', investigated amongst others with the code system MAGS. However, in MAGS and the typical real case air, res. N_2 enters the cryostat and freezes on liquid Helium cooled surfaces. To enable MAGS to handle the experimental conditions of EVITA the equation of state for water was extended down to about 80 K. While for the water vapor satisfying data were found, for water ice the data base is small and extrapolations were necessary.

In magnet safety analysis arcs are important events. The model development for arcs enclosed in a cavity has been continued. Two models are now available : A 1d model, applicable for 'inline' arcs, i.e. arcs ignited by the rupture of a conductor where the arc bridges the two ends and a 2d model to analyze shorting arcs, i.e. arcs burning between adjacent turns in a coil. Both models have been developed at University of St. Petersburg and are based on first principles. The 2d model allows to determine especially the damage of the conductor insulation, a prerequisite to decide on formation of secondary arcs in the winding pack. These models will be included into the MAGS module SHARC.

For sharp transients of the coil current, hysteresis and coupling losses in a conductor, caused by the transient magnet field, may be important for quench initiation. To handle such situations the module EDDY has been set up. It takes the 3d magnet field, calculated with module EFFI at different times, determines the time derivative of the field and calculates the power released in the conductor and the jacket mesh elements for the winding pack analyzed.

Validation of MAGS was done by recalculation of the Q3D experiments. For a single selected experiment with low quench propagation velocity an acceptable agreement could be achieved. The essential modifications of the GANDALF module, analyzing the Helium flow in the cable, were made for heat transfer, friction factor and integration scheme. In terms of heat transfer the coefficient downstream of a quench front has been adjusted to the values known from bath cooled conductors. For the coefficients upstream of the quench front a model developed for heat transfer in tight rod bundles of nuclear power reactors has been applied. The main difference between the old and the new heat transfer correlation is that the new gives lower Nusselt numbers for tight bundles. The same source provided also a model for the friction factor which was included consistently. In terms of integration scheme a second order scheme is applied for the convective term in the energy equation. The combination of assumptions must now be checked by other runs of the Q3D experiment.

The models included in the CRYOSTAT module have been documented in a report [1]. Validation is going on in terms of recalculation of selected ICE experiments and the pretest calculations for the EVITA experiments.

The investigation of arcs burning within a winding pack has been continued. First the 1d arc model has been included into MAGS and applied for an arc shorting five turns in the high field of a TF

coil during dump. The arc cavity walls had to be assumed to be from steel, ablating at a lower rate than the glass epoxy insulation. The main results are a peak current in the shorted turns of almost 250 kA and a energy conversion in the arc of about 25 MJ. The resulting globular cavity had a diameter of 0.08 m. Peak temperature was the evaporation temperature of steel, which is found only locally at the cavity surface.

The same case was also analyzed using the 2d model, however, in a stand alone version. This includes only a simple electrical circuit model. The arc plasma is oriented horizontal between the turns in layer 3, see Fig. 1. Initially the left electrode of the arc was on the surface of the jacket and the right electrode on the surface of the strands, i.e. there was a hole in the jacket. At the end of the transient the arc has ablated the cable space cross section of both conductors to about 50%. The jacket and radial plate, between the conductors, is eroded for two conductor diameters and the insulation around the cables almost for four conductor diameters. There is some discrepancy between the real 3d pattern of the winding pack and the 2d model of the arc but the approximation is considered to be good enough for the questions investigated here. From the figure we can conclude that secondary arcs are possible between turns where the insulation is destroyed, assuming the necessary ignition voltage is available.
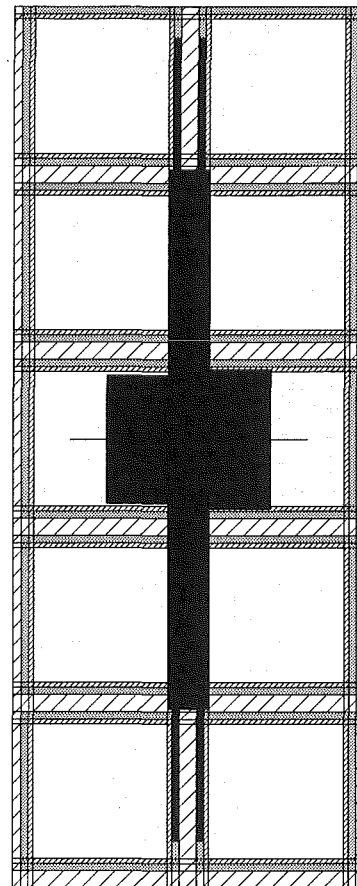
Fig. 1: Cross section through five layers of a TF double pancake.
Coarse hatched : radial plate, dark gray : insulation, fine hatched : cable jacket, gray : cable space, black : arc cavity. The cavity is formed by an arc shorting five turns during dump.

For determination of the resistance of an arc the arc current is an essential input parameter. Considering an 'inline' arc of a cable having a thick steel jacket, e.g. as for the CS coil, an electrical bypass or shunt is formed by the steel jacket and the ratio of the shunt to arc resistance determines the current distribution. The shunt resistance R_{sh} has three contributions: a) to pass the current from the strands to the jacket inner surface and back, b) to redistribute the current within the jacket and c) to force the current along the jacket, corresponding to the arc length. These contributions are investigated with the CRESJ experiments (Contact REsistance Strand Jacket).

Before the experiment was started, the contact resistance was calculated for the case of the ITER-CS1-conductor taking the information supplied by literature. By that it appeared that the transition resistance between the cable and the jacket depends on the transition area, beside other effects. Because this dependence is inverse, it seemed favourable, to introduce an area independent term called „Area Related Transition Resistance" (ARTR) with the dimension resistance times area. This ARTR has been calculated to be $7*10^{-7}$ Ωm^2.

Thereupon this ARTR of two ITER-CS1-conductor-specimens from different charges was measured using the experiment assembly shown in the Fig. 2. The measurements are made with the assumption, that the conditions of the ARTR are constant within a conductor type and independent of the length of the examined specimen. In case of CS1.1B ARTR was measured to be $1.1*10^{-6}$ Ωm^2 and in case of CS1.2B a value of $4.2*10^{-7}$ Ωm^2 has been measured.
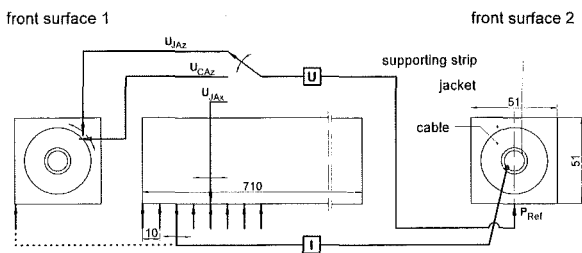
Fig. 2: Electrical circuit used to measure the contact resistance between the strands of a superconducting cable and jacket.

To make use of the ARTR in computer codes it seems advantageous to convert the ARTR into an equivalent volumetric resistance R_{eq} by assuming a thickness of the transition area of e.g. $d_{ass} = 0.1$ mm. Furthermore using R_{eq}, the equivalence between electrical and heat conduction and a computer program like CATIA-ELFINI it is possible to calculate the total shunt resistance R_{sh} in dependence of the length of the arc. Assuming an arc of 20 mm length values of R_{sh} of $1.8*10^{-4}$ Ω in case of CS1.1B and $1.2*10^{-4}$ Ω in case of CS1.2B are calculated. The contribution of the jacket along the arc length is $2*10^{-5}$ Ω.

Literature:

[1] G. Boenisch : Post calculation of an ICE/LOVA experiment with the MAGS module CRYOSTAT. Forschungszentrum Karslruhe, Internal IRS-Report (Febr. 1999)

Staff:

G. Bönisch
R. Meyder
G. Schmitz

SEA 5
3d Quench Analyses for the Toroidal Field Model Coil with the Code System MAGS

For the toroidal field model coil, to be tested in the TOSKA test facility at Forschungszentrum Karlsruhe, 3d quench analyses have been performed. The analysis included magnet field, electrical circuit and thermal analysis for 4 pancakes of the coil and coolant piping outside of coil as well.

The transient considered is: Quench in a pancake and dump delayed by 5 s. The analysis showed that there is no dramatic temperature rise. Peak temperature is in the range of 300 K for the quench initiating turn. Quench in the other pancakes was initiated as well via the inlet manifold as by thermal conduction via the pancake to pancake joint. The quenched lengths, however, were small. The heat released in the radial plates, due to dump induced eddy currents, pressed cold Helium from the center of the cables to the in- and outlet and stopped the quenched length growth. The pressure in the coolant system, except for a initial spike of 1 MPa stays close to the design value.

Staff:

G. Bönisch
R. Meyder

SEP 2
Environmental Impact of Tritium and Activation Products

Staff:

J. Ehrhardt
I. Hasemann
W. Raskob

Dose assessments for potential European ITER sites are an ongoing task. In the present working period, dose assessments for releases into the atmospheric under routine and accidental conditions (based on a draft working document of NSSR-2) which contain either tritium and/or activation products were performed for an Italian site [1]. Mainly potential individual doses and areas affected by protective measures were evaluated for three types of accidents, all of them placed within the event sequence categories IV ('extremely unlikely events') and V ('hypothetical sequences'). The results of both the accidental and routine release scenarios were also compared to site independent dose limits defined in the frame of ITER.

Annual doses from routine releases (CAT-I) are close to 1 μSv/a for the atmospheric source terms. In none of the release scenarios of category CAT-IV the ITER limits were exceeded. In addition, relevant characteristic quantities (e.g. 95% fractiles) of the early dose distributions from the hypothetical scenarios of type CAT-V are below 50 mSv or 100 mSv, values which are commonly used as lower reference values for evacuation in many potential home countries of ITER. These site specific assessments, together with those performed in 1997 and 1998, confirmed that the proposed release limits and thus the derived dose limits for a generic ITER site are unlikely to exceed the national criteria for evacuation. Other protective actions such as sheltering, relocation and food banning were investigated and only banning of agricultural products was found to be important.

Therefore, investigations have been started to evaluate the present guidelines with respect to tritium release. When investigating potential foodbans, intervention levels, established under the impression of the Chernobyl accident and derived mainly for cesium have to be applied for all longer living radionuclides (> 10 days). Tritium however shows a completely different behaviour with respect to its highly dynamic change in concentration in feed- and foodstuffs. In addition, the dose conversion factor compared to cesium is lower by more than two orders of magnitude. Therefore, work has been started to evaluate the appropriateness of the present regulation. In addition, a more realistic estimation of the time dependency of the accidental releases will also allow a more realistic assessment of potential countermeasures.

Within the BIOMASS (BIOspheric Modelling and ASSessment) project testing of tritium models for routine releases into the atmosphere and hydrosphere is ongoing. Five different scenarios have been set up covering both fixed environmental conditions to test individual model features and using measured data from sites in Canada, Russia and France to test the overall performance of existing assessment codes for routine releases. NORMTRI [2] together with a computer code describing the water movement in the upper soil are participating in the comparative calculation study. For the scenario on the Canadian site, results obtained with NORMTRI were closest to the measured values.

Literature:

[1] W. Raskob, I. Hasemann and L. Di Pace, Summary of Dose Assessment for Greifswald, Cadarache and an Italian Site with updated source terms from ITER NSSR-2. Report FZKA, Forschungszentrum Karlsruhe, under preparation

[2] W. Raskob, Description of the Tritium Model NORMTRI for Releases under Normal Operation Conditions. Report KfK-5364, Kernforschungszentrum Karlsruhe, 1994

Studies for ITER

ERB 5004 CT 970009 (NET/96-438)
High Voltage Components and Sensor Calibration for the ITER TF Model Coil (TFMC)

Background

The nominal operation voltage of the ITER toroidal field (TF) coils is 10 kV across the winding. The ITER TF model coil has been designed and is being constructed by the ITER Home Team of the European Union therefore for 10 kV, too. In the POLO Project the technology of superconducting poloidal field coils for tokamaks was demonstrated in the frame of a task of the European Fusion Technology Programme end of the eighties. Typical high voltage components needed for such coils were developed. The experience gained shall be applied for the ITER TF model coil. Forschungszentrum Karlsruhe took over the obligation to organize the fabrication and the pretesting of these components. The following components shall be delivered to the industry consortium AGAN to be installed on the ITER TF model coil:
30 axial insulation breaks
3 radial insulation breaks
3 instrumentation wire feedthroughs
11 high voltage instrumentation cables with joint technique.
Based on the existing calibration facilities for temperature sensors (80) and Hall plates (2) the calibration of these sensors for the TFMC will be performed within this task, too.

Radial and axial insulation breaks, instrumentation wire feedthroughs and 80 calibrated temperature sensors were delivered to AGAN.

1. High voltage instrumentation cables with warm vacuum feedthrough

The first delivery of 180 m Kapton instrumentation cable had to be rejected because the bonding of the wrapped Kapton layers was poor. A 2nd batch was delivered mid April 1999. The assembly of the cables with the warm feedthrough connectors was started and completed in July 1999. The warm feedthrough connectors were leak tested before starting the assembly. Typical leak rate was < $1 \cdot 10^{-8}$ mbar·l/s. The connectors were closed with a dummy plug during testing. The length of the Kapton cable was 14 m. The 11 cables and connectors were tested with +/- 10 kV DC and 9.9 kV_{rms} AC accompanied by partial discharge measurements. The maximum apparent charge was 6.2 nC at 9.9 kV_{rms}. The minimum inception voltage was 1.7 kV $_{rms}$. This is more than twice as the proposed voltage for partial discharge measurement between conductor and radial plate.

A dummy joint for the connection of the instrumentation cables to the winding at low temperature is being constructed by AGAN and will be tested at Forschungszentrum Karlsruhe at operation conditions.

2. Sensor calibration

The test of the full size joint sample (FSJS) in SULTAN indicated that the magnetic field dependence of the TVO temperature sensors was 3 times larger than given in the data sheet. In further investigations performed at Forschungszentrum Karlsruhe it was found that there were also changes from lot to lot, too (Fig. 1) [1].

Therefore the application of these sensors in magnetic fields > 2 T are not suitable if they are used for calculating thermohydraulic properties where an accuracy of < 1% at 5 K is required. It was therefore decided to replace 15 TVO's by calibrated CERNOX sensors which have the necessary accuracy in the magnetic field.
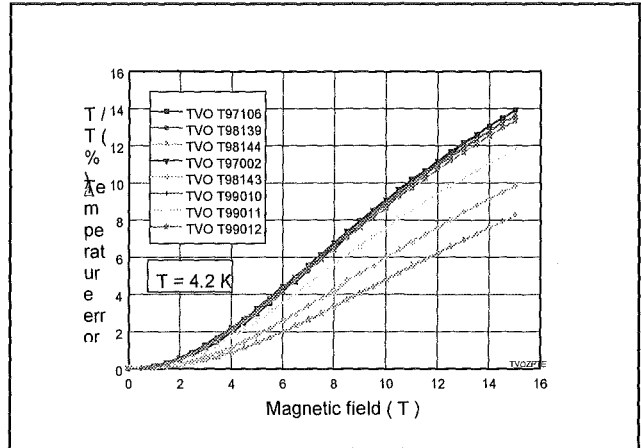
Fig. 1: The relative temperature deviation versus the magnetic field

3. Summary

- The present state of high voltage component fabrication looks as indicated in the following table:

Compo-nent	To-tal	In fabri-cation	On stock	In test	Tested	Deliv-ered	Note
Axial break	30	finished	9	-	-	21	2 spare parts
Radial break	3	finished	-	-	-	3	1 spare part
Feed-throughs	3	finished	-	-	-	3	1 spare part
Instrumen-tation cable	11 X 14 m	finished	11	-	11		Delivery on call
Connectors	11	finished	11	-	11		Delivery on call

The delivery of components is compatible with TFMC fabrication progress. For the instrumentation cable, the test results for the cold joint are needed to go ahead with the further fabrication steps performed by AGAN.

In addition to the 80 TVO temperature sensors 18 (3 spare sensors) CERNOX sensors were delivered to AGAN beginning October , 1999.

Literature:

[1] M. Süßer, F. Wüchner, Verhalten der TVO-Temperatursensoren im Magnetfeld, Forschungszentrum Karlsruhe, Interner ITP-Bericht, September 1999

Staff:

K. Bauer
S. Fink
M. Süßer
H.-J. Spiegel
A. Ulbricht
A. Völker
F. Wüchner
V. Zwecker

ERB 5004 CT 970082 (NET/97-458)
Acceptance Tests of Strands and Sub-Stage CICC's with Respect to Heat Treatment of TFMC Pancakes

The reaction heat treatments (HT) of the pancakes of the TFMC have to be controlled by measurements on short samples co-reacted with the pancakes. At each HT two pancakes are heat treated simultaneously, that means 5 HT (DP1 to DP5) for the TFMC are necessary. A sample holder containing 10 strand samples was thermally bonded to the pancake surface of each HT. Additionally, 6 sub-stage 316L jacketed CICC's (3 x 3 x 4 strand cable) were co-reacted with the DP2 heat treatment, of what 3 CICC's have to be prepared with additional steel (added steel) after the HT representing the influence of the radial plates within the TFMC.

Furthermore, 10 strand samples and 6 sub-stages Incoloy 908 jacketed CICC's (again 3 with added steel) are foreseen for co-reaction with the Incoloy dummy pancake.

All measurements were performed and the final report was submitted to EFDA in June 1999 [1]. The results can be summarized as follows:

- The strand samples located at the pancake surface during the heat treatments DP1 to DP5 show homogeneous data of the critical currents depending on both magnetic field and axial strain. This means that the interruptions at some heating procedures did not seem to have a negative effect on I_c.

- Sub-stage CICC samples:

  1. Stainless steel 316L jacket: The I_c vs ε characteristic confirming former investigations but the absolute data of I_c are lower than the 36 x I_c-strand values. The lack of cooling holes within the force grips decrease I_c drastically. The added steel enhances I_c for reasons which are not understood.

  2. Incoloy 908 jacket: The I_c data are generally increased due to lower prestrain with respect to the 316L conductors and the absolute data of I_c-CICC $\approx$ 36 x I_c-strand. The degradation of I_c of the added steel samples was expected, it amounts to 8 % at 13 T.

  3. The load transfer via added steel to the conductor enhances the prestrain (ε_m) at the "thin-walled" 316L sample but ε_m and the corresponding I_{cm} was not reached at the "thick-walled" Incoloy 908 sample due to the failure of the added steel.

Literature:

[1] W. Specking, H. Kiesel, Acceptance test of strands and sub-stage CICC's with respect to heat treatment of TFMC pancakes, Contract ERB 5004 CT 97 0082 (NET/97-458), Final Report, June 1999

Staff:

H. Kiesel
W. Specking (till July 31, 1999)

EFDA/99-514
ITER Tritium Plant Design

This task covers the design, integration and cost estimation of the following systems of the ITER RTO/RC Tritium Plant:

- Tokamak Exhaust Processing

- Hydrogen Isotope Separation

- Storage and Delivery

- Analytical Facilities

- Radiological and Environmental Monitoring for whole ITER

The design of all these systems is being carried out by TLK-Team with the sole exception of the Isotope Separation System, which is of the responsibility of ITER Canada.

In close interaction with the ITER Joint Central Team in Naka the new design requirements have been analysed and a set of design parameters have evolved. Interfaces have been defined and a safety design philosophy has been discussed. Within the frame of this Task a first outline flow diagram has been developed that takes into account the requirements of ITER-RTO/RC (reduced technical objectives/reduced cost). The developed flow diagram contemplates a Fuelling System, a Fuel Storage and Gas Supply System, a Front-End Permeator System, an Impurity Processing System, a Final Clean-up System, a Gamma-Decay System, an Analytical System, the required Auxiliary Systems, a Helium-3 Recovery System, an Isotope Separation System, an In-Bed Calorimeter Measurement Loop, and a Shut-down Recovery System.

A numbering system for documents, drawings, components and equipment is being agreed upon. A preliminary evaluation of the proposed ITER Radiological and Environmental Monitoring System has been carried out and various recommendations have been made. Further work has been agreed upon. Diverse analytic and instrumentation concepts have been discussed, evaluated, and compared from the point of view of specificity of the analysis, response time, accuracy, waste arising, costs, etc.

Staff:

C. Caldwell-Nichols
L. Dörr
M. Glugla
R. Lässer
R.-D. Penzhorn
T. Vollmer

Long-Term Technology Programme

Long-Term Technology Programme

1. The European Blanket Project (EBP)

The European Blanket Project (EBP) was established in late 1995 covering R&D work on:

- a water-cooled lead lithium-blanket (WCLL),

- a helium-cooled pebble bed blanket (HCPB), and

- structural materials (SM) for WCLL and HCPB.

At the end of 1996 a reorientation of the long-term blanket and structural materials activities within the EBP was proposed by the Commission and endorsed by the FTSC-P. The revised work programme for 1997/98 covered the period up to the end of the Fourth Framework Programme and concentrated on the development of DEMO-relevant Test Blanket Modules (TBM) for testing in ITER. This work has been documented in the ITER Final Design Report. In 1999 the main emphasis has been shifted to more general investigations, e.g. material issues including key issues of manufacturing technologies (WP A 3, B 3), development and characterisation of ceramic breeder and beryllium pebbles and pebble beds (WP B 8, B 9), development of tritium permeation barriers (WP A 4) and MHD issues (WP A 10). All design specific work for TBMs and related safety and reliability studies were finished in 1998 (WP A 1, A 2, B 1, B 2 (old), A 6, A 7, B 6, B 7) and transferred, respectively, to the „Preparatory Work on Power Plants" with emphasis on availability (PPA).

All three subprojects of the EBP utilize a harmonized work breakdown structure, comprising three levels: work packages, tasks, and subtasks. The contributions in this report are on the subtask level.

2 Other Long-Term Technology Activities

Besides the blanket-related tasks FZK contributes to the areas „Materials for DEMO", „Safety and Environment", „Socio-Economics", and „Reactor Studies".

Blanket
HCPB Concept

WP B 1
DEMO Blanket Feasibility and Design

B 1.1.1
Segment Design Adaptation to New Specification

An Assessment of the impact of irradiation effects (Be and ceramic breeder swelling, structural material embrittlement) on the DEMO blanket segment design was started but could be carried out only partially because of the limited information on the thermal and mechanical properties of irradiated ceramic breeder and beryllium pebble beds. For the new structural material EUROFER no data are available at all. Irradiation tests for MANET are limited to a damage of 15 dpa. The observed radiation-induced changes of the mechanical properties at this damage (hardening, embrittlement, loss in fracture toughness) are still tolerable. Irradiation tests of ceramic breeder and beryllium pebbles have been carried out up to sufficiently high burn-up, but have not yielded all information needed for design-related analyses. In particular swelling data for the breeder material and mechanical tests on irradiated pebbles are still missing. Furthermore, the development of models for the thermo-mechanical behaviour of pebble beds is not yet completed. The beryllium swelling at the DEMO lifetime of 20.000 hours can in principle be accommodated by the pebble bed porosity, but for the determination of the resulting bed pressures and bed/structure interaction likewise necessitates a thermal-mechanical pebble bed model.

The envisaged segment design adaptation to new DEMO specifications was not carried out because new specifications have not been provided.

The work package was terminated by the end of 1998. However, the activities are partially continued within the Fusion Power Reactor Conceptual Studies/Availability within the 5th Framework Programme.

Staff:

U. Fischer
S. Hermsmeyer
P. Norajitra
K. Schleisiek

WP B 2
TBM Adaptation to Next Step Machine

B 2.1.1
Impact of Reduced Performance Parameters of a Next Step Machine on TBM Testing and

B 2.2.1
Generic Design Modifications to Reduce TBM Size

The work on the test blanket module (TBM) design, analysis and integration for EDA/ITER (former subtask B 2.1.1) was completed by end 1998 [1,2]. Detailed nuclear, thermal-hydraulic and mechanical analyses have been carried out with respect to tritium breeding, nuclear heating, shielding, activation, afterheat generation, temperature and stress distribution. The results show that the HCPB-TBM fulfills all requirements specified for the test blankets in ITER. The design revision was completed, and the route for fabrication of the TBM was defined taking into account the results of the blanket manufacturing tests (see B 3.3.1). In total, the TBM feasibility was demonstrated.

The work on the new subtasks B 2.1.1 and B 2.2.1 envisaged for 1999 could not be started until now since the design and performance parameters of RTO/RC ITER are not yet available.

<u>Literature:</u>

[1] L.V. Boccaccini (Ed.): European Helium Cooled Pebble Bed (HCPB) Test Blanket; ITER Design Description Document, FZKA 6127, März 1999.

[2] S. Gordeev, T. Lechler, K. Schleisiek, H.-J. Fiek: Revised Design and Manufacturing of the EU-HCPB Test Blanket Module (TBM) for ITER (Subtask B 2.1.1). Forschungszentrum Karlsruhe, Interner IRS-Bericht, Dez. 1998.

<u>Staff</u>:

L. Boccaccini
H.J. Fiek, Fa. Ingenieurbüro Fiek
U. Fischer
S. Gordeev
S. Hermsmeyer
T. Lechler
P. Ruatto
<u>K. Schleisiek</u>
I. Schmuck
H. Tsige-Tamirat

WP B 3
Development of Manufacturing Techniques for HCPB Blanket and Pebble Bed Testing

B 3.1.1
HIP Joining of Cooling Plates and Blanket Box

a) Determination of Optimum Diffusion Welding Parameters of MANET 2

A basic test program was carried out to determine the optimum diffusion welding parameters of MANET 2. It comprised 11 welding specimens. Main parameters were:

Welding pressure: 15 to 150 MPa
Welding temperature: 980 and 1050 °C
Holding time: 110 and 180 min
Surface machining: grinding or dry milling
Surface roughness: 2.5 to 15 µm
Surface cleaning: etching or rinsing with acetone

Hipping and subsequent heat treatment (750 °C, 3h) was done in the HIP 3000 facility of FZK/IMF. To study the quality of the welding, extensive non-destructive tests were carried out consisting in ultrasonic inspection, metallographical and microprobe examinations, and mechanical testing.

The main conclusions from the tests can be summarized as follows:

1. Ultrasonic testing is able to detect complete lack of bonding, but is not suited to determine the quality of welding

2. At a temperature of 980 °C and a surface roughness of a few microns, a welding pressure of 50 MPa is sufficient to produce diffusion weldings with high strength and ductility, irrespective of the method of surface machining and cleaning. A higher surface roughness can be tolerated when the welding pressure is increased.

3. In addition to good strength and ductility, satisfactory and reproducible fracture toughness results were achieved when the welding surfaces were machined by dry milling.

4. Etching of the surfaces has no advantage against cleaning with acetone.

Additional diffusion welding tests are planned with the new structural material EUROFER.

b) Diffusion Welding of FW and Cooling Plates

The diffusion welding experiments using hot isostatic pressing (HIP) to produce fusion blanket components out of MANT II with internal cooling channels were continued in specimens with first-wall and cooling plate geometries at welding pressures reduced compared to those employed in the previous series of experiments.

The plates were welded in two successive HIP welding steps ("two-step HIP process"). In the first step, the joined halves of a plate were covered on the outside with support plates out of a molybdenum alloy so as to protect the internal cooling channels, and then packaged in a sheet jacket, evacuated, and seal-welded. After the first HIP step, the specimen is separated into two equal parts. One of the parts is then subjected to another HIP step at a very high gas pressure with the cooling channels open.

The joining surfaces of the specimens had been ground or milled to a surface roughness, $R_T \leq 6$ µm, and then pickled.

Zirconium wires had been inserted into the cooling channels as a getter material. Quartz glass mats were used as separators in the encapsulated first HIP step.

Post-welding examination shows tolerable deformation of the channel webs in both types of plates. The second HIP cycle again considerably improved the quality of the welds in all specimen plates. However, in the first-wall plates, the quality attained was not sufficient because ductility is too low.

For the first time, sufficient strength levels were achieved in the cooling plates with their very narrow welding surfaces of the cooling channel webs; they extended up to a maximum of 638 MPa for the limit of elasticity, and to a maximum of 652 MPa for the tensile strength. The ultimate elongation levels are between 2.3 and 10.5 %. The interim layer in the joining area detected in micrographs of earlier experiments is less pronounced this time, especially in the milled specimens. In the light of the strength results obtained in this series of experiments, no clearcut advantage can be seen for either process of machining the joining surfaces, i.e. grinding or milling.

c) Qualification of Diffusion Welding for Manufacturing of Curved Components by Solid-HIP-Technology

Diffusion Welding (DW) by Solid-HIP-Technology is one of the fabrication techniques that are envisaged for manufacturing of blanket components, e. g. First Wall (FW) and cooling plates (CP). But Solid-HIPping can likewise be used for joining of other sub-components of the blanket box, e.g. for welding of the CPs into the FW box.

At the end of 1998 a program was started to investigate Solid-HIPping for manufacturing of blanket relevant, i. e. curved structures. For the first test "HIPping of curved structures" the geometry shown in Fig. 1 was chosen.
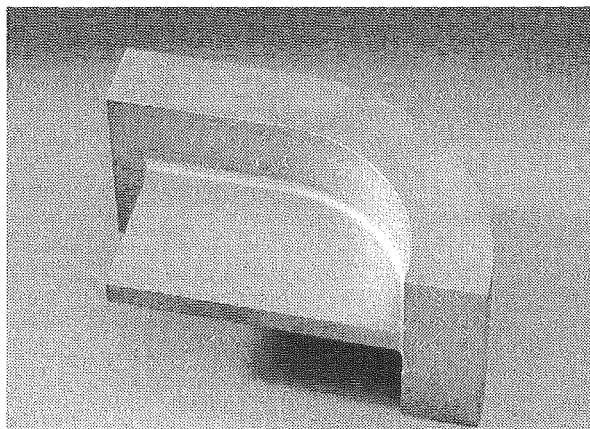
Fig. 1: Specimen for HIPping of curved structures

The Figure shows a part of the bent FW plate and the appropriate edge of a CP. In order to reduce cost for manufacturing of the specimen, we decided to omit the cooling channels in the FW plate as well as in the CP.

Manufacturing of the specimen was started end of 1998. The FW dummy was bent to raw shape and then milled to final shape. The CP dummy was milled to final shape without any further step. The surfaces to be joined by Solid-HIPping were prepared by dry milling with a surface roughness of $R_T \sim 4$ µm. A higher quality could not be achieved by dry milling with the equipment available. Finally, the surfaces to be joined were cleaned in a 4-step procedure using ultrapure solvents. After joining FW and CP the specimen was first seal-welded under

vacuum by electron beam welding and then HIPped at 980°C with a pressure of 100 MPa for 3h at FZK/IMF. The HIP-cycle was followed by a heat-treatment, 750°C for 3h in the same facility.

In order to investigate the quality of bonding, 9 samples for tensile tests as well as 7 samples for charpy impact tests were manufactured by spark erosion (Fig. 2).
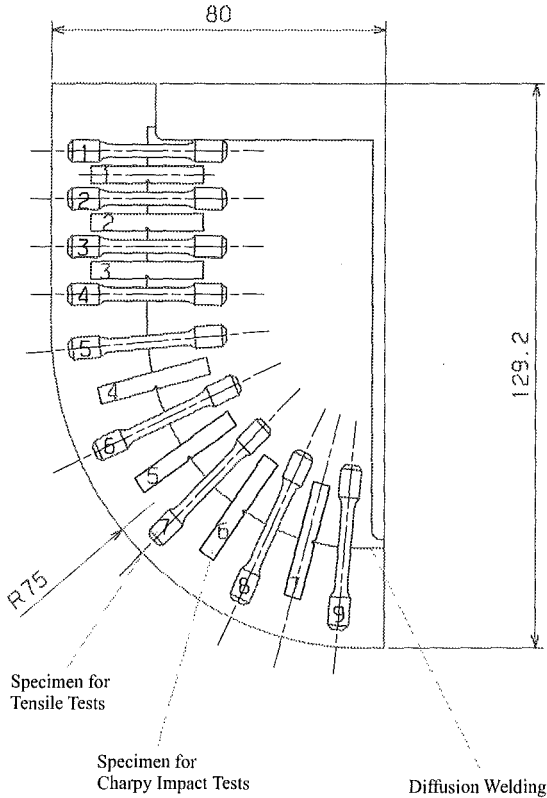
Fig. 2: Cutting plan for manufacturing of samples for tensile charpy impact tests

The tensile tests as well as the charpy impact tests showed mechanical properties of the diffusion welded joints that were in general in the range of the base material. This is a first demonstration of the feasibility of Solid HIPping of curved structures applying optimum HIP-parameters found in the basic test program on specimens with plane surfaces to be joined (see section a) above).

d) Manufacturing of a Semi-scale Mock-up

The manufacturing of a semi-scale mock-up (SSM) is an integral demonstration of the feasibility to manufacture the structural parts of a HCPB blanket according to the reference fabrication procedure. The size of the mock-up is 500 x 250 x 280 mm. The FW box includes 8 cooling channels and five cooling plates which may be replaced by dummy plates. The most important manufacturing steps to be demonstrated with this mockup are:

- Fabrication of a plane FW plate with integrated cooling channels according to the "grooved plate method"

- Bending of the FW plate to the U-shape of the box

- Machining of the bent FW plate to final shape including the welding ribs

- Welding of cooling or dummy plates to the FW box.

All required manufacturing techniques were tested and qualified in the preceeding R&D program. Among others, a small-scale FW section was fabricated (see Fig. 3), and a large dummy plate was welded into a stiff U-frame simulating the FW box.

The fabrication of the SSM consists of more than one hundred manufacturing and testing steps, partly carried out in collaboration with industrial partners or research institutes. The main machining steps of the FW plate are:

- Milling of the plane half-plates to raw shape;

- Milling of the grooves for the cooling channels;

- Milling of the final shape including preparation for diffusion welding.
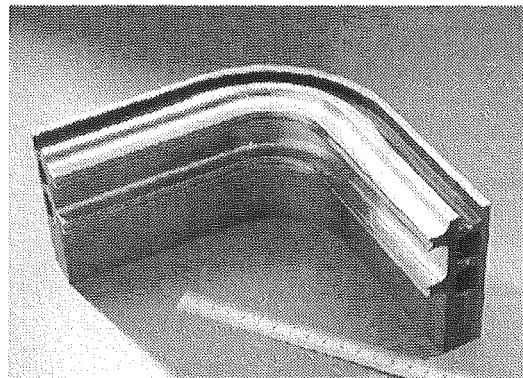
Fig. 3: Bent FW section after machining to final shape

During seal welding of the inner seams before diffusion welding unexpected thermal problems arose from the scale up of the plate's length (tested 300 mm, now demanded 1000 mm). The increase in exposure time caused the torch to overheat. After several attempts to improve the torch had failed, it was decided to apply an alternative fabrication technique, a "two step HIP" process. In the first HIP-cycle it was exposed to 980 °C at 10 MPa in an evacuated 2 mm mild steel canister. After opening the canister a second HIP-cycle was applied (980 °C, 50 MPa). Then the plate was annealed under argon in the same facility.

The quality of the DW was investigated by high resolution ultrasonic device. Poor quality of the joint was found at the solid edges of the FW plate. In order to improve the quality in this region, two additional EB welded seams (36 mm deep) plus one more annealing procedure were carried out.

For bending the First Wall plate the optimum parameters were found in preceding tests with a 4 cooling channel plate. A bending force of more than 10 MN was calculated for the SSM-FW. Applying the above mentioned parameters caused the FW plate to break before reaching the envisaged bending angle of 90 °C
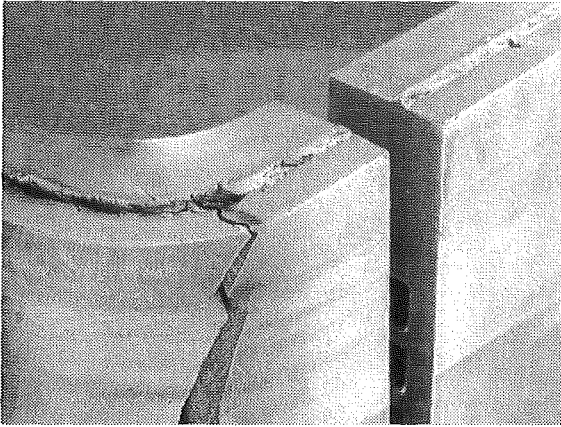
Fig. 4: SSM FW plate broken during bending

To find the reason for the failure, FEM analyses were carried out for the first HIP step. The result was, that the geometry of the FW (ratio of rib's width to cooling channel pitch and solid edges width) leads to a ratio of joining pressures of 10 to 1 for plate and edge. Thus the HIP pressure of 10 MPa in the first HIP step leads to a joining pressure of only 3 MPa in the FW plate's edges which was too low to achieve a sufficient bonding quality and leak-tightness of the bonding zone. So the second HIP-step could not lead to an improvement of the bonding quality. This explains the failure of the plate during bending.

To terminate the task a second SSM with two cooling channels was designed and planned. Its manufacutring was started in August 99.

Literature:

[1] E. Rigal, G. Le Marois, T. Lechler, G. Reimann, K. Schlei-siek, L. Schäfer, P. Weimar: Development of FM Steels Diffusion Bonding Technologies for Blanket Manufacturing Applications. ISFNT-5, Roma, Sept. 1999.

[2] T. Lechler, H.J. Fiek, S. Gordeev, K. Schleisiek: Manufacturing of a semi-scale Blanket Box Mock-up of the European HCPB Blanket. ISFNT-5, Roma, Sept. 1999.

[3] T. Lechler, K. Schleisiek, H.J. Fiek: Development of Manufacturing Techniques for EU-HCPB Blanket Segments and Test Modules. Forschungszentrum Karlsruhe, Interner IRS-Bericht, March 99.

[4] G. Reimann: Diffusionsschweißversuche in Heißisostatischen Pressen zur Herstellung von Plattenbauteilen mit inneren Kühlkanälen für Fusionsblankets, Forschungszentrum Karlsruhe, Interner IMF 1-Bericht, August 1999

Staff:

B. Dafferner
H.J. Fiek, Fa. Ingenieurbüro Fiek
S. Gordeev
P. Graf
J. Heger
H. Kempe
E. Nold
G. Reimann
L. Schäfer
K. Schleisiek
L. Schmidt
P. Weimar

B 3.2.1
HEBLO Tests and Construction of Test sections for HEBLO and HE-FUS3

1. HEBLO Test section: Final assembly and integration of the test rig in HEBLO

Following steps of the final assembly were accomplished successfully:

- Filling of the pebble beds: The pebble beds were filled by the company Goraieb Versuchstechnik within the FZK area. For this work and for the following sealing welding a special safety glove box was used. For the cavity of about 450 cm^3 for Be and about 110 cm^3 for Li_4SiO_4 without components a total amount of 0.614 kg Be pebble bed and 0.141 kg Li_4SiO_4 pebble bed were filled. The estimated maximum packing factors lie between 81-82 % for Be pebble bed and 63-64 % for Li_4SiO_4 pebble bed, respectively.

- After the seal welding of the test section and after flanging the helium coolant tubes a leak-poof with high He pressure at 8 MPa was carried out successfully.

- To avoid heat losses during the experiments the test section was thermally insulated with layers of glass wool and stone wool (Fig.2) before assembling into the safety tank (Fig. 3) with an overall leak proof as final step of the assembly.

After completion of the test section assembly the whole test rig was mounted into the HEBLO facility with all electrical and thermocouple connections. The first function tests of the whole loop with all equipment were done successfully. The He mass flow could be achieved for the first experimental scheme which meets well the layout condition. The heating plate function was tested stepwise up-to a high temperature of 700 °C and showed a perfect condition.
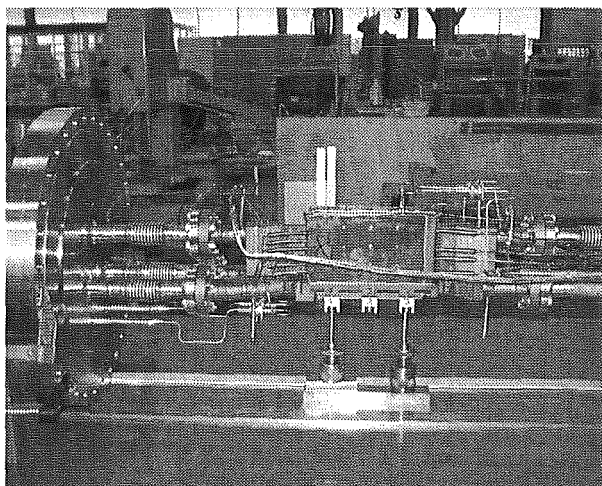
Fig. 1: Test section assembly including pebble bed filling, seal welding and high pressure leak proof at 8 MPa.

Outlook

The first experimental series with steady state conditions will be carried out till the end of this year. The next experimental series with temperature transient conditions will be started in the year 2000. Accompanying calculations are in preparation at the moment.
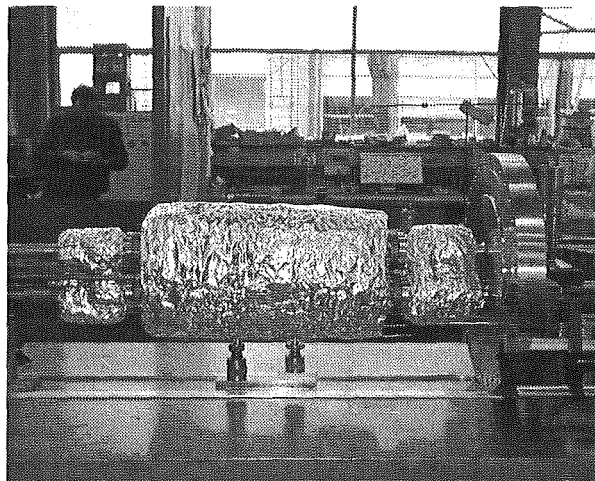
Fig. 2: Thermal insulation of the test section before inserting into the safety tank.
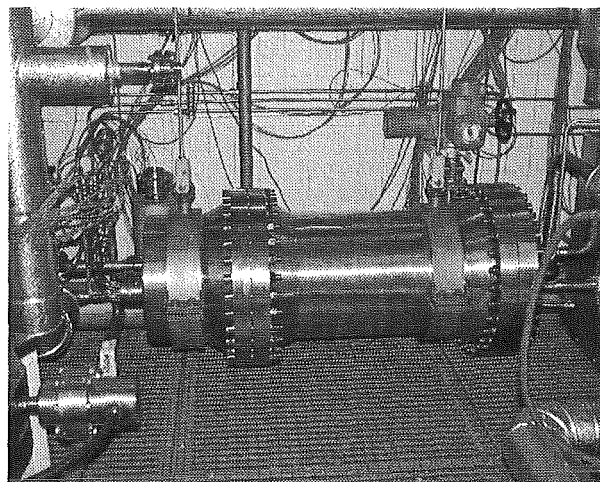
Fig. 3: Integration of the whole test rig with the safety tank and the inserted test section into the HEBLO facility.

2. HE-FUS3 Test section: Final report on the design

The contribution of FZK to the design of the HE-FUS3 test section was completed in 1998. Report [1] describes the corresponding work which consists of some general design considerations, a conceptual design proposal, thermohydraulic and thermal-mechanical calculations.

Literature:

[1] S. Gordeev, K. Schleisiek, I. Schmuck,"Contribution to the Design and Analysis of a HCPB Blanket Mock-up for Testing in HE-FUS (Subtask B 3.2.1)", Forschungszentrum Karlsruhe, Interner IRS-Bericht, Oktober 1998

Staff:

S. Gordeev
H. Lehning
P. Norajitra
D. Piel
G. Reimann
R. Ruprecht
K. Schleisiek
Schmuck

B 3.3.4
Help in the Detail Design of an In-pile Test Module

1. Test module analysis

The Helium Cooled Pebble Bed (HCPB) Blanket is one of two blanket concepts being developed within the European Blanket Project (EBP) for DEMO as a prototype fusion power plant. The design of the HCPB blanket requires good knowledge of thermo-mechanical longtime behaviour of ceramic breeder and beryllium pebble beds under neutron irradiation. Therefore an in-pile test is to be performed in the High Flux Reactor (HFR) at Petten/Netherlands to concentrate on the effect of neutron irradiation on the thermal-mechanical behaviour of the HCPB breeder pebble beds at DEMO representative levels of temperature and defined thermal-mechanical loads [1-3]. In this framework a number of experimental and modelling activities are being pursued at NRG Petten and FZK.

The basic element for the in-pile test module is a cylinder of ferritic-martensitic steel with a horizontal bed of ceramic breeder pebbles sandwiched between two beryllium beds, see Fig. 1 [2,3]. The beds are separated by ferritic-martensitic steel plates, which are either allowed to 'float' between the neighbouring pebble beds or are rigidly connected to the structure. Two gas gaps at the breeder bed and partially at the beryllium bed circumference provide the thermal barriers needed to force the heat produced in the breeder to flow axially obtaining a radial temperature distribution in the ceramic breeder pebble bed as flat as reasonably possible.
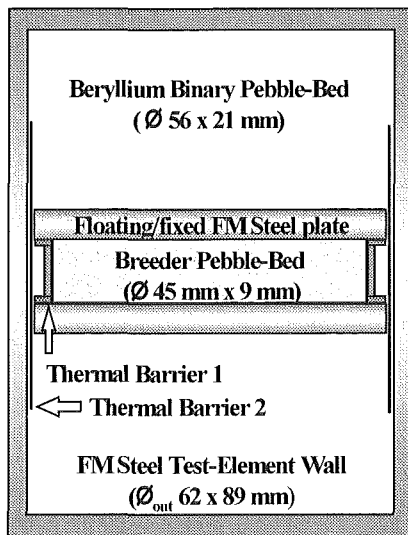
Fig. 1: Schematic of HCPB pebble bed assembly for in-pile testing in HFR Petten.

Main interest of pebble bed behaviour are non-linear elasticity and inelastic deformation due to compaction, swelling and thermal creep effects. Activities to properly model this behaviour using numerical tools have recently started.

Some calculations have been carried out at FZK using the capability of the computational program ABAQUS to compute the behaviour of the test module filled with frictional materials, which are typically like granular soils. In particular, the Drucker-

Prager model is used to describe the shear failure mechanism of the granular material and the Cap model to bound the yield surface in hydrostatic compression and to provide an inelastic hardening mechanism to represent plastic compaction. The models are calibrated with experimental results from uniaxial and triaxial tests [4].

Modelling activities started at NRG and FZK to enable analysis of the thermal-mechanical and in-pile behaviour of pebble bed assemblies. The application of these material models is necessary to determine the influence of the bed compaction and thermal creep on the structural integrity. A major issue concerned the assessment of the plates constraint condition. Of further importance was the design evaluation for the thermal barriers.

The calculations showed that the differences in constraint condition (floating versus fixed plate) for the breeder beds in the test element appear to be rather small after longer term operation. The HCPB team has decided to depart from the constraint condition with fixed plates. The analysis has led to a reconsideration of the initial test matrix published earlier [2,3]. It has been proposed to adjust the test matrix with a variant for a Li_2TiO_3 pebble bed. Li_2TiO_3 pebbles [5] are being developed as an alternative breeder material to the reference material Li_4SiO_4.

As an alternative to the binary beryllium pebble bed considered so far, monosized beryllium pebble beds are under closer investigation. This allows simple filling procedures for the beryllium pebbles because demixing of pebbles with different size cannot occur, leads to homogenous beryllium distribution in the beds which has advantages in their physical behaviour and simplifies the interpretation of thermal-mechanical calculations.

2. Pre-tests of breeder pebble bed assemblies and benchmark activities

As preparatory activities for the in-pile testing of pebble bed assemblies, NRG is performing out-of-pile experiments with prototypical pebble bed assemblies in preparations of the fabrication of the in-pile modules. The results of these tests can be used to bench-mark the ongoing HCPB activities on thermo-mechanical modelling of pebble beds interacting with the embedding structure [6].

In particular a series of tests denominated "SCATOLA" have been proposed to compare different computational approaches in the calculation of the mechanical behaviour of pebble bed.

2.1 SCATOLA-experiment

The basic set-up of SCATOLA is a cylindrical pebble bed assembly: the ceramic pebble bed (Li_4SiO_4 in the presented cases) is enclosed between two plates that are fixed at their circumference, see Fig. 2. A rod is connected to the lower plate and is allowed to slide within a tube that is connected to the upper plate. In this way the relative movement of the plates can be measured at various temperatures and times. A screwed cap allows to fix the assembly in a reproducible way. The two plates are 'semi-floating': they are constrained in the outwards direction by the cap but their inward movement is only prevented by the pebble bed. The actual displacement of the two plates is measured with respect to each other. Two basic versions of the SCATOLA are available: one out of MANET (12%Cr-Steel) and one out of T91 (9%Cr-Steel). Plates of 3.0 to 5.5 mm thickness have been used.
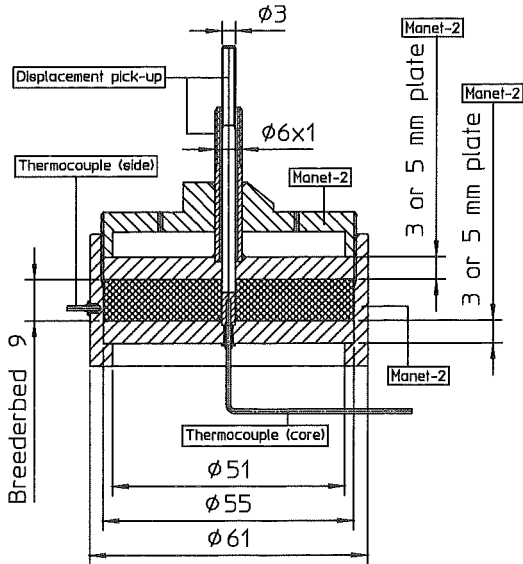
Fig. 2: Details of typical 'SCATOLA' test-element.

The SCATOLA is heated up slowly in a furnace and is instrumented with two thermocouples placed in the bed measuring the temperature at the centre and at the cylindrical wall interface, respectively.

2.2 Bench-mark

The heating tests of the SCATOLA device with Li_4SiO_4 pebble bed are suitable for simple bench-mark exercises to compare different computational approaches in the modelling of the mechanical behaviour of granular materials. Due to the higher expansion coefficient of the orthosilicate in comparison to the structural material, a pressure arises at the interface between the structural materials and the pebble bed. The related axial deformation of the box will be measured in the experiment during the heating and the subsequent cooling of the device.

The development and testing of material models of granular materials suitable for stress analysis calculation are the goals of this bench-mark. For the development of these models the results of the experimental investigations performed at the FZK on Lithium Orthosilicate pebble beds are at disposal [7]. The data base contains results of Oedometric tests for a range of temperature up to 850°C and pressure up to 7 MPa and triaxial tests at ambient temperature.

2.2 Calculation results

Some preliminary calculations have been carried out at the Forschungszentrum Karlsruhe using the capability of the computational program ABAQUS to model frictional materials, which are typically like granular soils (see section 1). At present, the calculation only concerns a first heating. However, this model can be expanded taking into account the subsequent cool-down phase and creep phenomena.

Fig. 3 shows a comparison between the calculated (by NRG and Forschungszentrum Karlsruhe) and measured value of the axial displacement for the SCATOLA configuration with 3 mm plates.
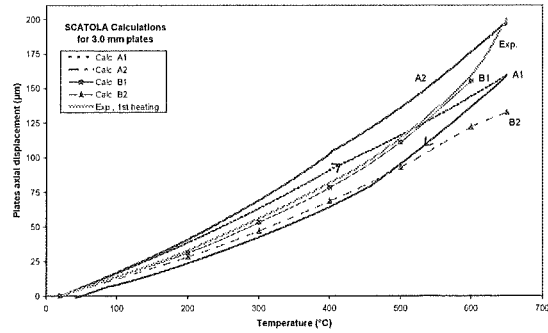
Fig. 3: Comparison between measured and calculated values of the axial displacement [6].

A1 and A2 are calculations performed by NRG, B1 and B2 by Forschungszentrum Karlsruhe.

Literature:

[1] S. Hermsmeyer, S. Malang and K. Schleisiek, "Design considerations for a HCPB test section for in-pile testing", in: Proceedings CBBI-7, NRG Report 21099/99.23482, Petten, February 1999.

[2] J.G. van der Laan, R. Conrad, K. Bakker, J.H. Fokkens, S. Hermsmeyer, S. Malang, B.J. Pijlgroms, K. Schleisiek, C. Sciolla and R. van Tongeren, "In-pile testing of submodules for the HCPB DEMO blanket concept at the HFR Petten", in: Proceedings of the 20th SOFT (1998), pp. 1243-1246.

[3] J.G. van der Laan, R. Conrad, K. Bakker, J.H. Fokkens, S. Hermsmeyer, S. Malang, B.J. Pijlgroms, K. Schleisiek, C. Sciolla and R. van Tongeren, "In-pile testing of HCPB submodules at the HFR Petten ", in: Proceedings CBBI-7, NRG Report 21099/99.23482, Petten, February 1999.

[4] L. Bühler, J. Reimann, E. Arbogast, K. Thomauske, „Mechanical behaviour of Li_4SiO_4 in a blanket typical geometry", presented at ISFNT 5, Rome, September 1999.

[5] Roux et al., paper to be presented at ICFRM-9, October 1999.

[6] J.G. van der Laan, R. Conrad, K. Bakker, L.V. Boccaccini, J.G. Boshoven, L. Bühler, J.H. Fokkens, M.A.C. van Kranenburg, B.J. Pijlgroms, J. Reimann, "Design analyses and pre-tests for the irradiation of HCPB pebble-bed assemblies", presented at ISFNT 5, Rome, September 1999, to be published.

[7] A.Y. Ying, M.A. Abdou, L. Bühler, M. Enoeda, S. Malang, Y. Ohara, J. Reimann „Summary of laboratory experiments and modelling for thermomechanical properties and interactions of solid breeder pebble bed materials", presented at ISFNT 5, Rome, September 1999.

Staff:

L. Boccaccini
S. Hermsmeyer
S. Malang
K. Schleisiek
F. Wolf

WP B 4
Tritium Control and Requirement for Permeation Barriers

B 4.2.1
Manufactoring of Test Section for Tritium Permeation Experiments

An important operational and safety issue for fusion reactors is the permeation of tritium through structural materials. For the HCPB blanket, tritium gets mainly to the environment by permeation from the helium coolant system through the INCOLOY 800 steam generator walls into the steam cycle. Therefore, the tritium permeation mechanisms through this material are of large interest.

The goal of the present investigations was, therefore, the development of permeation barriers by in-situ oxidation of the INCOLOY 800 surface.

Permeation experiments with INCOLOY 800 disks were performed both in JRC/Ispra and in FZK using different experimental set-ups. Deuterium permeated from a high pressure gas side to a low pressure gas side. The high pressure gas contained a given amount of H_2O.

The important result is that for all specimens after some days of operation the permeation fluxes are much lower than those for the bare material. This reduction is larger by a factor of 20 at temperatures around 250°C and larger by two orders of magnitude at temperatures $\geq$ 450°C.

The permeation reduction due to the formation of these oxide layers is sufficiently large in order to obtain a relatively small Coolant Detritiation System for a Be- or W-coated First Wall.

The Task WP B 4.2.1 has been terminated end of 1998; the work is documented in [1,2].

Literature:

[1] A. Perujo, H. Feuerstein, J. Reimann, „Task B42-Final Report, Tritium permeation reduction through the HCPB steam generator by in-situ oxidation", European Commission, Joint Resarch Centre, Environment Institute, Renewable Energies Unit, I-21020 Ispra, Technical Note No1.99.90, 1999

[2] A. Perujo, H. Feuerstein, J. Reimann, „The oxidation kinetics of incoloy 800 and its deuterium permeation behavior"ICFRM-9, October11-15, 1999, Colorado Springs, USA

Staff:

Perujo (JRC/Ispra)
J. Reimann (FZK)

WP B 7
Demonstration of Blanket Reliability

B 7.1.3
Contribution to Common Blanket System Data Base

Common Data Base

This Subtask is connected with the Tasks B 7.2.2 , A 7.1.3 and A7.2.3. All data used there will be inserted in a common data base. The use of the same data for different design options allows to limit error sources in comparative evaluations. The activity was officially terminated in December 1998. But in general, in future availability and safety analyses the completion of the common failure data base would be one of the most important activities.

Probabilistic Fracture Mechanics Assessment

Currently used failure rates for availability studies are usually obtained from in-service experience of various classes of components and welds. No information about material parameters and loading uncertainties is usually part of the analysis.

An activity was therefore started with the aim of establishing failure rates that are based on in-service loading condition as well as on the fracture mechanics description of present or assumed flaws. A probabilistic analysis was performed which allows to assess the uncertainty in material and loading parameters using a fracture mechanics assessment procedure.

A reference case was chosen from the currently developed ITER test blanket module with data taken from the literature and from current design analyses.

Staff:

H. Riesch-Oppermann
H. Schnauder

B 7.2.2
TBM System Availability

The availability/unavailability of the HCPB Test Blanket System is an important accompanying factor in design and development. The proceeding can be only performed stepwise because newer findings lead to permanent improvements of the design and movements in the main points of consideration.

Improvements of knowledge from R&D work, concerning the welding procedures and more detailed thermal and structural mechanic design calculations lead to changes and simplifications. A new consideration of the HCPB blanket test module for ITER, together with the external cooling circuits, became necessary [1]. The results show a high availability for the test module. But, the cooling circuits dominate the overall result. The availability varies between 96 and 99%, dependent on the MTTR. The test module unavailability participates to the total result with less than 2%.

The analysis shows that in case of the test modules and on the background of ITER, the results are acceptable as there is sufficient space for modifications, if necessary without decreasing the availability in an unacceptable manner. In case of the cooling circuits the design is also not critical. Improvements in the availability seem to be possible in cases, that the results are judged to be at the limit of acceptance. The project was terminated in December 1998.

Literature:

[1] H. Schnauder, Availability Analysis of the modified HCPB Test Blanket System for ITER, Forschungszentrum Karlsruhe, Internal IRS-Report, Nov. 1998

Staff:

H. Schnauder

WP B 8
Development of Ceramic Breeder Pebble Beds

B 8.1
Development and Characterization of Ceramic Pebbles

B 8.1.1
Development and Characterization of Li_4SiO_4 Pebbles

Within the framework of the development of the data base on properties of lithium orthosilicate (Li_4SiO_4 + SiO_2) and lithium metatitanate (Li_2TiO_3 + TiO_2) pebbles relevant to their utilisation in the Helium cooled pebble bed blanket (HCPB) long time annealing experiments (aging) in blanket-typical atmosphere have been carried out at Forschungszentrum Karlsruhe [1]. To achieve representative End-of-Life DEMO conditions for the pebbles, it has been chosen in the test a temperature of 970 °C and an annealing time of 96 days. In 1998 a first long time annealing experiment was performed on pebbles of lithium orthosilicate, lithium metazirconate and lithium metatitanate (agglomeration-sintering production method). Following the selection of the extrusion-spheronization-sintering as fabrication method to produce the lithium metatitanate pebbles, it was decided to start a new long time annealing experiment to test the extruded Li_2TiO_3 pebbles. In order to repeat some measurements of their characteristics also lithium orthosilicate pebbles were annealed in the experiment. There were:

*   2 specimens of overstoichiometric Li_4SiO_4 + SiO_2 pebbles supplied by Forschungszentrum Karlsruhe and fabricated by SCHOTT Glaswerke by melting-spraying process. The diameter of the pebbles was in the range 0.25 mm-0.63 mm. One specimen was conditioned at 1000 °C for 15 days in air (thermal conditioning) before the long time annealing, the other one was not pre-annealed;

*   1 specimen of overstoichiometric Li_2TiO_3 + TiO_2 pebbles supplied by CEA and fabricated by extrusion and sintering process. The diameter of the pebbles was in the range 0.9 mm-1.2 mm. For this material a pre-annealing of 10 hours at 500 °C in air was performed before starting the long time annealing.

The experiment was done in an oven consisting of three tubes of Al_2O_3, one tube for each specimen, with separate purge gas flow (Fig. 1). At the tube inlets the pressure of the purge flow and its H_2O content were measured. The water content in the purge flow was also measured at the outlets together with the mass flow. Sintered steel filters have been used at the tubes outlets to have a qualitative indication of the vaporisation of lithium from the pebbles. The purge flow was 0.6 l/h of 99.9 % He + 0.1 vol % H_2 .

Sampling of all the specimens was made at the beginning and after the thermal conditioning. Then the sampling was done after 14 and 96 days for the two specimens of Li_4SiO_4 and after 3 and 96 days for Li_2TiO_3. To characterise the ceramics the following analyses have been performed:

*   chemical analyses. The measurements of Li-content have been done using the atomic emission spectroscopy (AES), the X-ray fluorescence analysis (XFA) has been used to measure the amount of Si, Zr and Ti;

*   X-ray diffraction analysis (XRD) for the phase composition analysis;

*   scanning electron microscopy (SEM) and light-microscopy for the structure analysis;

*   He-pycnometry and Hg-porosimetry for density and porosity measurements;

*   Brunauer, Emmet and Teller (BET) method for the specific surface area measurement;

*   crush load determination;

During the experiment 2 vpm of water were measured in the purge flow at the inlet of each pipe. This value was practically constant. After several weeks stationary values of water content were reached at the outlet of each pipe. About 3 vpm were measured for the conditioned lithium orthosilicate pebbles, about 1 vpm for the not conditioned lithium orthosilicate and about 12 vpm for the lithium metatitanate.

Results

Considering the results of the examinations the following conclusions can be drawn:

*   In Li_4SiO_4 the thermal conditioning produces the largest changes in the structure, but, after 14 days of annealing at 970 °C, it is not possible to recognise any difference in the structure between the conditioned and the not conditioned pebbles. The thermal conditioning does not cause any significant difference also in the other characteristics of the pebbles after the aging. As previously observed, during the annealing the only significant change in the orthosilicate pebbles is the diffusion of metasilicate through the material. After 14 days of annealing there is a reduction of the specific surface area from 0.26 m^2/g to 0.09 m^2/g. The measured density of the pebbles is about 96 % of the theoretical density and it does not change during the experiment. To investigate the change in the mechanical stability during the annealing at each sampling crush load measurements were performed on 80 pebbles having a diameter of 0.5 mm. The initial average value of about 8.9 ± 3.2 N is reduced to 4.2 ± 1.6 N at the end of the annealing.

*   In Li_2TiO_3 the pre-annealing at 500 °C has no significant effect on the structure of the material. During the annealing there is an increase in the grain size (it is about 1.5 µm at the beginning and, after 96 days, it grows up to about 25 µm). After 3 days the pebbles became black, but this colour change does not correspond to any change in the microstructure of the pebbles, and no additional phase could be detected. The colour change was caused by a slight oxygen sub-stoichiometry of the material. After the annealing in Li_2TiO_3 there is a slight reduction of the porosity and an increase of the density from 85% to 90% of the theoretical density. The specific surface area of 0.11 m^2/g is reduced to 0.07 m^2/g after 96 days. the average crush load was measured on 80 pebbles of 0.8 mm diameter. After 3 days annealing the average crush load decreased from 41± 12 N to 35± 7 N, and remained practically constant till the end of the experiment.

In comparison with the previous long time annealing now the purge flow contained a very small quantity of water. The reduction of the amount of water in the new aging experiment had the only consequence to accelerate the process of reduction of the ceramic materials with the consequent change in the colour of the pebbles. In fact the titanate pebbles were black after 3 days (in the previous experiment they needed 48 days to become black) and the silicate pebbles became grey.

Literature:

[1] G. Piazza, M. Dalle Donne, H. Werle, E. Günther, R. Knitter, N. Roux, J.D. Lulewicz, "Long term Annealing of Ceramic Breeder Pebbles for the HCPB DEMO Blanket". Proceedings of the CBBI-7, 14-16 Sept. 1998, Petten, the Netherlands.

Staff:

C. Adelhelm
E. Günther
E. Kaiser
D. Knebel
R. Knitter
G. Piazza
H. Ziegler
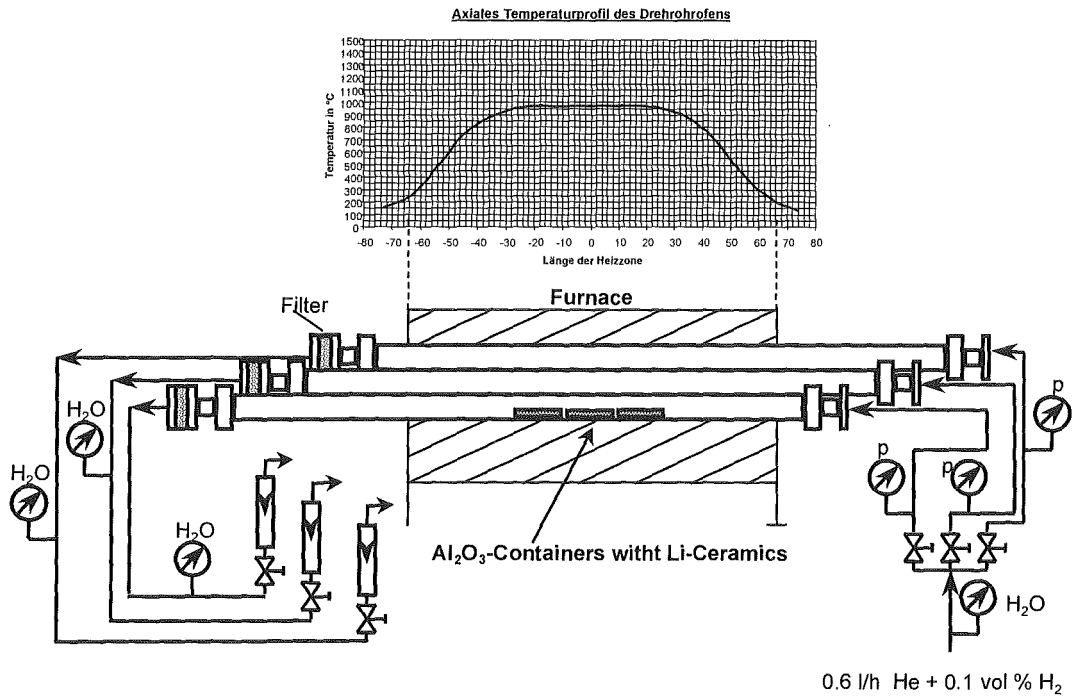
Fig. 1: Schematic of the equipment used in the annealing experiments

B 8.3.1 Out-of-Pile Pebble Bed Tests and Model Development

In order to describe the interaction between ceramic breeder and beryllium pebble beds and the structural material in ceramic breeder blankets, the characteristic properties of these pebble beds in the relevant temperature and pressure ranges must be known.

Uniaxial compression tests with Li_4SiO_4 pebble beds were performed in a temperature range between ambient and 900 °C and pressures up to 8 MPa. Corresponding experiments with a smaller parameter variation were carried out with Li_2TiO_3, Li_2ZrO_3, and Li_2O pebble beds.

Triaxial tests were performed at ambient temperature in order to determine the inner friction of pebble beds.

Biaxial experiments with blanket relevant pebble bed heights were performed in order to investigate the macroscopic flow of particles.

From the uniaxial tests, empirical correlations for the moduli of deformation for the different materials were determined both for the first stress increase and decrease. For Li_4SiO_4 pebble beds first relationships for thermal creep of are given, for details see [1, 2]. Fig. 1 shows the temperature dependence of the deformation modulus for the first stress increase
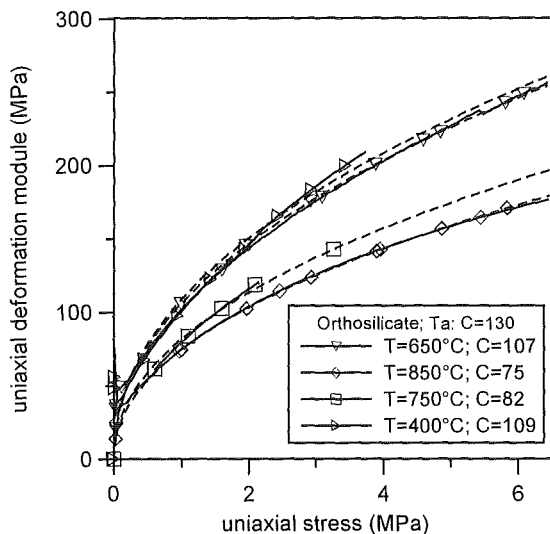
Fig. 1: Uniaxial deformation module (1st pressure increase) for Li_4SiO_4 pebble beds

The results from the biaxial tests showed that a macroscopic movement of pebbles becomes neglible already at very small ratios of horizontal to vertical stresses. Using the results from the uniaxial and triaxial experiments, this behaviour can be well described with the ABAQUS-code, see [3].

Literature:

[1] J. Reimann, E. Arbogast, M.Behnke, S. Müller, K. Thomauske, Thermomechanical behaviour of ceramic breeder and beryllium pebble beds, ISFNT-5, Sept. 20.-24,1999, Rome, Italy

[2] A.Y. Ying, M.A. Abdou, L. Bühler, M.Enoeda, S. Malang, Y.Ohara, J. Reimann, Summary of laboratory experiments and modelling for thermomechanical properties and interactions of solid breeder pebble bed materials,.this conference.

[3] L. Bühler, J. Reimann, E. Arbogast, K. Thomauske, Mechanical behaviour of Li_4SiO_4 pebble beds in a blanket typical geometry, this conference.

Staff:

J. Reimann
E. Arbogast
L. Bühler
K. Thomauske

WP B 9
Behaviour of Beryllium under Irradiation

B 9.1.1
Characterization of Beryllium Pebbles

Although beryllium has no structural function in the blanket, microstructural and electrical properties are important, as they might influence the material behavior during both normal and off-normal reactor operating conditions like plasma disruptions. To confirm the conservative assumptions about the electrical resistivity of the beryllium pebble bed made in the course of the electromagnetic analyses, this property has been measured as a function of temperature and applied load. The microstructural changes were analysed by means of both optical microscopy and Rutherford backscattering spectrometry.

1. Material

The material used for the analyses consists of two types of beryllium pebbles (pebble diameter Φ= 0.1-0.2 mm and Φ= 2 mm) produced by the Brush Wellman company. The 2 mm pebbles were produced by Fluoride Reduction Process (FRP), which is an intermediate step in the process of winning beryllium from ore [1]. Although some perfect spheres are found, the shape is generally not perfectly spherical. Since they are an intermediate product, these pebbles contain significant amounts of impurities, notably fluorine and magnesium.

On the other hand, the 0.1-0.2 mm pebbles were made by Inert Gas Atomization (IGA). This process involves break up and rapid cooling of a molten metal stream to form pebbles [1]. This pebbles are very close to spherical in shape and have the purity level of other commercial beryllium products.

2. Experimental techniques

The 2 mm beryllium pebbles were analyzed by the Rutherford backscattering spectrometry (RBS) using a 1.6 MeV He$^+$ beam collimated to 0.8 mm. The backscattered particles were detected with two surface barrier detectors placed at 140° and 180° and with an energy resolution of 12 keV and 15 keV respectively. The detectors and the ion beam were placed in the same horizontal plane and the pressure inside the measuring chamber was about 10^{-4} Pa. Some 0.1-0.2 mm pebbles were studied using a He$^+$ microbeam of 6 μm. In this way we can avoid the effects of the surface shape on the RBS spectra. The metallographic characterization of both the 2 mm FRP and 0.1-0.2 mm IGA pebbles was carried out by means of optical microscopy.

Resistivity measurements have been performed for both a single size pebble bed (pebble diameter Φ= 0.1-0.2 mm or Φ= 2 mm) and a binary pebble bed (pebble diameter Φ= 0.1-0.2 mm and Φ= 2 mm). The pebble bed column with a lengh l=21 mm is enclosed in an insulating alumina tube with a radius r=5 mm. The ends of the tube are closed by two pieces of steel which are used to apply the force (measured with a balance) and make the electrical contacts. A constant current of 250 mA was applied and the voltage drop along the Be pebble bed column was measured. For the temperature measurements the alumina tube was placed inside a tubular furnace. The temperature was monitored with a thermocouple in contact with the inner alumina tube. In order to avoid the bending of the column containing the pebble bed due to the applied force the column was placed inside a steel tube isolated by sapphire balls. The possible influence of the l/r ratio on the resistivity was checked in a pebble bed column with a length of 11.5 mm and a radius of 19.5 mm at room temperature. All the measurements were carried out at ambient atmosphere.

3. Results

Fig. 1 shows a typical metallographic structure of the 2 mm FRP beryllium pebbles.

Macroscopically, the pebbles show a relatively large number of surface indentations probably due to the fact that during the fabrication process, very hot (or still partially molten) beryllium pebbles come in contact with cold and already solidified ones. The optical microscopy revealed both large pores of various size (a pore size of 0.1-0.2 mm has been often observed and a microporosity usually oriented along the crystal axis perpendicular to the basal plane. Furthermore, a large number of pebbles presents, near the external surface, a dense region the depth of which usually reaches 0.2-0.3 mm. In this region, the pebbles usually show a metallographic structure characterized by the presence of large grains (average grain size 100-300 μm). On the other hand, the remaining part of the pebbles shows a metallographic structure characterized by relatively small grains the average size of which is 50-100 μm. This kind of pebble structure (which has been already observed in other types of pebbles subjected to fast thermal treatments) is typically generated during the cooling phase of the fabrication process.
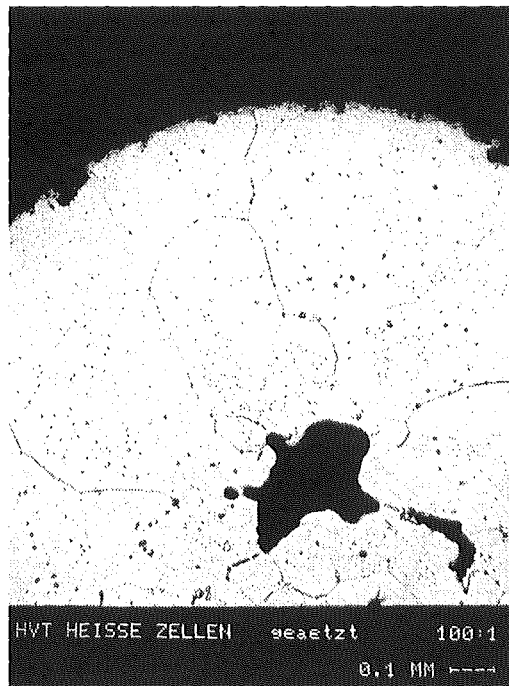
Fig. 1: Typical metallographic structure of a 2 mm FRP beryllium pebble (etched).

The Rutherford backscattering (RBS) spectrum of a 2mm Be pebble is shown in figure 2. The results indicate the presence of most of the impurities reported by the producer [1]. The oxygen concentration profile, shown in figure 3, is below the value corresponding to the existence of a pure BeO layer at the surface. These results can be interpreted assuming the presence of BeO regions surrounded by metallic Be. The BeO is therefore probably distributed along the grain boundaries as revealed by the optical microscopy. When the pebbles are submitted to loading/unloading cycles at high temperatures a large increase in the amount of oxygen has been observed as

shown in figure 4. On the other hand the signals of the other impurities do not show any significant changes.
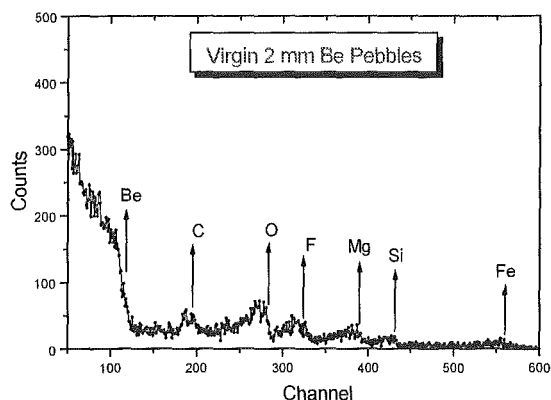
Fig. 2: RBS spectrum of a 2 mm Be pebble.
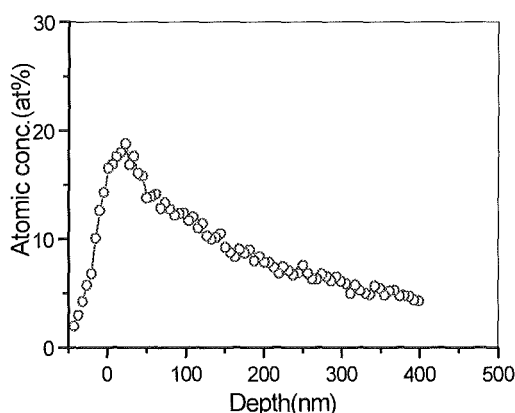
Fig 3: Depth profile of the oxygen obtained from the spectrum of figure 2.
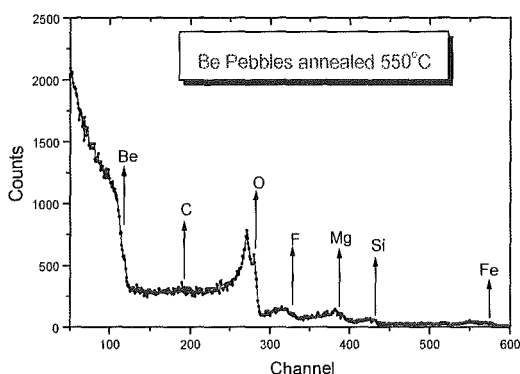
Fig. 4: RBS spectrum of a 2mm pebble after heating at 550°C in open air.

In the case of the single-size 2 mm pebble bed, the electrical resistivity of the bed decreases drastically to about 10^{-4} Ωm by applying an external pressure. After this first drop, the resistivity shows an almost linear decrease with the applied pressure. The same trend appears for the single size 0.1-0.2 mm pebble bed, but the resistivity values are about one order of magnitude higher than in the case of 2 mm pebbles because of its larger BeO content. The lowest resistivity values were found for the case of a binary pebble bed. The initial drastic drop in the electrical resistivity is probably due to the formation of electrical contacts promoted by the mechanical arrangement of the

pebbles due to the applied load. After that, the resistivity of the bed decreases almost linearly with the applied pressure.

After a mechanical cycling the electrical resistivity of the bed never reaches its initial value for zero pressure, but it remains about one order of magnitude below the original value, as shown in figure 5.
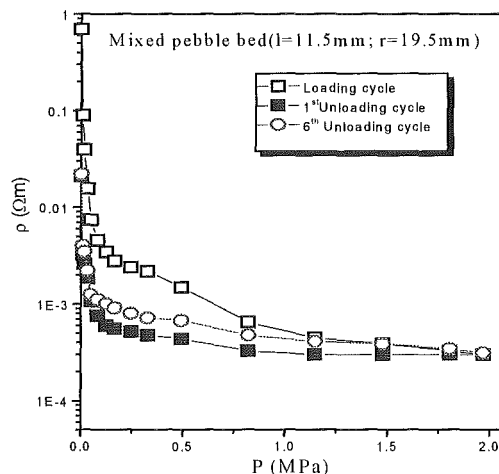
Fig. 5: Loading/unloading cycling behavior of the electrical resistivity at room temperature.

After several loading/unloading cycles the resistivity curves do not show any significant change with respect to the first unloading curve, thus indicating that a stable condition has been reached. This behavior is essentially the same as that observed in the case of the mechanical behavior of a pebble bed.

When the pebble bed is heated during the loading cycle the resistivity increases almost linearly with the temperature.

After the cooling of the pebble bed the resistivity measurements have been repeated and the results were compared with the curves obtained at the beginning (see Fig. 6). Although the curves were similar there was a shift of the resistivity to higher values after the heating cycle. This increase of the resistivity can be related with an increase of the BeO layer of the pebbles during the measurements at high temperature. In fact, RBS measurements show an increase of the oxide content of the pebbles during the heating.

Literature:

[1] D. E. Dombrowski, Personal Communication, 1998.

Staff:

E. Alves
L.C. Alves
E. Kaiser
A.A. Melo
M.F da Silva
F. Scaffidi-Argentina
J.C. Soares
F. Weiser
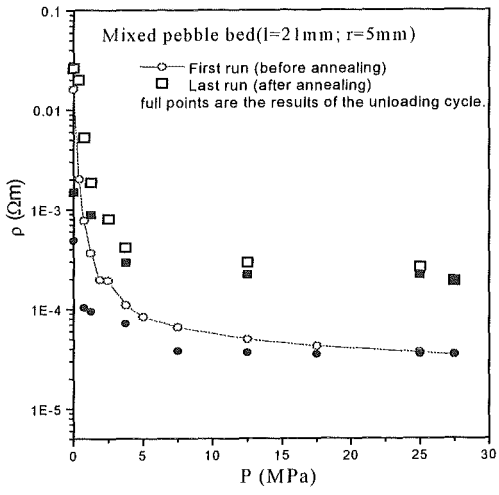
Fig. 6: Resistivity curves obtained before and after the measurements at 550°C.

B 9.2.1
Investigation of the Thermal-Mechanical Behaviour of Beryllium Pebble Beds

In a helium cooled pebble bed blanket (HCPB) the neutron multiplier is arranged as pebble beds between flat cooling plates. Therefore it is necessary to investigate the thermal and mechanical properties of beryllium pebble beds under representative conditions. The results of this investigation have an important influence on the design of HCPB blankets. The task foresaw the following activities on beryllium pebble beds:

• Uniaxial compression tests with $T_{room} \leq T \leq 450$ °C and triaxial tests ($T \approx T_{room}$) with monosized, and binary beds;

• Fabrication of a test section (HECOP) for the investigation of heat transfer through uniaxially compressed beryllium pebble beds and first operational tests.

Compression tests

For the modelling of the interaction between ceramic breeder and beryllium pebble beds and the structural material, the characteristic properties of these pebble beds in the relevant temperature and pressure ranges must be known.

Uniaxial compression tests with monosized and binary beryllium pebble beds were performed in the past for ITER-blanket relevant temperature and pressure ranges and empirical correlations for the moduli of deformation were established.

During this year, triaxial compression tests for monosized and binary beds were performed [1]. These tests are required in order to describe the macroscopic movement of particles in the bed. The most important quantity is the internal pebble bed friction angle. Using a presentation as shown in the next figure, the friction angle increases with increasing values of the ordinate. The fig. 1 shows that the data for the beryllium beds are distinctively higher than those for the other granular materials which consist of fairly spherical pebbles with much smoother surfaces (including Li_4SiO_4 pebble beds).
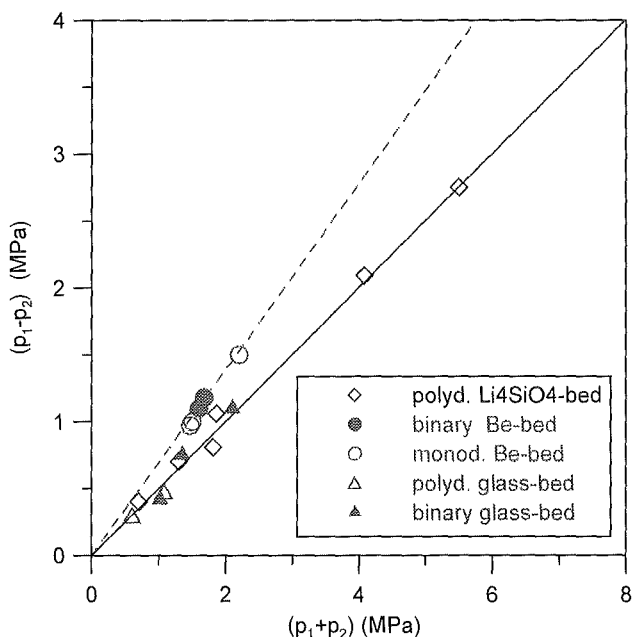
Fig. 1: State of perfect plasticity of different granular materials

The present data in combination with the corresponding results for ceramic breeder pebble beds enable now the calculation of the thermomechanical interaction between pebble beds and the

blanket structure for ITER blanket conditions. For DEMO-blanket conditions this data base must be extended to higher temperatures

HECOP experiment

In order to investigate the heat transfer through uniaxially compressed beryllium pebble beds a test facility was designed. The design of the machine was guided by minimisation of uncontrolled heat losses and a reliable measurement of the temperature gradients in the bed. The device will be built-up in a glove box already used for beryllium experiments (Fa. Goraieb Versuchstechnik) and consists of the following main parts:

• electro-hydraulically controlled mechanical press ($p_{max} \approx$ 6 MPa);

• electrical heat supply and control system ($T_{max} \approx$ 650 °C);

• Cooling system including heat exchanger;

• test section: heating plate, cooling plate, guard heater (fig. 2);

• instrumentation: pressure and displacement transmitters, thermocouples, electric power measurement device, flow meters, hardware and software for experiment control and data acquisition.
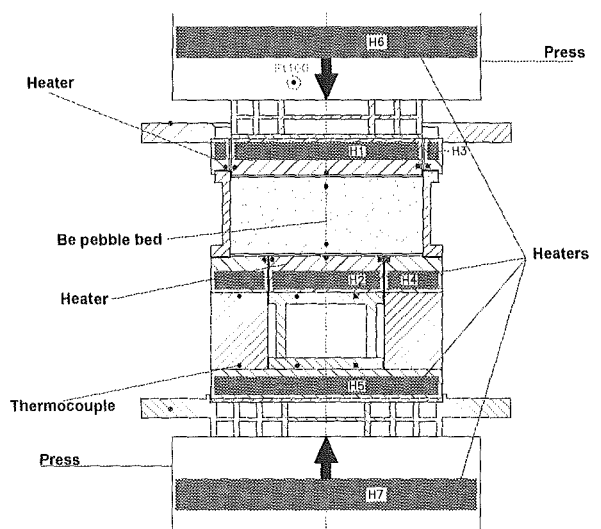
Fig. 2: Schema of the HECOP test facility

An important feature of HECOP is to allow independent adjustment of temperature and pebble bed strain. In the first months of the next year HECOP will be completed and tested, and it is foreseen to have the first results on the heat transfer parameters of a beryllium single size pebble bed till the end of the next year.

Literature:

[1] J. Reimann, M. Behnke, "Experiments on the Thermomechanical Characterisation of Beryllium Pebble Beds". 4th IEA Int.Workshop on Beryllium Techn. for Fusion, FZK, Karlsruhe, Germany, Sept. 15-17, 1999

Staff:
G. Hofmann
G. Piazza
J. Reimann

B 9.3.1
Behaviour of Beryllium Pebbles under Irradiation

A large number of beryllium specimens have been irradiated in US DOE Office of Fusion Energy Sciences experiments in the Experimental Breeder Reactor II (EBR-II) in Idaho Falls, ID, and the Fast Flux Test Facility (FFTF) in Richland, WA. With the increased difficulty for performing irradiation experiments, due in part to the shut down of FFTF and EBR-II and other reactors worldwide, these specimens have become even more valuable. The EBR-II test, COBRA-1A, included four beryllium pebble product forms, and thereby provides fast neutron irradiated materials for postirradiation testing. Post-irradiation test results are presented on density change measurements, tritium release by assay, stepped-temperature anneal, and thermal ramp desorption tests, and helium release by assay and stepped-temperature anneal measurements, for Be pebbles from two manufacturing methods, and with two specimen diameters.

1. Description of the Materials, Irradiation and Fluence

The COBRA-1A vehicle, irradiated in EBR-II starting on November 26, 1992, contained a number of beryllium specimens in canisters C03 and D03 located in below-core positions in capsules B-390 and B-391, respectively. Both capsules were of weeper design, so that reactor coolant was in direct contact with each canister, and canisters were helium filled to provide a heat transfer medium. Experimental details of the capsules are described in [1]. The capsules were removed from the reactor upon removal of the COBRA-1A2 vehicle on September 26, 1994. At that time, EBR-II ceased to operate. Neutron dosimetery and damage calculations for these irradiations are described in [2]. Canisters contained beryllium in several product forms including 1-mm pebbles in D03 and 3-mm pebbles in C03 from Brush Wellman, and 1-mm pebbles in C03 from Nippon Gaishi Co. (NGK). 5-mm pebbles from Brush Wellman were also irradiated, but will not be discussed here. The production of ^{4}He and tritium has been calculated for beryllium irradiated in the COBRA-1A2 experiment in the Experimental Breeder Reactor II. Reaction rates were based on adjusted neutron spectra determined from reactor dosimetry measurements at the specific elevations in the region of the beryllium capsules.

2. Experimental Results

2.1 OM and SEM

Figure 1 provides examples of 1 mm and 3 mm pebbles using optical microscopy (OM). It demonstrates that beryllium pebbles vary significantly in size and many contain surface irregularities, including depressions and seams. Also, stereo pairs were produced using scanning electron microscopy (SEM), and quantitative depth measurements can be obtained for surface features of interest. It was found that both unirradiated and irradiated specimens contain two types of shallow surface depressions, in the order of 100 μm in diameter and in the order of 5 μm in diameter. Evidence for fine surface porosity due to irradiation was not found.

2.2 Swelling Measurements

Density measurements following irradiation (V) gave 1.795 ±0.011 g/cm^3 and prior to irradiation (V$_0$) 1.810 ± 0.033 g/cm^3. The resultant swelling (V-V$_0$)/V$_0$ was 0.83%, smaller in magnitude than the sample-to-sample variability for the unirradiated density (1.86%) but similar to the variability in the irradiated samples (0.6%).
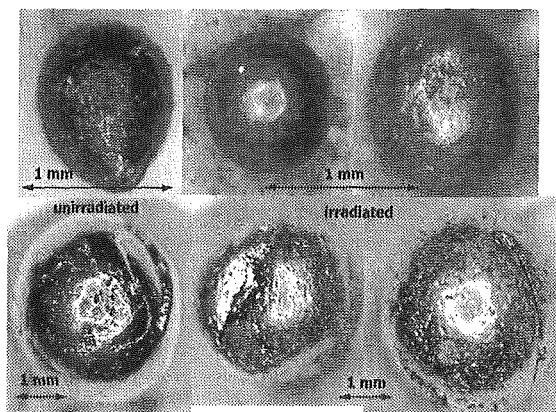
Fig. 1: Examples of 1 mm and 3 mm beryllium pebbles

2.3 Tritium Assay

The measured tritium assay results provide interesting comparisons to produced or predicted values. These assay results, all measured in duplicate, are decay-corrected to May 1997. For each material type, the ratio of measured-to-produced tritium was calculated and is shown, with the produced value being as calculated by Greenwood [2]. Note the 1-mm pebble measured/produced ratios, for both C03 and D03 materials, are low, at a consistent 0.71-0.73, with the 3-mm measured/produced ratio much higher at 0.93. The less-than-1 ratios indicate an in-situ diffusive loss of tritium during irradiation at temperature in the reactor, 388°C for the C03 and 395°C for the D03. A comparison of the ratios provides evidence that in-reactor loss of tritium is dependent upon pebble diameter size, with greater loss in the 1-mm pebbles than for the 3-mm pebbles.

2.4 Tritium Release by Stepped-Temperature Anneal

The C03 stepped anneal tests results, using a sample size of 5 pebbles show that the total cumulative tritium fraction released at 350-850°C was 75% of the total inventory. The anneal times ranged from 6 hrs to 25 hrs at each temperature step. An additional anneal step was added at 850°C, in order to increase the cumulative fraction released at that temperature. The residual tritium remaining after all the anneal steps, measured by melting the sample at 1700°C, was about 25% of total inventory. Therefore, the cumulative plus residual total adds to 10.38 appm, slightly higher than the measured assay results of 9.03-9.96 appm.

For the D03 stepped anneal test, a larger sample of 10 pebbles, and longer-time anneal steps were used, with the final 850°C step held for 72 hours. This D03 test resulted in a much higher cumulative total tritium release than the C03 test. At 350-750°C, 20% was released, with 94% released by the end of the 850°C step. The residual tritium, at 6% of the total inventory, brought the cumulative plus residual total of 9.38 appm into excellent agreement with the assay results of 9.05-9.29 appm.

Note for both stepped anneal tests, less than 2% of the tritium inventory was released at 350-550°C. The D03 material showed an order of magnitude lower release rates at these lower temperatures, a fact which may be of great importance for in-reactor operation. A very consistent cumulative total of about 8.7% was released after 650°C for both materials. After 750°C, the cumulative tritium fraction released was 20-28% for both tests. The major difference between the two tests is seen at the 850°C step, though time duration at temperature is definitely a factor.

The plot of the stepped-anneal C03 test is shown in Figure 2, while the plot of the stepped anneal D03 test is shown in Figure 3.
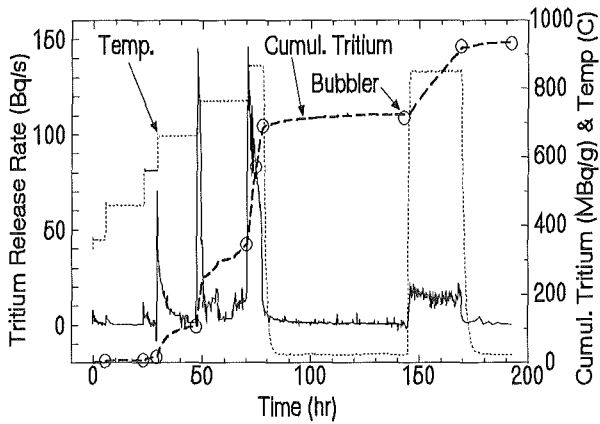
Fig. 2: Tritium release by stepped-temperature anneal for C03
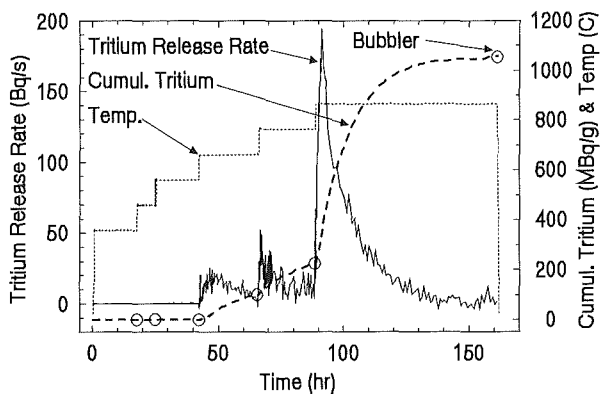
Fig. 3: Tritium release by stepped-temperature anneal for D03

In Fig. 2, the IC cumulative release curve in MBq/g, calculated from the release rate curve in Bq/s, was normalized to the collection bubbler results in MBq/g, by adjusting the IC baseline and/or IC calibration factor [3]. This method assumes the collection bubbler liquid scintillation results are always reliably accurate, therefore, the IC curve must be adjusted or normalized to obtain agreement.

For the D03 stepped-temperature anneal test shown in Fig. 3, the total cumulative released tritium at 350-850°C was 1050 MBq/g or 94% of the total inventory of 1120 MBq/g.

2.5 Tritium Release by Thermal Ramp Desorption

Tritium release kinetics used the method of linear thermal ramp heating at three linear ramp rates. The plot of the thermal ramp test data for the C03 Be material is shown in Figure 4. The figure shows all three test curves of release rate versus time, showing release rate on linear axis, and with the corresponding temperature profiles, for comparison purposes. The difference in the release curve shapes and peak widths can be seen clearly in this plot.

According to the release kinetics parameters as determined from this data, the parameter P, in Bq/g, is the "production" rate as measured by the assay test reported earlier, not as calculated from the fluence prediction; R, in Bq/g, is the measured total release from the sample as determined from the

bubbler liquid scintillation results; R/P, in percent, is the fractional release at end of test; the temperature, T_{max}, corresponds to the temperature of peak maximum release rate; and DF is the factor by which the release rate decreases, at 900 °C in 3 hours. The fractional release, R/P, is high in the 1-mm pebbles, >92% in all cases. The T_{max} for the three cases shows a slight increase with increasing ramp rate, from 882°C to 900° C, as expected. The DF is consistently low for this material, ranging from 3.1 to 11.4, even at the high hold temperature of 900°C, indicating only gradual continuing release at the hold temperature. These DF numbers are low compared with other studied beryllium specimens [4].
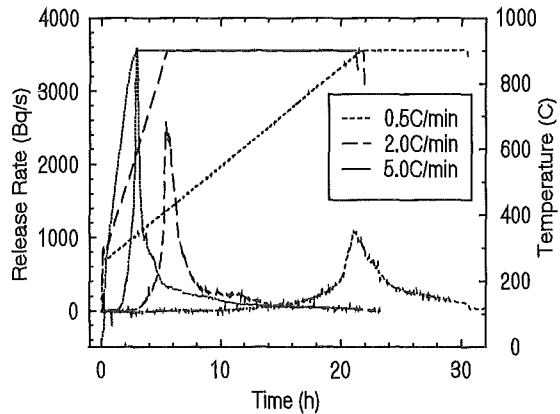
Fig. 4: Tritium release by thermal ramp desorption for C03

2.6 Helium Release

Helium assay for total helium was performed on single pebbles each of both 1-mm C03 and D03 material. Stepped-temperature anneal tests were performed on 15-pebble batch sizes for both the C03 and D03 pebbles. For the stepped-temperature anneal tests, multiple sequential helium measurements were taken at each temperature, with increment steps in sample temperature of approximately 100°C, from either 500°C-1100 °C for scoping tests, or about 800°C-1100 °C, for the final tests. Each temperature was held until some leveling off of ^{4}He was observed, at which point the temperature was raised to the next level. After the anneal tests, residual helium in the samples was determined by vaporization runs.

Helium release as a fraction of the total helium in the sample was markedly different for the C03 and D03 material, shown in Figures 5 and 6.
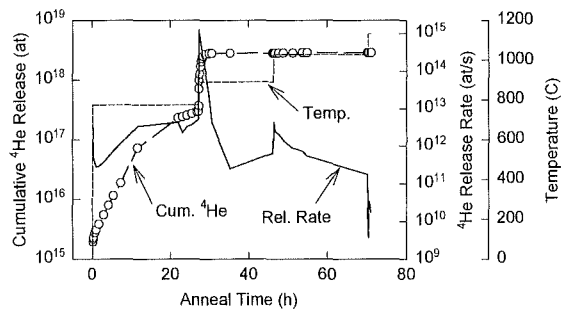
Fig. 5: Helium Release by Stepped-Temperature Anneal for C03
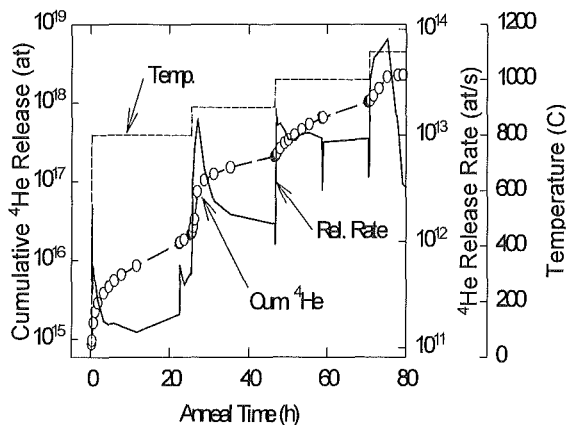
Fig. 6: Helium Release by Stepped-Temperature Anneal for D03

The C03 sample released virtually all of its helium after approximately 30 minutes at 1000°C. Sample D03, on the other hand, released only 62% of its helium even after about 1 hour at 1100°C. Absolute helium release was correspondingly lower for D03 at each temperature level.

In terms of helium concentration, the ^{4}He totals for C03 are 2941 and 2724 appm. The corresponding totals for D03 are 2574 and 2459 appm. The averages agree with predicted concentrations within ±5%.

Literature:

[1] Hamilton, M. L. , Ermi, R. M., Eiholzer, C. R., in IBID DOE/ER-0313/14 (1993) 3-13.

[2] Greenwood, L. R. and Ratner, R. T., in IBID DOE/ER-0313/21 (1996) 225-228.

[3] Baldwin, D. L. and Billone, M. C., J. Nucl. Mater. 212-215 (1994) 948-953.

[4] Scaffidi-Argentina, F. and Werle, H., Proc. 19th Symposium on Fusion Technology, Lisbon, Portugal, September 1996, p. 1431-1434.

Staff:

D.L. Baldwin
D.S. Gelles
L.R. Greenwood
H. Kawamura
B.M. Oliver
F. Scaffidi-Argentina

B 9.3.2
Irradiation of Beryllium Pebbles at High Helium Production Rates

In order to investigate the beryllium behaviour under End-of-Life (EOL) HCPB-DEMO blanket conditions, an irradiation test at high helium production rates (at least 3000 to 6000 appm/year) and, at the same time, high temperatures (up to 700 °C) would be strongly required.

Due in part to the shutdown of many reactors worldwide and in part to the probably low achievable fast flux in the presently available European and Japanese test reactors, only the Russian Federation is probably interested and/or capable in performing an irradiation at high helium production rates and, at the same time, high temperatures. In any case, the achievement of HCPB-DEMO EOL blanket conditions suggests the use of a fast breeder reactor as desired choice.

A preliminary conceptual study has been carried out by looking at the BOR-60 russian fast reactor.

The irradiation would be, in principle, feasible in the instrumented cell D-23 located in the row 5 of the reactor core. The irradiation channel there has a diameter of 35 mm and a length of 450 mm. This would allow the irradiation of three capsules with 30 mm outer diameter and up to 120 mm height in a relatively wide range of temperatures (i.e. 350-700 °C).

According to neutronic calculations, and assuming 200 days of reactor operation a year, it is possible to produce in beryllium in one calendar year of irradiation 3943 appm of helium, 8.1 appm of tritium and a damage dose of 9.6 dpa. Therefore, in order to achieve the desired 16000 appm of helium foreseen in beryllium at the HCPB-DEMO EOL, the irradiation time would be about 4 years.

A preliminary conceptual design of the irradiation test rig is shown in Fig. 1. One could have three irradiation capsules corresponding to three different temperatures (e.g. 350, 550, 700 °C), and each capsule could consist of several sub-capsules. Each capsule and each sub-capsule has to be hermetic and has to be filled with an inert gas (e.g. helium or argon) to provide a heat transfer medium.

Further investigations are underway in order to demonstrate whether such an irradiation test is really feasible.

Staff:

V. Chakin
U. Fischer
F. Scaffidi-Argentina
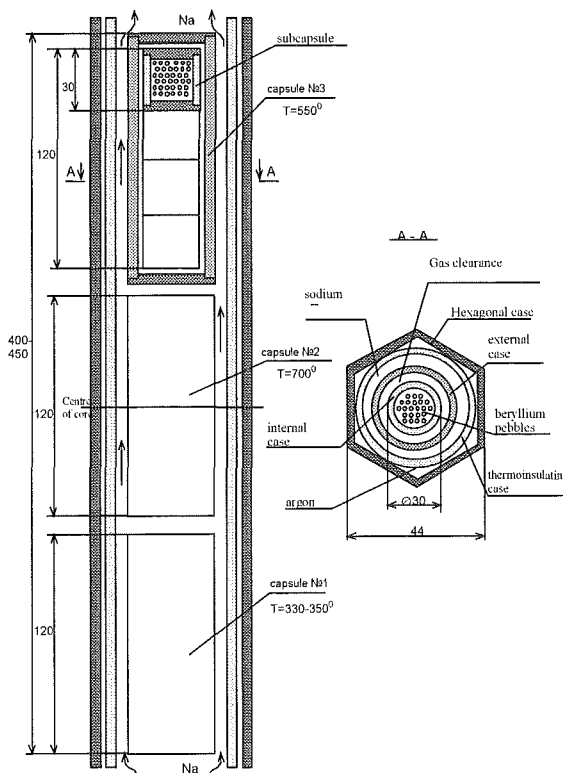
Fig. 1: Preliminary conceptual design of the irradiation test rig for beryllium irradiation in the BOR-60 fast reactor.

Blanket
WCLL Concept

WP A 2 / PPA 2.2
ITER Test Blanket Module Feasibility & Design

A 2.1.3 / PPA 2.2.2
MHD Evaluation and Diffusion Bonding Technique Application, MHD related issues

The interaction of the circulating liquid metal with the plasma confining magnetic fields yields magnetohydrodynamic (MHD) effects, mostly expressed by a MHD pressure drop being orders of magnitude higher than in an ordinary hydrodynamic flow. Although in the actually considered WCLL (Water-Cooled-Lead-Lithium) concept [1,2] the overall MHD pressure drop is not a feasibility issue. MHD effects nevertheless may lead to an unfavourable performance of the blanket.

Therefore the pressure drop of the whole liquid metal path has been evaluated [3] in order to identify key positions contributing mostly to the overall MHD pressure drop. The results for the ITER Test Blanket Module (ITM) are shown in table 1.

Using Flow Channel Inserts (FCI) for the subdistributor channels as proposed by K. Schleisiek and L.Barleon a drastic reduction is expected compared with the previous design without FCI's (see table 1).

To verify the viability of the proposed fabrication technique of the FCI's with respect to the MHD pressure drop a small-scale test specimen [3,4] was designed and manufactured, which will be tested in the MEKKA facility.

A new analysis of the MHD flow in channels with „infinite" thick walls, relevant for the subdistributor channels in the header of the WCLL-ITM show a considerable reduction of the MHD pressure drop (up to 50% less) compared with the results of standard correlations [5].

In a first assessment of different advanced WCLL designs the liquid metal feeding inlet at the bottom of the blanket has been investigated. In this special design the feeding pipe was assumed to last over the whole poloidal length of the blanket.
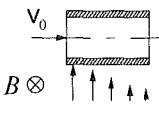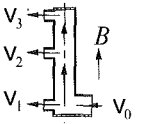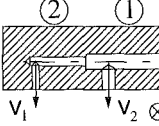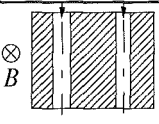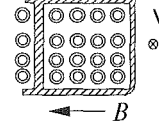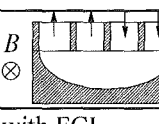
Section of MHD-flow	Geometry	a [m]	L [m]	V_0 [m/s]	M [/] $\cdot10^4$	N [/] $\cdot10^4$	c [/]	Δp WCLL ITM [MPa]	Δp WCLL DEMO [MPa]
Fringing field Inlet and Outlet	V_0, $B \otimes$	ITM 0.025 DEMO 0.138	ITM 0.85 DEMO 3.04[*1]	0.054[a] 0.001[b]	0.12[a] 0.67[b]	0.024[a] 7.171[b]	0.241[a] 0.039[b]	0.0461	0.016
Manifold and distributor	V_3, V_2, V_1, B, V_0	ITM 0.025 DEMO 0.138	0.78[a] 2.08[b]	0.054[a] 0.001[b]	0.24[a] 1.34[b]	0.096[a] 28.68[b]	0.241[a] 0.039[b]	0.1744	0.0155
Sub-distributor	② ① V_0, V_1, $V_2 \otimes B$	ITM no FCI 0.012① 0.009② ITM and FCI 0.011① 0.008② DEMO 0.012	0.74^c① 0.26^c② 0.74^c① 0.26^c② 0.85[b]	0.078^c① 0.139^c② 0.093^c① 0.176^c② 0.022[b]	0.12[a] 0.08[a] 0.11[a] 0.07[a] 0.12[b]	0.032[a] 0.014[a] 0.023[a] 0.008[a] 0.113[b]	7.03^c① 9.36^c② 0.143^c① 0.176^c② 14.85[b]	0.53① 0.37② 0.026① 0.020②	0.3457
Parallel feeding/ draining ducts	$\otimes$, B	ITM 0.009 DEMO 0.010	0.20[a] 0.42[b]	0.139[a] 0.029[b]	0.08[a] 0.10[b]	0.014[a] 0.103[b]	9.36[a] 17.82[b]	0.0560	0.2925
Breeding zone down/ upwards.	V_0, $\otimes$, $\longleftarrow B$	0.063[a] 0.080[b]	ITM 3.64 DEMO 22.00	0.001[a] 0.003[b]	0.61[a] 0.78[b]	13.09[a] 5.542[b]	0.966[a] 0.761[b]	0.0313	0.4777
Grid spacer		0.063[a] 0.080[b]	ITM 0.12 DEMO 0.20	0.001[a] 0.003[b]	0.61[a] 0.78[b]	13.09[a] 5.542[b]	c remains c_H 7.73[a] c_H 4.76[b]	0.0080	0.004
U-turn	B, $\otimes$	0.063[a] 0.080[b]	0.49[a] 0.78[b]	0.001[a] 0.003[b]	0.61[a] 0.78[b]	13.09[a] 5.542[b]	0.966[a] 0.761[b]	0.0051	0.0168
Δp_{total}	with FCI without FCI							0.317 1.222	1.1682

Table 1: Pressure drop of two different blanket types, the WCLL-ITER Test Module (ITM) [2] and the WCLL-DEMO [1]. The WCLL designs have been calculated without any electrical insulation. [a] WCLL-ITM, [b] WCLL-DEMO. [*1] Ducts to outer blanket segment, [*2] 3D pressure drop due to bends, [*3,4] rear and front channel velocity

Due to the restricted space the pipe cross section has to be small, therefore the flow velocity becomes very high. To avoid the resulting prohibitively high MHD-pressure drop an electrical insulation (at least the technique of Flow Channel Inserts (FCI)) should be foreseen.

<u>Literature:</u>

[1] Giancarli, L. et al. (1992), Water-cooled lithium-lead blanket design studies for DEMO reactor, Fusion Technology 21, 2081

[2] Fütterer, M. and Giancarli, L. (1997): Design description document (DDD) for the european water-cooled Pb-17Li test blanket module, CEA Saclay Rapport, SERMA/LCA/2125, Dec. 1997

[3] Stieglitz, R., Fiek, H.J., Schleisiek, K. Barleon, L.: MHD-Design consideration related to the EU – WCLL – Blanket Concept, Subtask A 2.1.3. Forschungszentrum Karlsruhe Interner IATF-Bericht, Jan. 99.

[4] Kast,G. (1998), Nuclear Fusion Project Annual Report of the Association Forschungszentrum Karlsruhe/Euratom, Oct. 1997-Sept.1998, FZKA 6200/EUR 18621 EN, p.116

[5] Bühler, L., (1998) MHD Flows in Thick-walled Ducts, FZKA 6066.

<u>Staff:</u>

<u>L. Barleon</u>
H. J. Fiek
K. Schleisiek
R. Stieglitz

WP A 3
Blanket Manufacturing Techniques

A 3.2
Contribution to FW Fabrication

In 1998 a design modification was elaborated which uses flow channel inserts (FCI) to reduce the MHD pressure drop in the ducts distributing/collecting the Pb-17 Li in the tube plate of the WCLL test blanket module for ITER. The FCI is a thin-walled steel tube covered with a ceramic electrical insulater. To allow the insertion of the FCI's the tube plate is split into three layers which are joined subsequently by diffusion bonding (HIP). As a first step to develop this fabrication technique a small-scale test specimen was manufactured. Ultrasonic inspection showed good quality of the diffusion weld between the tube and the enclosing plates. To verify the effectiveness of the FCI to reduce the MHD pressure drop, tests are envisaged in the GALINA facility of FZK/IKET. For these tests the test specimen was equipped with ducts for pressure drop measurements, probes for electrical potential measurement and with outer tubing. The tests are going to be performed within this year.

Another manufacturing technology developed for the HCPB blanket with potential applicability to the WCLL blanket is the bending of plates with cooling channels, in case of the WCLL circular channels or inserted tubes with an intermediate copper compliant layer to prevent crack propagation. Preliminary bending tests using either massive plates or plates with drilled holes were successfully carried out in 1998. As the next step a test plate with three cooling tubes was manufactured by diffusion welding of two half plates with semi-circular grooves and embedded tubes covered with a 0.1 mm copper layer.

After EB seal-welding the plate was exposed to a He bombing test were it showed leak tightness (10^{-4} mbar l/s) which was considered acceptable for the plate to be hipped (Fig. 1).

The plate was then HIPped at 980 °C/50 MPa. Subsequent high resolution ultrasonic inspection evidenced that no bonding was achieved during HIPping. A possible explanation is that a minor crack in one of the tubes opened during the HIP process, and pressure gas penetrated into the joining zone. To confirm this presumption, the test piece is now re-opened by dry milling for further inspection. If possible, HIPping of the plate will be repeated.

This report includes also work carried out in Oct. – Dec. 1998 under former Subtask 3.4.2.

Literature:

R. Stieglitz, L. Barleon, H.-J. Fiek, K. Schleisiek: MHD Design Considerations Related to the EU-WCLL Blanket Concept. Forschungszentrum Karlsruhe, Interner IATF-Bericht (März 1999).

S. Gordeev, T. Lechler, K. Schleisiek, H.-J. Fiek: FZK Contribution to the Development of Manufacturing Techniques for the EU-WCLL Test Blanket Module (TBM). Forschungszentrum Karlsruhe, Interner IRS-Bericht (Jan. 1999).

Staff:

H.J. Fiek, Fa. Ingenieurbüro Fiek
S. Gordeev
T. Lechler
K. Schleisiek
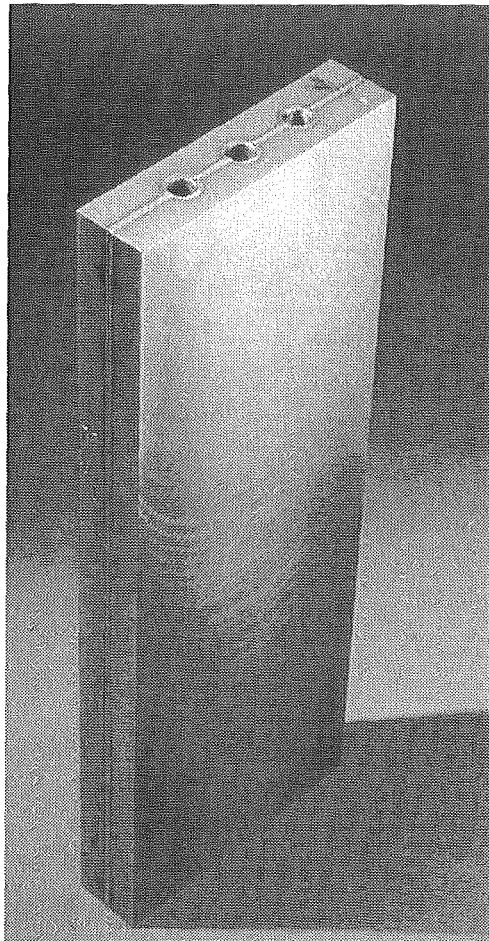
Fig. 1   Seal welded WCLL FW plate before diffusion welding in a HIP facility

WP A 4
Permeation Barrier Qualification

A 4.1.2
Fabrication and Characterisation of Permeation Barriers made by Hot-Dipping

Hot dip aluminising with subsequent heat treatment seems to be a promising coating method to fulfil the goals required for a tritium permeation barrier (TPB). In order to optimise the coating structure in view of the demands of a TPB, a suitable heat treatment has to be carried out after aluminising. During the transformation of the brittle phase Fe_2Al_5 two more ductile layers are formed: an external layer (FeAl) and an internal layer (α-Fe(Al)). The two layers are separated by a band of pores, which was formed due to the Kirkendall effect. The formation of pores should be suppressed by using high pressure during the heat treatment. If no pores would be formed during the process it is likely that the tritium permeation rate can be reduced and the mechanical properties of the system should be improved as well.

Hence, the hot dip aluminised samples were HIPped in an argon atmosphere at 5, 1000, 2000 and 3000 bar resp., the temperatures and times chosen corresponds to the instruction for austenisation and tempering for F82H-mod. steel.
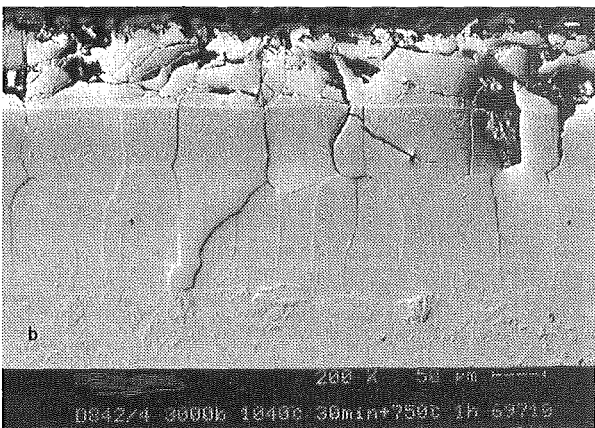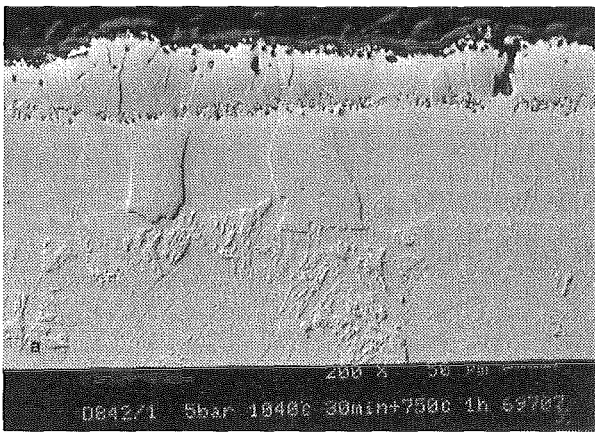
Fig.1: Cross sections of hot dip aluminised F82H-mod. sample sheets after heat treatment (1040 °C / 30 min, 750 °C / 1 h) under a) 5 bar and b) 3000 bar.

The metallographical examination shows that the superimposed pressure during the heat treatment has suppressed the forma-tion of pores (see fig. 1 a and b). Unfortunately the brittle phase Fe_2Al_5 was not completely transformed into ductile phases.

Line scan analysis shows that the heat treatment carried out at 5 bar leads to a completely transformation of the brittle Fe_2Al_5 layer into two ductile compounds: FeAl and α-Fe(Al) (fig. 2a). Samples which were heat treated at high pressure still have a brittle layer on top of the surface besides the two ductile compounds (fig. 2b). The transformation was not completed yet.
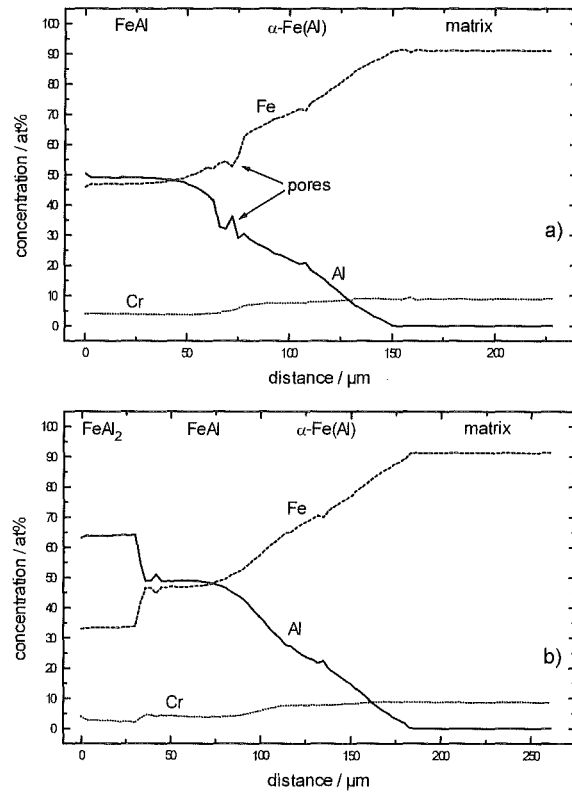
Fig. 2: EPMA line scans of hot dip aluminised F82H-mod. sample sheets after heat treatment (1040 °C / 30 min, 750 °C / 1 h) under a) 5 bar and b) 3000 bar.

The influence of the HIP process on hot dip aluminised specimens can not be neglected. Two effects were observed on the HIPped samples:

• The formation of pores were suppressed successfully.

• Fe_2Al_5 was not completely transformed into the ductile phases FeAl and α-Fe(Al).

The absence of the pores could have a positive influence on the reduction of the permeation rate. Hence, permeation measurements of HIPped samples have to be done.

Literature

[1] H. Glasbrenner, J. Konys, K. Stein-Fechner, FZK report FZKA 6353, 1999

Staff:

H. Glasbrenner
J. Konys
K. Stein-Fechner
Z. Voß
O. Wedemeyer

A 4.2.2
Permeation Reduction Factors (PRF) in Gas and Corrosion in Pb17Li

The test facility developed by FZK-HIT for measuring permeation rates of D_2 through metals under different conditions had to be moved for some reasons into another building. After calibration a first test campaign in the new location was already started in order to reproduce the results obtained before the move. Firstly, permeation rates for bare MANET sheets were measured up to 300 °C. In a second series bare F82H-mod. was tested between 250 and 500 °C.

Permeation behaviour of tritium permeation barriers (TPB) in Pb-17Li is of great interest. Hence, a special device (named Corelli) was developed and constructed in ENEA Brasimone, Italy. For this experiment we have coated a complex shaped specimen by hot dip aluminising and subsequent heat treatment.

Staff:

H. Glasbrenner
O. Wedemeyer

WP A 7
Demonstration of Blanket Reliability

A 7.1.3
Contribution to Common Blanket System Data Base

This Subtask is connected with the Tasks A 7.2.3, B 7.1.3 and B 7.2.2. All data used there will be inserted in a common data base. The use of the same data for different design options allows to limit error sources in comparative evaluations. The activity was officially terminated in December 1998. But in general, in future availability and safety analyses the completion of the common failure data base would be one of the most important activities.

A 7.2.3
TBM System Availability

The availability/unavailability of the WCLL Test Blanket Module (TBM) including the Test Blanket Auxiliary Systems (TBAS) is an important factor concerning the availability of ITER. The availability is determined by failure rates and the mean repair/exchange times (the down times for repair or exchange) of the components. There exist large uncertainties leading to different interpretations of the importance of systems and the definition of acceptable down times.

The availability/unavailability of the WCLL-test blanket system including the Pb-17Li system and the water cooling loops was analysed. The unavailabilities have been calculated for mean times to repair or exchange ranging from two to eight weeks. The overall availability varies between 96.3 and 86.2%. The influence of the test module on the overall availability is low, it is about 0.3 %.

The analysis also shows that in case of the test modules and on the background of ITER, there is space for modifications, if necessary without decreasing the availability in an unacceptable manner. Improvements in the availability seem to be possible especially in cases the results are judged to be at the limit of acceptance. The activity was terminated in December1998.

Staff:

H. Schnauder

WP A 10
MHD Effects

A 10.1.1 and 10.2.1
Evaluation of Natural Convection and
Turbulence, Natural Convection Experiments

1) Introduction

In currently investigated liquid-metal (LM) blankets for fusion reactors the LM - a lithium-lead alloy - serves mainly as breeding material [1]. The externally forced flow required for a continuous circulation of the breeding material is very weak and has within the breeding zone typically mean velocities on a scale of a few mm/s. Therefore, buoyant flow may become dominant in the whole blanket influencing heat transfer and the distribution of the concentration of the tritium generated within the liquid metal breeder [2].

Buoyant flow in breeding blankets can be caused by temperature gradients within the LM due to volumetric heating and the heat removal through the cooled walls and/or tubes. The knowledge of the velocity distribution is important for the evaluation of the heat transfer and is of special interest with respect to the concentration distribution of the tritium generated within the liquid metal [3].

In order to avoid tritium hot spots in the corner near the first wall a transport velocity of at least 10^{-6} m/s is necessary.

Out of pile experiments on natural convection of volumetric heated LM under MHD-conditions cannot be realized because any electrical heating would interact with the MHD phenomena to be investigated. Therefore we decided to restrict our experiments to the investigations of the natural convection flow between a heated and a cooled plate. With the experimental verification of numerical results reliable predictions of the flow patterns appearing in the blanket can be made.

In order to investigate the influence of the size and the direction of a magnetic field on the behaviour of natural convection three types of experimental arrangements, described in the last annual report [4] are used.

Below the experiments are reported which are conducted with the most relevant type with respect to WCLL application namely the vertical arranged box in a horizontal oriented magnetic field.

2) Experiment

A flat box test section has been operated in the superconducting solenoid magnet of the MEKKA facility at FZK [5]. This test section [4], with a heated (by 20 electrical heater rods) vertical and a cooled vertical 20 mm thick copper wall, filled with NaK, allows to operate with a heat flux of up to 15 W/cm^2 and enables Rayleigh numbers up to 10^5. The cooled wall is kept at constant temperature of about 100°C by a boiling pool of water. The other walls are of 1.5 mm stainless steel. To homogenize the boiling heat transfer a particle bed of glass spheres is used; the vapor from the boiling pool is recondensed outside the magnet. A four pole thermocouple probe (TEMPO probe) placed within the liquid metal in the center of the test section allows to measure temperature fluctuations as well as fluctuations of the local temperature gradient.

3) Theory

Additional to a 2-dimensional description shown in [4] the magnetohydrodynamic buoyant flow is investigated using full numerical simulation techniques by codes especially developed

for strong field MHD flows [6] and by using the commercial software package CFX to which electromagnetic coupling terms have been added [7]. Both approaches are compared with analytical predictions [8] to verify the numerical models. While the first numerical model is an efficient means to calculate flows in rectangular cavities, the latter one which requires larger storage and cpu time can be used for the evaluation of flows in geometries closer to engineering applications.

4) Results

In Fig. 1 a typical signal of the temperature oscillations measured with the TEMPO probe is given for a constant power of 7200 W and for different Hartmann numbers M from M = 0 to M =1600.

As long as oscillations are observed the signals of the TEMPO probe at a fixed position in the midplane indicate a fluctuation of the convection cells with a frequency of about 0.1 Hz around this position.
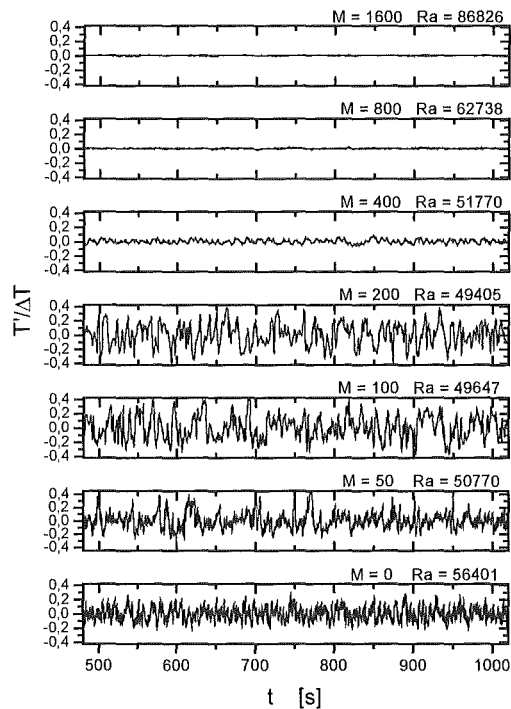
Fig. 1: Dimensionless temperature oscillations at a constant power (7200 W) and at different Hartmann numbers.
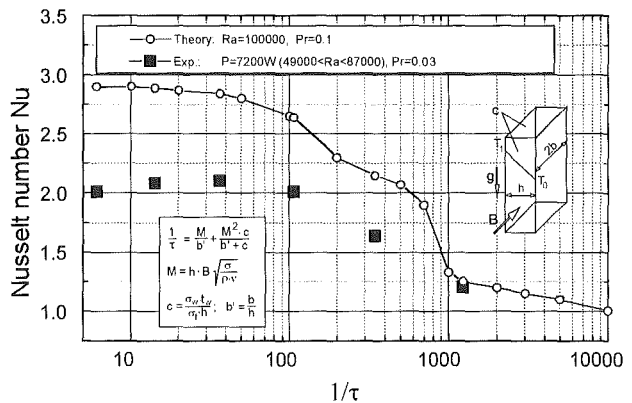
Fig. 2: Measured and theoretically predicted Nusselt number Nu as a function of the damping parameter 1/τ

In Fig. 2 the measured and theoretically (2D-calculations) predicted influence of the magnetohydrodynamic damping, expressed by the damping factor $1/\tau$, on the Nusselt number is shown.

The free convection between the heated side and the cooled side shows the expected increase of damping with increasing $1/\tau$ from 0 to 10000, corresponding to an increase of the Hartmann-number M from 0 to 1800. Therefore the Nusselt number of the heat transfer, is strongly reduced with increasing Hartmann-numbers even at Rayleigh-numbers Ra = 10^5.

5) Summary and Conclusions

The experiments on natural convection conducted in a flat vertically oriented box with a horizontal magnetic field (type c) arrangement) confirm the theoretically predicted [4] consequences of an applied magnetic field on the flow distribution and the related heat transfer.

From these experimental results, completed by the theoretical analysis, follows that under fusion relevant conditions (Hartmann numbers M $\cong$ 5000, Rayleigh numbers Ra $\leq$ $5*10^7$) the free convection of the liquid metal in flat cavities will be reduced to one big vortex for the vertical arrangement of the cavity and the corresponding heat transfer, between hot and cold plates will be by conduction only, reducing the Nusselt number to 1.

Therefore we finally conclude that natural convection under fusion blanket conditions does not play an important role in improving the heat transfer but that the residual, large scale flow within the cavity may help to avoid locally enhanced tritium permeation due to hot spots.

Literature:

[1] Giancarli, L. et al. (1992), Water-cooled lithium-lead blanket design studies for DEMO reactor, Fusion Technology 21, 2081

[6] Stieglitz, R.; Barleon, L. (1997), MHD aspects and experimental activities in fusion blanket designs, Proc. IEA Intern. Workshop on Liquid Metal Blanket Experimental Activities, Paris, France, Sept. 16-18, 1997.

[3] Barleon, L.; Burr, U.; Mack, K. J.; Müller, U. (1997) Natural Convection Phenomena in Magnetic Fields of Liquid Metal Fusion Blankets, Ref. [2]

[4] Kast, G. (1998), Nuclear Fusion Project Annual Report of the Association Forschungszentrum Karlsruhe/Euratom, Oct. 1997-Sept.1998, FZKA 6200/EUR 18621 EN, p. 121

[5] Barleon, L.; Mack, K. J.; Stieglitz, R. (1996) The MEKKA-facility, a flexible tool to investigate MHD-flow phenomena, FZKA-5821

[6] Mößner, R. 1996, Dreidimensionale numerische Simulation von Naturkonvektionsströmungen unter dem Einfluß von Magnetfeldern, FZKA 5748.

[7] DiPiazza, I. and Bühler, L. (1999), Numerical simulation of buoyant magnetohydrodynamic flows using the CFX- code, FZKA 6354.

[8] Bühler, L. (1998), Laminar buoyant magnetohydrodynamic flow in vertical rectangular ducts, Physics of Fluids, vol 10, p223.

Staff:

L. Barleon
L. Bühler
U. Burr
P. Jochmann
I. DiPiazza
K. J. Mack
R. Stieglitz

Structural Materials

SM 1.1.1
Work on OPTIFER- and F82H-mod. alloys

Structure Analysis after Irradiation

The martensitic 9 - 12% CrMoVNb steels have advantageous properties like sufficient high-temperature strength, corrosion resistance and a good thermophysical behaviour. In nuclear technology these materials have been used as wrapper and cladding for fuel elements in Fast Breeder Reactors. These materials have been exposed to neutron fluences well above 100 dpa, in the typical Fast Breeder Reactor temperature range of 380 - 630 °C, there were negligible shifts of the DBTT (ductile to brittle transition temperature) or reduction of the USE (upper shelf energy). The material was not very sensitive to He-induced high temperature embrittlement or void formation. These 9-12% CrMoVNb steels have another advantage. They are much less activated after neutron irradiation than, for example, the austenitic Cr-Ni-alloys. However, a critical effect of low temperature irradiation-induced hardening and embrittlement occurs. This negative observation was that in the fusion-relevant temperature range of 250 - 400 °C these materials exhibit a remarkable shift of DBTT towards higher temperatures. This behaviour occurs at moderate neutron fluences of only few dpa. However, it was also shown that the effect can be reduced by chemical modifications, for example, by operating with Cr-contents in the range of 9%.

For the low-activation properties the overall analysis showed that elements like Cr, V, Ta and Si as well as B and Ti can be used further without restrictions. Whereas the elements Mo, Ni and Nb have to be eliminated to very low concentrations. But these are important elements, because Mo acts as matrix hardener and Nb as a carbide forming element to control the prior austenitic grain size. For the alloys, the following proposals were made by our and other laboratories: Mo has to be substituted by W and the grain size stabilizer Nb by Ta or Ti. But further impurity elements like Ag, Eu, Tb, Ho and Bi have very low concentration limits of much less than 1 ppm. This was the basis for further variations in the chemical compositions of these types of steels and further irradiation programs.

At the Forschungszentrum Karlsruhe, Institut für Materialforschung I, different alloys have been developed based on the experience with martensitic steels. These alloys are called OPTIFER in the European Long-Term-Program for Fusion Technology and they are investigated together with a Japanese and an ORNL batch. These new OPTIFER alloys on the basis of the 7 - 10% CrWVTa have an improved fracture toughness and DBTT and tensile and creep rupture strengths that are approximately comparable with those of martensitic 9 - 12% CrMoVNb steels.

Experimental Procedure

A series of ferritic/martensitic developmental alloys have been investigated after irradiation in the HFR (Petten, Netherlands). These new 7-10%CrWVTa alloys have been optimized towards long-term activation and the properties are compared with the conventional 9-12% CrMoVNb steels. The comparison contains two alloys from FZK (OPTIFER - type), the commonly investigated IEA alloy F82H and an ORNL - 9Cr2WVTa material. The heat treatments have been optimized for the different alloys to achieve a fine grain size and optimized mechanical properties. Table 1 summarizes the heat treatments, the grain size of the former austenitic grain and the hardness.

The irradiation of impact and tensile samples was performed at the HFR (High Flux Reactor) in Petten, Netherlands, and was set to 250, 300, 350, 400 and 450 °C, for 95 FPD (Full Power Days) up to a dose of 0.8 dpa.

Table 1: Heat treatments, grain size and hardness of the alloys

Heat	Heat treatment	ASTM grain size	Hardness HV 0.4
OPTIFER Ia	1075°C30min+780°C2h	6.5	199
OPTIFER II	950°C2h+780°C2h	7.5	206
F82H	1040°C30min+750°C2h	6.5	227
ORNL 3791	1050°C30min+750°C2h	8.5	245
MANET II	965°C2h+1075°C30min +750°C2h	7.5	274

The impact tests were performed in an instrumented facility which was installed in the Hot Cells (see SM 1.2.1, MANITU). The tensile tests were performed in a static mechanical tensile testing machine with a strain rate of 1% min^{-1}. The fracture zones of the impact specimens were studied by means of SEM (Scanning Electron Microscopy) and the chemical analysis was performed by EDX (energy dispersive x-ray analysis). For the microstructural investigations TEM (Transmission Electron Microscopy) and EDX methods were used to examine the unirradiated and irradiated materials.

Results

Fracture Surface Analysis

The fracture surfaces and the microstructure of the unirradiated and irradiated impact samples at 250 and 450 °C have been investigated systematically. The fracture analysis was carried out on samples of the range of ductile to brittle transition or upper shelf. These are the samples which were strongly influenced by the irradiation, especially at the lower irradiation temperature of 250 °C.

The unirradiated samples of the upper shelves are broken completely ductile and the surfaces are covered with transgranular dimple formations. Although the unirradiated low-activation alloys have nearly the same DBTTs, the topography of the fractures was slightly different. The unirradiated OPTIFER Ia samples of the USE had very flat and large dimples in the center of the fracture. In the range of DBTT the cleavage areas of the fracture are larger. Their size corresponds to the prior austenitic grains. The ductile fracture surface of OPTIFER II (USE, T_{test} = 26 °C) (Figure 1A) is rougher in the topography than in OPTIFER Ia, but the cleavage areas have about half the diameter compared with the lath package sizes; Figure 1B.

After the irradiation at 250 °C of OPTIFER Ia, structures of grain surfaces became visible between the dimples. At the irradiation temperature of 450 °C, T_{test} = -60 °C, this effect was stronger and a clear mixed mode of inter- and transgranular brittle fracture could be seen in the range of DBTT; Figure 2A. In OPTIFER II a similar development could be observed, but in a much finer structure; Figure 2B. The measurements of the cleavage and intergranular areas are comparable again to the package size of the laths.
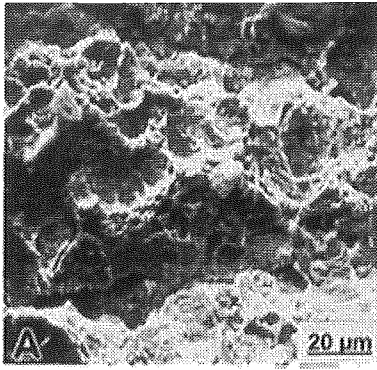
Fig. 1A: Fracture surfaces of OPTIFER II, 0 dpa: Dimple formation (T_{test} = 26 °C);

Fig. 1B: Fracture surfaces of OPTIFER II, 0 dpa: Cleavage formation (T_{test} = -60 °C)

Fig. 2A: Fracture surfaces in the range of DBTT, T_{irrad} = 450 °C, 0.8 dpa: OPTIFER Ia (T_{test} = -60 °C);

Fig. 2B: Fracture surfaces in the range of DBTT, T_{irrad} = 450 °C, 0.8 dpa: OPTIFER II (T_{test} = -20 °C)

Fig. 3A: Fracture center of ORNL 3791: 0 dpa, T_{test} = -60 °C
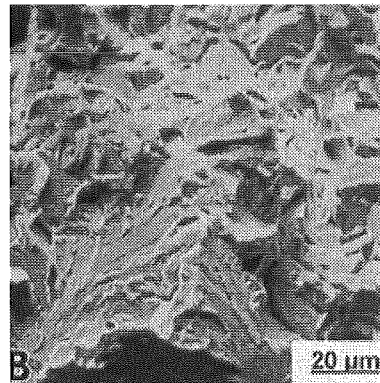
Fig. 3B: Fracture center of ORNL 3791 0.8 dpa, $T_{irrad.}$= 250 °C, T_{test} = -60 °C

The samples of F82H always have, under all material conditions, a transgranular cleavage or dimple fracture. On the ductile fracture surfaces of ORNL 3791, there was no difference between the unirradiated and irradiated material. In the brittle fractures of the unirradiated material, in the range of the DBTT, intergranular areas could be found. The cracks in the material pass the prior austenitic grain boundaries, Figure 3A. But after the irradiation at 250 °C the fracture mode changed to transgranular cleavage fracture; Figure 3B. After the irradiation at 450 °C, the typical martensitic mixed mode of cleavage areas and deep drops with dimples could be observed; Figure 3C. The fracture behavior of MANET II could be compared with the behavior of OPTIFER II under both unirradiated and irradiated conditions.

Microstructure

In the metallographic cuts no significant change could be observed in the etched structures for the different alloys and material conditions. Only by means of hardness measurements a small increase of hardness after the irradiation at 250 °C could be determined in all samples. After the irradiation at 450 °C the materials showed a small tendency to soften.
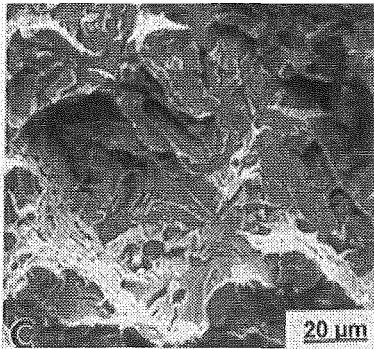
Fig. 3C: Fracture center of ORNL 3791 0.8 dpa, $T_{irrad.}=$ 450 °C, T_{test} = -30 °C
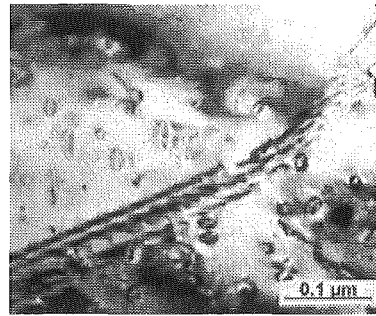
Thin foils have been investigated in the TEM in order to determine the microstructure and the irradiation effects. In the unirradiated state the typical lath structures, lath packages and the prior austenitic grains of these martensitic steels could be seen. The lath boundaries were decorated with the $M_{23}C_6$ precipitates($(Cr,Fe,V)_{23}C_6$). The precipitation concentrations were between 2.0 and 2.5 wt.%. Depending on the different alloying elements further primary carbides could be detected, e.g. TaC (OPTIFER Ia and II, F82H), WC (OPTIFER Ia), or Zr(C,N) (MANET II). In the $M_{23}C_6$ precipitates in the lath boundaries of the W-alloyed heats, W could also be found in $(Cr,Fe,V, W)_{23}C_6$. This microstructure did not change during irradiation up to 450 °C.

After the irradiation, in the matrix, in between the lath boundaries, He-bubbles, dislocation loops and α' precipitates could be found. These irradiation induced phenomena have been recorded quantitatively in all materials, irradiated at 250 and 450 °C (Tables 2-3). The highest concentration of bubbles (3.8×10^{18} cm^{-3}) and dislocation loops could be identified in OPTIFER II after the irradiation at 250 °C; Figures 4A,B. The bubbles were concentrated in the dislocations of the lath matrix. The highest concentration of the coherent α' precipitates ($\varnothing$ 2 nm) was determined in OPTIFER Ia; Figure 5. In the F82H and ORNL 3791 alloys, it was difficult to detect these He bubbles. The data in Tables 2 and 3 are the highest concentrations in e.g. one or two laths, while large areas are without any visible bubbles. That is, the bubble parameters in Tables 2 and 3 reflect local density and size distributions rather than average values and therefore should not be used to verify the overall helium concentration.
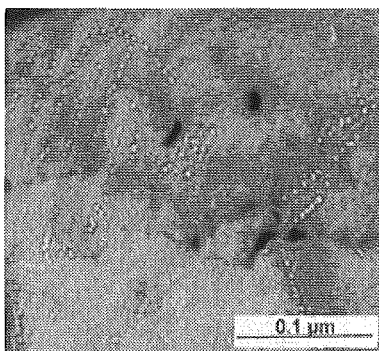
Fig. 4A: Microstructure of OPTIFER II, 0.8 dpa, $T_{irrad.}$=250 °C: He bubbles

Fig. 4B: Microstructure of OPTIFER II, 0.8 dpa, $T_{irrad.}$ = 250 °C: Dislocation loops

Fig. 5: Microstructure of OPTIFER Ia, 0.8 dpa, $T_{irrad.}$ = 250°C: Coherent α' precipitates.

At the higher irradiation temperature of 450 °C, the dislocation loops and the very fine coherent α' precipitates could not be detected, except in the matrix of the F82H. In this material a high density of fine precipitates (1.9×10^{16} cm^{-3}) has been observed. Some Fe_2W (Laves phase) could be found in the prior austenitic grain boundaries, but this phase was induced by thermal treatment. In all materials recovery with the formation of sub-grains could be determined. The observed He bubbles were fixed in the sub-grain boundaries and dislocations.

Discussion

It is an important task to reveal the reason for the embrittlement of martensitic steels under lower irradiation temperatures. These results give more information about the irradiation behavior of 8-9% Cr steels, especially the low-activation variants. An important aspect is the content of helium in these materials; Table 4. But not only the helium bubbles contribute to the strengthening of the material. Dislocation loops and α' precipitates also induce irradiation hardening by forming barriers for dislocations. Remarkable is the fact that at this low irradiation temperature of 250 °C, the three irradiation-induced defects in the material matrix - helium bubbles, dislocation loops and α' precipitates appear always in all materials.

In Table 4, the calculated helium contents and the tendencies of the mechanical properties are listed. The shift in DBTT can be compared with the results of other authors, but the low-activation alloys show a more moderate ΔDBTT/He-content behaviour, perhaps due to the lower chromium contents. The shift of the tensile properties do not show a clear dependence on the helium content or ΔDBTT. Certainly, the influence of the microstructure and the fracture development are of importance.

An important point is to find out the distribution of the boron in the material. The alloys, F82H and ORNL 3791, with the lower helium content showed an inhomogeneous distribution of helium bubbles. The main reason probably is the coarse distribution of the borides in the material. In MANET II and the OPTIFER alloys there was a high density of helium bubbles due to higher contents of boron. In previously investigated alloys, Cr-Fe-borides could be found at the triple points of the lath package boundaries. But the helium is not only produced by boron; other elements and their reactions with the neutrons contribute to this gas formation.

In any case, it was observed that higher quantities of irradiation-induced defects cause higher strengthening in the steel matrix. The highest hardness differences could be found in the alloys MANET II and OPTIFER Ia and II with the highest defect rate. In these alloys matrix strengthening was observed. The fracture modes were transcrystalline. But at a higher irradiation temperature, 450 °C, the boundaries lost their strength during the recovery of the matrix, which encouraged the mixed fracture mode, in the cleavage fracture with about 1/3 intercrystalline proportions. Interestingly, the F82H alloy had a similar behaviour. The fine irradiation-induced precipitates in the matrix perhaps influence the properties of the material. In the ORNL 3791 alloy there was the opposite behaviour. The grain boundaries strengthened during the irradiation, the material got softer and at the irradiation temperature of 450 °C, the fracture mode was like in the unirradiated state, which was seen in MANET II or the OPTIFER alloys. This material has not such a strong tendency to intergranular fractures during lower irradiation temperatures. Perhaps the higher silicon content improves this material behaviour. Silicon will not influence the carbide formation. In a solid solution it can contribute to the strengthening of the matrix. During the irradiation, the silicon could diffuse out of the matrix and could agglomerate. Softening of the matrix can occur.

The data presented are very encouraging and support the further development of these martensitic steels with low-activation properties for fusion reactors. All these results were combined with the experience of other laboratories to design a further alloy which is called EUROFER.

Literature:

[1] E. Materna-Morris, M. Rieth, K. Ehrlich: Mechanical Properties and Microstructure of HFR-Irradiated Ferritic/Martensitic Low-Activation Alloys, Effects of Radiation on Materials, 19th International Symposium, ASTM STP 1366, Seattle, USA, 1998.

[2] R. Lindau, E. Materna-Morris, L. Schafer, M. Schirra: Characterization of the Ferritic-Martensitic 8% Chromium Steel F82H-mod., 20th Symp. on Fusion Techn., Marseille, France, 1998.

[3] E. Materna-Morris, A. Möslang, R. Lindau, M. Rieth, K. Ehrlich: He-Effects on Mechanical Properties and Microstructure of RAFM Steels after Irradiation. Presentation: IEA Workshop on Reduced Activation Ferritic/Martensitic Steels. 1.-2. Nov. 1998, Petten, The Netherlands.

[4] E. Materna-Morris, M. Schirra: Variationen in den chemischen Zusammensetzungen von 8-12%Cr-Stählen und deren Einfluß auf das Bruchverhalten. 18. Tagung des DVM-Arbeitskreis „MNP": Bauteilversagen durch Mikrodefekte, S. 207-212, 24.-25. November 1998, München.

[5] H.D. Röhrig, M. Rieth, B. Daffener and E. Materna-Morris: V-Alloy Embrittlement by Irradiation in a Cooling Gas Environment. ICRFM-9, Colorado Springs, USA, 1999.

Staff:

B. Bennek-Kammerichs
B. Dafferner
K. Ehrlich
W. Kunisch
E. Materna-Morris
B. Neufang
H. Ries
M. Rieth
O. Romer

Table 2: Quantitative analysis of the irradiation effects at 250 °C					
Heat	He bubbles' size [nm]	He bubbles' density [cm⁻³]	He bubbles' location	Density of loops [cm⁻³]	Density of α' [cm⁻³]
OPTIFER Ia	2	1.5×10^{16}	D, H	5.9×10^{15}	1.0×10^{16}
OPTIFER II	3	3.8×10^{18}	D	2.6×10^{17}	2.1×10^{15}
F82H	1.5	1.4×10^{17}*	H, S, P	1.9×10^{16}	7.5×10^{15}
ORNL 3791	2	1.1×10^{15}*	D, P	1.0×10^{15}	3.5×10^{10}
MANET II	2	3.6×10^{16}	D, S, P	1.4×10^{15}	3.8×10^{15}

D = Dislocations, S = Sub-grain boundaries, P = Precipitates, H = Homogeneously distributed,

* = Maximum concentration

Table 3: Quantitative analysis of the irradiation effects at 450 °C					
Heat	He-bubbles' size [nm]	He-bubbles' density [cm^{-3}]	He-bubbles' location	Density of loops [cm^{-3}]	Density of $\alpha`$ [cm^{-3}]
OPTIFER Ia	2	5.7×10^{15}	D, S, P	-	-
OPTIFER II	6	1.2×10^{15}	D, S	-	-
F82H	3	3.7×10^{16}*	H, D	-	1.9×10^{16}
ORNL 3791	3	4.6×10^{15}*	D	-	-
MANET II	4	1.1×10^{16}	D, P	-	-

D = Dislocations, S = Sub-grain boundaries, P = Precipitates, H = Homogeneously distributed,

* = Maximum concentration

Table 4: Calculated He content after complete ^{10}B burn-up irradiation temperature and the Δ-values of the mechanical properties after $T_{irrad.}$ = 250 °C.					
	OPTIFER Ia	OPTIFER II	F82H	ORNL 3791	MANET II
max. He	60 appm	60 appm	<20 appm	<10 appm	70 appm
ΔDBTT	105	95	65	25	145
$\Delta R_{p0.2}$	83	22	39	-	-
ΔR_m	-7	-62	-35	-	-
ΔA	-7.5	-9.2	-6.2	-	-

SM 1.1.2, SM 1.2.1, SM 1.4.1, SM 1.5.2
HFR Irradiation Programs

1. HFR Phase IA

Within the former low dose irradiation program MANITU (0.2, 0.8 and 2.4 dpa) the Charpy properties of different international promising low-activation ferritic/martensitic steels had been studied. The investigations had shown that the 9Cr-2W-0.25V-0.07Ta-0.1C US-heat, referenced as 'ORNL', had yielded the lowest ductile-to-brittle transition temperatures (DBTT) in the irradiation temperature range of 250-450 °C. Compared to the ORNL steel the OPTIFER alloys showed worse DBTT values with differences of up to 120 K in the lower irradiation temperature range. This unfavourable embrittlement behaviour could be related mainly to the boron content of the OPTIFER alloys [1].

The follow-up program HFR Phase IA concentrated on the investigation of European low-activation steels (OPTIFER, OPTIMAX, BATMAN, LA12) at a fixed dose level of 2.4 dpa and at irradiation temperatures of 250/300/350/400/450 °C. But different to the MANITU irradiation program, here the OPTIFER alloys had been heat treated for optimum Charpy properties, i.e. austenitization at 900 °C for 2 hours and annealing at 780 °C (OPTIFER-Ia and II) or 750 °C (OPTIFER-IV) for half an hour.

The new results for the OPTIFER steels are shown in figure 1 in comparison with the DBTT values for ORNL heat from MANITU at 2.4 dpa.
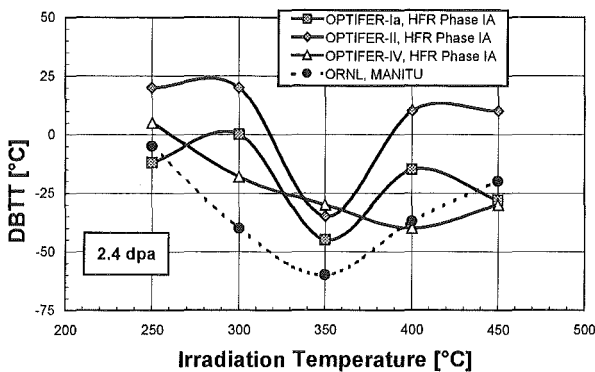
Fig. 1: Ductile-to-brittle transition temperature vs. irradiation temperature of the OPTIFER alloys with optimum heat treatment compared to the ORNL steel.

As can be clearly seen, the differences in DBTT between the OPTIFER alloys with optimum heat treatment and the ORNL heat are 60 K in the worst case. With respect to the boron content of the OPTIFER alloys (see table below) and therefore to the helium embrittlement these results show that the European fusion material development programme (from OPTIFER I through VII to EUROFER) leads to a significant improvement of the embrittlement behaviour of ferritic-martensitic low activation steels.

Alloy	Cr [%]	W [%]	V [%]	Ta [%]	B [ppm]
ORNL	8.9	2	0.23	0.06	-
OPTIFER-IV	8.5	1.2	0.23	0.15	40
OPTIFER-Ia	9.3	1	0.26	0.07	61
OPTIFER-II	9.5	(1.2 Ge)	0.28	0.02	59

Another phenomenon, which can be seen in figure 1 is the deterioration of the DBTT values for irradiation temperatures

above 350 °C. For 12Cr-NiMoV steels prior investigations (e.g. [1]) have shown a nearly complete recovery from neutron irradiation embrittlement in the temperature range from 400-450 °C. This and other comparative studies lead to the conclusion that tantalum is responsible for a principally high resistance against irradiation embrittlement on the one hand and for a slight increase of the high temperature embrittlement after irradiation on the other hand. Further considerations and examinations are discussed in detail in [2].

As an appendage to the HFR Phase IA program some specimens of the American reference alloy V-4Cr-4Ti have been used to fill the free space in the irradiation capsule. The goal was to investigate the applicability of vanadium alloys for fusion technology. Figure 2 shows the Charpy test results before and after irradiation.
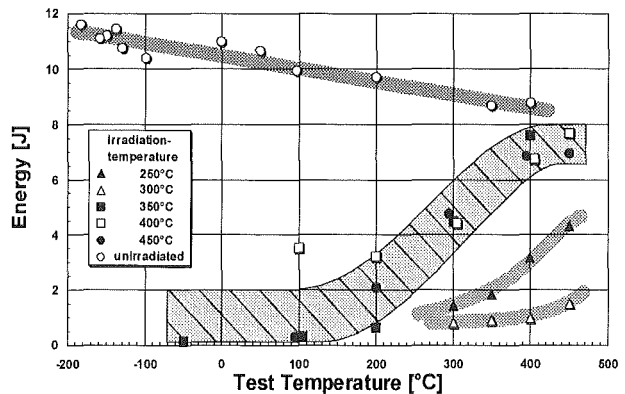
Fig. 2: Impact energy before and after irradiation to 2.4 dpa vs. test temperature.

It can be seen, that such promising results as gained with the un-irradiated material cannot be obtained after irradiation. The DBTT values at low irradiation temperatures are even worse than those for the 'ancient' MANET-I steel at higher temperatures, they seem to be influenced by chemical embrittlement due to the uptake of interstitial gases from the irradiation environment (for further details refer to [3]).

2. HFR Phase IB

A further irradiation program has been performed using the same parameters as before (irradiation temperatures from 250-450 °C, dose level of 2.4 dpa). This HFR Phase IB program concentrates mainly on technological studies. Due to a lot of transportation problems and delays the examinations will start in February 2000 instead of October 1999. The results to be expected will be:

● A study of EB and WIG weldments with F82Hmod and diffusion weldments with MANET-II.

● A characterisation of F82Hmod HIP base material and the influence of the notch root.

● The influence of different annealing treatments on the mechanical properties of OPTIFER and F82Hmod.

● Further insights for the improvement of the chemical composition (OPTIFER without boron, JLF1).

3. HFR Phase IIB (SPICE)

The lay-out of the irradiation (SPICE) in the HFR is completed. The start is due for September 2000. The design provides space for 180 Charpy, 80 tensile and 100 fatigue specimens. The

irradiation temperatures are 250/300/350/ 400/450 °C and the dose level is 15 dpa.

Literature:

[1] M. Rieth, B. Dafferner, H.-D. Röhrig, J. Nucl. Mat. 258-263 (1998) 1147-1152.

[2] R.L. Klueh, D.J. Alexander, M. Rieth, J. Nucl. Mat. 273 (1999) 146-154.

[3] H.-D. Röhrig, M. Rieth, E. Materna-Morris, B. Dafferner, ICFRM-9, October 1999, Colorado, USA.

Staff:

J. Aktaa
B. Dafferner
W. Kunisch
H. Ries
M. Rieth
O. Romer

SM 1.3.1
Correlation between Microstructure and Mechanical Properties

A stress-induced cleavage fracture model has been established to describe the microstructural effects on cleavage fracture (DBTT and toughness USE) of ferritic-martensitic 7-12%Cr steels [1,2]. Assisted by model calculations the effects of micro-structural modifications of conventional 9-12Cr1MoVNb and reduced activation 7-9CrWVTa steels by alloy composition (W, Ta, N and Cr content), austenitisation and tempering temperature as well as long term ageing (500-650°C) and irradiation-induced defect hardening ≤ 450°C with superimposed helium [3,5] generation on DBTT and toughness shift has been analysed [2]. Additionally, the effect of irradiation and microstructure on the shape of ductile-brittle transition [4] and the correlation between DBTT and long time creep rupture strength was considered. Supported by this study, the possibilities of further optimisation of these steels are discussed through variation of alloy composition and the use of proper thermomechanical heat treatments to improve impact properties at comparably high creep strength [4]. In the following the main results regarding neutron irradiation effects are presented.

1. Dynamic fracture model

In accordance with experimental observations the dynamic embrittlement transition of 21/4-12Cr steels is caused by stress-induced multiple micro-cracking ahead the crack tip which suppress the ductile rupture process [1,2]. Cleavage fracture by unstable micro-crack propagation is assumed to occur if the maximum principle stress at a characteristic distance ahead of the crack tip exceeds a critical value. Taking into account the sample geometry-dependent stress intensity, this description corresponds to a condition where locally the material strength σ_{c^*} at a critical strain ε^* to nucleate a micro-crack of critical length l^* is larger than the dynamic fracture stress σ_f^*. Thus the condition $\sigma_{c^*} \geq \sigma_f^*$ describes the regime of cleavage fracture below DBTT. The micro-crack nucleation develops primarily at larger precipitates ($M_{23}C_6$, M_6C, intermetallic phases) and lath or primary austenite grain boundaries by stress-induced debonding of interphases. In accordance with the Griffith's criterion, the fracture stress can be written as $\sigma_f^* = (4\ E\ \gamma_{eff}/\ l^*\ \pi)^{0.5}$, where E(T) is the Young's modulus and γ_{eff} the effective interface energy dependent on plastic deformation and critical micro-crack length l^*. The fracture stress depends via the parameters l^* and γ_{eff} strongly on the microstructure. The flow strength $\sigma_{c^*} = \sigma_0\ (\varepsilon^*) + \sigma_e(T, \dot{\varepsilon})$ can be described by the superposition of the athermal strength $\sigma_0(\varepsilon^*)$ and the temperature dependent thermally activated component $\sigma_e(T, \dot{\varepsilon}) = P\ \exp\ (-\ \beta_d\ T)$. The parameter $\beta_d(\dot{\varepsilon}) = (\beta_0 - \beta_1\ \ln\dot{\varepsilon})$ describes the temperature and strain rate ($\dot{\varepsilon}$) behaviour by the constants β_0, β_1, and P is the maximum thermal flow stress (Peierls stress) at T=0. With these expressions the relative shift $\Delta DBTT/DBTT_0$, induced by microstructural changes can be described by [1,5] eq. 1

$$\frac{\Delta DBTT}{DBTT_0} = \frac{K_d}{P}\left[\left(\Delta\sigma_0\left(\varepsilon^x\right) - \Delta\sigma_f^x\right) + \left(\sigma_f^x - \sigma_0\right)\frac{\Delta P}{P}\right] - \frac{\Delta\beta_d}{\beta_d}$$

(1)

whereby parameter $K_d(\beta_d) \geq e$ and $\Delta > 0$ yields for an increase. The function $K_d(\beta_d, DBTT_0)$ shows a broad minimum at $DBTT_0 = 1/\beta_d$ for $K_d = e$, which can be used as good approximation for ferritic-martensitic 21/4-12Cr steels (i.e. $DBTT_0 = 200$ K, $\beta_d = 0.005$). In eq.1 the first term describes the effect of a change in athermal plateau strength $\Delta\sigma_0$ and local fracture stress $\Delta\sigma_f^*$ on the relative $\Delta DBTT$ shift. The second and third term describe the additional influence of a change in thermally activated strength component either by a change in Peierls stress, ΔP,

and/or $\Delta\beta_d$ respectively strain rate sensitivity $m = \delta\ln\sigma_e/\delta\ln\varepsilon = \beta_1 T$, because for $\beta_0 = $ constant it yields:

$$\frac{\Delta\beta_d}{\beta_d} = \frac{\Delta\beta_1\ \ln\dot{\varepsilon}}{\beta_d} = \frac{\Delta m}{T\beta_d}$$

(2)

The change $\Delta\beta_d/\beta_d$ is related to the activation volume of deformation $A_v = k\ T/\ \sigma_e\ m$ by $\Delta\beta_d/\beta_d = -\ m/(T\ \beta_d)\ \Delta A_v/A_v$. The relation eq.1 remains independent on sample geometry if the fracture mechanism and work hardening don't change drastically. It demonstrates, that the absolute shift $\Delta DBTT$ depends besides the initial value $DBTT_0$ on superimposed changes of $\Delta\sigma_0$, $\Delta\sigma_f^*$, $\Delta P/P$ and Δm, $\Delta\beta_d(\Delta\beta_1, \Delta\varepsilon)$ which are affected by alloy composition, heat treatment and irradiation.

The fracture stress in accordance with the Griffith's criterion depends on micro-structure beside the effective surface energy γ_{eff}, which can be influenced by crack-tip plasticity and impurity segregation to fracture surfaces mainly on the critical micro-crack length $l^*(dk, dp)$. It is also strongly affected by the prior austenitic grain size dK as well as on the size dP as well as the volume content and distribution of the coarser precipitates involved in the micro-crack nucleation process. With the assumptions that $l^* = x\ dp$ and $l^* = y\ dK$, the fracture stress can be approximated by

$$\sigma_f^* \cong k_{f,g}/\left(d_K\right)^{1/2} + k_{f,p}/\left(d_p\right)^{1/2}\ \text{with}$$

$$k_{f,p} = \left(4E\gamma_{eff}/x\right)^{1/2}$$

(3)

whereby the parameters $k_{f,p}$ and $k_{f,g} = f(\gamma_{eff}, x, y, E)$ via x, y depend via x>>1, y≤dK on precipitate morphology and grain distribution. It is related to fracture toughness by $K_c = \sigma_f^*\ (\pi\ l^*/2)^{1/2} = (2\ \gamma_{eff}\ E)^{1/2}$ which decreases with decreasing crack-tip plasticity γ_{eff}. For $l^* = $ const. because $\Delta\sigma_f^* \propto \Delta K_c$ the $\Delta DBTT$ shift is related to toughness shift ΔK_c by eq.1. Since $\sigma_f^* = \sigma_c + \Delta\sigma_c^*$, the critical yield stress σ_c at DBTT describes mainly cleavage fracture stress and micro-crack nucleation behaviour. Taking into account also stress-induced ductile rupture appearance, $\sigma_{f,d}$, and parabolic strain hardening $\Delta\sigma_c \propto (\varepsilon)^{0.5}$ with the work to fracture $w_d = S\sigma(\varepsilon)\ d\varepsilon$ and the approximation for its change $\Delta w_d/w_d \approx \Delta USE/USE_0$, the correlation between DBTT and Upper Shelf Energy (USE) shifts can approximated by

$$\frac{\Delta DBTT}{DBTT_0} \cong -\alpha\frac{\sigma_{f,d}}{P}\frac{\Delta USE}{USE_0}$$

(4)

where the parameter $\alpha(\sigma_0) \leq 1$ depends weakly on σ_0; the normalized shift $\Delta DBTT/DBTT_0$ increases nearly linearly with increasing toughness reduction $-\Delta USE/USE_0 = V$. The slope $\alpha\ \sigma_{f,d}/P \geq 1$ increases especially with increasing ductile fracture stress $\sigma_{f,d}$ and decreasing Peierls stress P.

1.1 Irradiation hardening and helium effects

The irradiation-induced hardening is given by the additive contributions

$$\Delta\sigma_i = \Delta\sigma_{a,i} + \Delta\sigma_{a,He} + \Delta\sigma_{e,i}$$

(5)

of larger athermal defects $\Delta\sigma_{a,i}$ like loops, incoherent and coherent precipitates above the shearable limit $d_p \geq d_{c,s}$ as well as helium bubbles $\Delta\sigma_{a,He}$ of larger size $d_{He} \geq d_{c,s}$ and additionally thermally activated defect clusters $\Delta\sigma_{e,i}$ (vacancies, interstitials,

helium) of size below $d_{c,s}$. Thermal stress changes dependent on deformation mechanism may be caused by a change in the Peierls stress, ΔP, or activation volume $A_v = k\ T/\ \sigma_e$ m respectively strain rate sensitivity $m = \delta ln\sigma_e/\delta ln\varepsilon$, more pronounced at higher $DBTT_0$ and thus stronger athermal strengthening. Allowing an additional change in fracture stress $\Delta\sigma_f^*$, the irradiation-induced shift $\Delta DBTT/DBTT_0$ according eq.1 can be written as

$$\frac{\Delta DBTT}{DBTT_0} = \frac{K_d}{P}\left[\Delta\sigma_{a,i} - \Delta\sigma_f^* + \Delta\sigma_{a,He}\right] - \frac{\Delta\beta_{d,i}}{\beta_d} \quad (6)$$

where $\Delta\beta_{d,i}/\beta_d = \Delta m_i\ /\ T\ \beta_d = -m/\ T\ \beta_d\ \Delta A_{v,i}/A_v$ is affected by irradiation-induced thermal defect strengthening via changes in activation volume or strain rate sensitivity, Δm_i.

For doses below saturation ($\leq$ 5dpa for 7-12Cr steels) the irradiation-induced defect hardening can well be described by $\Delta\sigma_{a,i} \cong k_i\ (dpa)^x$ with x = 0.25 to 0.5, whereby above 0.1 displacements per atoms (dpa) x approaches to 0.5. The athermal hardening by helium bubbles is given by $\Delta\sigma_{a,He} \cong k_{He}\ (c\ C_{He})^{0.5}/\ d_{He}$ according to the Orowan by-pass mechanism. Here, c C_{He} is the helium concentration inside the bubbles of mean diameter d_{He}, which fraction c of total content C_{He} and k_i, k_{He} are temperature-dependent constants influenced by the shear modulus and Burgers vector. A change in fracture stress $\Delta\sigma_{f,i}^* = \Delta\sigma_{f,d}^* - \Delta\sigma_{f,He}^*$ may result from helium, $\Delta\sigma_{f,He}^*$, and defect generation, $\Delta\sigma_{f,d}^*$, via a change of micro-crack nucleation stress. Helium segregation to fracture relevant surfaces reduces fracture stress by the reduction of crack-tip plasticity and γ_{eff} which might be expressed by $-\Delta\sigma_{f,He}^* = k_{f,He}\ (z\ C_{He})^y$ with $y \cong 0.5$ and the constant $k_{f,He}$, whereby z is the fraction of helium at fracture surfaces. By irradiation-induced hardening of the matrix the local interphacial stresses/strains at coarse precipitates might be reduced additionally giving an increase in σ_f^*. With these assumptions eq. 1 becomes

$$\frac{\Delta DBTT}{DBTT_0} = \frac{K_d k_i}{P} S (dpa)^y - \frac{\Delta m_i}{T\beta_d}$$

$$S = \left[1 + k^* \frac{(C_{He})^{1/2}}{(dpa)^y} + \frac{\Delta\sigma_{f,d}^*}{\Delta\sigma_{a,i}} + \frac{(\sigma_f^* - \sigma_0)\Delta P}{\Delta\sigma_{a,i}P}\right] \quad (7)$$

whereby $-\Delta m_i/T\ \beta_d$ is affected by small defect clusters containing fraction $c \cdot C_{He}$ of helium and $k^* = k_{f,He}\ z^y/k_i$ is a constant. Allowing an additional irradiation-induced decrease in strain rate sensitivity via $\Delta m_i \approx (dpa\ c\ C_{He})^{1/2}$, the radiation-induced shift $\Delta DBTT/DBTT_0$ of 7-12Cr steels within the regime of defect hardening $\leq$ 450°C should increase at lower doses with $(dpa)^y$ and $(C_{He})^{0.5}$ until saturation is achieved. The slope $\Delta DBTT/DBTT_0$ vs. $(dpa)^{1/2}$ depends mainly on the ratio $K_d k_i/P$ but also in multiactive way via the bracket and strain rate sensitivity term in eq.2 on the distribution of helium in clusters c, bubbles b, fracture surface z and other defects o, whereby $c+b+z+o=1$. For 7-12Cr steels at higher doses above 5 dpa irradiation strengthening $\Delta\sigma_{a,i} + \Delta\sigma_{a,He}$ mostly saturates and thermal cluster strengthening might convert to athermal ones by progressive defect growth. Thus in absence of an irradiation-induced coherent precipitate formation $\Delta\beta_{d,i}/\beta_d$ should go through a maximum with increasing dose and then approaches asymtotically to $\to$0.

2. Experimental results on neutron irradiation effects on dynamic embrittlement and comparison with model predictions

As shown in Fig. 1a of [1], the shift $\Delta DBTT/DBTT_0$ increases with increasing $(dpa)^{0.5}$ for the conventional 9-11Cr1MoVNb steel MANET-I and for the reduced activation 7,6-9,3Cr($\leq$2)WVTa steels by neutron irradiation in the HFR at 300°C to higher doses $\leq$ 15 dpa. The MANET-I steel, where a greater amount of $\leq$ 85 appm He was formed by [10] B transmutation below $\approx$ 1 dpa shows the strongest shift and reaches at 5 dpa with $\Delta DBTT/DBTT_0 \leq$1.1 nearly saturation. From the observed slope $k_s = k_i\ K_d/P = 0.607(dpa)^{-0.5}$ the hardening coefficient $k_i = 250.5$ MPa/$(dpa)^{0.5}$ has been calculated with the values P= 1322 MPa and K_d=3.204 as derived In comparison the 7-9Cr($\leq$2)WVTa but also the 9Cr1MoVNb steels mainly due to reduced athermal irradiation hardening much smaller irradiation induced embrittlement shifts. With $\Delta DBTT/DBTT_0 \leq$ 0.3 for $\leq$ 2.4 dpa, the 2W- 0.018Ta steel F82H has the most favourable properties and k_s amounts to only 0.208(dpa)$^{-0.5}$ which yields a coefficient k_i= 85 MPa(dpa)$^{-0.5}$ for P= 1118 MPa and K_d= 2.737 estimated. The irradiation strengthening of 7-12Cr steels as found by TEM examinations is caused by small dislocation loops, clusters and He-bubbles
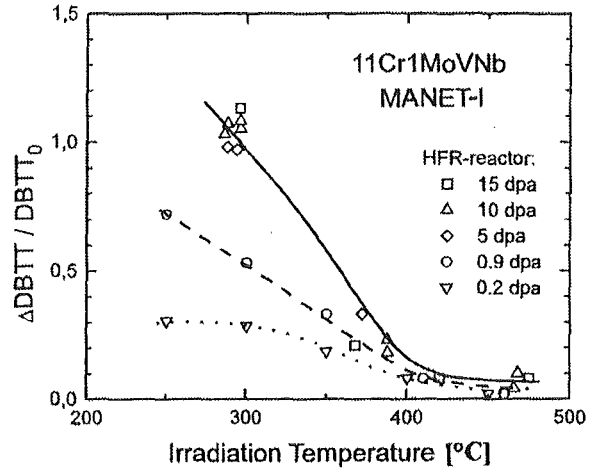
Fig. 1: Shift $\Delta DBTT/DBTT_0$ of 11Cr1MoVNb - MANET-I steel in dependence of irradiation temperature.

By various published results it is shown that helium contributes only weakly to hardening above 350°C, but in combination with a decrease in work hardening below 350°C has an stronger effect by enhanced nucleation of shearable defect clusters. Fig. 1 shows for the MANET-I steel the observed influence of the irradiation temperature T_i (250-480°C) on $\Delta DBTT/DBTT_0$ shift after neutron irradiation to different doses. Obviously, the embrittlement shift in accordance with irradiation hardening $\Delta\sigma_i$ decreases sensitively with increasing irradiation temperature by defect recovery and growth, more pronounced for the saturation region at higher doses. It achieves with $\leq$ 0.1 small values above around 400°C, where normally the transition from irradiation hardening to softening in martensitic 7-12Cr steels occurs.Though, helium production is completed at $\leq$1dpa embrittlement still increases distinctly and does not saturate at lower irradiation temperatures $T_i \leq$ 250°C above 0.2 dpa. These observations show that primarily irradiation defect hardening causes dynamic embrittlement shift and to lesser extent helium by a possible reduction of the fracture stress below 450°C. However, helium contributes to thermally strengthening below 350°C by enhanced nucleation of small defect clusters and thus additionally changes strain rate sensivity and/or Peierls

stress. For most 21/4-12 Cr steels irradiated to $\leq$ 23 dpa at 300-459°C a clear tendency of saturation in V shift above 5 dpa is visible as found for MANET-I at T_I=300°C and 5-15 dpa. But in certain steels like 21/4Cr2W, 5Cr2WV shift V go through a weak maximum possibly mainly due to the observed weak softening in tensile tests at higher dpa. Fig.2 shows the irradiation temperature dependence of shift V for various unstabilized and $Ta_,(Nb),V$ stabilized 7-12Cr steels with $\approx$0.1C at higher temperatures 365-550°C and doses 2.3-116 dpa. It demonstrates, that after going through a minimum an increase in V shift appears torwards higher temperatures. That results from an irradiation-enhanced ageing (IEA) process either by growth of precipitate and/or new precipitate formation, which reduces dynamic fracture stress and might change hardening too. It is of interest, that the increase in $V(T_I)$ of about 0.3-0.4 for the irradiated steels 9CrWVTa at 365-450°C and unstabilized 8.8Cr1MoMnSiNi0.11C (EM10) at 470-550°C is similar as the at 550-650°C, $\leq$ 8760 h thermally aged $F82H_{mod}$ steel, where the coarse (200 nm) intermetallic Laves phase $(Fe,Cr)_2W$ at lath boundaries appears. In the irradiated 5Cr2WV steel M_7C_6 carbides form at 350-400°C, which increases $V\leq$ 1. Fig.3 shows for different 7-11Cr steels the correlation between the $\Delta DBTT/DBTT_0$ and ductile toughness shift -$\Delta USE/USE_0$ observed at constant 2.4 dpa between 250 and 450°C. According to the model, the normalized shift $\Delta DBTT/DBTT_0$ increases with increasing reduction in toughness -$\Delta USE/USE_0$ by slopes equal or greater than 1. The conventional MANET-I,II steels show at lower slope and the largest shift in DBTT ($V\leq$1.1) and USE ($U\leq$0.5). On the other hand the 7-9CrWVTa steels similar to the conventional 9Cr1MoVNb steel with reduced chromium content show at larger slopes > 1, improved toughness with distinct smaller relative $\Delta DBTT$ and -ΔUSE shifts. Here the smallest values has again with -$\Delta USE/USE_0$ $\leq$ 0.2 and $\Delta DBTT/DBTT_0$ $\leq$ 0.56 the 7,6Cr2WVTa steel F82H. These differences mainly reflect the existing higher ductile fracture stresses of martensitic 7-9Cr steels together with weaker irradiation hardening. For all steels at lower T_I=250°C always V > U.

Fig. 2: Irradiation temperature dependency of $\Delta DBTT/DBTT_0$ shift for various 7-12Cr steels with $\approx$ 0.1 C at higher temperatures (365-550°C) and 2.3 - 116 dpa. Additionally data for 550-650°C thermally aged steel $F82H_{mod}$ are indicated.

2.1 Dynamic fracture stress

Fig. 4 shows the influence of irradiation temperature (250-450°C, HFR) upon dynamic irradiation hardening $\Delta\sigma_{i,0°C}$, upon the critical fracture stress $\sigma_c = \sigma_{y,DBTT}$ and the embrittlement shift V for the conventional 11Cr1MoVNb (MANET-II) steel, for 0.2 dpa. By using that and derived P, β_{d_i} K_d data from the dependence $DBTT(\sigma_{y,dyn})$, the shift V is also compared with

model predictions. The steels MANET-I and II show a quite similar behaviour: A weak irradiation-induced increase of σ_c at higher T_I, a continuous decrease in dynamic irradiation hardening $\Delta\sigma_{i,0°C} \leq$ 170 MPa and $V\leq$ 0.31 shift with decreasing T_I, which is well described by model. Against MANET-II the behaviour of the 0.08Ta-0.02 N stabilized 7,6Cr1WVTa steel Opt.Ia is different. Again at the lower T_I the critical fracture stresses for irradiated material is larger than for the unirradiated ones. Against Opt.Ia, the higher 2W containing steels F82H, ORNL show distinctly higher σ_c and weaker dynamic irradiation hardening at similar P, σ_0 values and thus smaller embrittlement shifts in agreement to predictions. At the highest T_I= 450°C, a weak decrease in fracture stress σ_c becomes visible in both

Fig. 3: The correlation $\Delta DBTT/DBTT_0$ vs. - $\Delta USE/USE_0$ for various 7-12Cr steels following neutron irradiation at 250 to 450°C

Fig. 4: The influence of irradiation temperature (250-450°C, HFR) upon irradiation hardening $\Delta\sigma_{i,-50°C}$, fracture stress σ_c and shift V of 11Cr1MoVNb (MANET-II)

Optifer Ia and 2W steels F82H, ORNL, which might be indicate already the IEA effect with the onset of irradiation-enhanced Laves phase formation. Additionally, for all W-Ta steels the remaining dynamical hardening $\Delta\sigma_i$ = 40-105 MPa observed at 450°C is higher in Opt.Ia steel, indicating possibly fine MC

carbide precipitations by the IEA process. For thermally ageing condition at 500-650°C this steel shows compared to others no ageing-induced softening. In Fig.5, the dynamic critical fracture stress data σ_c are plotted against the measured dynamical stresses σ_0 + $\Delta\sigma_{i,-50°C}$ for various conventional and reduced activation 7-11 Cr steels in unirradiated and at 0.2 dpa, 250-450°C irradiated states. As shown, there is a clear trend to increase fracture stress σ_c with increasing strengthening ranging between 662 to 995 MPa, particularly for the low irradiation temperature 250°C, where defect clusters form predominantly. The reduced activation 7-9CrWVTa steels, especially the higher 2W containing steels F82H, ORNL show for a lower athermal plateau stress σ_0 due to enhanced recovery and higher A_{c1b} temperatures against 9-11CrMoVNb steels distinctly higher fracture stresses σ_c and a stronger hardening-induced increase. Otherwise, the conventional steels MANET-I,II, exept of K-heat show quite larger irradiation hardening σ_0 + $\Delta\sigma_{i,-50°C}$ but lower fracture stresses σ_c. Furthermore, the 9Cr1,2GeVTa steel Optifer II (σ_c=662-773 MPa) shows at larger stresses σ_0 + $\Delta\sigma_{i,-50°C}$ the lowest σ_c values at the higher T_i=450°C. These low fracture stresses result from the coarse GeO, Al_2O_3 oxydes formed on prior austenitic grain boundaries by the desoxydation process. Probably, by irradiation defect formation the local interphase stresses are increased at these particles under dynamic loadings. The higher fracture stress of W-Ta containing 7-9Cr2WVTa steels may be explained by the stronger W- enrichment in semi-coherent $(Fe,W)_{23}C_6$ precipitates which develops further during creep exposure by diffusion of W to grain boundaries. Tungsten segregation to grain boundaries gives rise finally to brittle intermetallic Laves-phase formation in the 2W steel F82H$_{mod}$.
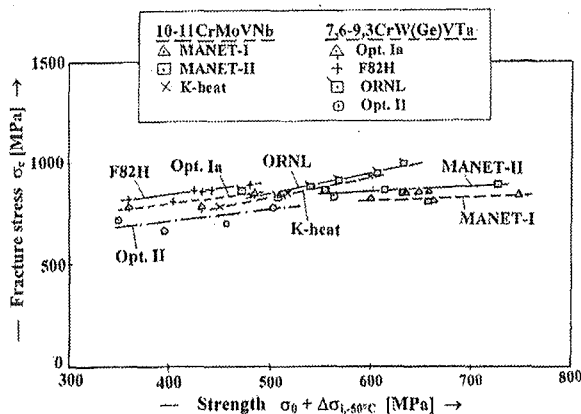
Fig. 5: Correlation between dynamical fracture stress σ_c and hardening σ_0 + $\Delta\sigma_{i,-50°C}$ for various unirradiated and in HFR irradiated 7-11Cr steels at 0.2 dpa, 250-450°C

3. Conclusions

The irradiation-induced increase in $\Delta DBTT/DBTT_0$ shift of V≤1.2 for 21/4-12Cr steels in accordance to model predictions can be primarily described by superposition of strong athermally and thermally activated defect hardening at lower (T_i≤ 400°C) and comparably weaker embrittlement through reduction in fracture stress by irradiation-enhanced ageing with carbide coarsening and/or new precipitate formation at higher temperatures. It can be assisted eventually by He-bubble decoration at fracture surfaces. The main results are:

i) Embrittlement shift V increases with increasing dose with $(dpa)^{0.5}$ and decreases with temperature T_i within the hardening region below 450°C. It is stronger for 12Cr1MoVNb- (V≤1.1),

12CrWV (V≤1.2) and bainitic 21/4Cr (V≤1.2) steels. For most steels saturation of embrittlement appears above 5 dpa.

ii) The 7-9Cr(1-2)WV(≤0.15)Ta and 9Cr1MoVNb steels show in comparison to conventional 12Cr1MoVNb steels lower embrittlement V and toughness shifts U=-$\Delta USE/USE$ due to their higher fracture stress and weaker irradiation hardening, less compensated by their higher strain rate sensitivity. For most 7-12Cr steels fracture stress increases weakly with irradiation hardening, whereas strain rate sensitivity is decreased particularly at the lower T_i=250°C, where thermal defects are generated.

iii) Some steels go through a minimum in V≤0.23 around 450°C; DBTT shift V increases again with increasing irradiation temperature as expected from an irradiation-enhanced ageing effect. For higher 2W containing steels like F82H this occurs by an irradiation-enhanced Laves phase formation giving rise to V≤0.3.

iv) Helium might contribute to dynamic embrittlement mainly below 350°C by enhanced thermal hardening and to a lesser extend by a reduction in fracture stress above 350°C.

v) Between $\Delta DBTT/DBTT_0$ and toughness shift -$\Delta USE/USE_0$ there exists a correlation, whereby V>U particularly at higher temperatures 393-420°C and fluences due to an irradiation-enhanced ageing process.

Literature:

[1] D. Preininger, "Charakterisierung des Gefügeeinflusses auf den Srödbruchübergang von ferritisch-martensitischen 7-12%Cr Stählen". Proceedings. of Materials Week'98, Vol. III, March (1999) p.87-92, ISBN-3-527-29940-8, Wiley - VCH.

[2] D. Preininger , „Effect of microstructure on the ductile to brittle transition of ferritic-martensitic 7-12%Cr steels". Proceedings of Intern. Conference STAINLESS STEELS'99, Chia Laguna Sardinia, Italy, 6-9.June 1999, AIM. Vol.2: Innovation in Processes and Products, p.87-96, I- Milano, Associazione Italiano di Metallurgia, ISBN 88-85298-34-6.

[3] R. Lindau, A. Möslang, D. Preininger, M. Rieth, H.D. Röhrig; J. Nucl. Materials 271&272 (1999) p.450-454. „Influence of helium on impact properties of reduced-activation ferritic/martensitic Cr- steels"

[4] D. Preininger; „Characterisation of microstructural effcts on the ductile to brittle transition of 9-12CrMoVNb and 7.9CrWVTa steels", ICFRM-9, Oct.(1999) Colorado Springs.

[5] D. Preininger ; „ Modelling of irradiation damage and helium effects on the dynamic embrittlement of 7-12Cr steels" ICFRM-9, Oct. (1999) Colorado Springs.

[6] G.R. Odette and D. Preininger; Invited paper: „A unified model of fracture toughness of steels in the transition region; ICFRM-9, Oct. (1999) Colorado Springs.

Staff:

D. Preininger

SM 1.5.1
Lower Temperature and Low Dose Irradiation

1. Introduction

The knowledge of fracture mechanisms is important to qualify the method of the so-called "Local Approach". With respect to global failure criteria this mechanism-based fracture description is combined with a numerical stress analysis. Limitations of the local approach originate from different fracture mechanisms. Therefore it should be verified with materials data of irradiated notched and/or precracked samples for real application in a DEMO-blanket design. From a low temperature low dose irradiation those specific materials data will be obtained.

2. Irradiation facility

During a first negotiation with the Central Research Institute for Structural Materials (CRISM) "Prometey", in St. Petersburg, about the possibility of a low temperature low dose irradiation it was agreed in a joint memorandum to define a proposal for the realization of an irradiation in an WWR-M type materials testing reactor.

The conditions for irradiation and postirradiation testing should be:

- Irradiation of precracked and/or notched specimens of RAF/M materials, like F82H mod., in the WWR-M-reactor at a temperature between 70 to 300° C (to be defined) up to a damage of 2 dpa.

- The postirradiation tensile tests between - 150° C and 300° C together with scanning electron microscopy of the crack appearance, should be performed in the hot cells of CRISM "Prometey".

3. State of the art

As a result of the joint discussion the following actions were agreed:

- CRISM "Prometey" prepares the temperature controlled He-loop including neutron monitoring.

- FZK determines the shape and quantity of samples to be irradiated, the parameter field of the postirradiation tensile tests, i.e. temperatures and strain rates and the amount of microstructural examinations.

Staff:

C. Petersen
D. Rodrian
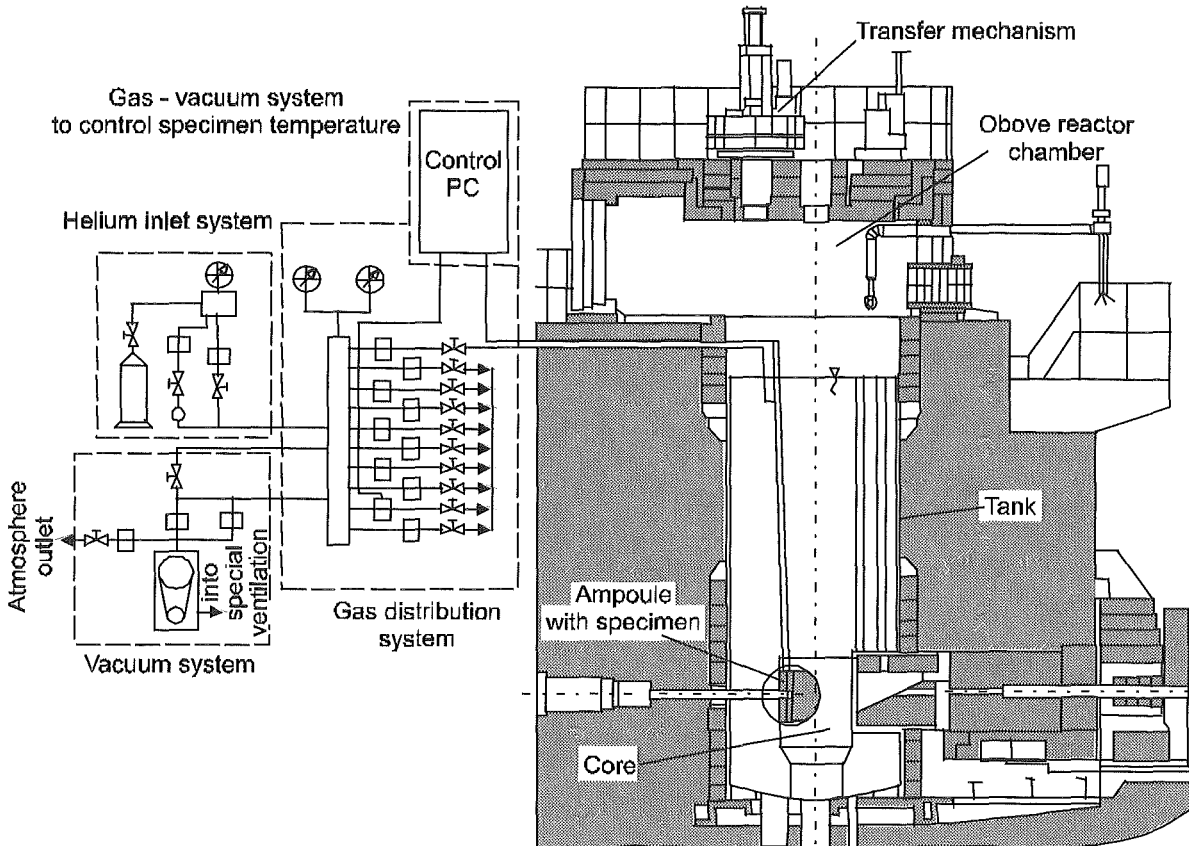
Fig. 1: Vertical cross section of the WWR-M-reactor with the gas-vacuum system to control specimens temperature

SM 2.1.1 and SM 2.2.3
Metallurgical and Mechanical Characterization of RAFM Steels

Material Development

In the frame of the European Technology Program the Japanese steel F82H-mod. is being investigated parallel to the European steel OPTIFER. The Optifer-steel group is completed by 2 batches with and without Boron, to investigate the influence of irradiation on He-formation.

Work on F82H-mod.

The characterization work of the physical/mechanical properties is finished and documented. Both, in the reference condition and after ageing treatments, minimum values for tensile- and creep-behaviour are available up to the design limit of 550°C – 20 000 h ([1-5] and Annual Report 97/98).

Work on OPTIFER

The shorttime work (tensile and toughness tests) are finished and documented ([6,7] and Annual Report 97/98). The longtime tests to quantify the creep behaviour, inclusive of ageing behaviour and temperature transients, are experimentally finished. The ageing behaviour over the maximum design range (550°C - 20 000h) can be described by the Hollomon-Jaffe-parameter $P=T_K$ (18+log t). This means, ageing treatments (550°C - 3300 h or 600°C - 1050 h) are equivalent for 550°C 20 000 h [7]. The influence of different parameters (T/t-combinations) on tensile-, creep- and Charpy-tests is described.

A main point of the activities on OPTIFER and F82H-mod. was the influence of different ageing treatments and variations of T/t-combination by the Hollomon-Jaffe-parameter ($P=T_K$ (c+log t)). The influence of the toughness characteristics after different ageing treatments for two LA steels is given in table 1.

Table 1: Toughness characteristics from Charpy-V-tests

Alloy heat	Heat-treatment		FATT[1] °C	DBTT[2] °C	68 J °C
OPTIFER-IVc(W) 986778	homog.950°2h/l+ 1075°30'/L+750°2h/L (Ref. I) 950°30'/L+750°2h/L (Ref. II)		-46 -57	-60 -72	-66 -82
"	Ref.I+550°-5000h	P=17,86	-37	-43	-45
"	Ref.I+580°-3300h	P=18,36	-35	-50	-52
"	Ref.I+600°-1050h	P=18,36			
"	Ref.I+600°-5000h	P=18,94	-41	-43	-45
"	Ref.I+625°-1250h	P=18,94	-34	-41	-45
"	Ref.I+650°-330h	P=18,94	-38	-51	-53
"	Ref.I+625°-5000	P=19,49	-36	-45	-54
"	Ref.II+550°-5000h		-65	-87	-92
"	Ref.II+600°-5000h		-51	-69	-82
F82H-mod(2W) 9741-Platte 3-8	960°30'/L+750°2h/L		-	-35	-
"	1040°38'+750°2h (Anl.)		-10	-20	-27
9741-Platte 3-10	1040°38'+750°2h (Anl.)		-35/-10	-42/-20	-20/-52
9741-Platte 3-10	Anl. + 550°5000h		-31/0	-34/-10	-40/-10
9741-Platte 3-10	Anl. + 600°5000h		-16/+5	-10/+8	-24/+4

[1]FATT=Fracture Appearence Transition Temperature (50% cristalline spot)

[2]DBTT=Ductile Brittle Transition Temperature ($\approx$ 0,5 upper shelf)

Work on EUROFER

First material ($\varnothing$ 100 mm bars) from the new European LA-alloy EUROFER is available. Hardening-, annealing- and transformation-test have been started as first characterisation work.

Literature:

[1] M. Schirra, S. Heger, A. Falkenstein; Das Zeitstandfestigkeits- und Kriechverhalten des niedrigaktivierenden Stahles F82H-mod., Abschlußbericht, FZKA 6265, Mai 1999

[2] K. Ehrlich, A. Möslang, M. Schirra; Physical Metallurgy and Creep Ruptures Properties of F82H-mod. and OPTIFER with Ageing Effect, Milestone 4 Meeting, 1/2. March 1999, Petten-Netherlands

[3] Influence of thermal ageing on tensile and impact bend properties of the steel grades OPTIFER and F82H-mod., Journal of Nuclear Materials 271-272 (1999) p. 455-458

[4] S. Heger, M. Schirra; Zusammenstellung von Kriechkurven aus verschiedenen Versuchsprogrammen. Teil XIII=F82H-mod., Forschungszentrum Karlsruhe, Interner IMF 1-Bericht, März 1999

[5] R. Lindau, L. Schäfer, E. Materna-Morris, M. Schirra; Characterisation of the ferritic-martensitic 8% chromium steel F82H-mod., 20th Intern. Symp. on Fusion Technology (SOFT), Marseille, F, Sept. 7-11, 1998

[6] M. Schirra, S. Kempe, H. Kempe, M. Klotz, H. Zimmermann, J. Lapeña; Untersuchungen zu physikalischen und mechanischen Eigenschaften der OPTIFER-Legierungen, FZKA 6167, April 1999

[7] M. Schirra, H. Kempe, M. Klotz; Festigkeits- und Kerbschlaguntersuchungen zur Alterungsbeständigkeit der OPTIFER-Legierung, Jahrestagung Kerntechnik, 18.-20.5.99, Karlsruhe, Beitrag 808, Seite 579-583

Staff:

E. Daum
K. Ehrlich
A. Falkenstein
P. Graf
S. Heger
E. Materna-Morris
M. Schirra
H. Zimmermann

SM 2.2.2
Thermal and Isothermal Fatigue Properties of Base Metal

1. Introduction

Structural components of a DEMO-blanket are subjected during service to alternating thermal and mechanical stresses as a consequence of the pulsed reactor operation. Of particular concern is the fatigue endurance of Reduced Activation Ferrite-Martensite (RAFM) steels like the Japanese steel F82H mod. and the German steel OPTIFER IV under cyclic strains and stresses produced by these temperature changes. In order to design such structures, operating under combined mechanical and thermal cycling, fatigue life has to be examined in isothermal fatigue tests for materials data generation and in thermal fatigue for verification of design codes.

In this report isothermal mechanical (LCF) and thermal low-cycle fatigue (TCF) data with and without hold times of the RAFM steels F82H mod. and OPTIFER IV are compared, partly to those of MANET II ferrite-martensite steel. First results of postirradiation TCF experiments of MANET II and a Russian ferrite-martensite steel 12Cr-1.5NiMo are available as well as cold reference data for F82H mod.

2. Experiments

Cylindrical samples of F82H mod. and OPTIFER IV, respectively - solid in case of LCF and hollow in case of TCF - have been used for the experiments. Both materials have been tested in air under LCF- and under TCF-conditions, respectively.

The LCF tests have been performed with computer-controlled MTS servohydraulic testing machines operating in strain controlled push-pull mode. Triangle wave forms are applied with constant strain rates of 3×10^{-3} 1/s in case of LCF tests. More detailed informations about the test procedure are received from [1].

For the LCF experiments, solid specimens of 77 mm length and of 8.8 mm diameter in the cylindrical gauge length of the specimen have been used. The initial gauge length of the axial extensometer is 21 mm.

The TCF test rig consists of a stiff load frame for mechanical clamping of the sample, which is directly heated by the digitally controlled ohmic heating device. Cylindrical specimens are used with similar outer dimensions as the above mentionned solid specimens, but with a wall thickness of 0.4 mm. Variable strain rates are applied at TCF test mode, due to the constant heating rate of 5.8 K/s and variable temperarure changes.

Since both, temperature and mechanical strain cycling are taking place, mechanical strain is available only after subtraction of the thermal strain from the net strain.

In the case of TCF the influence of two different normalizing temperatures - 1075°C and 950°C - upon cylic lifetime on OPTIFER IV hollow cylindrical specimens has been studied. In both cases the tempering temperature was regulary T=750°C.

3. Results

First results from LCF experiments with hold-times at 550°C indicate, that for tension hold-times below one minute MANET II samples show higher numbers of cycles to failure than those of F82H mod. material.

For hold-times equal or larger than three minutes, F82H mod. samples reveal an isothermal creep/fatigue restistance which is significantly better (about 25% for t_H = 10 minutes) in comparison to MANET II samples.

The thermal fatigue behavior of the RAFM steel OPTIFER IV with the lower normalizing temperature of 950°C shows significantly smaller thermal fatigue lifetimes as compared to OPTIFER IV, normalized at 1075°C.
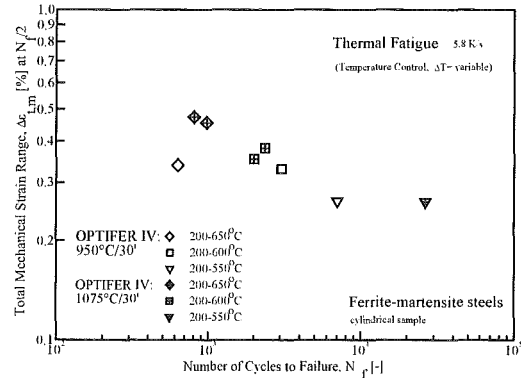
Fig. 1: Comparison of thermal fatigue behavior between two normalizing temperatures of the RAFM-steel OPTIFER IV

First TCF experiments experiments on F82H mod. with hold-times have been started, but due to the longer testing time, the amount of data up to now is too small to give a clear tendency.

4. Postirradiation thermal fatigue experiments

In a German – Russian cooperation on Scientific and Technological Cooperation between Forschungszentrum Karlsruhe (FZK), IMF II, Karlsruhe and Central Resarch Institute for Structural Materials (CRISM) "Prometey", St. Petersburg, a programme for postirradiation thermal fatigue was defined. As irradiation facility the WWR-M-type reactor in Petersburg Nuclear Physics Institute (PNPI) with vacuum temperature control is used.

The neutron irradiation in the WWR-M-type reactor of PNPI was realized at 300 °C with a fluence of about $6 \bullet 10^{24}$ n/m^2, i.e. 0.55 dpa (Fe) according to NRT-model, The irradiation was conducted with two hermetic closed aluminum ampules at a flux of $3 \bullet 10^{13}$ n/(s cm^2).

Fig. 2: Irradiation history of MANET II and 12Cr-1.5NiMo at about 300°C.

Two types of postirradiation test facilities are available. In remote-controlled Russian thermal fatigue facilities installed in a "hot" chamber postirradiation tests are running and a modified German thermal fatigue facility was shipped to Russia.

Thermocyclic tests of preirradiated Russian type cylindrical specimens with notches up to 10 ^{4} cycles are performed on Russian TCF-machines at (CRISM) "Prometey", St. Petersburg, by heating the sample in an electric furnace under air atmosphere up to 350 °C for 10 min and following cooling in distilled water down to 50 °C for 1.5 min.

In the Russian type cylindrical specimen thermal cycling generates cracks of $0.01 \div 0.02$ mm length in the four notches as the stress concentrators. Up to 10^4 cycles cracks grow slowly and along with these first cracks other cracks are generated. Cracks commonly have transgranular character, but sometimes intergranular cracks are detected in the steel F82H-mod. The qualitative examination of crack appearance is displayed in Table 1. Practically, a neutron irradiation of MANET-II and 12Cr-1.5NiMo up to $6 \bullet 10^{24}$ n/m^2, i.e. 0.55 dpa (Fe) according to NRT-model, does not influence the thermal fatigue crack nucleation of these materials. But on F82H mod. crack initiation in unirradiated state appears already above N_c = 6000 cycles at total strain levels of $\Delta\varepsilon_{tot}$ = $0.16 \div 0.18$ % [2].

The irradiation dependence holds quite similar for isothermal fatigue and has been attributed to quick "sweeping out" of preformed irradiation defects by the cyclic plastic strain. However, that fact in no way means that the irradiation influence on materials cyclic degradation could be neglected in case of "in-pile" fatigue. The interaction of simultaneous deformation and irradiation, not possible in postirradiation tests, may result in the accelerated damage. The study of both, the mechanical and thermal fatigue under irradiation, however difficult this may be, is therefore getting an urgent material science problem in designing fusion reactors.

Another set of ampule devices with German type cylindrical hollow specimens made of F82H mod., MANET II and 12Cr-1.5NiMo, that had been qualified during an experimental irradiation in respect to temperature distribution, maintainance of constant irradiation-temperature of about 300 °C and neutron monitoring, are still under irradiation in the WWR-M-type reactor of PNPI to reach a level of 2 dpa.

Literature:

[1] E. Diegele, C. Petersen, J. Aktaa and R. Schmitt: "Cyclic Behaviour of Structural Materials for the First Wall of Fusion Reactor", FZK-Nachrichten, Vol. 31, Issue 1/99 (in German)

[2] L. A. Belyaeva, A. A. Zisman, C. Petersen, V. A. Potapova and V. V. Rybin, "Thermal Fatigue Crack Nucleation in Ferritic-Martensitic Steels before and after Neutron Irradiation" to be presented on ICFRM-9, Colorado Springs, 10. – 15.10.1999.

[3] G. Filacchioni, C. Petersen, F. Rézaï-Aria and J. Timm: „A European Round Robin in Thermo-mechanical Fatigue Behavior of a 9%Cr Low Activation Ferrite-Martensite Steel", presented on 3rd ASTM-Symposium on Thermomechanical Fatigue Behavior of Materials, 4.-5. Nov. 1998, Norfolk, Virginia, USA. To be published in ASTM-STP 1371.

[4] F. Armas, M. Avalos, I. Alvarez-Armas, C. Petersen and R. Schmitt: „Dynamic Strain Aging Evidences during Low Cycle Fatigue Deformation in Ferritic-Martensitic Stainless Steels", Journal of Nuclear Materials. Vols. 258 – 263, (1998), pp. 1204 – 1208

[5] Petersen: „Thermal Fatigue Behavior of Low Activation Ferritic-Martensitic Steels", Journal of Nuclear Materials, Vols. 258 – 263, (1998), pp. 1285 – 1290.

Table 1: Appearance of the cracks of more then 0.01 mm length ("+"present, "–" absent)

Material, state	$\Delta\varepsilon_{tot}$ 0.13÷0.14% $\bullet 10^3 N_c$			$\Delta\varepsilon_{tot}$ 0.16÷0.18% $\bullet 10^3 N_c$			$\Delta\varepsilon_{tot}$ 0.21÷0.23% $\bullet 10^3 N_c$			$\Delta\varepsilon_{tot}$ 0.31÷0.33% $\bullet 10^3 N_c$		
	3	6	10	3	6	10	3	6	10	3	6	10
MANET-II Unirradiated	–	–	–	–	–	–	–	–	+	–	–	+
MANET-II Irradiated	–	–	–	–	–	–	–	–	+	–	–	+
12Cr-1.5NiMo Unirradiated	–	–	–	–	–	–	–	+	+	–	+	+
12Cr-1.5NiMo Irradiated	–	–	–	–	–	–	–	+	+	–	+	+
F82H-mod. Unirradiated	–	–	–	–	+	+	+	+	+	+	+	+

[6] L. Belyaeva, A. Orychtchenko, C. Petersen and V. Rybin: „Postirradiation Thermocyclic Loading of Ferritic-Martensitic Stuctural Materials", Journal of Nuclear Materials, Vol. 271&272, (1999), pp. 151 – 154.

[7] A.Zisman, V. Rybin, C. Petersen and R. Schmitt: "Multiplicative Model for Out-of-phase Thermal Fatigue Degradation of Ferritic-Martensitic Steel MANET II", Journal of Nuclear Materials, Vol. 264, (1999), pp. 234 – 237.

[8] J. Aktaa, H. Kiewel and D. Munz, "Viscoplastic Material Models in Failure Analysis of Components," in Proc. of the 7th Int. Symp. on Plasticity and Its Current Applications, Cancun, Mexico, January 1999, pp. 689 - 692.

[9] H. Kiewel, J. Aktaa and D. Munz, "Application of an extrapolation method in thermocyclic failure analysis," Computer Methods in Applied Mechanics and Engineering, accepted for publication, 1999.

Staff:

J. Aktaa
M. Klotz
C. Petersen
M. Pfeifenroth
D. Rodrian
R. Schmitt

SM 3.1.1
Thermal Fatigue Scoping Tests under Hydrogen Atmosphere

1. Introduction

During service structural components of a DEMO-blanket are subjected - under corrosive atmospheres - to alternating thermal and mechanical stresses as a consequence of the pulsed reactor operation. Of particular concern is the thermal fatigue endurance of Reduced Activity Ferrite-Martensite (RAFM) steels under test conditions and in atmospheres close to those operating in the reactor.

2. Test facility

The Vacuum Thermal Cycling Fatigue (VTCF) test facility consists of a stiff load frame, built in a vacuum vessel, for mechanical clamping of the sample, which is directly heated by the digitally controlled ohmic heating device. To apply a hydrogen partial pressure of 10^{-3} to 10^{-1} mbar, valves, transducers and the pump have to be modified and a laboratory safety system must be installed.

3. State of the art

The call for tenders and procurement of hydrogen feeding and safety system is initiated, to modify an existing vacuum facility for thermal fatigue tests under hydrogen atmosphere.

Staff:

C. Petersen
D. Rodrian

SM 3.5.1
Corrosion of RAFM Steel in Liquid Pb-Li

The use of Pb-17Li alloy as breeder material for a fusion reactor requires an assessment of its compatibility with the structural materials. Hence, the martensitic low activation steels MANET I, Optifer IVa and F82H-mod. have been exposed to flowing Pb-17Li at 480°C for maximal 8000 h. The flow rate of the corrosive medium Pb-17Li was 0.3 m/s.

The corrosion tests have been carried out in a special device named PICOLO (Pb-Li corrosion loop). The construction of the loop allows the change of specimens during the operation without cooling down the whole circuit. In order to investigate the corrosion kinetics of the steels some specimens from the loop were removed after 1000, 2000, 3000, 4000, 6000 and 8000 h exposure. The adherent Pb-17Li was removed from the specimen surface by washing in a mixture of CH_3COOH, H_2O_2 and C_2H_6O (1:1:1) in order to determine the weight change.

EPMA line scan analyses have been carried out on specimens exposed to Pb-17Li for 1000 and 8000 h resp. across this observed layer. It was found that the Fe and Cr content of this porous surface layer decreased with longer exposure times, leaving a scale which was relatively enriched by the steel elements which are known to have a very low solubility in Pb-17Li. In the case of Optifer IVa and F82H-mod. the constituents W and V were found to be enriched, in the case of MANET I the concentration of the elements Mo and V are increased in this porous layer compared to the bulk material. The line scans measured on F82H-mod. after exposure times of 1000 h and 8000 h are shown in figure 1 and 2.
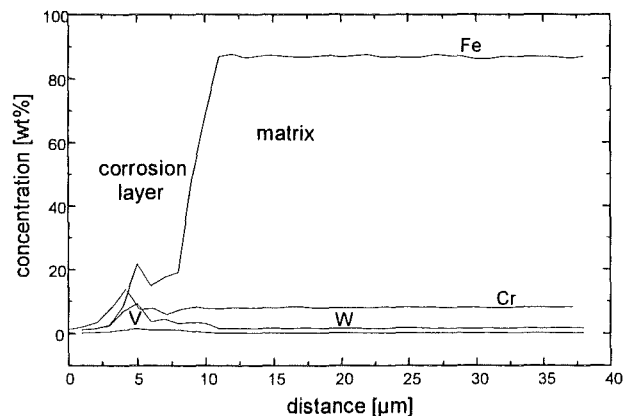
Fig. 1: EPMA line scan across the cross section of F82H-mod. after 1000 h exposure to Pb-17Li at 480 °C.
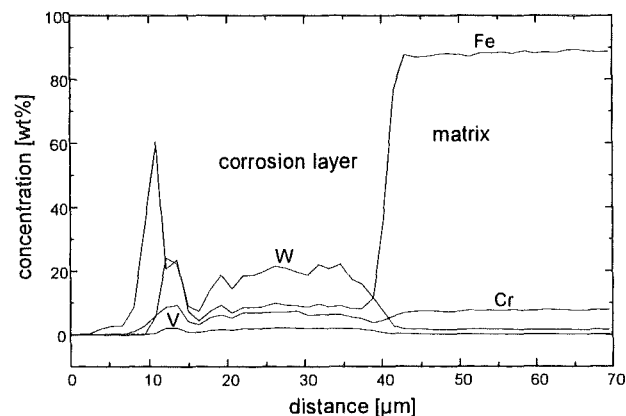
Fig. 2: EPMA line scan across the cross section of F82H-mod. after 8000 h exposure to Pb-17Li at 480 °C.

Unfortunately, the corrosion layer can only be seen on some areas of the specimens. Probably the most parts of this layer were removed during the washing procedure together with the adherent Pb-17Li. For future investigation, corrosion specimens will not be washed after exposure to liquid metal. Thus it will be possible to analyse the complete corrosion layer in future.

An additional corrosion mechanism is responsible for the beginning of the corrosion attack of Pb-17Li to the steels besides the corrosion phenomena of leaching out of the main steel elements followed by the dissolution of the steel matrix. Investigations have revealed that the steel surface is covered with a few nm thin oxide layer protecting the material. The compound formed on the surface of each steel investigated is the spinel $CrMn_2O_4$ which was detected with XPS analysis. Probably this oxide scale is formed during the vacuum heat treatment which was undertaken with every steel before exposure.

Additionally to the bare alloys coated specimen are under investigation now. The coatings on Al-base were produced by various techniques: VPS, CVD+MOCVD and Hot Dip. After 4000 h exposure there seems to be no influence of Pb-17Li to the coatings. Further analysis is still required.

Literature:

[1] K. Stein-Fechner, J. Konys, H. Glasbrenner, Z. Voß, Tagungsbericht Jahrestagung Kerntechnik '99, 18.-20. Mai, Karlsruhe (1999), 677.

[2] K. Stein-Fechner, H. Glasbrenner, J. Konys, Z. Voß, EUROCORR 99, 30 August – 2 September 1999, Aachen, Germany.

Staff:

H. Glasbrenner
K. Stein-Fechner
Z. Voß

SM 4.5.1
Diffusion Welding (Solid HIP, Uniaxial)

A diffusion welding experiment has been carried out at 980 °C under uniaxial pressure. The following parameters are varied:

1. Steel grade: MANET-II; F82H mod; OPTIFER-IV.

2. Uniaxial pressure: σ_p = 16; 22; 29; 35; 48 MPa.

3. Roughness of the welding surfaces: 0,5 µm $\leq R_z \leq$ 8,5 µm.

4. Thermal treatment after welding: T_{AU}; T_{AN}.

5. Test method: tensile-, bending-, impact bending tests.

To obtain a nearly complete material contact, a high contact pressure is necessary in diffusion welding. However, the real components are passed through by a number of cooling channels which are located close to each other with only small ridges that are to be welded remaining in-between. By the contact pressure these ridges are both upset and buckled.

For the steel MANET-II upsetting at T = 980°C, 1 h, amounts to - ε [%] = $K_1 \sigma^{n1}$, where K_1 = 3.5 x 10^{-4}, n_1 = 2.8 and σ is given in MPa. For example, at σ = 20 and 50 MPa, the loss of ridge heigth or upsetting at T = 980°C is -ε = 1.54 % and 20 %, respectively. Simultaneous bending or buckling of the ridges amounts to 0.13 mm only at a contact pressure of σ = 38.5 MPa and a slendernes ratio of ridges S = H : B = 12 : 2 = 6 (Fig. 1). An impact pressure of 48.2 MPa causes the buckling at S = 6 to increase by a factor of 10. Buckling D at the pressue σ = 48.2 MPa (at T_{DS} = 980°C) as a function of the slendernes ratio S of the ridges may be calculated as follows: D (σ = 48.2 MPa) = K_2 x S^{n2}, where K_2 = 1.49 x 10^{-2} and n_2 = 2.54.

In the tests, the impact pressure varied between 16 and 48.5 MPa. The tensile properties of the welded OPTIFER-IV steel specimens always corresponded to those of the base material. Impact energy A_v, however, increased with the contact pressure (Fig. 2). Pressures above 36 MPa did no longer result in any improvement. This notch impact toughness which amounts to a maximum of 40 % of the base material may probably be sufficient.

Staff:

L. Schäfer
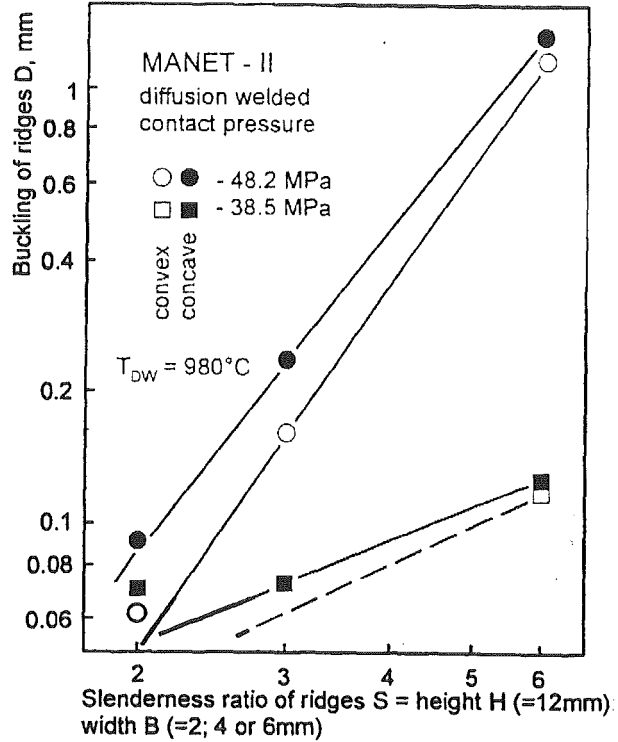
Fig. 1: Buckling of ridges of MANET-II steel in dependence of the slenderness ratio height: width.
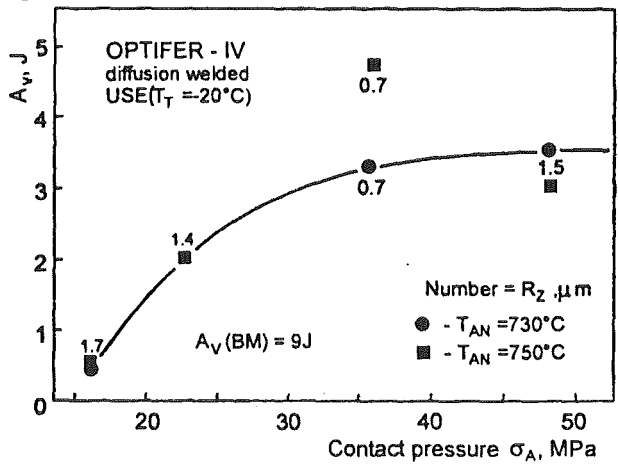
Fig. 2: Impact energy A_v of the diffusion welded RAF-steel OPTIFER-IV in dependence of the contact pressure during welding.

SM 5.1.1
Mechanical Design Code Rules for RAFM Steels

General part:

The objective of this task is to develop a design code for blanket modules, built from RAFM (reduced activation ferritic-martensitic) steel. The basis for the code development is the ISDC (ITER Structural Design Code), which exists in an interim but not yet complete version (Dec. 98). In this interim version, low temperature (LT) rules are given, high temperature (HT) rules are still missing. There are two major problems to be solved:

I. Assessment of the LT-rules.

    These rules present two alternative routes. Due to their lower ductility RAFM steels may not meet some of the limits given in the first path allowed from ISDC. Or, in other words, the limitations on the design, that are allowed from the second path (low ductility) in the ISDC may then be too restrictive.

II. Formulation of HT rules.

    As a first step, it is proposed to adopt these rules from the ASME. According to this approach, this, finally, will result in the formulation of a so called 'special code case'.

Fracture Mechanics:

New rules have been formulated on the basis of the British R6 fracture mechanics code. This approach is a two-criteria method based on linear fracture mechanics and on plastic limit analysis. These rules are currently tested with verification analysis for different crack size and locations in an ITER-like first wall geometry under several loading conditions.

Currently there are several discrepancies that let the proposed rules not be considered as 'conservative', as they should from the philosophy of a design code. This may result in a change of the rules so far given.

Moreover, for a special FW geometry (with rectangular shape), simplified methods of calculating K factor are proposed on the basis of weight functions. Finally, this method needs only a stress analysis of the defect-free component.

Staff:

E. Diegele
G. Rizzi

SM 5.2.1
Fracture Mechanics Studies

Objective

The objective of this subtask is the development and application of methods that enable the generation of design-relevant fracture mechanics material parameters on the basis of micromechanical failure models.

A characteristic feature of these models is the utilisation of a 'hybrid' approach, which means extraction of material parameters for brittle or ductile fracture from (fracture) mechanics experiments by accompanying Finite Element Stress analyses.

The main advantage of this so-called 'Local Approach' with respect to global failure criteria is the fact that a mechanism-based fracture description is combined with a numerical stress analysis. Geometrical size effects are thus already accounted for within this approach. Limitations of the local approach originate from different fracture mechanisms. Knowledge of fracture mechanisms is therefore essential, so that fractography invariably is an essential part of the evaluation of the experiments.

Local fracture criteria establish a link between metallurgy and mechanical engineering and they are currently being incorporated into design codes such as the R6 code of British Energy, where Local Approach methodology is covered in a special appendix issued in 1999 [1].

Experimental results, fractography

A comprehensive quantitative fractographic analysis was performed on the F82Hmod notched round bar specimens that were tested previously. Images taken from the fracture surface and from sections perpendicular to the fracture surface (i.e. in axial direction) were analysed using REM techniques. Qualitatively, presence of large plastic deformation was found to be responsible for a transition of the fracture mode from pure transcrystalline cleavage fracture as commonly observed in the lower shelf region of ferritic steels to mixed trans-/intercrystalline fracture with pronounced initiation of axial cracks affected by the presence of martensite laths. Plastic deformation leads to shear fracture of carbide decorated martensitic structures. Ductile damage caused by void formation was also observed. Quantitative results were obtained from image analysis of the fracture surfaces. Local fracture toughness values were determined using measurements of the size of fracture origins together with results of the fracture stress calculations from Finite Element analyses. The spatial distribution of fracture initiation sites was recorded. It will be used in future calculations and serves as indicator if the numerical description of fracture is appropriate and if transferability of results to different specimen geometries is possible.

For the transferability assessment, tests on pre-cracked specimens are necessary. For this purpose, a pre-cracking rig for the generation of circumferential fatigue pre-cracks is under construction. Pre-cracking is done by rotational bending with continuous monitoring of crack depth.

Modelling

Evaluation of cleavage fracture parameters was performed using a hybrid approach combining experimentally observed results with stress analyses using Finite Element calculations. Typical results were already reported [2]. It is, however, subject to current research how statistical inference can be made for the Weibull stress at cleavage fracture. Following the development of the WEISTRABA FE-postprocessor routine at FZK [3], a novel statistical approach was used. This approach enables direct assessment of statistical distributions instead of confidence limits for parameters and it was successfully applied to cleavage fracture data of a RPV steel made accessible within a Round Robin organised by the European Structural Integrity Society (ESIS) [4]. Participation in this Round Robin was considered beneficial also with respect to possible calibration of WEISTRABA results and because of additional experience gained with different material data. Using the novel statistical approach of the resampling technique, it was possible to identify outliers in the F82Hmod data, which could later be confirmed by fractographic analysis. This is a quite important result for future investigations because it allows pre-selection of specimens for immediate fractographic examination based on the results of the numerical evaluation.

Ductile damage affects cleavage fracture in two ways: first, the stress field is changed due to the presence of voids, second, the population of potential cleavage fracture sites is changed because of competition between void formation and cleavage initiation. Change of stress field is accounted for via use of continuum mechanics damage models, while the competitive processes have to be modelled in terms of probabilities.

The WEISTRABA routine was extended and is now capable of calculating the local risk of fracture in a specimen, a quantity which depends on the stress distribution at fracture and which serves as an important quantity for model verification by comparison of numerical results with experimentally obtained fracture origin distributions.

Perspective

Continuous interaction between metallurgy and mechanical design is necessary to provide both sides with the respective information that is necessary to obtain mechanism-based geometry-independent descriptions of fracture in the ductile-to-brittle transition regime.

Irradiation effects can be considered, provided that fracture mechanisms are known. This will be subject of future investigations in the framework of SM 1, where also the impact of irradiation on fatigue pre-cracks has to be investigated.

Literature:

[1] British Energy Generation Ltd, Assessment of the integrity of structures containing defects R/H/R6, Rev. 3, Appendix 17 'Guidance on Local Approach Methods', 1999.

[2] Nuclear Fusion Project Annual Report of the Association Forschungszentrum Karlsruhe / EURATOM October 1997 – September 1998, FZKA 6200, November 1998, 139.

[3] H. Riesch-Oppermann, A. Brückner-Foit, WEISTRABA – A code for the numerical analysis of Weibull stress parameters from ABAQUS Finite element stress analyses, FZKA 6155, August 1998.

[4] H. Riesch-Oppermann, FZK Contribution to the ESIS TC 8 Numerical Round Robin on Micromechanical Models (Phase II, Task B1), FZKA 6338, September 1999.

Staff:

J. Aktaa   H. Riesch-Oppermann
E. Diegele   G. Rizzi
M. Klotz   M. Walter
C. Petersen

SM 5.3.1
Materials Quality Control and Distribution

Based on the substantial experience with developmental re-
duced activation ferritic martensitic steels, produced as labora-
tory melts of 50 kg, a RAFM steel of the 9CrWTaV type, called
EUROFER 97 had been drafted under the leadership of FZK in
close co-operation of different European Associations (CEA,
ECN, FZK). BÖHLER EDELSTAHL GmbH in Austria was finally
selected as manufacturer for about 3.5 tons semi-finished
products (plates, forging, filler wire and tubes).

The major goals for the procurement of such a large-scale heat
are as follows:

- Gaining experience in producing a high-purity steel in an
  industrial scale.

- To what extent can experiences made with developmental
  alloys be transferred to large-scale metallurgical processes.

- Gaining experience in the fabrication of semi-finished prod-
  ucts by means of traditional manufacturing processes like
  rolling, forging and drawing as well as by means of ad-
  vanced technologies like powder-metallurgy.

- Gaining experience in manufacturing a ½ -scale mock-up of
  a blanket module with respect to workability, weldability,
  HIPping and other production-related properties.

- A characterization program will yield relevant mechanical
  properties of the material.

The production of EUROFER 97 is well in progress. The pre-
material was vacuum-melted and vacuum-remelted and, after
specific heat-treatments and forging, supplied to the production
process of the semi-finshed products.. The production of bars
plates and filler wire is finished, the final inspection and approval
has not yet been carried out, but is expected for October 1999.
The production of tubes is delayed, for the numerous necessary
production accompanying tests. The delivery of tubes is planned
for December/January. The bars have been distributed recently
and the distribution of the plates and filler wire is scheduled for
October/November.

First results of tensile tests at room temperature and elevated
temperature (550°C) show that the tensile properties are at the
upper boundary compared to the developmental alloys. Metal-
lographic examinations reveal a relative small grain size (ASTM
10) compared to e.g. F82H mod.(ASTM 4-5). These results
raise good hopes for the properties of the other semi-finshed
products.

Staff:

R. Lindau

SM 5.7.1
Development of Miniaturized Push-pull (Creep-) Fatigue Specimen

As long as Tokamak type facilities are the primary path towards commercial fusion power reactors, (creep-)fatigue remains one of the main lifetime limiting failure modes of structural materials as the limited data from reactor and higher energy accelerators have shown. The development of a miniaturised push-pull (creep-)fatigue specimen is essential in order to minimise flux gradients within the gauge volume and to fully utilise the available irradiation region of an intense neutron source like IFMIF. The requirements for a suitable miniaturised specimen include (i) data that represent material specific properties for widespread loading conditions, (ii) ability for fully remote handling operation before, during and after (creep-) fatigue testing, and (iii) universality, that is one common specimen design for different fatigue behaviour (e.g. cyclic softening/hardening) or loading conditions (e.g. thermal/isothermal fatigue). The early availability of a suitable miniaturised specimen helps also to use limited fission reactor volume in a very effective manner.

According to an initial literature survey, there are still a variety of push-pull fatigue specimens used in the international materials test programmes. Both cylindrical and hourglass shaped geometries are used with gauge diameters typically ranging from 3-10 mm. Mainly to meet the requirements for high flux neutron sources it is desirable to reduce the overall specimen size as much as possible but still maintaining remote handling capability in hot cells.

From experience in earlier programmes we can conclude that the minimum wall thickness should not be smaller than about 15 times the maximum grain size. Assuming a maximum grain size of 80-100 μm in typical RAFM steels, the minimum gauge diameter therefore should be not less than 1.5 mm. Other boundary conditions include remote controlled specimen clamping, clamping of extensiometers and resolution limit in strain controlled fatigue tests. Based on these requirements, a specimen geometry has been developed and optimised with elasto-plastic finite element calculations. Special emphasis has been put on the radius of curvature at the end of the gauge length to achieve throughout the gauge volume homogeneous stress-strain fields in uniaxial push-pull fatigue conditions. The proposed fatigue specimen has a cylindrical geometry with a gauge width of 2 mm, a gauge length of 7.6 mm and a total length of 25.6 mm.

strain controlled conditions and compared with standard push-pull fatigue specimens having a cylindrical geometry with 8 mm diameter and a gauge length of 18 mm (A. Nishimura, ICFRM-9, Oct. 10-15 1999, Colorado springs, to be published in JNM).
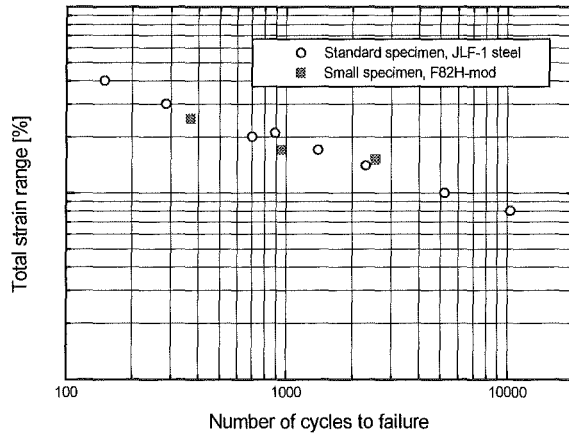
Fig. 2: Fatigue life of standard and miniaturized fatigue specimens at T = 20°C

Fig. 2 shows, that inspite the slightly different materials and the limited statistics, the fatigue life of both specimens are in good agreement, indicating that the miniaturized specimen is able to produce material intrinsic fatigue data.

Staff:

S. Baumgärtner
G. Bürkle
E. Diegele
A. Möslang
G. Rizzi

Fig. 1: Suggested miniaturised push-pull fatigue specimen

Initial tests with such miniaturised fatigue specimens made of F82H-mod steel were performed at room temperature under

SM 6.1.1
Irradiation in a Temperature Controlled Test Rig
of BOR 60

1. Objectives

In an energy generating fusion reactor structural materials will be exposed to very high dpa-levels of about 100 dpa. Due to the fact, that fast reactor irradiation facilities in Europe are not available anymore, a cooperation with a Russian institution will be implemented.

2. Irradiation facility

During a first negotiation in Dimitrovgrad between State Scientific Centre Research Institute of Atomic Reactors (SSC RIAR) and Forschungszentrum Karlsruhe Technik und Umwelt (FZK), about future planning of a cooperation in the field of irradiation in a test rig with temperature measurement for BOR 60 of reduced activation ferritic-martensitic (RAF/M) steels, the following items had been discussed:

- Tensile, sharpy and low cycle fatigue specimens of RAF/M steels will be irradiated in a test rig of BOR 60 at a temperature less than 340° C. First in position D-23, where temperature measurement is possible and later up to 30 dpa in an identical position of the row 5 of BOR 60.

- The postirradiation tensile, sharpy and low cycle fatigue tests together with microscopy will be performed in the hot cells of SSC RIAR.

3. State of the art

As a result of the joint discussion the following actions were agreed:

- SSC RIAR prepares the test rig including temperature measurement and neutron monitoring.

- FZK determines shape, quantity and position of samples in the rig - if the occasion arises also with other European associations - to be irradiated, the parameter field of the postirradiation tests and the amount of microstructural examinations.

Staff:

C. Petersen
D. Rodrian

SM 6.2.1
TEM and SANS Investigations after Irradiation

Whether or not helium generated by inelastically scattered fusion neutrons will influence relevant mechanical properties like irradiation hardening, ductility, embrittlement fracture toughness and fatigue life at lower irradiation temperatures, is a matter of concern and subject of ongoing discussions. To get a better understanding of how helium might influence properties it is necessary to analyze the helium bubble morphology and to get a better understanding of their temperature stability and their growth mechanisms during higher temperature exposure. Unfortunately, the experimental observation of these bubbles using transmission electron microscopy (TEM) is difficult because of their tiny sizes, generally often less than 2nm, and because of the fact that these steels are magnetic. Small-angle neutron scattering (SANS) is therefore an appropriate technique to investigate this phenomenon, as also shown by previous studies performed by R. Coppola et al. In this task TEM and SANS analysis will be combined and applied to RAFM steels that have been preirradiated either by α-particle implantation or by reactors neutron.

The investigations performed up to now were done on F82H-mod specimens. After fabrication the samples were submitted to the reference heat treatment: 40 min. at 1040°C plus 2h at 750°C. Samples approximately 1 cm^2 in surface and 0.4 mm thick had been homogeneously implanted according to table 1.

Table 1: α-particle implantation conditions

Irradiation temperature	250 °C
α-particle energy	0-104 MeV
Damage production rate	$(0.6-2) \times 10^{-6}$ dpa/s
Helium production rate	$(6-12) \times 10^{-4}$ appm He/s
Helium concentration	400 appm
damage dose	(0.40-0.67) dpa

After irradiation some of the specimens were submitted to 2h thermal annealing (at 525°C, 825°C and 975°C) in high vacuum, together with non-implanted samples of the same material (one for each temperature) serving as a reference to isolate the SANS signal arising from the He-bubbles. A sample of the same material submitted to thermal annealing at 250°C for a duration equivalent to the implantation time (5 days) served as a reference for the implanted sample and was not further thermally treated.

Following helium implantation to 400 appm at 250 C, microstructural examinations revealed very small helium bubbles. However, large areas within grains or martensitic laths might appear during the TEM investigation where bubbles are hardly visible or even invisible, although the helium has been homogeneously implanted. From the analysis of various F82H specimens it can be concluded, that in agreement with observations on other ferritc/martensitc steels the appearance and morphology of helium bubbles varies locally with microstructural features. Fig. 1 shows the microstructure of a helium implanted F82H charpy specimen with relatively large helium bubbles nucleated mainly in dislocation networks (partly out of contrast), subboundaries and, if present, at the surface of precipitates. In other regions with much lower densities of internal surfaces, the mean free diffusion path of helium atoms is smaller. In the latter case, bubble radii at the resolution limit of 1-2.5 nm have been measured. That is, even if the helium generation might be highly uniform (e.g. cyclotron implantation, fusion neutrons), the final bubble morphology depends at least

at lower irradiation temperatures largely on local microstructural features.
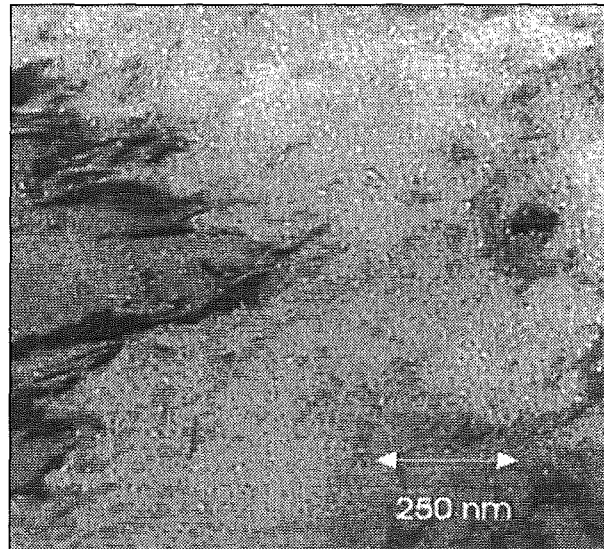
Fig. 1: TEM picture of He-bubbles in F82H after implantation with 400 appm He at 250 °C

Since only a fraction of bubbles might be visible in TEM micrographs, reliable density distributions can hardly be derived. Consequently, also an estimate of the bubble volume fraction from TEM data might be affected by large uncertainties, resulting in an apparent helium concentration which might deviate substantially from the nominally implanted helium concentration. This is why SANS analyses might be a viable option because they can principally detect much smaller void and/or bubble diameters.

The postirradiation heat treatment and the TEM analyses have ben performend at Forschungszentrum Karlsruhe, while the SANS measurements were carried out under the leadership of ENEA at the D11 instrument of the ILL Grenoble with sample-to-detector distance of 1.46 m and a wavelength of 6 Å. Calibration to absolute SANS cross-sections was obtained by measurement of 1 mm of water in a quartz cell. The data were treated by the ILL standard programs. A horizontal magnetic field of 1.4 T was applied perpendicular to the incoming neutron beam in order to fully align the magnetic moments in the sample. In the following a summary of the SANS measurements is given where emphasis is put only on those results that can be directly compared with the TEM investigations.

The He-bubble volume distribution functions, obtained at 825 °C and 975 °C show according to Fig. 2 that a dense population of small bubbles (below 10 Å in radius) is accompanied especially at 975 °C by a secondary distribution of bubbles one order of magnitude larger. No such bimodal distribution is found at lower temperatures where only a well defined peak centered around 15 Å size has been observed, in fine agreement with the value of 16 Å determined from TEM. Furthermore at 975 °C the densities of the two bubble populations are almost one order of magnitude larger than at 825 °C. Finally, there is an increase of a factor of 5 in the relative value of the bubble volume fraction from 250 °C to 825 °C and of about 50% from 825 °C to 975 °C. The corresponding volume fractions ΔV, determined by integration of the $D(R)$'s, are reported in the second table together with the average bubble radii R_b. There is a large uncertainty on these data, arising both from the uncertainty in background subtraction and in the limited available Q-range, which result in large error bands. Such uncertainties do not however affect the relative values and these results are consistent with what is expected from the bubble growth by

post-implantation annealing and observed by TEM. As a matter of fact the initial bubble distribution produced by low temperature implantation is modified by the growth of larger bubbles at the expense of the smallest ones or by coalescence of the He atoms implanted in the matrix.

Fig. 2: He-bubble volume distribution functions (proportional to bubble volume per unit volume) vs bubble radius in Å for the following temperatures: a) 250 °C, b) 825 °C and c) 975 °C. The dashed areas represent the 80% confidence band.

It should be emphasised that these results, although carefully analyzed, need further confirmation especially at high Q-values in order to improve the uncertainty band at small bubble radii.

The He-bubble volume distribution functions from SANS analysis are consistent with TEM observations and show that a uniform bubble distribution evolves during high temperature annealing into a bimodal one with a population of bubbles as large as 100 Å approximately. It can be already concluded from the present TEM and SANS analyses that a combination of SANS and TEM leads to a better understanding of the overall bubble distribution and the thermal stability of helium bubbles in RAFM steels after high temperature excursions.

Table 2: He bubble volume fraction, ΔV, and average radius R_b (Å) from SANS analysis (* with a secondary bubble population aound 100 Å)

Annealing temperature	ΔV	R_b
250 °C	0.0015	15
825 °C	0.0079	5
975 °C	0.0123	5*

Literature:

[1] R. Coppola, M. Magnani, R.P. May, A. Möslang; "Study of He-Bubble Growth in a Martensitic Steel for Fusion Reactors"; XI Internat. Conference on Small-Angle Scattering, New York, May 17-28 1999, Published in Journ. of Applied Crystallography.

[2] R. Coppola, M. Magnani, R. May and A. Möslang; "Study of helium buble growth in alpha implanted F82H-mod martensitic steel"; Internat. Conference on Fusion Reactor Materials 9 (ICFRM-9), Colorado, October 10-15 1999, to be published in Journ. of Nucl. Matter.

Staff:

G. Bürkle
A. Möslang

SM 6.3.1
ODS-RAFM Behaviour Specification and Characterisation of a RA Heat

The efficiency of future fusion power plants is strongly dependent on the operating temperature. Presently considered conventional RAFM steels for structural applications limit the operating temperature to around 550 °C. Oxide Dispersion Strengthened (ODS) materials would allow to increase the operating temperature by about 100 K. Therefore it seems to be necessary to develop Reduced Activation ODS alloys on the basis of the 9%Cr RAFM steels using the results of prior activation calculations.

On a common "Kick-Off-Meeting" on ODS-alloys in Karlsruhe on June 23rd, 1999, the subtask leaders exchanged their knowledge and arranged the future work and strategy for ODS material development.

Three pathways for the development of suitable RA-ODS alloys seem to be promising:

1. Commercial alloys and variations

2. Developmental alloys

3. Variation of existing RAFM steels

First results of preliminary activation calculations show the feasibility of reduced activation ODS-steels. A comparison of several mechanical properties (tensile, creep) between a commercial 19%-Cr ODS Fe-base alloy, RAFM steels e.g. F82H mod., conventional steels and developmental RAFM steels show the potential for fusion reactor applications at elevated temperatures (Fig. 1).
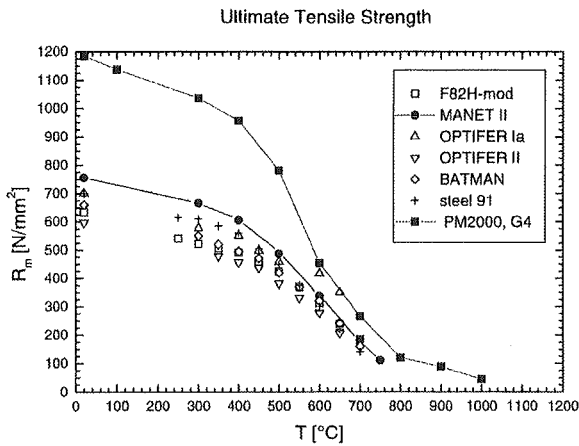
Fig. 1: Tensile strength R_m of commercial ODS-alloy (PM2000) and different steels.

Potential manufacturers have been contacted and first steps for the production of an ODS RA/FM steel on the basis of EUROFER have been undertaken. Other developmental alloys are still under discussion.

Staff:

R. Lindau

Neutron Source

Neutron Source

ERB 5004 CT 970072 (NET/97-453)
Evaluation and Refinement of the Conceptual Design of the Experimental Test Assembly of the D-Li Neutron Source

Following the recommendations of the FPCC, the IEA/IFMIF Subcommittee proposed a new activity for 1999. The objective was to maintain the viability of the project, to study technological key issues, to evaluate cost optimization and to be in a position to begin engineering design and development work in the near future. Following that, new tasks were defined by the design leaders. The IFMIF work continues to be coordinated by the international leadership team as for the CDA phase (1994-1996) and CDE phase (1997 – 1998).

The need to develop a structural material that can withstand the high-energy neutron flux environment expected for the first wall and blanket regions of deuterium-tritium (D-T) fusion reactors is recognized as one of the key challenges remaining in the program aimed at producing commercial fusion power. IFMIFs mission is (i) to provide a neutron source with an energy spectrum simulating that of fusion neutrons at sufficient intensity and irradiation volume to test samples of candidate materials up to about full lifetime of anticipated use in a fusion DEMO reactor in a reasonably short operation time, and (ii) to calibrate data generated from fission reactors and particle accelerators. Initial studies have indicated that a volume of about 0.5 L is required in a region producing a flux equivalent to 2 MW/m^2 (0.9 x 10^{18} n/m^2-s) or greater. A fraction of this volume, about 0.1 L would be available at a flux equivalent to 5 MW/in^2 for accelerated testing. The design concept consists of a 40 MeV deuteron accelerator. The deuterons interact with a flowing liquid lithium target (D-Li) producing high energy neutrons with a peaked flux around 14 MeV. The resulting high energy neutrons will interact with a set of test assemblies located immediately behind the Li-Target. Designs for the four major technical subsystems

● Accelerator System

● Lithium Target System

● Test Facility System, and

● Conventional Facilities

have been developed in parallel during the CDA phase and extended during the CDE phase (1997-98). In 1999, progress was reviewed and checked with international conference calls and by meetings of each of the three main facility groups (Accelerator, Target and Test Facilities). Meetings of the Subcommittee and design leaders were held to review the results of the work and to plan for the work in 2000.

Within the present key element technology phase, the activities at Forschungszentrum Karlsruhe concentrate on key engineering development items of the Test Facility System as well as on an optimization of the suitability and of costs. Below, the activities of the reporting period are summarized. [1,2,3,4].

1. Test Facilities Design improvements

During the year 1999, a staged and reduced cost concept was proposed by the Japanese colleagues. One part of the cost reduction was suggested to result from size reduction and simplification of the IFMIF test cell design. This was achieved by going from two test cells to one test cell as a result from skipping the IFMIF 500 mA accelerator upgrade option. Furthermore, the NaK cooled test assembly option was cancelled.

In a third step the test cell size was reduced. This is shown in the figures 1,2 and 3. The depth of the test cell was shrunk to 2.5 m.
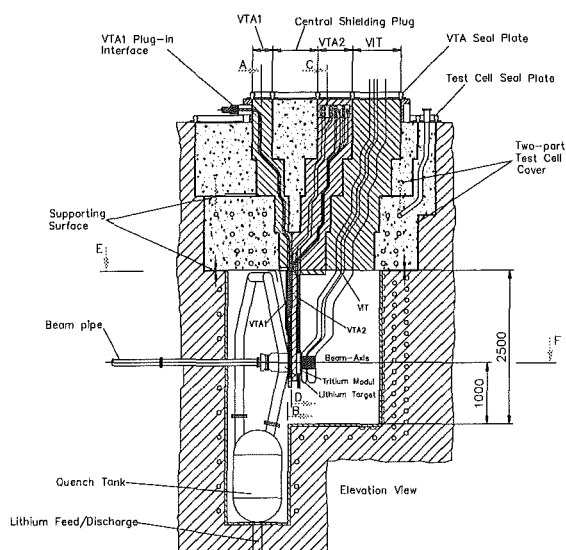
Fig. 1: Elevation view of the reduced size test cell. The cell is now 2.5 m long, 2.5 m high and 3 m wide. The shielding body from the CDA design could be eliminated and due to the reduced span the test cell cover can be less heavy. The VTA's got only minor design changes.
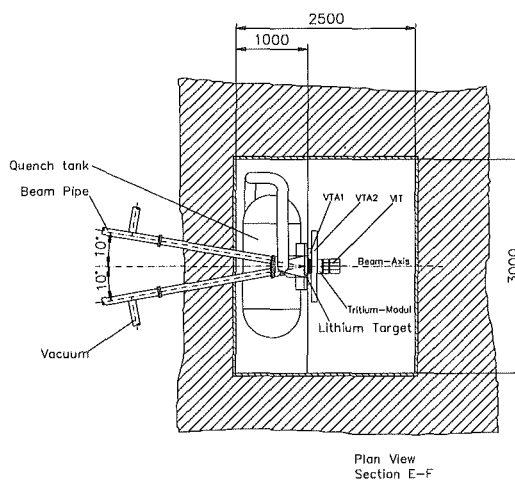
Fig. 2: Plan view of the reduced size test cell. Remarkable is that in the new design the beam lines come in at the same elevation.
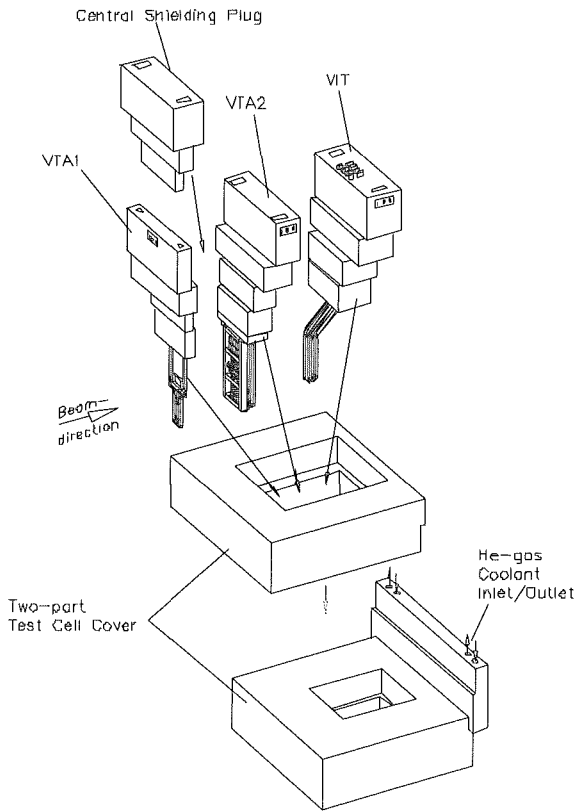
Fig. 3: Explosion view of the VTA's, VIT and the reduced size two part test cell cover.

One main achievement is that also after size reduction of the test cell the original mission of IFMIF could remain unchanged.

2. Neutronics and Users Aspects

Neutronics work has focused in the reporting period on improvement of the IFMIFs irradiation capabilities, on further cross section evaluation and on the analysis of the IFMIF simulation experiment performed earlier. The nuclear data evaluation work was done in co-operation with the Institute of Nuclear Power and Engineering (INPE), Obninsk, Russian Federation.

2.1 Improvement of the IFMIF irradiation conditions

The irradiation conditions in the IFMIF test cell are characterized by hydrogen (H) and helium (He) gas production and by the primary knock-on atom (pka) distribution and displacement damage production (dpa). For iron, a comparison of H, He and dpa production rates between DEMO first wall and IFMIF high flux test region is given in table 1.

Table 1: Comparison of irradiation parameters for iron in the high flux test region of IFMIF with DEMO first wall data. Appm is atomic parts per million, dpa is displacements per atom and fpy is full power year.

Irradiation parameter	IFMIF	DEMO
Total neutron flux [n/(s cm^2)]	$4 \times 10^{14} - 10^{15}$	7.1×10^{14}
Hydrogen Production [appm/fpy]	1000 – 2500	780
Helium production [appm/fpy]	250 – 600	198
Displacement production [dpa/fpy]	20 – 55	19
H/dpa ratio [appm/dpa]	35 – 50	41
He/dpa ratio [appm/dpa]	9.5 – 12.5	10.4

With respect to materials development IFMIF meets all DEMO first wall requirements and especially the gas to dpa ratios are covered quite well.

Since the general data like H, He and dpa production look quite good it is not easy to understand why further improvements for the irradiation capabilities are necessary. Characterizing displacement damage includes also the spectral distribution of the primary knock-on atoms. This distribution depends strongly on the neutron spectral distribution. The important point is the defect morphology generated under neutron irradiation. Low energetic neutrons preferably produce Frenkel defects while higher energetic neutrons produce more likely large defect cascades that leads finally to different changes in material properties. For that reason it is really necessary to achieve also for the pka-spectra a good agreement between IFMIF and DEMO conditions.

The displacement damage is calculated by use of the standard NRT-model. The function W(T) gives the fraction of displacement damage as a function of pka-energy. This function allows to characterize the ratio of point defects versus displacement cascades. The objective is to adjust the IFMIF neutron field in such a manner that the IFMIF and DEMO W(T) function fit best. The comparison of the IFMIF and DEMO neutron spectra shows some lack of low energy neutrons for IFMIF.

In order to find out how sensitive the neutron spectrum impacts on the W(T) function a sensitivity study was carried out. The W(T) functions were calculated for a DEMO first wall spectrum as it is and for cases with the neutron flux set to zero below a certain neutron energy threshold. The result is shown in figure 4.
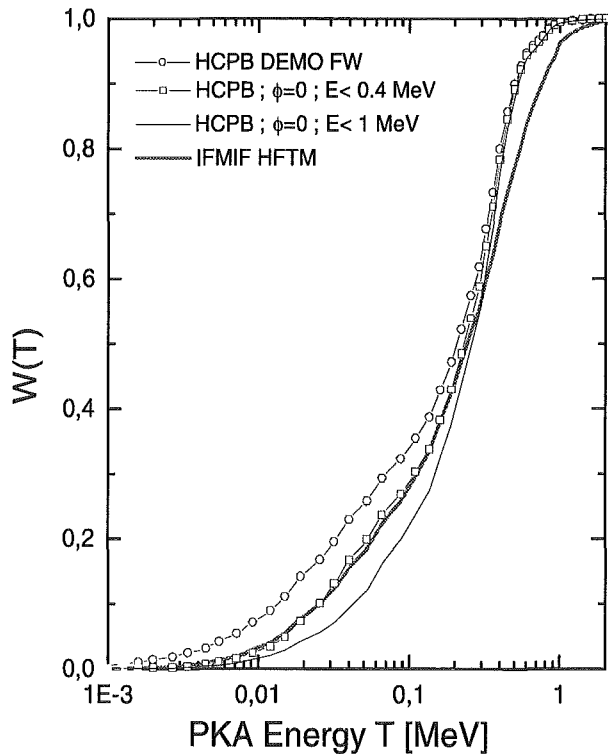
Fig. 4: Comparison of W(T) functions for the Helium Cooled Pebble Bed (HCPB) DEMO blanket ant the IFMIF high flux test region.

Not shown are neutrons for a threshold below 0.1 MeV which make almost no effect on the W(T) function. For a 0.4 MeV

threshold DEMO is quite close to IFMIF and for a 1 MeV threshold DEMO drops significantly below IFMIF. That means, that the IFMIF neutron spectrum suffers most from missing neutrons in the energy range between 0.1 MeV and 0.4 MeV. In order to generate neutrons in this energy range a neutron moderator/reflector component placed in the IFMIF test cell was expected to be a good choice.

The IFMIF test cell is designed to house three test modules for the high, medium and low flux region. To put additionally a neutron moderator in the test cell is not simple. Due to the high loads the moderator material must have a high melting point, a good thermal conductivity and good neutronic properties as high back scattering, good neutron multiplication and low neutron absorption. As a material that combines these properties tungsten was selected. An advanced test module design for the medium flux test region foresees in-beam fatigue irradiation experiments with an universal testing machine (UTM). The UTM is placed at the front part of the medium flux region. Figure 5 shows a horizontal cross section for that setup.
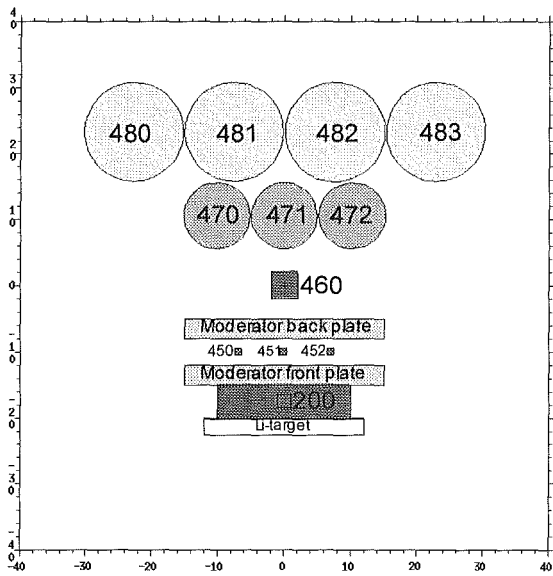
Fig. 5: Horizontal cross section throughout the IFMIF test cell. The deuteron beams come from the bottom. Cell 200 represents the high flux region, cells 450 – 460 represent the medium flux region and cells 470 – 483 the low flux region. The tungsten moderator is mounted within the UTM frame and it is divided into a front and a back plate.

The cells used in the Monte Carlo MCNP-4B calculations are numbered from #200 to #483. The moderator component is placed within the frame of the universal testing machine. The three in-beam fatigue specimen (#450, #451 and #452) are located in between the moderator plates. The tungsten moderator plates are dimensioned as 30 cm wide, 20 cm high and 3 cm thick.

MCNP calculations show that the nuclear and gamma heating peak load is about 1.5 W/g. With an active He-gas cooling system mounted to the He-cooling loop of the UTM the W-moderator can be operated safely at 400°C.

The main objective is to improve the neutronic conditions in the high flux test region. However, the moderator cannot only change the neutron spectrum selective for the high flux region. The neutron field is altered due to neutron scattering and (n,2n) reactions in the moderator everywhere in the IFMIF test cell with

a growing effect in downstream direction. Thus, for the high flux region only a moderate change of the neutron spectrum occurs which results in a small shift of the W(T) function as shown in the top plot of figure 6.

For the medium and low flux positions the IFMIF W(T) function shifts significantly towards DEMO and slightly surpasses the curve in the intermediate energy range. A representative plot for the medium and low flux positions is given in the bottom plot of figure 6.
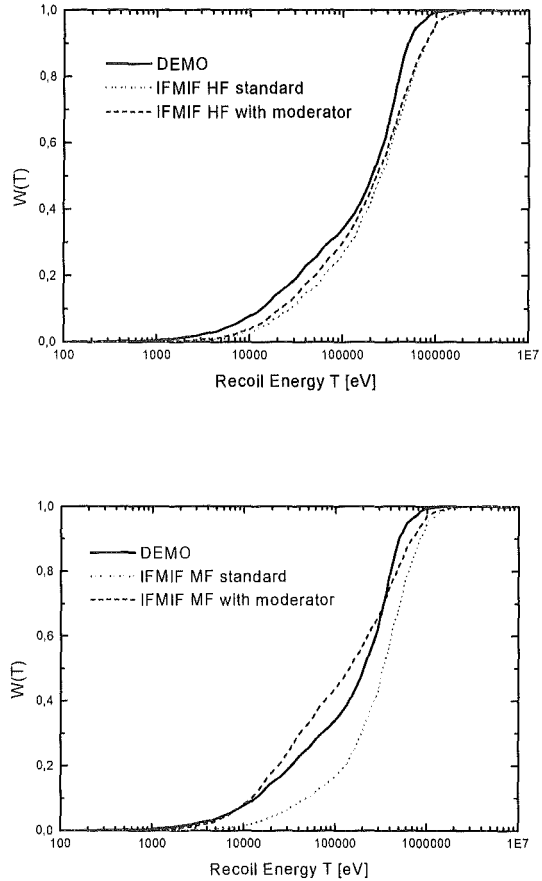
Fig. 6: Comparison of W(T) function for DEMO and IFMIF for iron. The top plot shows a representative location in the high flux region (HF) and the bottom plot shows the situation in the medium flux region (MF). The dotted line stands for the standard case and the dashed line for the moderator case.

It clearly shows that the IFMIF W(T) function can be improved and therefore the point defects to cascades ratio in IFMIF irradiated samples can be well adjusted to DEMO requirements by a neutron moderator of the proposed design.

Furthermore, in the medium flux region also ceramic breeding materials like Li_2O, Li_4SiO_4 etc. are planned to be irradiated. Lithium consists of the two stable isotopes ^6Li and ^7Li. The tritium breeding reaction in fusion reactors is mainly driven by about 95% through the $^6Li(n,t)^4He$ reaction with a very high thermal neutron capture cross section. The tritium reaction in ^7Li has a threshold of about 3 MeV. Comparing the tritium breeding capabilities between IFMIF without a moderator and DEMO shows that in the IFMIF medium flux region due to the high energy neutrons the tritium production is for about 50%

governed by ^{7}Li. The neutron moderator, however, can considerably lower the ^{7}Li fraction of the total tritium production and thus also improve the irradiation conditions for breeding ceramics. This topic is still under investigation and further results are expected soon.

In general it was found that a neutron moderator component levels the gas to displacement damage ratios for iron as listed in table 2. The required data for DEMO first wall are for H/dpa = 41 appm/dpa and for He/dpa = 10.4 appm/dpa as listed in table 1. Comparing table 2 with these requirements shows that in the high flux region the use of a W-moderator leads to an improvement of about 5 %. In the medium and low flux regions, however, a significant drop of the gas to dpa ratios occur right to the required values. The only drawback of the moderator is that the total production rates in the medium and low flux regions decrease.

Table 2: The tables show the conditions in the high, medium and low flux regions at typical locations for the flux and damage parameters in iron. The top table is for the standard case without moderator and the bottom table is for the tungsten moderator case.

	High Flux	Medium Flux	Low Flux
Flux [n/(s cm**2)]	6.7E+14	1.5E+14	4.4E+13
Hydrogen [appm]	1621	597	123
Helium [appm]	419	153	31.5
Damage [dpa]	33.9	9.7	2.3
H/dpa [appm/dpa]	47.7	61.4	53.6
He/dpa [appm/dpa]	12.3	15.7	13.7

	High Flux	Medium Flux	Low Flux
Flux [n/(s cm**2)]	8.0E+14	3.1E+14	2.5E+13
Hydrogen [appm]	1631	381	30.3
Helium [appm]	421	97.8	7.8
Damage [dpa]	35.9	9.2	0.7
H/dpa [appm/dpa]	45.4	41.4	42.0
He/dpa [appm/dpa]	11.7	10.6	10.8

2.2 Intermediate Energy Neutron Cross Section Evaluations for Medium and Heavy Nuclides

The Intermediate Energy Activation File (IEAF) is now complete for all target nuclides from Z=6 (carbon) to 83 (bismuth). For each of these elements, all the target isotopes present in the European Activation Library EAF-97 are included. For every target, IEAF comprises activation and transmutation cross sections for all kinematically allowed reactions up to 150 MeV incident neutron energy. EAF-97 is also the source of the data below the neutron energy of 20 MeV. IEAF was prepared according to the ENDF-6 format rules using the option MT=5 with LAW=0 file on MF=6.

2.3 Preparatory Work for Evaluating d+Li and n+Li Cross Sections

For improving the physics basis of the McDeLi neutron source routine, an evaluation of deuteron cross sections on Li-6 and Li-7 for the deuteron energy range 40 ... 0 MeV is required. The nuclear models employed in the known cross section calculation codes, however, are not valid for very light target nuclei such as the lithium isotopes. Therefore, development of suitable methods was started, again in co-operation with INPE Obninsk. Part of these methods will also be useful for evaluating the interaction of neutrons with lithium, which is likewise required, not so much for effects in the lithium target of IFMIF (where the deuteron interactions dominate) but in view of IFMIF irradiations

of breeding materials. A joint publication about these developments is being prepared.

2.4 Measurement of IFMIF Source Neutron Spectrum

An experiment had been carried out in 1997/1998 in which 40-MeV deuterons from the Karlsruhe Isochronous Cyclotron impinged on a thick lithium target. Results of this experiment for the radioactivity production (Tritium and Be-7) in the lithium target were given in the previous report. The analysis of the neutron spectrum measurement by multifoil activation in co-operation with JAERI, Tokai-mura, Japan was finished in the present reporting period [5]. The neutron spectrum is shown in Fig. 7.
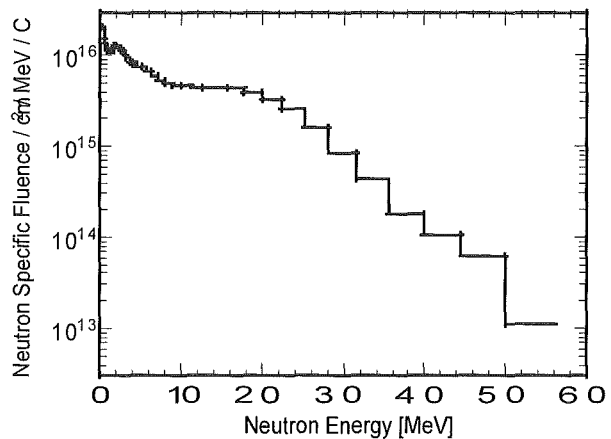
Fig. 7: Evaluated neutron spectrum in the Li-target

2.5 Measurement of Structural Materials Activation in IFMIF Neutron Field

The knowledge of the neutron spectrum enabled also an analysis of the structural materials activation measurement which had been made within the same experiment [6], also in co-operation with JAERI, Tokai-mura, Japan. Four samples, the standard chromium-nickel-molybdenum steel SS-316, the low activation chromium-tungsten steel F82H, pure vanadium, and the V-4Ti-4Cr alloy, were irradiated simultaneously for 2 hours at a flux density of about 10^{11} n/cm^2/s. On each sample, gamma-ray spectrometry with an efficiency calibrated high purity germanium detector was then repeatedly performed after cooling times ranging from 1 hour to 5 months. In total, 44 different radionuclides having halflives between 42 minutes and 5.3 years were identified. The expected radioactivities were calculated using the ALARA inventory code and the IEAF cross section library (see section 2.2 above). The calculation-experiment comparison resulted in C/E ratios which are given in Table 3.

The seven C/E values given in italics deviate from unity for well-known reasons not connected with IEAF evaluations [6]. Among the remaining 69 C/E ratios, 52 (= 75%) do not deviate from unity by more than a factor of 2 if their experimental uncertainties are taken into account. This indicates a less-than-perfect but satisfactory performance of this first version of IEAF. A similar test for the IEAF evaluations proper, without the EAF data incorporated for energies below 20 MeV, can be made by considering only those activation reactions not contained in EAF: (n,pα) and (n,dα) reactions as well as any reactions having thresholds above 20 MeV. Of the 12 C/E values in Table 4 satisfying this criterion, 7 (= 58%) fulfil the above condition.

Table 3: Calculation-to-experiment ratios C/E for induced radioactivity (Blank field: nuclide not found in experiment. *Italic* numbers: see text. Estimated experimental uncertainty ±10% except where indicated)

Nuclide	$T_{1/2}$	SS-316 C/E	F82H C/E	V-alloy C/E	V-pure C/E
Ca-47	4.5 d			0.49 ±15%	0.71
Sc-43	3.9 h			0.024±30%	
Sc-44	3.9 h			1.50 ±20%	
Sc-44m	2.4 d			0.71 ±30%	
Sc-46	84 d	< 1.29	0.22	0.91	0.77
Sc-47	3.4 d		*6.50*	*7.73*	*8.67*
Sc-48	44 d	1.16	0.69	0.98	1.05
V-48	16 d	2.70	2.70	1.11	1.14
Cr-48	22 h	4.54 ±30%	3.25 ±30%		
Cr-49	42 m	0.80 ±40%	0.46 ±30%	0.75 ±15%	
Cr-51	28 d	1.06	1.08	1.00	*0.0004*
Mn-52	5.6 d	3.28	3.78	*0.05 ±25%*	
Mn-54	312 d	1.05	1.06		
Mn-56	2.6 h	1.11	1.12		
Fe-52	8.3 h	2.49 ±50%	2.33 ±15%		
Fe-59	45 d	0.85			
Co-55	18 h	2.69	*0.004*		
Co-56	77 d	3.60	*0.02*		
Co-57	272 d	1.02	0.80 ±15%		
Co-58	71 d	1.13	1.21		
Co-60	5.3 a	1.01	0.04 ±15%		
Co-61	1.7 h	4.48 ±40%			
Ni-56	6.1 d	1.61			
Ni-57	36 h	1.25 ±20%	0.95 ±30%		
Y-87	80 h	0.30 ±20%			
Y-87m	13 h	0.08 ±30%			
Y-88	107 d	1.01 ±35%			
Zr-86	17 h	0.03 ±25%			
Zr-88	83 d	1.01 ±60%			
Zr-89	78 h	1.25			
Zr-97	17 h	0.03 ±20%			
Nb-90	15 h	13.7			
Nb-92m	10 d	1.23		<0.92	<1.32 ±30%
Nb-95	35 d	1.63			
Nb-95m	87 h	1.17			
Nb-96	23 h	1.76			
Mo-90	5.7 h	1.69 ±60%			
Mo-93m	6.9 h	1.17 ±20%			
Mo-99	66 h	1.26			
Tc-99m	6.0 h	1.26	1.17 ±40%		
Ta-182	114 d		1.29		
Ta-183	5.0 d		1.20 ±20%		
Ta-184	8.7 h		3.10 ±40%		
W-187	24 h		0.54		

Literature:

[1] A. Möslang (ed.), IFMIF International Fusion Materials Irradiation Facility, Conceptual Design Evaluation Report, FZKA 6199, Forschungszentrum Karlsruhe, January 1999

[2] A. Möslang et al., Suitability and Feasibility of the International Fusion Materials Irradiation Facility (IFMIF) for Fusion Materials Studies, 17th IAEA Fusion Energy Conference, October 19-24, 1998, Yokohama, Japan

[3] E. Daum, How to improve the irradiation conditions for the International Fusion Materials Irradiation Facility IFMIF, ICFRM-9, Oct. 10-15, 1999, Colorado Springs, USA, to appear in Journal of Nucl. Mat.

[4] E. Daum, K. Ehrlich, K. Jitsukawa, S. Matsui, A. Möslang, The International Fusion Materials Irradiation Facilty IFIMIF - An Overview on User Aspects, ISFNT-5, Sept. 19-24, 1999, Rome, Italy, to appear in Fus. Eng. and Des.

[5] F. Maekawa, U. von Möllendorff et al., Proc. ISFNT-5, Rome, Sept. 1999

[6] U. von Möllendorff, F. Maekawa et al., Proc. ISFNT-5, Rome, Sept. 1999

Staff:

G. Bürkle
E. Daum
K. Ehrlich
U. Fischer
H. Giese (now at IHM)
F. Maekawa, JAERI
A. Möslang
U. von Möllendorff
P. Wilson

Nuclear Data Base

ND 1.2.1, ND 1.2.2, ND 1.3.1, ND 2.1.3
Nuclear Data Base

The development of a nuclear data base is an integral part of the Long-term Fusion Technology Programme. In the framework of this programme, FZK contributes to the development and qualification of the European Fusion File (EFF), the European Activation File (EAF) and the International Fusion Evaluated Nuclear Data Library (FENDL).

Integral Data Testing and Sensitivity/Uncertainty Analyses for EFF-3 Data Evaluations

In the framework of the EFF project, integral data tests and sensitivity/ uncertainty analyses are being performed as part of the QA (quality assurance) procedure for new and updated EFF data evaluations. This includes benchmark analyses based on Monte Carlo calculations for suitable integral experiments as well as sensitivity and uncertainty calculations using the Monte Carlo point detector technique to assess the data related uncertainties.

Beryllium

According to the EFF priorities, the main focus over the reporting period was on the new EFF-3.0 ^{9}Be evaluation. In addition to the previously reported analysis of the KANT spherical shell experiment [1], the time-of-flight (TOF) experiment of FNS/JAERI on a 15.24 cm thick Beryllium slab (with measurements of angular neutron leakage flux spectra) has been investigated and sensitivity/uncertainty analyses have been performed for the two experiments [2].

The neutron multiplication, measured in the spherical shell experiment, can be reproduced within 1% with EFF-3 ^{9}Be-data. The associated calculated uncertainty due to uncertainties of the related cross-section data (excitation function) is at the same level. In the FNS slab experiment, the calculated leakage flux uncertainties are at a similar level. There is, however, a trend for an increasing uncertainty with increasing angle. For the total leakage flux, e. g., the uncertainty increases from about 0.5% at small forward angles to about 1.5% at 66.8 degrees. The uncertainty of the flux above 13 MeV is between 1.5% (low angles) and 7% (66.8 degrees). These uncertainties, however, do not yet take into account the uncertainties of the secondary distribution (energy, angle) of neutrons emitted through the (n,2n)-reaction which may dominate the total uncertainty.

When comparing calculated and measured neutron flux integrals at the various angles considered in the FNS TOF experiment, good agreement is observed with the new EFF-3 ^{9}Be-evaluation (Fig. 1). There is, however, still an inconsistency to the results of the spherical shell experiments where there is a significant underestimation of the measured leakage spectra in the energy range around 1 MeV with EFF-3 data. This is also true for FENDL-1 and –2 Beryllium data, whereas the old EFF-1 data show the best agreement. There are indications that this inconsistency is caused by differences in the secondary energy-and/or angular distributions. This suggests to re-analyse the secondary energy and angle distribution data of Beryllium with regard to their effect on the neutron flux spectra.

Iron

Benchmarking of the new ^{56}Fe EFF-3.1 data evaluation has been performed for the FNS iron slab experiment with measurements of angular neutron flux spectra [3] and the FNG bulk shield experiment for ITER [4]. A clear improvement over the previous ^{56}Fe evaluations has been found for the neutron spectra although the high energy component (E>10 MeV) is still underestimated by about 10 % in most cases. There is excellent
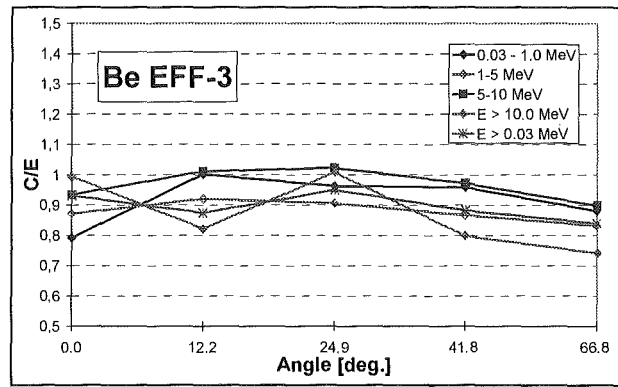
Fig. 1: FNS/JAERI Beryllium slab TOF-experiment: calculation vs. experiment (C/E) for neutron flux integrals
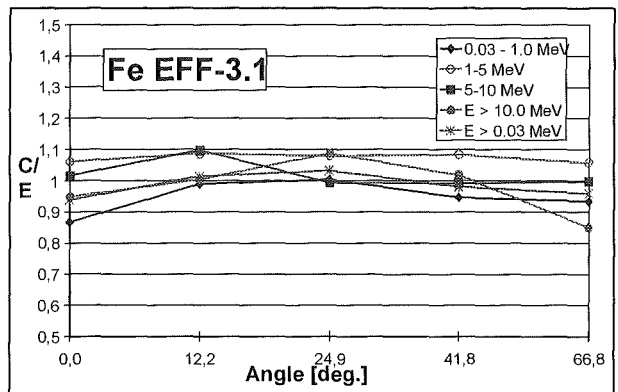
Fig. 2: FNS/JAERI Iron slab TOF-experiment: calculation vs. experiment (C/E) for neutron flux integrals

agreement between calculated and measured neutron flux spectra in the FNS experiment, see e. g. Fig. 2 for the neutron flux integrals. Photon flux spectra are in general well reproduced even at the deepest location in the bulk shield experiment. Sensitivity and uncertainty analyses based on the Monte Carlo point detector technique have been started for the FNS Iron slab TOF experiment.

Development of Monte Carlo Sensitivity and Uncertainty Computational Schemes

With the current EFF-programme, the development of computational schemes was started to enable sensitivity/uncertainty calculations of secondary distributions on the basis of the Monte Carlo point detector technique with the objective to implement it into the MCNP code. The Legendre coefficients of the secondary angular distributions (SAD) have been identified as suitable parameters for Monte Carlo SAD sensitivity calculations. Over the reporting period, the basic Monte Carlo algorithm for the calculation of the sensitivities to these parameters with the differential-operator method has been developed. The next step is dedicated to the elaboration of the detailed formulae taking into account the specific kind of responses (point detector) and the characteristics of the MCNP code.

EFF-3 Co-Variance Data Processing with Extended Options

Co-variance data with extended options for secondary distributions are being introduced in EFF-3 data evaluations to

enable corresponding uncertainty calculations. Co-variance data for ^{56}Fe (EFF-3.0, file 33 for excitation functions, file 34 for angular distribution data, see Fig. 3) and ^{9}Be (EFF-3.0, file 33) have been become available so far. These co-variance data have been processed in the VITAMIN-J group structure and applied with sensitivity/uncertainty calculations for Beryllium and Iron integral experiments using both the deterministic and the probabilistic approach. For iron, a considerably reduced uncertainty has been obtained with the Fe-56 EFF-3.0 covariance data. On average, the calculated uncertainty is reduced by a factor 2 as compared to EFF2.4 and by a factor 3 as compared to FENDL-1 (ENDF/B-VI).

Literature:

[1] Nuclear Fusion Project, Annual Report of the Association Forschungszentrum Karlsruhe/EURATOM October 1997 – September 1998, FZKA-6200, EUR-18621EN (November 1998), pp.147-48.

[2] U. Fischer, R. L. Perel, H. Tsige-Tamirat, Monte Carlo Uncertainty Analyses for Integral Beryllium Experiments, 5th International Symposium on Fusion Nuclear Technolpgy, Rome, 19-24 September 1999.

[3] U. Fischer, Y. Wu: Benchmark analyses of the TUD and FNS iron transmission experiments with EFF-3.0, -3.1 and FENDFL-1, -2 data, Report EFF-Doc-686, April 1999

[4] U. Fischer, Y. Wu, W. Hansen, D. Richter, K. Seidel, S. Unholzer: Benchmark analyses for the ITER Bulk Shield Experiment with EFF-3.0, -3.1, and FENDL-1, -2 nuclear cross-section data, Report EFF-Doc 693, April 1999

Staff:

U. Fischer
I. Kodeli (Josef-Stefan-Institute Ljubljana)
R. Perel (Hebrew University of Jeruslalem)
H. Tsige-Tamirat
E. Wiegner
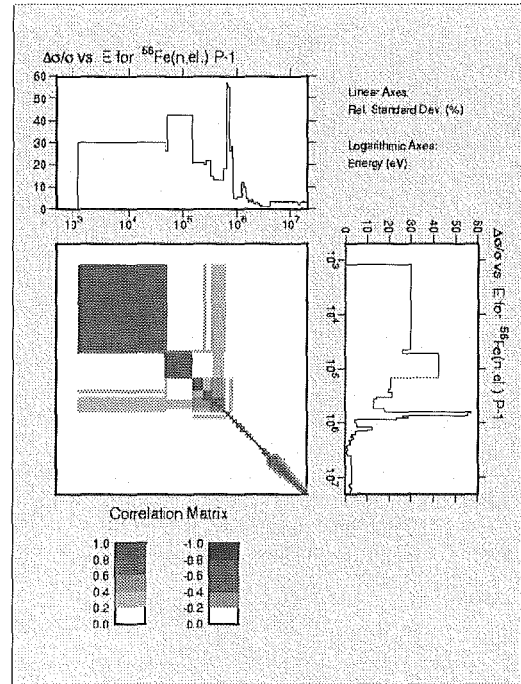
Fig. 3: ^{56}Fe EFF-3 co-variance matrix for the first order Legendre coefficient of the elastic scattering angular distribution.

ND 2.2.2
Activation Library

14-MeV activations by TU Dresden

Safety and environmental assessments are essential parts of fusion device development to ensure the attractiveness of fusion power. Safety analyses of plant designs, such as Next Step Device (ITER) or DEMO, require among other things a reliable data base for neutron-induced radioactivity.

A joint effort of integral experiments has been started to validate the European Activation System (EASY) [1] which represents the reference system for the ITER design. Its main components are the European Activation File (EAF) and the inventory code FISPACT developed at Culham.

Activities induced in fusion reactor materials in a white spectrum of fast neutrons ranging up to energies of 20 MeV are investigated at Karlsruhe. 14-MeV neutrons (fusion peak) are used by TUD, in collaboration with CCA Sergiev Posad and RRC „KI" Moscow, to activate the same materials. In the first phase SS316 (the structural material chosen for ITER; correctly specified AISI 316 LN (IG)) and the low-activation steels MANET and F82H were irradiated [2]. Also in the second phase of the experiments, structural materials were used, namely the vanadium alloys V3Ti1Si, V4Ti4Cr and V5Ti2Cr [3], which are considered as advanced materials because of their low-activation behaviour. In 1999 the investigations were extended to the potential structural material SiC and to the breeder material Li_4SiO_4.

The irradiations were carried out at the high-intense neutron generator SNEG-13 [4] at Sergiev Posad. The neutrons were generated by the interaction of 280-keV deuterons with tritium absorbed in a Ti layer deposited on a rotating target, resulting in a mean neutron energy at sample position of 14.93 MeV with a spread of 0.54 MeV f. w. h. m. of the peak. The applied neutron fluences were determined via activation measurement of niobium foils by the reaction $^{93}Nb(n,2n)^{92m}Nb$.

The activation profile of SiC and of Li_4SiO_4 suggested to start the irradiations with a short one (30 min) and with fluences of about 10^{11} neutrons/cm^2 to measure the dominant activities with half-life of some minutes produced mainly on the Si isotopes.

The results of this first step of measurements analysed with EASY-97 are presented in Tables 1 and 2.

Literature:

[1] R. A. Forrest, J.-Ch. Sublet and J. Kopecky, The European Activation System, Proc. Int. Conf. On Nuclear Data for Science and Technology, Trieste, May 19-24, 1997, ed. by G. Reffo, p. 1140.

[2] H. Freiesleben, V. Kovalchuk, D. Markovskij, D. Richter, K. Seidel, V. Tereshkin and S. Unholzer, Experimental investigation of radioactivities induced in fusion reactor materials, Fusion Engineering and Design 42(1998)337; Nuclear Fusion Project, Annual Report of the Association Forschungszentrum Karlruhe/EURATOM, Oct. 1996 – Sept. 1997, comp. by G. Kast, FZKA 6050, 1997, p. 131.

[3] K. Seidel, R. A. Forrest, H. Freiesleben, V. D. Kovalchuk, D. V. Markovskij, D. Richter, V. I. Tereshkin and S. Unholzer, Measurement and analysis of radioactivuty induced in vanadium alloys by 14-MeV neutrons, Proc. Of the 20th Symposium on Fusion Technology, Marseille, Sept. 7-11, 1998, p. 1361; Nuclear Fusion Project, Annual Report of the Association Forschungszentrum Karlruhe/EURATOM, Oct. 1997 – Sept. 1998, comp. by G. Kast, FZKA 6200, 1998, p. 149.

[4 V. D. Kovalchuk, et al., Neutron generator SNEG-13; neutron and photon field characteristics, Report IAE-5589/8, Russian Research Centre "Kurchatov Institute", Moscow, 1992.

Staff:

H. Freiesleben
D. Richter
K. Seidel
S. Unholzer

Table 1: Radionuclides produced in **SiC**, their half-life, the γ-rays used to determine the activity, the relative contribution of various nuclear reactions and the ratio of calculated-to-experimental activity (C/E) obtained for several decay times, as well as their percentage (f_D) to the total γ-dose rate at these times.

Radio-nuclide	Half-life (min)	γ-Energy (keV)	Reaction Contribution (%)	Decay Time (min)							
				2.97		7.17		12.8		24.1	
				f_D	C/E	f_D	C/E	f_D	C/E	f_D	C/E
^{27}Mg	9.46	844 1014	$^{30}Si(n,\alpha)$ 92.5 $^{27}Al(n,p)$ 7.5	1.03	0.99	2.59	1.02	7.79	1.02	27.6	0.99
^{28}Al	2.25	1779	$^{28}Si(n,p)$ 99.5 $^{29}Si(n,d)$ 0.5	95.0	0.85	88.8	0.91	70.5	0.92		
^{29}Al	6.57	1273	$^{29}Si(n,p)$ 97.5 $^{30}Si(n,d)$ 2.5	3.90	0.96	8.57	1.00	21.5	0.96	52.9	1.05

Table 2: Radionuclides produced in **Li$_4$SiO$_4$**; symbols as in Table 1.

Radio-nuclide	Half-life (min)	γ-Energy (keV)	Reaction Contribution (%)	Decay Time (min)					
				4.43		10.5		20.9	
				f_D	C/E	f_D	C/E	f_D	C/E
^{27}Mg	9.46	844 1014	^{30}Si(n, α) 97.0 ^{27}Al(n,p) 3.0	1.36	**0.87**	4.87	**0.83**	21.3	**0.83**
^{28}Al	2.25	1779	^{28}Si(n,p) 99.5 ^{29}Si(n,d) 0.5	93.4	**0.83**	79.8	**0.81**		
^{29}Al	6.57	1273	^{29}Si(n,p) 97.5 ^{30}Si(n,d) 2.5	5.17	**0.99**	15.2	**0.99**	47.5	**0.99**

ND 2.2.3
White-Spectrum Activations for Validation of the European Activation File (EAF)

A sample of SiC was activated in the d-Be neutron field at a flux density of about 2×10^{11} n/s/cm^2 for 19 hours. Gamma spectrometry with an efficiency calibrated HPGe detector was performed after different cooling times ranging from 23 min to 256 days. Analysis of the data is in progress.

Samples of pure nickel and copper were activated mainly to check the most important production reactions for Co-60 in fusion neutron fields, ^{60}Ni(n,p)^{60}Co and ^{63}Cu(n,α) ^{60}Co. Surprisingly, several of the *C/E* ratios for the more important product nuclides are around 1.4, which suggests an error in the expertimental fluence normalization rather than in the cross sections. A re-analysis of this experiment in this respect is in progress. Independently, an activation product not predicted by the EAF-based calculation was identified: Fe-59 from the ^{63}Cu(n,pα)^{59}Fe reaction. The cross section for this reaction, averaged over the d-Be source spectrum, was found to be 20 μb $\pm$ 20%.

The planned irradiation of a Li$_4$SiO$_4$ sample has required some special preparations. Because of the strong space dependence (inhomogeneity) of the d-Be neutron field, the geometry of the irradiated sample is important, and a powder sample is impractical. Therefore, Li$_4$SiO$_4$ was fabricated into solid discs of 10 mm diameter and 1.5 mm thickness by a hot pressing/sintering process. Two such samples were given to TU Dresden to be used in their 14-MeV activation experiments. Our own irradiation of a disc will be made shortly.

Staff:

H. Giese (now at IHM)
U. von Möllendorff
H. Tsige-Tamirat

Safety and Environment

SEAFP 2
Long Term Safety Program

**Task S 5:   Less Conservative and More Realistic
                    Analyses**

Subtask 1:   Removal of Conservatisms

A shorting arc at the bus bar of a TF coil is considered as a key event for future reactor safety studies. Previous investigations have shown that a quench in the shorted coil is necessary in order to keep a possible damage to the cryostat wall within limits.

In a first analysis a quench was achieved only shortly before the current in the shorted coil reached its peak value. I.e. there is a danger that a quench might not be initiated. To achieve the quench earlier and more safe a model considering hysteresis and coupling losses in the conductor was included in a second analysis. As expected, the quench was initiated earlier, however the difference is not large. Further investigations should be made to get a better understanding of the arc behavior at the bus bar and the quench propagation from the bus bar to the coil. Special care must be taken for short formation between adjacent pancakes and turns because shorts within the coil can bridge turns and pancakes so that they are excluded from the designed current path and are lost for energy deposition. Apart from this shorted turns reduce the inductance of the coil and increase the coil current.

Staff:
R. Meyder

Preparatory Work for a Power Plant Conceptual Study

Preparatory Work for a Power Plant Conceptual Study

Field: Plant Availability

PPA 1 High Heat Flux Components

PPA 1.3 Helium Cooling

PPA 1.3.2 Helium-cooled HHFC of Unconventional Design

High Heat Flux Components (HHFC) developed in the past focused on water cooling with typical heat loads of up to 20 MW/m^2. They were based on copper alloys with their exceptionally high thermal conductivity as structural material. The present aim is to exploit helium cooling of HHFCs with the special features of producing high-grade heat (for the benefit of power conversion), compatibility with helium-cooled blanket systems (economics), and its inert nature (avoiding chemical reaction hazards). Especially the high-grade heat calls for elevated coolant temperature and this, in turn, requires the use of refractory alloys as structural materials. Thus, the objective is to explore the manageable heat flux limits of helium-cooled divertor concepts that combine high thermal conductivity and high temperature resistant materials, good wall-to-coolant heat transfer characteristics and adequate coolant parameters, i.e., temperature, pressure and friction losses. Since a high wall-to-coolant heat transfer is considered as a key requirement, the task has been divided into two subtasks, PPA1.3.1reviewing conventional designs like wall roughening, ribs, swirl promoters etc., and this subtask PPA1.3.2 addressing unconventional heat transfer enhancement methods, in particular the porous media concept.

Main features of proposed concept

Considerations are based on a single-null divertor of the radiative type located at the bottom of the tokamak, similar to the configuration used in ITER. Thus, a large fraction of the total heat flowing into the divertor region has to be absorbed by the inboard and outboard target plates, constituting the heaviest loaded components with substantially peaked particle and heat flux profile. Therefore, the considerations focus on a typical unit cell (i.e., a single channel) of the target plates in terms of heat removal capability and lifetime performance, but taking into account the overall divertor configuration with respect to coolant parameters and heat rejection. Assumed divertor main data derived from PPA plant layout are summarised in Table 1. Key features of a possible target plate design are listed in Table 2.

Table 1: Typical thermal-hydraulic divertor characteristics

Total fusion power	3607 MW
Total power to divertor	672 MW
Outer/inner strike point radii on target plates	8.9 m / 6.1 m
Fraction of divertor power onto target plates	0.42
Coolant inlet/outlet temperature to divertor	400 / 800 °C
Coolant pressure inlet/outlet	8 / 7.2 MPa
Coolant mass flow rate	325 kg/s
Circulator power	48 MW

As armor material the only candidate left is tungsten (W) or a W-alloy based on wide experience from plasma facing components development in the past. Molybdenum alloy (TZM) or W have been chosen for the structure of the target plates with regard to thermal conductivity, high temperature strength and compatibility with the W armor. Ferritic martensitic steel is envisaged for the bulk of the divertor because of fabricability, neutron irradiation resistance, cost and thermo-mechanical properties.

The coolant temperatures are chosen according to a viable flow scheme in the divertor and to the structural materials involved along the following guidelines: (i) The temperature in the target plate structural material is dictated by embrittlement and strength arguments and should lie in the range 600–1200°C for TZM and 600-1800°C for W. (ii) The structural temperature in the rest of the divertor (dome, liners, casing etc.) should enable the use of ferritic martensitic steel, i.e., <650°C. (iii) The overall coolant inlet and outlet temperature should be suited for power conversion at acceptable pumping power. (iv) The limited wall-to-coolant heat transfer causes a substantial temperature difference that has to be taken into account (e.g., 500°C at 20000 W/m^2/K). These arguments lead to the flow scheme of routing the coolant first through the divertor body with inlet/outlet temperature of 400/600 °C and subsequently through the target plates with inlet/outlet temperature around 600/800 °C.

Table 2: Typical divertor target plate design values

Linear power to divertor target plates (per toroidal unit length)	3 MW/m
Coolant bulk temperature in target plates at points of peak heat flux	650 - 700 °C
Heat transfer enhancement system (see Fig. 1)	porous medium
Reference heat transfer coefficient (HTC) wall-to-coolant	20,000 W/m^2/K
Target plate unit cell dimensions (toroidal x poloidal)	0.036 m x 1.6 m
Structural material of target plate	TZM or W-alloy
Coolant channel inner diameter	0.028 m
Tungsten armor thickness (castellated)	3 mm

The target plate conceptual design is based on the porous medium (PM) heat exchanger concept that promises to provide sufficient wall-to-coolant heat transfer coefficient (HTC) of the order of 20000 W/m^2/K and beyond. The peripheral flow scheme has been adopted to a unit cell shown in Fig. 1. Helium is fed through the inner small tube, flows in two parallel paths in peripheral direction through the PM annulus and exits via the "half-moon" shaped channel. The PM insert covers only the heavily loaded part of the target plate, typically 0.6 m of the 1.6m long channels.
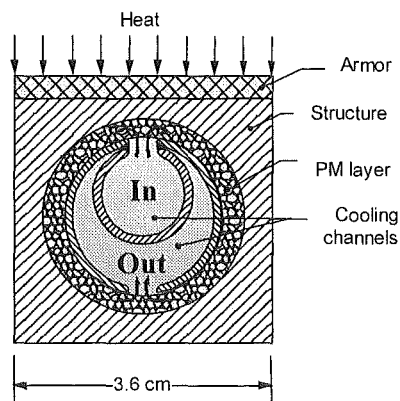
Fig. 1: Cross section of a target plate channel with porous media heat transfer enhancement

Results and limits of proposed concept

Parametric analyses have been performed related to the heat balance and thermal-hydraulics of the overall divertor, to local thermal-hydraulics in a typical flow channel adopting various types of PM heat enhancement designs, and to 3D thermal stress and deflection of a typical unit cell of the target plate.

Specific results for the set of parameters given in Tab. 1 and 2 are outlined below.

The pumping power of 48 MW for the whole heat transport system (corresponding to 7.1% of the total thermal divertor power) scales with the inverse of the system pressure and, hence, could be reduced on the expense of higher pressure. 60% of the pressure drop in the entire divertor circuit occurs in the 0.6 m long PM inserts, where the assumed fraction (42%) of the total divertor power produces an average heat load of, e.g., 5 MW/m^2. The mean temperature rise there amounts to ~170°C with a similar poloidal distribution as the applied heat load profile. Thus, local gas temperatures and, consequently, structural temperatures can become excessive for strongly peaked profiles. There is some freedom (perhaps ±50°C) to adapt the coolant inlet/outlet temperature to fit into an overall plant heat removal system.

The thermo-mechanical analysis focused on exploring the tolerable heat flux at the divertor plate with respect to temperature, stress and deflection limits. As mechanical constraints a 2-point support and a 3-point support of the 1.6 m long channels have been investigated. The results are listed in Tab. 3 for the two variants of structural materials and the conditions specified in Tab. 1 and 2. From each column the smallest heat flux value must be taken as the tolerable limit (bold face numbers in Tab. 3). It is obvious that the 2-point support must be ruled out because of excessive deflection, since for both materials the deflection criterion allows only a heat flux up to 1 MW/m^2. For the 3-point support the v. Mises criterion is the most stringent one, leading to tolerable heat loads of approximately 4 and 5 MW/m^2 for the W and TZM option, respectively. If the HTC could be improved, the tolerable heat loads would go up, for instance doubling the HTC would gain about 40%. The armor thickness can be increased by several mm before it becomes a limiting factor.

Table 3: Heat flux limits in MW/m^2 for target plates made of tungsten and molybdenum alloy

Structural material	W-Alloy		Mo-Alloy	
Type of channel support	2-pt	3-pt	2-pt	3-pt
Temperature criterion for heat sink (1800°C for W, 1200°C for TZM)	12	12	5.5	5.5
Temperature criterion for armor (2000°C)	10.5	10.5	9.5	9.5
v. Mises stress criterion (3Sm limit)	8.2	**3.9**	6.5	**4.8**
Deflection criterion (1 mm transverse)	**1**	>10	**0.7**	>10

Uncertainties in the results and open issues

The achievable HTC of PM, made of refractory materials in order to stand the high temperature, needs experimental proof with helium cooling. The value assumed in this study (20000 W/m^2/K) seems to be realistic, but the potential for improvements is judged to be small.

Uncertainties in the assessment are further induced by the mechanical properties of the structural materials. The data used are for stress relieved, unirradiated condition. Effects of irradiation, fabrication, alloying, component size, recrystallization and stress concentration are largely unknown. They may, in part, compensate each other.

Fabrication techniques for PM heat exchangers with refractory alloys are in the early stage of development. In particular, reliable bonding of the PM in form of bonded particles or 'foam' with the heated structure is essential and needs to be demonstrated. Detachment can perhaps lead to unstable overheating.

The PM concept with peripheral flow has limited design flexibility against varying heat flux profiles, especially for large heated length and substantial power peaking. Tailoring the cross sections in longitudinal direction could help but would complicate fabrication. The other PM designs considered have shown excessive pressure loss or complicated manifolding.

There are a number of life-limiting factors that have to be explored in the long run, i.e., embrittlement, low cycle fatigue, swelling, erosion of the W armor, wall/coolant interaction, activation, leak tightness, plugging and instrumentation.

The sizeable coolant pipes of at least 4 pipes per cassette with inner diameter of about 100 mm may raise space problems in the port region. (Please note that supply lines for 3 cassettes must be accommodated per port.) In-situ repair of divertor components will be very limited. Instead, complete cassette replacement and hot cell repair should be envisaged in case of damage or malfunction.

Conclusions

Analysis of the porous media heat exchanger concept for application in high heat flux design has shown that peak heat fluxes up to 5 MW/m^2 are feasible with unconventional, helium-cooled divertor concepts, given that the operating temperature in the only structural materials deemed viable (molybdenum and tungsten alloys) must not fall below 600-700°C for reasons of embrittlement. The potential for further improvements through better heat transfer, material characteristics and design optimisation are marginal when compared to uncertainties in specifying the required heat load at the divertor plates. Coolant parameters can be kept in an attractive range for power conversion, e.g., inlet/outlet temperature of 400/800°C at 8 MPa, compatible with conditions in helium-cooled blanket concepts.

Staff:

S. Gordeev
K. Kleefeldt

PPA 1.4   Liquid Metal Cooled Divertors

Staff:

PPA 1.4.2 Evaporation Cooled Liquid Metal Divertor

J. Reimann
L. Boccaccini

Divertor designs based on evaporation cooling are characterised by the operation at high temperatures, small temperature differences and near atmospheric pressures. Primary and secondary stresses are, therefore, small.

During the preparatory phase of the PPA-Study, two evaporation cooled liquid metal (ECLM) divertor concepts were evaluated : i) a concept based on pool boiling, and ii) a concept which employs characteristic features of high heat flux liquid metal (LM) heat pipes, however, avoiding some performance limiting mechanisms of these systems.

Concerning the pool boiling concept, a literature review revealed that alkali metals are best suited; amongst those the LM eutectic NaK is the most attractive, operating at about 800 °C and 0.1 MPa. Maximum heat loads of $Q_{max} \approx$ 5-6 MW/m^2 were achieved in applications without magnetic field. The presence of high magnetic fields is expected to reduce the maximum achievable heat flux by about 50 % which results in values too low for divertor components subjected to the highest heat loads. However, this concept might be still attractive for divertor components with smaller heat loads due to its extreme simplicity in respect to design and technology.

In the second concept, the LM is transported by capillary forces in a porous layer to the heat loaded zone and evaporates at the surface of this porous layer. As porous layer a plasma sprayed structure is anticipated consisting of the same material as the submodule structure; the thickness in the heat loaded zone is about 0.5 mm. The LM enters slightly subcooled the submodule from one side and flows slowly in a U-shaped duct with a poor electrical conductivity; the vapour exits the submodule at the other end. Again, alkali metals are best suited; two options are considered: Na operating at $\approx$ 875 °C and $\approx$ 0.1 MPa and Li at 1200 °C and $\approx$ 0.035 MPa.

The operation at high temperatures enables high power conversion efficiencies. The latent heat of the metal vapour is transferred in a helium-cooled condenser to a high pressure helium system with a closed cycle gas turbine. With Na at 875 °C, efficiencies of 47.5 % were evaluated. For the blanket system using Li at 1200 °C, an efficiency of 57 % was assessed. Both the liquid and vapour metal system including the condenser should be positioned within the vacuum vessel, therefore, only helium pipes would penetrate the vacuum vessel.

The most important issue are the maximum removable heat loads. Heat fluxes of larger than 9 MW/m^2 were reported for Na/W heat pipes without reaching CHF. Significantly higher values are predicted for very pure liquid metal systems.

A 2d temperature and stress analysis was performed with the FE code ABAQUS for the submodule operating with Na at 875 °C. Taking into account the low system pressure the primary stresses are negligible and the secondary stresses can be maintained far below the maximum acceptable stress limit.

Open issues are MHD effects on the transport of liquid in the capillary structure and the influence on the evaporation process, the material compatibility between the liquid metal and the insulating duct material, and neutron irradiation effects on the structural material (tungsten) and the insulator material.

PPA 2   Blankets

PPA 2.3   Improved Helium Cooled Pebble Bed Blanket

PPA 2.3.1   Improved HCPB Blanket Concept

In the European Fusion Programme of 1999 preparatory work has been carried out for a fusion power plant study that is planned to start in 2000. This study will focus on the commercial attractiveness of a fusion plant, particularly on achievable power level, net efficiency and availability. As part of the activity, the Forschungszentrum Karlsruhe was asked to assess the potential and limits of an "Improved Helium Cooled Pebble Bed (I-HCPB) blanket based on low-activation steel as structural materials and to propose a design of such a blanket.

Design description

The options for changes to the DEMO HCPB design selected during a conceptual design phase were (i) change of the coolant flow scheme and restructuring of the breeding region; and (ii) investigation of oxide dispersion strengthened (ODS) steel as structural material. The general blanket-box lay-out was kept. The option of radially varying the ^{6}Li content in the ceramic breeder to reduce the peak power density and push Tritium breeding exists but did not have to be employed for the design.
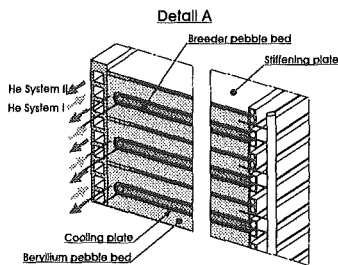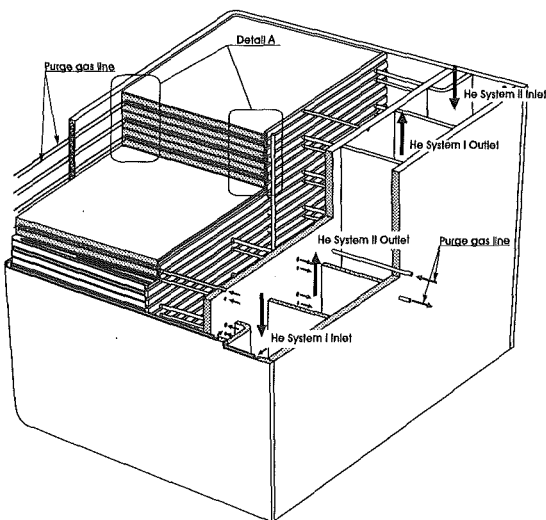

Fig. 1: Improved HCPB

Fig. 1 depicts a section from an outboard segment of the I-HCPB. A U-shaped First Wall (FW) of 25 mm thickness together with shielding and support structure provides a stiff blanket box. The FW coolant channels of 16x16 mm^2 cross section and 22 mm pitch lie in radial-toroidal planes; alternating directions of flow support a balanced FW temperature distribution, while the use of two separate cooling circuits enhances blanket safety.

The blanket box contains the breeding region with alternating shallow pebble beds of Beryllium and ceramic breeder that are separated by 5 mm-thick steel cooling plates. The plates adjacent to the ceramic breeder beds are designed as closed containers without mechanical connection to the FW. Additional stiffening plates are welded into the blanket box dividing the Beryllium bed into equal halves; they strengthen the box and provide extra cooling for the Beryllium beds. Coolant flow through the 3x3 mm^2 channels of 5 mm toroidal pitch is in radial direction.

FW cooling channels are connected in series with those in the breeding region. On leaving the FW, helium is fed by collectors into the radial channels of both breeder containers and stiffening plates. Void channels in the stiffening plates determine the distribution of mass flow through the two types of cooling plates in such a way that the same temperature rise is attained.

The concept of cooling plate containers and cooled stiffening plates has important consequences for operating the breeding zone. (i) The manufacturing limit on the minimal height of the ceramic breeder bed known from the DEMO HCPB is done away with; hence, the power density can be increased significantly without exceeding maximum breeder temperatures. (ii) The additional cooling of the Beryllium bed brought about by the stiffening plate is essential for increasing the power density in Beryllium, and for using a single-size Beryllium pebble bed that has a thermal conductivity much lower than the binary Beryllium bed in the DEMO HCPB. The lower packing fraction increases the margin for Beryllium swelling; in conjunction with a reduced radial extension of the breeding zone it could lead to a reduction of the Beryllium inventory by more than 30% of the DEMO HCPB.

Two different low-activation structural materials, EUROFER and ODS, have been considered. An I-HCPB based on the available EUROFER will have all the advantages discussed above. In addition, using as structural material an ODS steel would allow larger Helium outlet temperatures, increased electrical net efficiency and hence could be commercially more attractive. It was assumed that (i) EUROFER properties are identical to those of T91 and that (ii) mechanical ODS properties are those of T91 shifted to temperatures 100K higher.

Reference case calculations

With the two alternative structural materials so different regarding their stage of development, and with EUROFER found to allow an attractive design, it was decided to contrast two design cases based on EUROFER and ODS.

Table 1: I-HCPB blanket data

	EUROFER	ODS
Neutron power [MW]	3285	4160
Alpha-particle power [MW]	558	707
Energy multiplication	1.34	1.34
Thermal power [MW]	4960	6280
Blanket surface [m^2]	1187	1187
Average neutron wall load [MW/m^2]	2.8	3.5
Max. neutron wall load [MW/m^2]	3.5	4.4
Average surface heat load [MW/m^2]	0.47	0.60
Max. surface heat load [MW/m^2]	0.61	0.78
Coolant	He	He
- Inlet temperature [° C]	250	250
- Outlet temperature [° C]	500	550
- Pressure [MPa]	8	8
- Mass flow rate [kg/s]	3815	4025
- Pumping power, η= 0,8 [MW]	196	219
Net efficiency of power conv. system [%]	36.5	37.5
Electrical output [MW]	1810	2350

Neutronic input data came from a basic reactor model designed for the reactor study. Power data from I-HCPB specific neutronic calculations were linearly scaled to values suited for the potential of EUROFER and ODS, Tab. 1. Neutronic analyses show that Tritium breeding targets are reached and that the blanket's energy multiplication factor is attractively large.

Table 2: I-HCPB thermohydraulic/thermomechanical data

	EUROFER	ODS
Max. temperature breeder [°C]	887	878
Max. temperature Beryllium [°C]	564	598
Max. temperature stiffenung plate [°C]	532	617
Max. FW temperature [°C]	491	564
Helium velocity FW [m/s]	73.7	79.1
Helium velocity cooling plates [m/s]	20.7	22.8
Pressure drop FW [MPa]	0.096	0.108
Pressure drop cooling plates [MPa]	0.011	0.013

A 1D physical-basics model was employed to compute overall energy balance, coolant mass flow, heat transfer coefficients and pressure drop in a 66mm high unit cell of the blanket, see Tab. 2. 3D finite element models in the fluid code FIDAP were employed to compute fluid and blanket temperature distributions in the FW and breeding zone. A key information of these models is on the recuperator effect, whereby the maximum coolant temperature in the cooling plate is up to 70K above outlet temperature. Peak pebble bed temperatures were computed but are crude because they depend on 3D effects in the FW/breeding zone contact region that was not covered by the models.

For a de-coupled thermal-mechanical analysis, the unit-cell steel structure was modelled using the CAD code CATIA as a pre-processor for the finite element solver PERMAS ver.7. Fluid temperatures from the FIDAP FW model together with neutronic power data were used as input. The thermal analysis shows maximum temperatures in the corner of the FW. Stresses at the height of the FW webs between the coolant channels show local maxima, with the absolute stress maximum occurring in the corner of the FW. The back wall sees stresses of the same order at the location of the He outlet. The maximum total stress limit 3·S$_m$ is expected to be met for both design cases.

In a coolant leak accident load case, preliminary calculations suggest that stresses are uncritical when the box is pressurised to 2 MPa. This latter value implies the provision of a pressure control system that limits the pressure in the box to the tolerable 2 MPa in case of a coolant leak.

With the He outlet temperatures at values significantly above DEMO HCPB values, new He/water steam generator lay-outs were designed and optimised concerning the pressure drops, which influence the overall efficiency directly, and the steam generator size, which has implications for the required space and capital costs. The software tools for this design existed from previous work.

Table 3: I-HCPB steam generator design

	EUROFER	ODS
Number of steam generators	8	8
Power [MW$_{th}$]	620	785
He inlet temperature [°C]	500	550
He outlet temperature [°C]	250	250
Water inlet temperature [°C]	108	118
Water outlet temperature [°C]	470	520
Hydrostatic pressure [MPa]	11	11
Pinch point distance [K]	17.2	28.6

Tab. 3 shows live steam conditions selected for the two reference cases. With the steam generators in a power generation circuit with intermediate superheating and 4-step pre-heating, overall electrical blanket efficiencies could be raised by about 7% compared to the DEMO HCPB.

The lifetime of in-vessel blanket components is determined by the behaviour of the main blanket materials under the different operational loads. The dominating effect for Beryllium is radiation-induced swelling. The envisaged use of a single-size pebble bed with a porosity of almost 40% and the rather low operational temperature provides a good potential for reaching high fluences. Ceramic breeder materials have been irradiated to high burn-up values successfully, but at low damage to burn-up ratios. The planned experiments with high-energy neutrons are expected to confirm the suitability of these materials for high fluence, too. For the structural materials under consideration it is expected that a damage limit of 150 dpa (about 15 MWa/m^2) can be demonstrated in the future. This means a lifetime of the blanket segments of 3.4 to 4.3 FPY (= full power years).

To reach a blanket system availability of e.g. 0.8, the time needed to replace the complete blanket must be in the range of 9 to 13 months, or – if a cyclic 4-step replacement scheme is assumed – 2 to 3 months for one replacement step. In a well-designed plant with a developed technology the unscheduled down-times caused by premature blanket failures should be significantly less than the scheduled down-times. Assuming that a defective blanket segment can be replaced in half the time of one cyclic replacement step, i.e. 1 to 1.5 months, leads to the requirement that the failure rate for a single blanket segment must be significantly below 0.01 a^{-1}. Estimates for the HCPB DEMO blanket yielded an average blanket segment failure rate of this order of magnitude.

Limits of the proposed concept

Material temperatures and allowable stresses impose operating boundaries on the I-HCPB concept. (i) Preliminary one-dimensional calculations suggest that bed heights of 6mm for the ceramic breeder (probably the lower limit on the breeder bed at 10 times the pebble diameter) and 2x22.5mm for Beryllium can accommodate a maximum neutron wall load of 6MW/m^2 within the admissible ceramic breeder and Beryllium bed temperatures; (ii) maximum cooling plate temperatures in the stiffening plates are essentially determined by the helium outlet temperature. Calculations for the reference designs suggest that the maximum ODS cooling plate temperature is 30K below the limiting 650°C. This implies that the Helium outlet temperature could be lifted to 580°C; and (iii) stresses in the FW are due to a large radial temperature gradient caused by the surface heat flux. By reducing the FW steel from 4mm to 3mm it seems possible to accommodate a surface heat flux of about 1MW/m^2 and still keep surface temperatures at about 550°C, implying stresses close to the level of the ODS reference case.

Beyond these design measures, a high-temperature helium cooled divertor could make the divertor power available to the steam circuit and raise the electrical net efficiency significantly.

Literature:

[1] S. Hermsmeyer: Improved Helium Cooled Pebble Bed Blanket. Forschungszentrum Karlsruhe, Interner IRS-Bericht, Oktober 1999.

Staff:

U. Fischer_   S. Malang
S. Gordeev   K. Schleisiek
S. Hermsmeyer   I. Schmuck
K. Kleefeldt   H. Schnauder

PPA 2.4
First Advanced Lead Lithium Concept (TAURO)

PPA 2.4.2
MHD Related Issues

The magnetohydrodynamic (MHD) flow of the liquid metal coolant in the plasma facing ducts of the TAURO blanket concept has been analyzed. The walls of the channels are fabricated from SiC/SiC composite material which provides good electrical insulation, favorable for a reduction of MHD pressure drop. The insulation properties of the wall material are high enough that tangential wall currents are negligibly small. However, the resistance of the wall is not sufficient to confine currents to a particular channel. It has been shown that with the currently proposed wall conductivity strong electrical coupling between neighboring channels is possible. This has been taken into account in the analysis where the walls are not perfectly insulating. Results valid for any wall normal conductivity are derived for a model geometry similar to TAURO. The flow structure and pressure drop has been evaluated for the real designed geometry for both cases, for perfect insulation of the walls and for high wall-normal conductance. It has been shown that the increase of pressure drop with the wall conductivity is not really a crucial issue. However, the results show that the flow pattern is strongly affected and may become undesirable for heat transfer when the wall-normal conductivity exceeds a critical value.

The cross section geometry of the TAURO concept near the first wall has a typical shape that is sketched in the following figure in which the typical flow subregions are denoted by (1) for the central duct and (2) and (3) for the parts of the annular region.
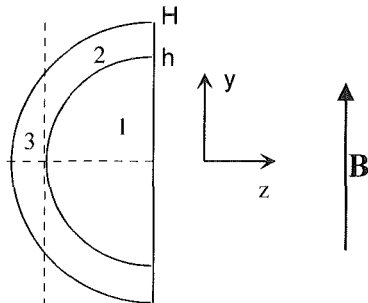

Fig. 1: Sketch of the typical geometry

For this geometry calculations were performed on the basis of an asymptotic analysis. Results for pressure drop and flow pattern were derived. Without going into details of the analysis some of the results are shown below.

Perfect insulation

For the case of perfect insulation, when no flow coupling is present, the annular part (3) and (2) carry the flow downward, while the central duct (1) returns the flow to the top of the blanket. The situation is sketched in Fig. 2 where the velocity in the core of the subregions is shown as a function of the transverse direction z. The velocity profile along magnetic field lines is uniform in the core but has very thin viscous layers near the walls. At the position z=-1 an internal free shear layer is created that has to match the jump in core velocity in the annular gap at this position. Concerning heat transfer it should be noticed, that near the first wall the flow velocity is small, and as a matter of fact, not optimal for convective heat removal. The overall pressure drop is small compared with the static pressure head and therefore not a crucial issue for the design.
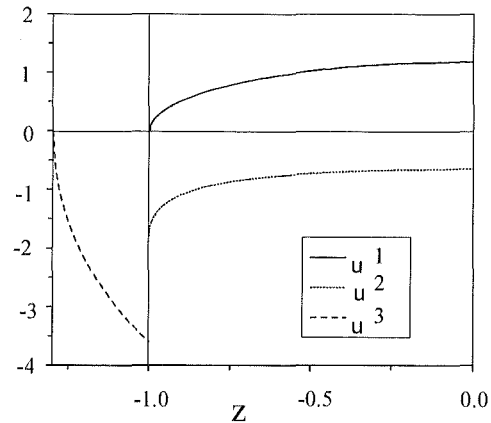
Fig. 2: Core velocity in subregions for insulating walls

Walls conducting in normal direction

If the walls have some normal conductance a coupling between neighboring channels is possible. Results are shown in Fig. 3. One result is that the part (2) of the annular gap couples to duct (1). As a consequence the velocities in large parts of both ducts become equal as shown in the figure. Near z=0 both subregions develop exponential velocity boundary layers. From Fig. 3 one can observe that the velocity in the part (2) of the annular gap is reversed in comparison with the insulating case that has been discussed earlier. As a consequence, the flow rate in part (3) is increased. The latter fact may be favorable with respect to heat transfer at the first wall, where especially the wall of part (3) receives the maximum surface heat flux. On the other hand the reversed flow in part (2) leads to a closed flow path that might be unfavorable for removal of internally liberated heat. Some changes in the design which are not explicitly outlined here can improve the MHD performance of the blanket with respect to heat transfer.
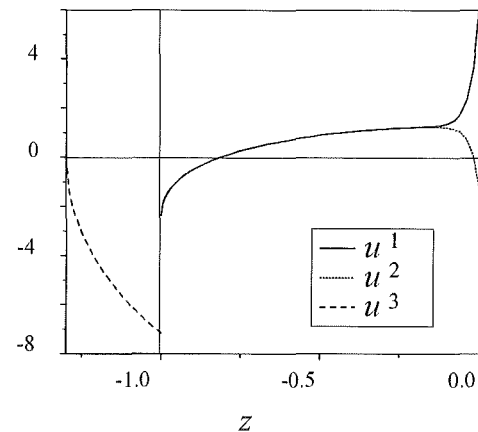
Fig. 3: Core velocity in subregions for high wall-normal conductance

Staff:

L. Bühler

PPA 2.5
Second Advanced Lead-Lithium Concept

PPA 2.5.1
Dual Coolant Blanket Concept

1. Introduction

In the frame of the EU power plant study planned to start in 2000 preparatory work based on an advanced dual coolant (A-DCL) blanket concept [1] has been carried out at Forschungszentrum Karlsruhe (FZK) in co-operation with CEA (Subtask PPA 2.5.2, SiCf/SiC composite related issues) as a proposal for further blanket development.

The A-DCL blanket concept with a self-cooled lead-lithium breeding zone and helium-cooled steel structure is based on the use of oxide dispersion-strengthened (ODS) steel as structural material and SiCf/SiC flow channel inserts (FCI) as electrical and thermal insulators. This avoids the need for insulating coatings on the steel structure inside the liquid metal flow channels (for MHD reasons) and allows a high exit temperature of the lead-lithium, which gives the potential for a high efficiency of the power conversion system. In this case, the SiCf/SiC FCIs have no structural function (i.e. no static pressure difference between inside and outside of the insert walls is expected). Therefore, neither a high strength nor a high thermal conductivity (i.e. a strong thermal barrier is favoured) of this material is required. Moreover, the use of ODS ferritic steel as structural material allows an about 100 K higher temperature limit of the first wall in comparison with MANET steel (Tmax-MANET-FW ≤ 550°C) used in the earlier EU DCL blanket concept for DEMO. For these reasons a higher neutron wall loading (resulting in higher power densities and surface heat load) could be allowed together with an enhancement of the thermal efficiency up to a value of ≈ 45% using a closed-cycle helium gas turbine in the power conversion system.

2. Main features

The structural design of an A-DCL outboard blanket segment is shown in Fig. 1 as a cut-out in an isometric representation with a radial depth of about 1 m, a toroidal width of about 1.4 m and a poloidal height of about 12 m. The whole blanket structure is made of ODS ferritic steel. The U-shaped first wall having a total thickness of 44 mm, together with the ODS steel grids forming the Pb-17Li coolant channels and the shielding structure, makes up a stiff segment box. Within the first wall parallel helium coolant channels (20×30 mm^2, pol.x rad.) are arranged on the radial-toroidal plane with 24 mm channel pitch and 4 mm thick webs which are passed by 14 MPa helium gas in alternating directions. The counter-flowing helium gas contributes to achieving a uniform temperature distribution in the external structure and, hence, to minimising the thermal stresses. Besides, separation of the helium supply systems 1 and 2 guarantees emergency cooling upon failure of a coolant system.

Within the segment box, radial-poloidal and toroidal-poloidal plates are welded together to form stiffening grids which also act as Pb-17Li flow separators (tor. 335 x rad. 240 mm^2 rectangular channels) and are rigidly welded to the external structure. At present, only the diffusion welding method is recommended in literature for the ODS joints. The blanket box is not expected to withstand the maximum helium coolant pressure because the use of a passive accident management scheme (pressure suppression system) is foreseen. The Pb-17Li, besides having the function of a tritium breeder and neutron multiplier, acts as a coolant as well. The Pb-17Li outlet temperature is dictated by compatibility issues and, for

efficiency reasons, needs to be maximised. Because of the high magnetic field present in the blanket region (~7 Tesla), the Pb-17Li needs to be electrically insulated from the steel wall despite the relatively low flow velocity (0.5 m/s). This is obtained by adding SiCf/SiC channel inserts (about 5 mm thick) which also act as thermal insulators (in order to maximise the Pb-17Li temperature without exceeding the allowable steel temperature). In this concept the most important specific requirements for SiCf/SiC which has no direct structural functions are a low electrical conductivity and low thermal conductivity, together with a compatibility with Pb-17Li at high temperatures. To keep the steel temperature sufficiently low, the ODS steel grids are cooled by 14 MPa helium gas after the first wall cooling.

The helium coolant gas enters the upper blanket segment at 300°C and is routed four times on its way downwards in a meandering flow through the segment walls containing the parallel coolant channels by means of a header system. After the last passage the helium temperature at the lower outlet of the segment walls attains a value of 440°C. On its flow upwards, it is passed through the channel arrays in the steel grids with U-shaped coolant channels and heated up to 480°C

	T_{Inlet} (°C)	T_{Outlet} (°C)	ΔT (K)
Overall He (14 MPa)	300	480	180
- FW He	300	440	140
- Grids He	440	480	40
Pb-17Li	460	700	240
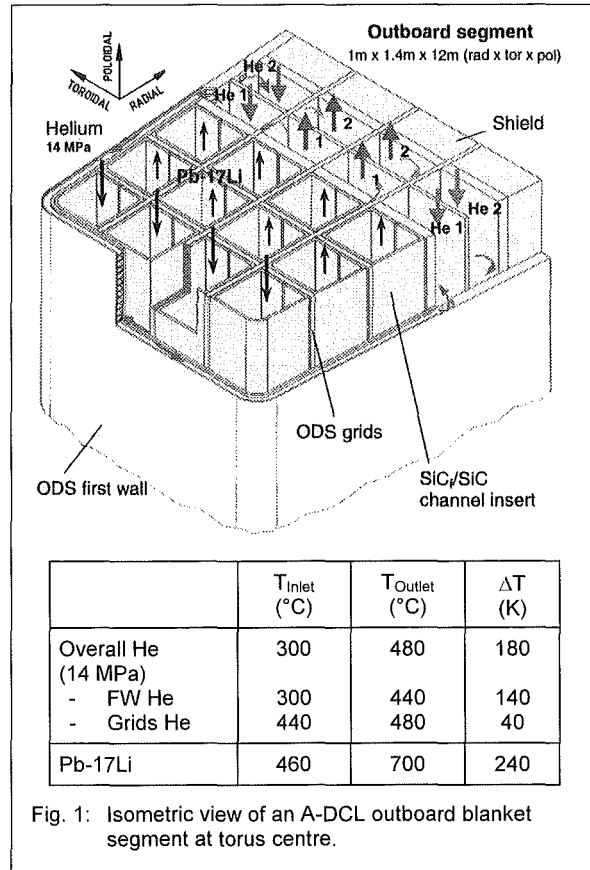
Fig. 1: Isometric view of an A-DCL outboard blanket segment at torus centre.

before leaving the blanket top.

The liquid metal Pb-17Li enters the top end of the blanket at 460°C, flows downwards through the four channels in the front zone and is heated to 630°C at the blanket bottom. It is then diverted into the two rear channel zones containing eight channels altogether, where it flows back to the top at lower velocity and leaves the blanket again at 700°C.

3. Methods of calculation and results

3.1 Neutronic calculations

Based on the PPA2 reactor parameters (geometry, size, power and neutron source distribution) for the base fusion machine provided by UKAEA Culham neutronic calculations have been performed with the MCNP Monte Carlo code using a 7.5 degree torus sector model including the intermediate gaps to determine the tritium breeding potential, and to provide the nuclear heating input data, i.e. the blanket power generation and the power density distribution in the blanket, for the subsequent thermohydraulic and thermomechanical calculations. Table 1 shows the neutronic calculation results serving as base data for the following reactor study with a TBR (without ports) of 1.09, an energy multiplication factor of 1.11, and maximum power densities in steel, Pb-17Li and SiC_f/SiC of 18, 13 and 5 MW/m³, respectively. The average neutron wall loads for the outboard and the overall blanket segments amount to 2.51 and 2.22 MW/m², respectively. For the linear extrapolation of the blanket power in the thermohydraulic and thermomechanical calculations the ratio avg. heat flux/avg. neutron wall load of 0.17 and the surface flux peaking factor (max./avg.) of 1.3 have been taken into account.

Table 1: Neutron-physical data used as basis for thermohydraulic and thermomechanical calculations

Fusion power (MW)	3607
Ratio avg. heat to avg. neutr. flux	0.17
Surf. heat flux peaking factor	1.3
Avg./max. neutr. wall load (MW/m²)	
- Outboard	2.51 / 2.79
- Inboard	2.05 / 2.55
- Overall segments	2.22
3D net tritium breeding ratio (TBR)	1.09
Energy multiplication factor	1.11
Max. power densities (MW/m³):	
- Steel	18
- Pb-17Li	13
- SiC_f/SiC	5

3.2 Material data

Since the material data for ODS steel are not yet available, the comparable data of the ferritic steel T91 were taken, e.g. the thermal conductivity λ (400-600°C) $\approx$ 29 W/mK, thermal expansion coeff. $\alpha \approx$ 12.0E-6 1/K and specific heat $c_p \approx$ 750 J/kg • K. For stress evaluation according to the RCC-MR code, the S_m values of T91 are assumed on the temperature level shifted upwards by 100 K, e.g. $S_{m,t\text{-ODS}} \approx$ 174/146/101 MPa at 500/600/700 °C, respectively, with t $\approx$ 10⁴h.

For Pb-17Li the same data as applied for the DEMO calculations are used, e.g. λ (600°C) $\approx$ 19 W/mK and c_p (600°C) $\approx$ 187 J/kg • K. The following data of SiC_f/SiC are used in the calculations: $\lambda \approx$ 2 W/mK and electrical conductivities $\sigma \approx$ 500 $\Omega^{-1}m^{-1}$. (measured value for CERASEP®N2-1).

3.3 Thermohydraulic layout, temperature and stress analyses

3.3.1 Temperature constraints and coolant temperatures

Two temperature limits are relevant for the blanket layout: a) the maximum temperature of the ODS steel, which is expected on the plasma facing surface of the FW at the equatorial plane of the outboard segments, should not exceed 650 °C due to a strong decrease of its creep rupture strength at this temperature; b) the maximum interface temperature between

the ODS and the stagnant Pb-17Li should not exceed 500 °C due to corrosion. To adapt to these boundary conditions, the coolant temperatures were chosen as follows: $T_{He, inlet}$ = 300 °C (in consideration of the secondary He circuit in the power conversion system), $T_{He, outlet}$ = 480 °C; $T_{Pb-17Li, inlet}$ = 460 °C (in consideration of the pinch point) and $T_{Pb-17Li, outlet}$ = 700 °C. The following detailed thermomechanical analyses were carried out for the outboard blankets because their thermal loads are higher than those at the inboard blankets, especially at the equatorial plane of the torus where the highest power densities together with the peak surface heat flux are expected.

3.3.2 Thermohydraulic layout

After fixing the coolant inlet and outlet temperatures (see above), the helium and Pb-17Li mass flow rates were pre-determined in a first step, omitting the heat exchange between the helium and Pb-17Li coolants. In a next step, the amount of this heat exchange was determined in detail by means of the temperature field calculations (see next section), thus leading back to a correction of the mass flow rates which were found to be less than 2% because of a strong heat insulating effect of the SiC_f/SiC FCIs with the chosen property. After this, all other thermohydraulic data, especially the heat transfer coefficient, pressure loss and pumping power for the helium flow as well as the velocity and MHD pressure loss for the Pb-17Li were computed. In order to enhance the heat transfer coefficient $\alpha_{He/wall}$ and, hence, to keep the maximum steel temperatures below the allowable limit, two surfaces of the He channels, excluding the web surfaces, are artificially roughened. As a result, $\alpha_{He/wall}$ is increased by factor of 2, as assumed in the DEMO calculations. To minimise the He pressure losses for the expected larger performance in the reference case than in the base case (Table 1), a relatively high He pressure of 14 MPa was chosen, which leads to a reasonable pumping power in the He loop of about 5% relative to the extracted power.

Based on a linear extrapolation of the surface heat flux and the neutron power, the thermohydraulic calculations were carried out for a range of the maximum surface heat flux between 0.1-1.5 MW/m².

3.3.3 Temperature and stress analyses

The 2D temperature and stress calculations have been carried out with the FE code ABAQUS. To identify the blanket performance limits dictated by the temperature constraints mentioned above, two separate temperature analyses were carried out locally for the first wall and for the blanket interior. After a comparison of the limit values obtained from both cases, the smaller one was taken as a reference case for the blanket. Then the corresponding 2D stress analysis for the FW was carried out for the reference case.

In the first wall calculations the blanket heat and neutron wall loads were varied, while the He velocity and the first wall thickness were taken as parameters. From the first results a He velocity of 40 m/s was found to be reasonable in view of the pressure loss leading to a symmetrical division of the meandering flow into four passages within the external walls of the blanket. Besides, a reasonable first wall thickness was preferred between 3 and 4 mm. The results of this analysis showed that a maximum allowable peak surface heat flux e.g. of about 1.0 MW/m² for the FW with 4 mm thickness and He velocity of 40 m/s could be achieved, which corresponds to an average neutron wall load of 4.5 MW/m². However, the maximum allowable peak surface heat flux could be even enhanced up to 1.5 MW/m² by choosing a FW thickness of 3 mm and a He velocity of 100 m/s, without paying attention to the pressure loss. In this case an adaptation of construction and of thermohydraulic layout has to be done more in detail, e.g.

reduction of the He channel pitch to cope with the primary stresses, and asymmetrical subdivision of the He passages to get the highest He velocity at the torus centre.

For the temperature field calculations of Pb-17Li the "slug flow" method was applied, i.e. quasi-transient calculation with heat conduction transverse to the flow direction. The calculation of the radial velocity profile of the Pb-17Li flow has shown that an increase of the near-wall velocity by at least a factor of 2 (corresponding to $\sigma = 1.0 \; \Omega^{-1}m^{-1}$) can be assumed conservatively. This was taken into account when correcting the near-wall heat transfer condition, especially at the rear side of the first wall. The calculations were carried out at varied neutron wall loads under preservation of the energy balance. These calculations yield a maximum allowable limit for the average neutron wall load of 4.0 MW/m², which can be considered as a reference case of this blanket concept. In Table 2 the main data for the reference case are summarised.

Table 2: Main data for the A-DCL reference case

Avg./max. neutron wall load (MW/m²)	4.0 / 5.0
Avg./max. surface heat load (MW/m²)	0.7 / 0.9
Blanket fusion power (MW): - Surface power (1187m² x 0.68 MW/m²) - Neutr. power (1187m² x 4 MW/m² x 1.11) Sum	 807 5270 6077
Coolant temp. in/outl (°C)/temp. rise (K): - Primary helium (blanket, 14 MPa) - PbLi - Secondary helium (18 MPa)	 300 / 480 / 180 460 / 700 / 240 280 / 650 / 370
Therm. efficiency (pow. conversion system)	0.46
El. pumping pow. for blanket cooling (MW): - Helium (14 MPa, η = 0.8) - Pb-17Li (η = 0.8) Total	 136 8 144
Thermal efficiency (blanket cycle)	0.44
El. power output from blanket cycle (MW)	2674
Lifetime prediction (mainly limited by steel): Displacement damage (dpa) Average neutron fluence (MWa/m²)	 150 15.1

The following 2D stress calculations for the first wall with 4 mm thickness for this reference case yield a maximum primary stress of 197 MPa at the front corners of the coolant channel (< allow. 261 MPa at 466 °C) and a maximum primary plus secondary stress of 413 MPa at the plasma facing surface (< allow. 418 MPa at 617 °C).

3.4 Power conversion system and thermal efficiency

A three-stage Brayton closed-cycle gas turbine (Fig. 2) was considered for the power conversion system, using both He and Pb-17Li exit temperatures. This solution has a decisive advantage in avoiding the contact of liquid metal with water. For the blanket coolant access a double wall tube construction (Pb-17Li in inner tubes/He in outer tubes) was used in order to prevent tritium permeation by a He barrier in the outer tube. Moreover, an additional SiC$_f$/SiC innermost tube provides for a thermal barrier by separating the hot Pb-17Li flow with a maximum temperature of 700 °C from the steel wall.

In case of a secondary He loop with 18 MPa He pressure and inlet and outlet temperatures of 280 °C and 650 °C, respectively, the thermal efficiency of this power conversion system amounts to 0.46. Taking into account the electrical pumping power for the blanket cooling of 144 MW in the reference case (Table 2, η = 0.8 assumed), the thermal efficiency of the blanket cycle equals 0.44. An additional investigation resulted in the fact that the thermal efficiency can

be even further increased by the integration of helium-cooled divertors with 953 MW power and an He exit temperature of 850 °C into this power conversion cycle. The examination of the heat exchangers for these cases resulted in a reasonable size and pressure loss.

4. Open issues

Since the A-DCL blanket concept is an advanced version of the DEMO DCL blanket concept which had been under development in the EU for several years before, the same reliable computation techniques and the same Pb-17Li properties are used. The material properties of SiC$_f$/SiC known at present should meet the requirements for these purposes, because the SiC$_f$/SiC FCIs have no structural functions at all to cope with. Open issues regarding the SiC$_f$/SiC material are the fabrication techniques, e.g. achievement of sealed surface to avoid the infiltration of Pb-17Li, production of a maximum FCI length (reduced number of joints), achievement of low thermal and electrical conductivity (enhances the thermal efficiency). For the ODS steel structure the open issues are primarily the strength data, the fabrication and welding methods. The assumption of the strength values of comparable ferritic steels having be on shifted to 100 K higher temperature level to achieve the value for ODS as recommended by material experts has to be examined. In addition, R&D work on in-pile experiments is required for both SiC$_f$/SiC and ODS.

5. Lifetime, maintainability and reliability

Since the SiC$_f$/SiC FCIs have no structural functions, it can be supposed that the ODS steel structure plays a decisive role for the lifetime of the blankets. The lifetime prediction assuming a displacement damage for ODS of 150 dpa yields an average neutron fluence of 15.1 MWa/m², corresponding to either 6.8 FPY at 2.22 MW/m² or 3.78 FPY at 4.0 MW/m².

At the present state of the reactor study, a detailed reliability analysis cannot be performed yet. The similar DEMO DCL blanket concept study yields e.g. an overall availability of > 86% and even > 98% for the external cooling circuits, taking into account the redundancy principle. For the A-DCL blanket concept, however, the following crucial reasons allow to assume a higher reliability than that of DEMO: No possibility of water-liquid metal reactions, higher strength of the structural material, and advance state of today's diffusion welding technology.

6. Conclusions

The A-DCL blanket concept is characterised by its simple construction and its simple function. The goal of this study is to investigate the potential of this blanket concept. Two temperature constraints for the FW (creep rupture strength) and the Pb-17Li breeding zone (corrosion) were taken into account. The latter was found to be decisive for the power limitation of this blanket concept. Detailed neutronic, thermohydraulic, thermomechanical and MHD calculations were carried out under the assumption of the specified PPA2 geometry and with an extrapolation of some material data that are not available yet. The calculations yielded a maximum allowable average neutron wall load of 4.0 MW/m² (corresponds to 0.9 MW/m² max. surface heat load) for the reference case. Assuming a three-stage Brayton gas turbine cycle for the power conversion system, a thermal efficiency for the blanket cycle of 0.44 was obtained. The max. allowable peak surface heat load for the FW could be enhanced to a value of about 1.5 MW/m² (a margin for e.g. peaking factor uncertainty) by reducing the FW thickness and increasing the He velocity.

The results of this study show that the A-DCL blanket concept has a high potential for further development due to its high

thermal efficiency and its simple concept solution that may have some open issues which are not too complex and are expected to be solved easily.

Fig. 2: Heat transfer diagram for a power conversion system using a 3-stage Brayton gas turbine
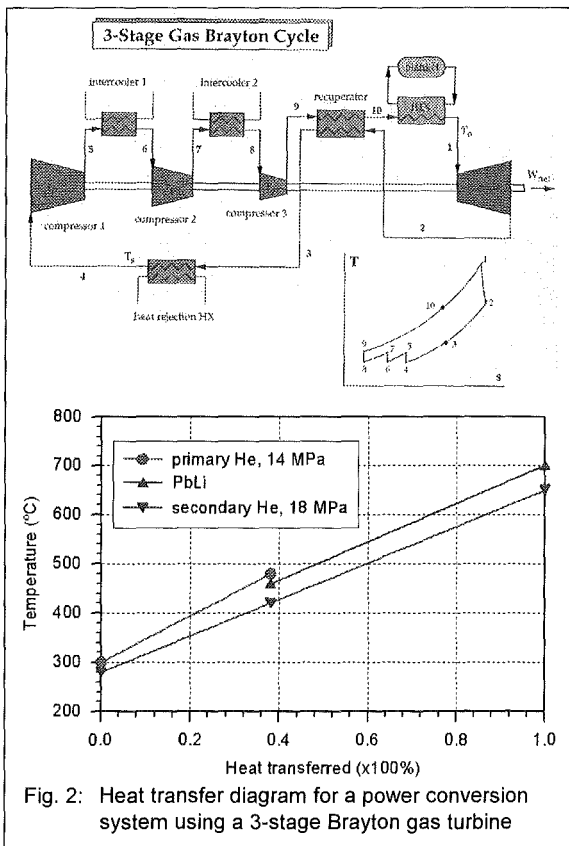
Literature:

[1] P. Norajitra, The Second Advanced Lead Lithium Blanket Concept Using ODS Steel as Structural Material and SiC$_f$/SiC Flow Channel Inserts as Electrical and Thermal Insulators (Task PPA 2.5), Executive Summary, Forschungszentrum Karlsruhe, Interner IMF III-Bericht, August 1999.

Staff:

L. Bühler
U. Fischer
K. Kleefeldt
S. Malang
P. Norajitra
G. Reimann
H. Schnauder

PPA 2.6
Advanced Ceramic Breeder Concept

PPA 2.6.1
Advanced HCPB Blanket Concept

1. Introduction

The Helium Cooled Pebble Bed (HCPB) Blanket [1] is one of the blanket concepts considered in the European Programme as a DEMO relevant blanket. Starting point of the present work was the analysis of the technological design limitations of this concept and the identification of the necessary improvements in view of its inclusion in the European Reactor Study. One of the most important limitations of the DEMO-HCPB concept is the relative low temperatures of the coolant helium (250°C inlet and 450°C outlet) leading to gross thermal efficiency of the conversion cycle of about 35%. The coolant temperatures are dictated by the maximum allowable temperature (about 550°C) of the ferritic-martensitic steel (EUROFER-97) used as structural material. The development of advanced materials with higher temperature limits will bring clear advantages in terms of helium outlet temperature and gross thermal efficiency.

In particular SiCf/SiC is a promising candidate [2]. It presents a high strength at temperatures greater than 1000°C, leading to potentially very high temperature of the coolant with the possibility to adopt power conversion cycles at a high thermodynamic efficiency. Furthermore, its inherently low induced radioactivity brings advantages in the area of safety, disposal and maintenance. On the other side despite some improvements reached in this last years important questions such as the degradation of thermal conductivity during irradiation, joining technology with low activation materials and the hermetic sealing remain severe issues for using this material as structural material in fusion applications.

To take full advantage of the potential of this structural material, a new blanket design has been proposed. The pebble beds have been arranged in parallel to the first wall; by this configuration a variation of the ^{6}Li enrichment and the ratio breeder/multiplier in radial direction is facilitated, reducing the required amount of beryllium, improving tritium breeding ratio and increasing the allowable neutron fluence by reducing the maximum ^{6}Li burnup and the tritium inventory in the beryllium multiplier. Finally, the adopted flow scheme based on tubes arranged in a shell in the first wall and in "meanders" in the breeding zone results in a decisive reduction of the coolant pressure drop.

2. Design Description of the A-HCPB Blanket

The Advanced Helium Cooled Pebble Bed (A-HCPB) Blanket (see Fig. 1) exhibits the same basic design features as the European DEMO HCPB blanket, which is based on the use of separate ceramic breeder and beryllium pebble beds placed between cooling plates. The concept of a segment box typical of DEMO with components height about 12 m, is here replaced by applying a poloidal and toroidal segmentation of the blankets, that leads to separated boxes with dimensions of about 1.4 x 0.6 x 0.6 m (toroidal x poloidal x radial). The boxes in a segment are supported by a common back plate, which allows to remove all the boxes in the segment together.

As in the HCPB blanket, the advanced concept is cooled by helium at high pressure flowing in tubes first in the first wall (FW) and then in the breeding zone (BZ). For safety reasons the helium flows in two completely separated loops. The FW is constituted by an U-shaped tube shell. This shell is formed by radial-poloidal tubes (16 mm internal diameter in the reference design) tied together for the whole width of the box. The coolant is flowing alternately in opposite directions to make the temperature distribution more uniform.

In the BZ, the thin beryllium and ceramic breeder pebble beds, toroidally-poloidally oriented, are confined and cooled by long tubes in the form of a meander; these meanders are bounded together to form cooling plates. The coolant helium flows inside these tubes through the BZ from the plasma to the vessel side.

As the BZ tubes have an internal diameter that is the half of the FW tubes, the outlet helium of each tube of the FW must feed 4 tubes of the "meander" region. The connection between large (in FW) and small (in BZ) tubes is realised in the back region with low neutron flux adopting the brazing joint technique. As the section of a FW tube and the jointed 4 BZ tubes have the same flow area, the helium velocity magnitude increases without discontinuity in the tubes from the FW to the BZ. The adopted flow scheme results in relatively low pressure drops.

An independent low pressure helium purge flow is used to extract the produced tritium from the beds. Hence, during normal operation the space inside the box is at the low purge gas pressure. A graphite reflector is used behind the BZ to improve the neutronic performance, to shield more effectively the magnets and to reduce stresses that arise inside the beds due to thermal expansion and swelling.
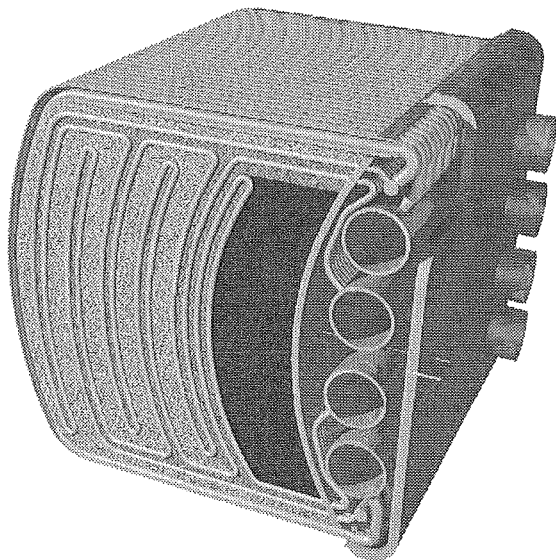
Fig. 1: Isometric view of the A-HCPB Blanket box

3. Material properties and design limits

The performances of the proposed concept are very strong dependent on the properties of the materials and on the design limits used in the assessment. Some of these properties and limits are at present not well known. Table 1 summarises the most important of these values assumed in this assessment.

The present design considers lithium orthosilicate (Li_4SiO_4) as ceramic breeder. The thermal conductivity of Li_4SiO_4 pebble bed has been measured and correlations are available for the design [3]; the maximum allowed temperature has been chosen 100 K lower than the phase transition at 1024°C, taking into account uncertainties due to hot spots. The maximum allowable temperature of beryllium is not well known, but swelling and degradation of mechanical properties consideration suggests to adopt a design limit of 700°C [4]. The thermal conductivity of binary beryllium beds has been measured in dedicated

experiments carried out in Forschungszentrum Karlsruhe leading to maximal values of 25 W m^{-1} K^{-1}. However, these experiments have been carried out at average temperatures in the beryllium bed up to 300°C and at differential thermal expansions between pebble bed and structure below 0.4 %, a value much lower than the one anticipated in the blanket with SiC$_f$/SiC as structural material (much lower thermal expansion coefficient than steel). It is expected that the thermal conductivity will be considerably higher in this concept.

Table 1: Material properties and design limits used in the assessment of the A-HCPB Blanket

Orthosilicate Pebble Bed	
Thermal conductivity (T= 500-900°C)	1.0-1.2 W m^{-1} K^{-1}
Max allowable temperature	920 °C
Max. allow. temp. at SiC$_f$/SiC interface	920 °C
Beryllium Pebble Bed	
Thermal conductivity (T= 500-700°C)	25 W m^{-1} K^{-1}
Max allowable temperature	700 °C
Max. allow. temp. at SiC$_f$/SiC interface	700 °C
SiC$_f$/SiC	
Thermal conductivity	15 W m^{-1} K^{-1}
Max allowable temperature	1300 °C
Young's Module	200 GPa
Poisson ratio	0.18
Thermal expansion coefficient	4.0·10^{-6} K^{-1}
Max. allowable primary stress	140 MPa
Max. allowable secondary stress	190 MPa

As far as SiCf/SiC is concerned, the values of the thermomechanic properties used in the present assessment have been taken from design values proposed in the TAURO project [5]. Some of these values must be interpreted as minimum requirements for application in fusion technology. A typical example of this is the assumed thermal conductivity of 15 W m^{-1} K^{-1} in the thickness without degradation under irradiation. At the present this ambitious goal is still far-away to be achieved.

The anisotropy of this composite material depending on the orientation of the fibers requires new methods in the design optimisation of the mechanical and thermal behaviour of components [6]. Criteria such as the von Mises stresses are not satisfactory for materials which present different properties along each orthotropic axis. However, at the present stage of the work, conventional stress criteria such as those suggested in the ARIES-I study [7] have been adopted in this assessment.

As far as the chemical compatibility of SiCf/SiC with beryllium and Li$_4$SiO$_4$ is concerned, a recent investigation at Forschungszentrum Karlsruhe [8] has shown that the unstable Be-SiC couple is kinetically hindered to form Be$_2$C and Si at temperatures up to 700°C and that SiC and Li$_4$SiO$_4$ are compatible, provided fibers are used with a low oxygen content. In fact SiO$_2$ reacts with Li$_4$SiO$_4$ producing lithium-metasilicate.

4. Calculations for the reference design.

On the basis of the core design described in section 2, neutronic and thermo-hydraulic calculations have been performed to optimise the design parameters to reach the self-sufficient condition for the tritium breeding ratio (TBR) with temperatures in the bed below the design limits. The necessary boundary conditions (reactor dimensions, neutron source distribution, surface heating, etc.) have been taken by the reactor model provided by UKAEA Culham (labelled PPA) [9]. However, the power level has been increased by about 25% to have an

average neutron wall load of 2.76 MW/m^2 leading to a peak neutron wall load of 3.5 MW/m^2 like that assumed in the DEMO reactor.

The results of these calculations are shown in Table 2, where the major parameters of the reference design of the A-HCPB blanket are collected. Table 3 shows the results of the core optimisation in terms of bed thickness and 6Li-enrichment. The power density and the maximum temperature in the bed and at the interface with the structural material have been calculated for the equatorial region of the outboard blanket, where the neutron wall load and surface heating have their peak values.

The operational conditions of the coolant are a pressure of 8 MPa and an inlet/outlet temperature of 350°C and 700°C, respectively. This seems a good compromise (for this level of power density) to keep the helium pressure as low as possible, to have acceptable pressure drops in the loops and assure high thermal efficiency for the conversion power cycle.

Table 2: Main Plant and Blanket Design Data

Overall plant	
Fusion power	4500 MW
Neutron power	3600 MW
Alpha-particle power	900 MW
Energy multiplication	1.24
Thermal power	5364 MW
Blanket system	
Neutron power	3276 MW
Alpha-particle power	558 MW
Energy multiplication	1.19
Thermal power	4456 MW
Blanket surface	1187 m^2
Average neutron wall load	2.76 MW/m^2
Max. neutron wall load	3.5 MW/m^2
Average surface heat load	0.47 MW/m^2
Max. surface heat load	0.61 MW/m^2
Coolant	He
- Inlet temperature	350 °C
- Outlet temperature	700 °C
- Pressure	8 MPa
- Mass flow rate	2449 kg/s
- Pumping power (η= 0,8)	83 MW
Net efficiency of power conversion system (with 46% gross efficiency)	44.8
Electrical output	1997 MW

Table 3: Results of the neutronic and thermo-hydraulic calculations for the A-HCPB blanket reference case for the equatorial outboard region (OSI = Li$_4$SiO$_4$)

No	Mat.	^{6}Li-enrich.	Equiv. thickn	Power dens.	Max. bed temp.	Max. inter. temp.
		%	mm	MW/m^3	°C	°C
1	Be	-	20	15.5	651	630
2	OSI	nat.	8	38.1	902	617
3	Be	-	30	11.7	668	621
4	OSI	nat.	8	30.4	826	600
5	Be	-	30	8.2	668	637
6	OSI	15	8	31.7	917	683
7	Be	-	30	5.7	674	655
8	OSI	35	8	28.8	889	678
9	Be	-	30	3.9	682	669
10	OSI	70	9	19.3	890	712
11	OSI	70	9	14.2	831	700
12	OSI	70	9	21.2	918	723

4.1 Neutronic design

Neutronic calculations have been performed with the MCNP Monte Carlo code [10] and nuclear data from the European Fusion File [11] to assess and optimise the breeding performance of the considered blanket concept and provide the nuclear heating input data for the subsequent thermal-hydraulic calculations.

Based on the reactor parameters and the neutron source distribution of the PPA reactor, a generic 7.5 degree torus sector model has been developed. This model includes the plasma chamber, four poloidal blanket/shield segments and a bottom divertor port with an integrated divertor of the SEAFP-type. The first wall profile has been adapted in an arbitrary way to the plasma boundary contour shape assuming a scrape-off layer of 15 cm at torus mid-plane. According to the MCNP reactor models, the blanket coverage amounts to 82 % with a resulting FW blanket surface of 1187 m^2 (1467 m^2 including the divertor port).

The calculation results for the A-HCPB Blanket Concept yield a tritium breeding ratio of 1.09 and an energy multiplication factor of 1.19 for the blankets (1.24 for the whole reactor). The calculated power density of the beds in the outboard equatorial region are shown in Table 3.

4.2 Thermohydraulic design

The temperature distribution in the core, the coolant temperatures, the helium mass flow and the pressure drops in the tubes have been calculated with a steady-state flow calculation (that takes into account the helium that flows first in the FW and then in the two different meander paths in the BZ) combined with a 1D conduction calculation scheme for the beds and the plates. The results in terms of maximum bed temperatures and interface temperatures are presented in Table 3I. Mass flow and pump losses for the whole blanket system are shown in Table 2. As far the pressure drops are concerned, a value of 55 kPa has been calculated for the pressure drop in the blanket and a value of 110 kPa has been

assumed for the remaining loop (main pipes, heat exchanger, etc.).

4.3 Thermo-mechanic design

2D thermo-mechanic calculations have been performed for the first wall with the structural program ABAQUS. The calculations yield a maximum temperature of 913°C in the SiCf/SiC structure at the plasma side and combined thermal and mechanical stresses below the 190 MPa limit.

4.4 Power conversion system

Two power conversion systems are alternatively considered. Both systems are characterised by a complete separation of the blanket cooling circuit and the power generation circuit. The first system is based on a Rankine process with a He/Water steam generator in between the two circuits. The resulting overheated live steam conditions are 670°C and 11 MPa. The main design parameters of the steam generator are listed in Tab. 4. The Q-T-diagram for the steam generators is shown in Fig. 2. Supposing a one time intermediate overheating in the steam power conversion circuit would result in a thermal efficiency of 44.2 %. Taking into account also the main blower power and the generator efficiency this will lead to an overall electrical efficiency of 41.1 %. The principle of the power generation circuit is given in Fig. 3.

The second power conversion system is based on a Brayton process. The intermediate heat transfer components are He/He heat exchangers which deliver the fusion energy to the closed Brayton circuit. The design calculation data of the He/He heat exchanger are also listed in Table 4. A corresponding Q-T-Diagram is given in Fig. 4.

The pressure drop in the Brayton process has a strong effect on the overall efficiency. Presently it is difficult to give definite numbers. Therefore, two values are considered for the pressure drop ratio ($\Delta p/p$): 0.05 and 0.08. These assumptions lead to an overall efficiency of 46.5 % and 44.5 %, respectively. The secondary pressure drop for the present example was estimated
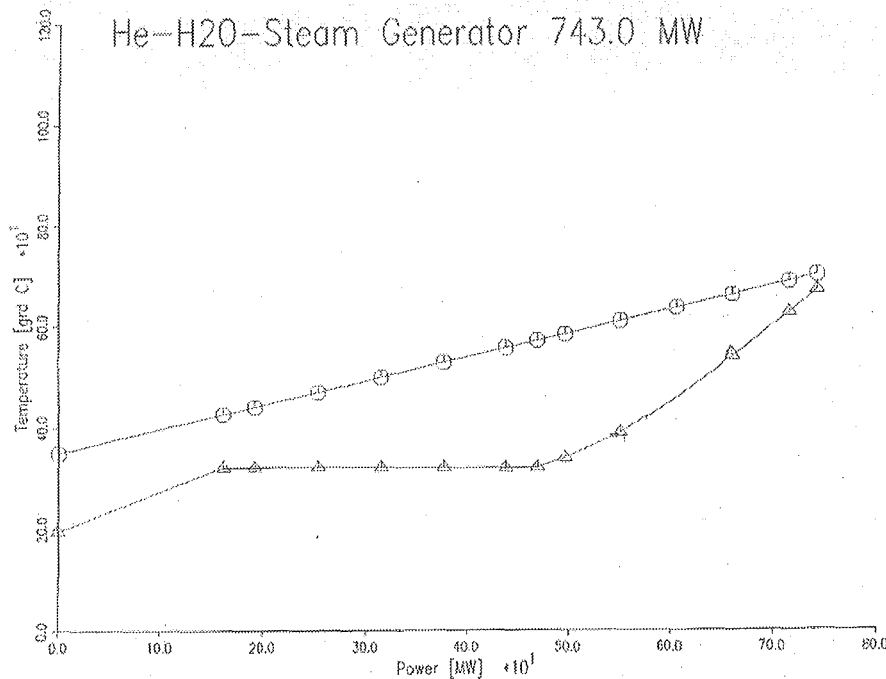

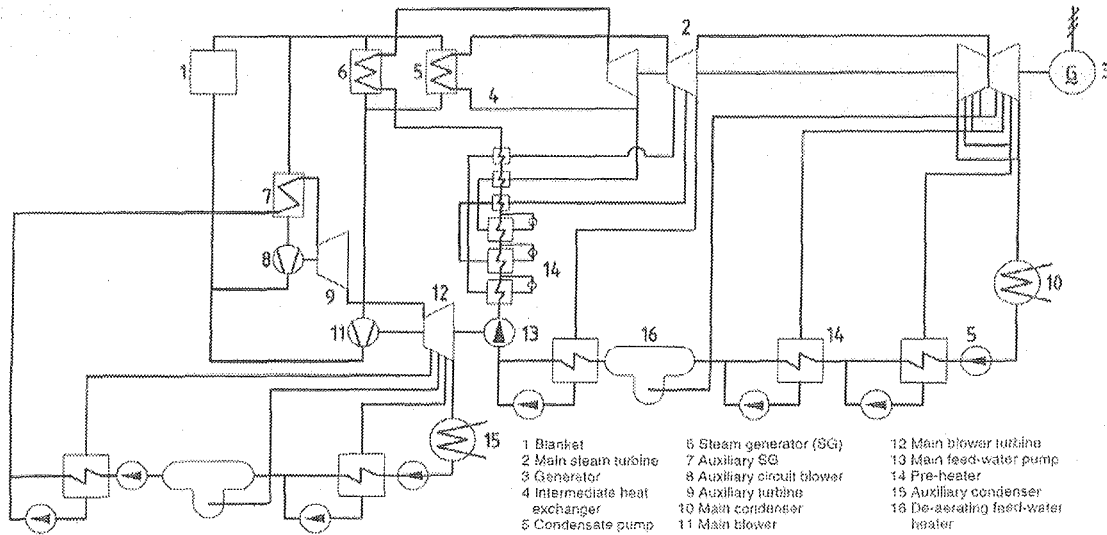Fig. 2: Q-T-diagram for the Rankine concept steam generator

Fig. 3: He-water power generation circuit according of the Rankine concept

	1 Blanket	6 Steam generator (SG)	12 Main blower turbine
	2 Main steam turbine	7 Auxiliary SG	13 Main feed-water pump
	3 Generator	8 Auxiliary circuit blower	14 Pre-heater
	4 Intermediate heat exchanger	9 Auxiliary turbine	15 Auxiliary condenser
		10 Main condenser	16 De-aerating feed-water heater
	5 Condensate pump	11 Main blower	

to be 0.4 MPa. If necessary, also half of the value would be reachable.

Table 4: Heat exchanger design calculation for a Brayton Process and a corresponding Rankine Process

	Rankine	Brayton
Medium	He/H$_2$O	He/He
Power [MW]	743	743
No. of units	6	6
$t_{p\ in}$ [°C]	700	700
$t_{p\ out}$ [°C]	350	350
p_p [MPa]	8.0	8.0
$t_{s\ out}$ [°C]	670	670
$t_{s\ in}$ [°C]	195	320
p_s [MPa]	18	18
Tube dimensions OD × s [mm]	25×2	22×2
Heat transfer area [m^2]	4 230	18500
Bundle type [1]	helical	helical
OD×H [m]	3.1 × 9.4	5.4 × 12.5
Δp_p [MPa]	0.095	0.052
Δp_s [MPa]	0.58	0.40

(1) Helical tube bundles contain a 0.6 m OD. inner cylinder

As far as the integration in the whole reactor is concerned, helium cooled divertors harmonise well with this blanket concept, working in the same temperature range. The heat produced in the divertors (~18% of the whole thermal heat) can be removed and integrated in the same heat removal system of the blankets, increasing the net efficiency of the whole plant.

4.5 Maintainability and reliability

At the present stage of the reactor study a detailed reliability analysis can not be performed yet. A sufficiently extended reliability data collection for components made by SiCf/SiC is not yet available and will presumably not be available in the next future. However, in the proposed design we have applied some design criteria that promise to manufacture components with high reliability. In fact, the number of connections between the high pressure coolant tubes have been minimised. The FW shell should be realised in one piece with the connections (brazing joints) only in back part of the box blanket where the neutron flux

is lower; also each "meander" should be realised in one or only few pieces with the connections sufficiently far from the FW region.

Furthermore, if a gas cycle in the power conversion system is adopted, the presence of water as coolant can be completely eliminated in the reactor avoiding the possibility of water reactions.
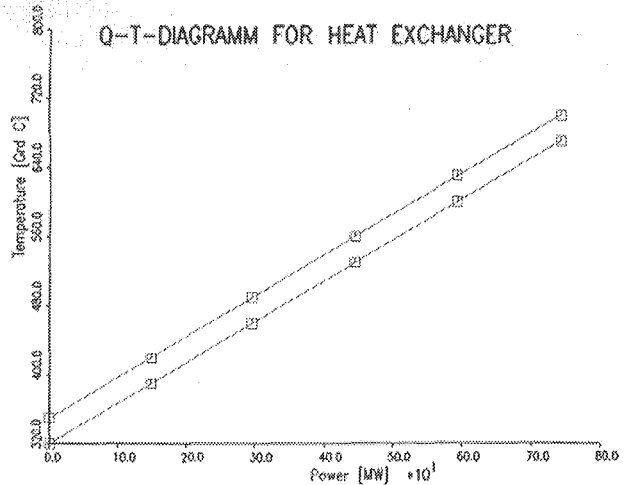

Fig. 4: Q-T-diagram for the Brayton concept steam generator

5. Performance limitations, lifetime and necessary R&D

Starting from the reference design, parametric analyses have been carried out to investigate the performance limitations of this concept in terms of helium temperatures, neutron wall load, surface heating and thermal efficiency.

A limit of 700°C for the outlet temperature of the helium is dictated by the design limit assumed for the maximum temperature in the beryllium pebble bed. This dictates also the maximum net electrical efficiency of about 45% (with reference to the power removed by the helium in the blanket) achievable in this concept. As far as the peak neutron wall load is concerned,

it is possible to find design combinations (with 16 beds and with 300-600°C helium temperatures) able to fulfil the design requirements up to 6 MW/m^2. The margin to increase the surface heating is much less, a value of 0.7 MW/m^2 seems a limitation due to the lower thermal stress parameter of SiCf/SiC in comparison, e.g., to the ferritic-martensitic steels.

Lifetime limitations of this concept are not well known; all the three core materials (beryllium, Li$_4$SiO$_4$ and SiCf/SiC) might limit the lifetime, namely beryllium due to swelling at high temperature, Li$_4$SiO$_4$ due to Li-burnup or dpa damages and SiCf/SiC due to the degradation of its properties under irradiation.

A large amount of R&D work is required especially for SiCf/SiC in order to have a qualified material for fusion application (see section 1). Tightness in general to all the coolants and in particular to helium at high pressure seems at the present the most severe issue. Finally, fabrication issues specific for this design must be addressed, such as the manufactoring of long tubes and shells made by tubes used in this concept as FW and cooling structure in the BZ. Further R&D work is required also for the breeder ceramic and beryllium to determinate its lifetime limitation during irradiation.

6. Conclusions

An advanced version of the HCPB blanket with SiCf/SiC as structural material has been presented; the reference design has been optimised for a peak neutron wall load of 3.5 MW/m^2 and surface heating of 0.6 MW/m^2. A potential advantage of this concept is the possibility to increase the helium temperatures (350°C inlet, 700°C outlet) achieving a gross thermal efficiency of about 46%. With these helium temperature, it is also possible to use a high pressure/high efficiency closed gas Brayton cycle as power conversion system avoiding water in the secondary cycle and increasing the safety of the concept. Furthermore, the pebble beds have been arranged in parallel to the first wall with advantages in reducing the required amount of beryllium and improving the neutronic performances. Finally, the adopted flow scheme results in a decisive reduction of the coolant pressure drop.

In principle, the combination of an inert and not activatable coolant such as helium with SiCf/SiC structures, permits to reach the highest safety and environmental standards in terms of accidental release, maintenance operation and waste disposal issues for a fusion power reactor. However, the success of this particular blanket concept and in general for all the blanket concepts using SiCf/SiC as structural material depends entirely on the future possibility to produce materials with the necessary requirements for fusion application (good thermal conductivity, hermetic sealing, joining technology, stability under irradiation).

Literature:

[1] M. Dalle Donne (Comp.), European DEMO BOT Solid Breeder Blanket, KfK 5429, Forschungszentrum Karlsruhe (1994).

[2] P. Fenici, A.J. Frias Rebelo, R.H. Jones, A. Kohyama and L.L. Snead, Current status of SiC/SiC composites R&D, Journal of Nuclear Materials 258-263 (1998) 215-225.

[3] M. Dalle Donne, A. Goraieb, G. Piazza and G. Sordon,Measurements of the effective thermal conductivity of a Li4SiO4 Pebble Bed, presented to the ISFNT-5, Rome (September 1999), to be published.

[4] F. Scaffidi-Argentina et al., Beryllium R&D for fusion applications, presented to the ISFNT-5, Rome (September 1999), to be published.

[5] L. Giancarli et al., Design requirements for SiCf/SiC composites structural material in fusion power reactor blankets, Fusion Engineering and Design 41 (1998) 165-171.

[6] Gasse and al., Progress on SiCf/SiC structures joining techniques and modelling for design analyses, Proc. of the 20th SOFT, Marseille (1998), pp.1235-1238

[7] S. Sharafat and al., ARIES-I Fusion-Power-Core Engineering, Fusion Engineering and Design 18 (1991), 215-222.

[8] H. Kleykamp, Chemical reactivity of SiC fibre reinforced SiC with beryllium and ceramic breeder materials, presented at the 9th Conf. On Fusion Reactor Materials, Colorado Springs, USA, 10-15 October 1999, to be published.

[9] Cook, UKAEA Culham, PPA parameters, e-mail of 12 March, 1999.

[10] F. Briesmeister (ed.): MCNP - A General Monte Carlo N-Particle Transport Code, Version 4A, LA-12625-M, November 1993, Version 4B March 1997

[11] P. Vontobel: A NJOY Generated Neutron Data Library Based on EFF-1 for the Continuous Energy Monte Carlo Code MCNP, PSI-Bericht Nr. 107, September 1991

[12] S. Malang, H. Schnauder and M.S. Tillack, Combination of a self-cooled liquid metal breeding blanket with a gas turbine power conversion system, Fusion Engineering and Design 41(1998) 561-567.

Staff:

L. Boccaccini
S. Gordeev
U. Fischer
S. Malang
H. Schnauder

Work for Wendelstein 7 X

Project Microwave Heating (PMW) for Wendelstein 7-X (ECH 1)

1. Introduction

The project includes the development, construction and operation of the 10 MW-140 GHz Electron Cyclotron Resonance Heating (ECRH) system in continuous wave operation (CW) for the stellarator W7-X at Greifswald in a collaboration between Forschungszentrum Karlsruhe, IPF Stuttgart and IPP Garching [1]. The stellarator plasma should be created and heated from the neutral gas by this ECRH system. With 10 MW heating power the plasma parameter region of long free mean path length, which is relevant for fusion reactors, can be reached. In addition, a stationary non-inductive current can be driven to influence the plasma profile for better plasma confinement. The 10 MW of rf-power should be obtained using ten 140 GHz gyrotrons each having 1 MW output power.

2. Development of Prototype Gyrotron

A 1 MW 140 GHz gyrotron with a chemical vapour deposition (CVD) diamond window for continuous wave (CW) operation and a single-stage depressed collector for energy recovery and improvement of efficiency has been designed and constructed in collaboration with CRPP Lausanne and TTE Vélizy [2] (Fig. 1). It operates in the $TE_{28,8}$ cavity mode and provides a linearly polarized $TEM_{0,0}$ Gaussian RF beam. The gyrotron consists of a diode MIG gun, an improved beam tunnel, a high-mode purity low-ohmic loss cavity ($<2kW/cm^2$), an optimised non-linear up-taper, a highly efficient internal quasi-optical mode converter employing an improved launcher together with one quasi-elliptical and two toroidal beam shaping reflectors and a horizontal RF output. The large single-stage depressed collector is at ground potential and is equipped with a beam sweeping magnet.

The new development uses the know how acquired in the development and operation of 118 GHz gyrotrons installed at CEA (Cadarache) and CRPP (Lausanne) [3], the know how both in developing and operating short-pulse gyrotrons at high output levels at Forschungszentrum Karlsruhe and the know how acquired in the development of a CVD diamond window at Forschungszentrum Karlsruhe (see window development). The 140 GHz/CW gyrotron for Wendelstein 7-X will be constructed in the framework of a collaboration between FZK Karlsruhe, CRPP Lausanne, TTE Vélizy, IPF Stuttgart and IPP Garching. The main design parameters of the maquette are listed in table 1.

Table 1: Design parameters of the 140 GHz/1MW, $TE_{28,8}$ gyrotron

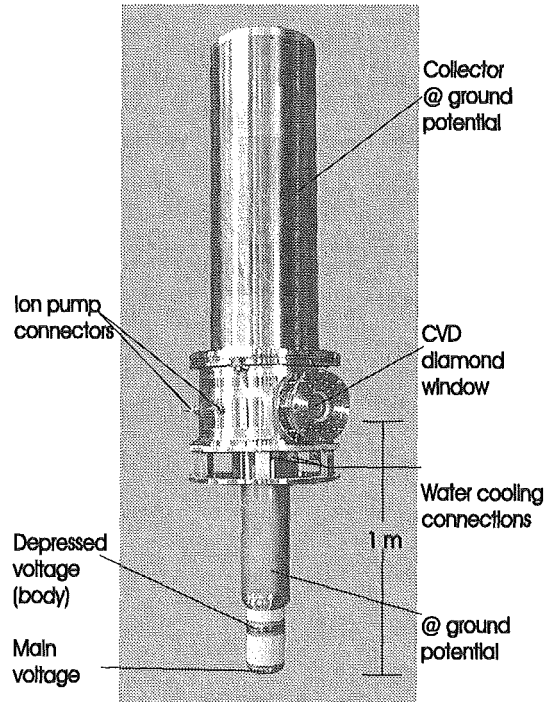|	
Accelerating voltage V_b	80 kV
Beam current I_b	40 A
Cavity magnetic field B_0	5,56 T
Beam radius in the cavity	10,1 mm
Average pitch angle (α)	1,5
Peak cavity wall loading	<2 kW/cm^2
RF power	1 MW, CW
Overall efficiency	45%
Window material	CVD Diamond

Fig. 1: Photograph of the 140 GHz gyrotron.

The first tube (maquette) has already been fabricated, baked out at 450°C and tested for leak tightness and HV-insulator strength.

First rf-tests will begin in December 1999 and will be performed on the long-pulse test stand located at the Forschungszentrum Karlsruhe. The superconducting magnet system has been built. It will be tested at Oxford Instruments and then shipped to Karlsruhe in November 1999.

3. Development of Quasi-Optical Transmission line

The prototype transmission line and the thermomechanical behaviour of the mirrors were investigated. The uncooled multi-beam waveguide mirrors (MBWG) and their alignment have been tested successfully. According to these results the construction of the MBWG mirrors was performed. Prototyp-mirrors will be built and tested. Two water cooled mirrors will be fabricated for the test stand at the Forschungszentrum. They allow to deflect the 1 MW Gaussian beam into the horizontal rf water load.

4. Auxilliary systems

To operate the maquette tube with a depressed collector at ground potential a new power supply for the depressed voltage U_b had to be installed. This power supply is designed for a depression voltage up to + 35 kV and a current up to 200 mA. It was successfully tested together with the HV long-pulse power-supply existing at the Forschungszentrum. The water cooling circuits for the test stand are installed. The measurements proved that the desired pressures and water flow rates could be achieved.

The microwave chamber to house the mirrors, water load and field distribution measurement devices for the rf-tests on the gyrotrons is erected. Minor changes are necessary to adapt it to the maquette tube.

Literature:

[1] Erckmann, V., Dammertz, G., Dorst, D., Empacher, L., Förster, W., Gantenbein, G., Geist, T. Kasparek, W., Laqua, H.P., Müller, G.A., Thumm, M., Weissgerber, M., Wobig, H., IEEE Trans. on Plasma Science , 1999, 27 (2), 538-546.

[2] Thumm, M., Alberti, S., Arnold, A., Borie, E., Dammertz, G., Erckmann, V., Garin, P., Giguet, E., Illy, S., Le Cloarec, G., Le Goff, Y., Magne, R., Michel, G., Piosczyk, B., Tran, M.Q., Wagner, D., Conf. Digest 24th Int. Conf. Infrared and Millimeter Waves, 1999, Monterey, California, USA, W-2.

[3] Tran, C., Giguet, E., Thouvenin, P., Garin, P., Pain, M., Alberti, S., Tran, M.Q., Thumm, M., Conf. Digest 23rd Int. Conf. Infrared and Millimeter Waves, 1998, Colchester, UK, 271-273.

Staff:

A. Arnold (Uni Karlsruhe)
E. Borie
G. Dammertz
P. Grundel
S. Illy
H. Kunkel
M. Kuntze
W. Leonhardt
G. Neffe
B. Piosczyk
M. Schmid
J. Szczesny
M. Thumm

Test of the Wendelstein 7-X (W 7-X) DEMO-Coil in TOSKA

For the construction of the superconducting stellarator W 7-X in Greifswald under the responsibility of IPP, Garching, the successful construction and test of a superconducting non planar DEMO-Coil was one of the most important milestones. The test of the W 7-X DEMO-Coil in the TOSKA facility was agreed within the frame of collaboration between the IPP Garching and the Forschungszentrum Karlsruhe. The coil was constructed by European industry (Noell, Würzburg, Germany; Ansaldo, Genova, Italy) under the responsibility of IPP Garching. It was foreseen to test the W 7-X DEMO-Coil in the background field of the EURATOM LCT coil in the TOSKA facility to achieve nearly the mechanical stress levels expected in the toroidal configuration. The test of the W 7-X coil in the TOSKA facility was also carried out as an intermediate step to prepare the TOSKA facility for testing of the ITER toroidal field model coil.

1. Installation of the W 7-X DEMO-Coil in TOSKA

The intercoil structure between LCT and W 7-X DEMO-Coil was delivered in advance and matched by epoxy resin impregnated fiberglass fillers to the surface of the LCT coil in the TOSKA vacuum vessel. Simultaneously the lifting procedure for the later installation was exercised by a frame having the outer dimensions of the W 7-X coil . The W 7-X coil mounted on the intercoil structure was delivered in July 1998. The coil was prepared by the following working packages for installation:

- Acceptance test after arrival: Visual inspection, high voltage insulation test, leak test and continuity test of the instrumentation.

- Assembling of the helium header of the prototype W 7-X coil

- Installation of the mechanical sensors (strain gauge rosettes)

- Check of the voltage tap assignment to the conductor joints and high voltage insulation test between winding and case

- Completion of current leads

- Definition of the test program and composition of a manual for testing

In October 1998 the coil was moved into the vacuum vessel of the TOSKA facility and mounted adjacent to the LCT coil. The W 7-X coil was connected to the TOSKA facility by the following work packages:

Lateral mechanical fixture of the configuration

- Installation of current lead support structure and current leads

- Adaptation of the superconducting bus bars between coil terminals and cold ends of the current leads, final assembling work and making of the Paschen tight electrical insulation

- Piping fitting between coil and TOSKA facility for supply and venting pipes and instrumentation capillaries

- Routing of high voltage and low voltage instrumentation cables to the feedthrough chamber or to the feedthrough sockets, respectively

- Final tests (overall leak test, high voltage insulation test, flow test, instrumentation continuity)

After repair of one leak located in the outer supporting tube of one current lead the system was ready for testing. The W 7-X DEMO-Coil during installation is shown in Fig. 1.

2. The test of the W 7-X DEMO-Coil

The cooldown was started middle of May 1999. The cooldown condition was 40 K temperature difference between winding case and intercoil structure. The cooldown rate was slowed down by not so well cooled structural parts like the coil support bearings. The cooldown was slowed down to 0.5 K/h and was then accelerated by increasing the temperature difference to this parts to 80 K. The averaged cooldown rate was then about 1 K/h. The superconducting state was reached on June 8, 1999 and the current test were started June 14, 1999. The test program was performed in the following steps:

- Load case A: W 7- X coil alone up to the quench current

- Load case B: W 7-X (14.7 kA) and LCT (14.0 kA) coil at rated currents

- Load case C: Overload W 7-X (up to quench current) and LCT at 14.0 kA

In load case A the coil achieved a quench current of 19.9 kA in fair agreement with the expected load line value extrapolated from the test coil measurements (Fig. 2). The adjustment of the thermohydraulic parameters was not easy caused by the low mass flow rate and the relatively high pressure drop for the W 7-X conductor. Further, losses in the header which could not be clarified completely , caused about 0.4 K temperature rise. This temperature difference could not be reduced by using a higher mass flow rate due to the pressure drop. These facts limited the winding inlet temperature to about 4 K. A leak appearing in one current lead support tube after cooldown caused a decrease of the vacuum. The heat conduction of the residual gas was investigated for the different components (Fig. 3), however, the header losses measured could not be related to poor vacuum conditions.

Load case B was achieved in stable operation over about 45 minutes. The stresses on the coil case were in fair agreement with calculations and some displacement transducers showed zero displacement. The other ones showed about 50 % of the displacement expected.

Load case C achieved a quench current of about 16.7 kA which was somewhat lower than expected (Fig. 2).

All components of the facility worked reliably. All quenches were reliably detected and actuated the dump circuit. The safety discharges were managed without helium losses to the atmosphere. The simultaneous operation of two magnets were handled without problems (Fig. 4). The impact of magnetic fringing fields on zero flux current transformers of the 30 kA power supply was found. The problem was solved by using the AC current transformers which had less accuracy but were sufficient to continue test program.

After successful performance of the test program the warm up was started July 22, 1999 in joint agreement with the IPP Garching. After achieving room temperature the coil was disconnected from the TOSKA facility and removed from the vacuum vessel. Mid of October 1999 the coil left Forschungszentrum Karlsruhe.

After the successful completion of the joint test of the W 7-X DEMO coil the manufacturing of the series coils was finally released.
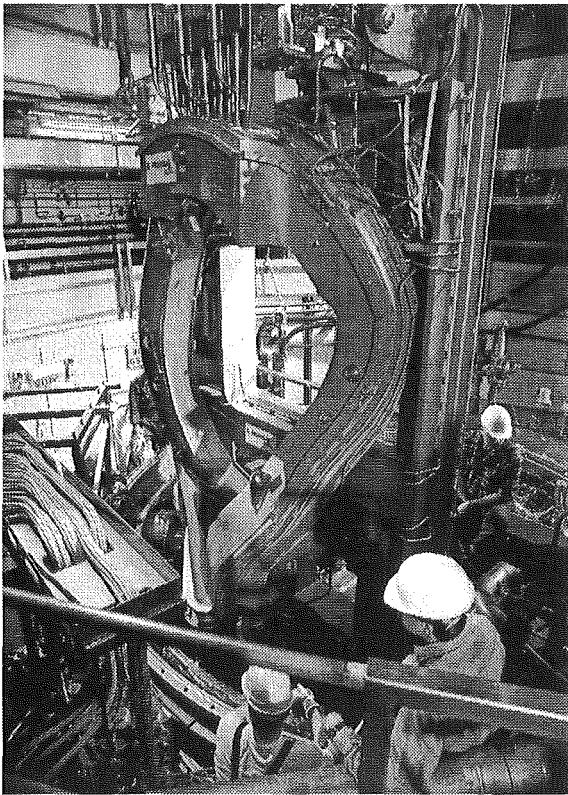

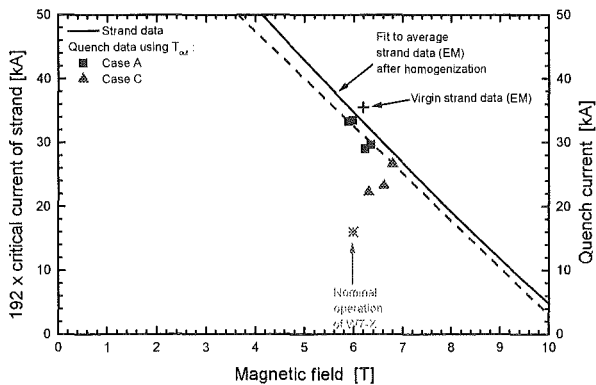Fig. 1: The W 7-X coil during lifting procedure in the TOSKA vacuum vessel

Fig. 2: Expected critical currents versus the magnetic field at 4.2 K deduced from single strand data given by the manufacturer (solid line) and measured quench currents of the W 7-X coil rescaled to 4.2 K. The dashed line is an eye-fit through the measured numbers without those showing a different quench signal
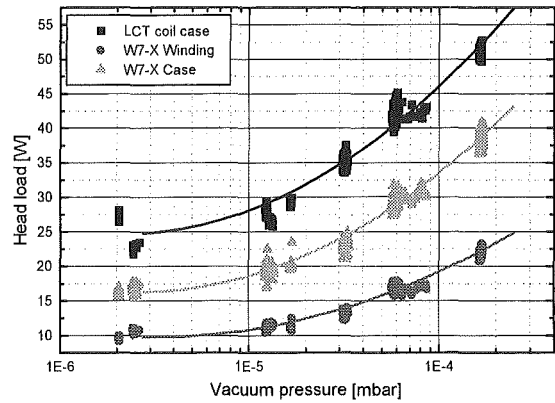

Fig. 3: Heat load on the different components (LCT coil case, W 7-X winding, and coil case) versus the heat conduction of the residual gas

Staff:

H. Bai (till Nov. 26, 99)
K. Bauer
M. S. Darweschsad
P. Duelli
S. Fink
G. Friesinger
A. Götz
R. Heller
W. Herz
A. Kienzler
H. Lahn
V. Leibbrand
A. Lingor
V. Marchese
W. Maurer
I. Meyer
G. Nöther
H.-P. Schittenhelm
K. Schweikert
E. Specht
H.-J. Spiegel
M. Süßer
A. Ulbricht
D. Weigert
F. Wüchner
G. Zahn
V. Zwecker
R. Meyder
W. Kerbstein
K. Rietzschel (till July 30, 99)
W. Eppler (since Aug.1, 99)
W. Ratajczak
G. Schleinkofer
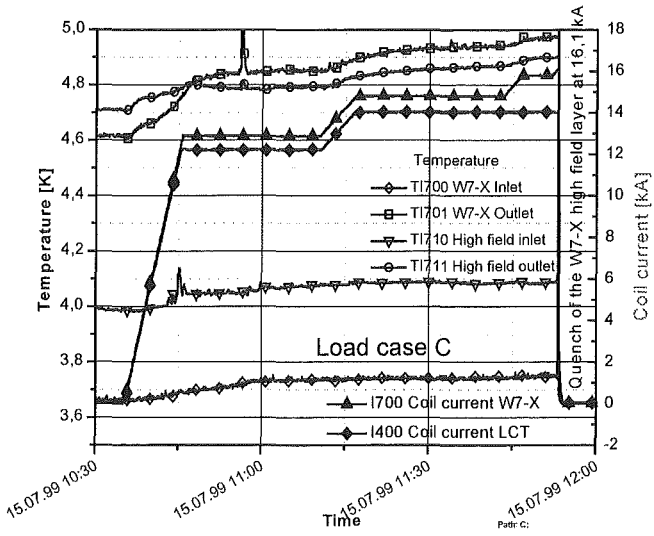O. Langhans
G. Dittrich
A. Völker

Fig. 4 : The temperature and current traces during the ramp up
of W 7-X and LCT coil

Appendix I: FZK Departments Contributing to the Fusion Project

FZK Department	FZK Institut/Abteilung	Director	Ext.
Institute for Materials Research	Institut für Material- und Festkörperforschung (IMF)	I. Prof. Dr. K.-H. Zum Gahr	3897
		II. Prof. Dr. D. Munz	4815
		III. Prof. Dr. H. Haußelt	2518
Institute for Pulsed Power and Microwave Technology	Institut für Hochleistungs-Impuls- und Mikrowellentechnik (IHM)	Prof. Dr. M. Thumm	2440
Institute for Nuclear and Energy Technology	Institut für Kern- und Energietechnik (IKET)	Prof. Dr. U. Müller	3450
Institute for Reactor Safety	Institut für Reaktorsicherheit (IRS)	Prof. Dr. D. Cacuci	2550
Institute for Technical Physics	Institut für Technische Physik (ITP)	Prof. Dr. P. Komarek	3500
Central Experimental Department	Hauptabteilung Versuchstechnik (HVT)	Dr. K. Schubert	3114
- Hot Cells	- Heiße Zellen (HVT-HZ)	Dr. W. Nägele	3650
- Tritium Laboratory Karlsruhe	- Tritiumlabor Karlsruhe (TLK)	Dr. R.D. Penzhorn	3239
Central Department for Data Processing and Electronics	Hauptabteilung Prozeßdatenverarbeitung und Elektronik (HPE)	Prof. Dr. H. Gemmeke	5635

Contributing:

Institute for Nuclear and Particle Physics, Technical University Dresden	Institut für Kern- und Teilchenphysik der Technischen Universität	Prof. Dr. H. Freiesleben	0351/4635461
Underwater Technology Centre of the Institute of Materials Science University of Hannover	Unterwassertechnikum Hannover des Instituts für Werkstoffkunde der Universität Hannover	Prof. Dr.-Ing. Dr.-Ing. e.h.mult. H. Haferkamp	0511/7624311

Appendix II: Fusion Project Management Staff

Head of the Research Unit	Dr. J.E. Vetter	ext. 5460 e-mail: joerg.vetter@pkf.fzk.de
Secretariate:	Mrs. I. Sickinger	ext. 5461 e-mail: ingeborg.sickinger@pkf.fzk.de
	Mrs. I. Pleli	ext. 5466 e-mail: ingrid.pleli@pkf.fzk.de
	Mrs. V. Lallemand	ext. 5466 e-mail: vera.lallemand@pkf.fzk.de
Project Budgets, Administration, Documentation	BW. G. Kast	ext. 5462 e-mail: guenter.kast@pkf.fzk.de
Studies, ITER / NET Contracts, Superconducting Magnets, Gyrotron Development	Dr. J.E. Vetter	ext. 5460 e-mail: joerg.vetter@pkf.fzk.de
Tritium Technology, Structural Materials	Dr. H.D. Röhrig	ext. 5463 e-mail: roehrig@pkf.fzk.de
	DI. S. Gross	ext. 5468 e-mail: Sigurd.Gross@pkf.fzk.de
Blanket Technology	DI. A. Fiege	ext. 5465 e-mail: albert.fiege@pkf.fzk.de
	DI. W. Bahm	ext. 6578 e-mail: werner.bahm@pkf.fzk.de

Address:

Forschungszentrum Karlsruhe GmbH
Nuclear Fusion Project Management

Post Office Box 3640, D - 76021 Karlsruhe / Germany

Telephone No: **07247-82- Extensions .....**

Telefax No: **07247-82-5467**

Telex No: **17 724 716**

world wide web: **http://www.fzk.de/pkf**